# NANOSCALE MATERIALS IN CHEMISTRY

# NANOSCALE MATERIALS IN CHEMISTRY

*Edited by*

**Kenneth J. Klabunde**

**WILEY-INTERSCIENCE**

**A John Wiley & Sons, Inc., Publication**

New York • Chichester • Weinheim • Brisbane • Singapore • Toronto

*To Linda*

# CONTENTS

# PREFACE

Nanotechnology is almost a household word now-a-days, or at least some word with "nano" in it, such as nanoscale, nanoparticle, nanophase, nanocrystal, or nano-machine. This field now enjoys worldwide attention and a National Nanotechnology Initiative (NNI) is about to be launched.

This field owes its parentage to investigations of reactive species (free atoms, clusters, reactive particles) throughout the 1970s and 1980s, coupled with new techniques and instruments (pulsed cluster beams, innovations in mass spectrometry, vacuum technology, microscopes, and more).

Excitement is high and spread throughout different fields, including chemistry, physics, material science, engineering, and biology. This excitement is warranted because nanoscale materials represent a new realm of matter, and the possibilities for interesting basic science as well as useful technologies for society are widespread and real.

In spite of all this interest, there is a need for a book that serves the basic science community, especially chemists.

This book was written to serve first as a advanced textbook for advanced undergraduate or graduate courses in "nanochemistry", and second as a resource and reference for chemists and other scientists working in the field. Therefore, the reader will find that the chapters are written as a teacher might teach the subject, and not simply as a reference work. Therefore, we hope that this book will be adopted for teaching numerous advanced courses in nanotechnology, materials chemistry, and related subjects.

The coverage of this volume is as follows: First, a detailed introduction of nanotechnology and a brief historical account is given. This is followed by masterful chapters on nanosize metals by Gunter Schmid, semiconductors by Marie Pileni, and ceramics by Abbas Khaleel and Ryan Richards. The next chapters deal more with properties, such as optical properties by Paul Mulvaney, magnetic properties by Chris Sorensen, catalytic and chemical properties by the editor and Ravi Mulukutla, physical properties by Olga Koper and Slawomir Winecki, and finally a short chapter on applications of nanomaterials by John Parker.

The editor gratefully acknowledges the contributing authors of these chapters, who are world renowned experts in this burgeoning field of nanotechnology. Their enthusiasm and hard work are very much appreciated. The editor also acknowledges the help of his students and colleagues, as well as his family for their patience and understanding.

<div align="right">Kenneth J. Klabunde</div>

# CONTRIBUTORS

DR. ABBAS KHALEEL,    Dept. of Chemistry, UAE University, Al-Ain, United Arab Emirates

PROFESSOR KENNETH J. KLABUNDE,    Dept. of Chemistry, Kansas State University, Manhattan, KS 66506

DR. OLGA KOPER,    Nanoscale Materials, Inc., 1500 Hayes Drive, Manhattan, KS 66502

DR. RAVICHANDRA S. MULUKUTLA,    Department of Chemistry, Kansas State University, Manhattan, Kansas 66506

DR. PAUL MULVANEY,    Advanced Mineral Products, School of Chemistry, University of Melbourne, Parkville, VIC 3052, Australia

DR. JOHN C. PARKER,    1588 Clemson Dr., Naperville, IL 60565

PROFESSOR MARIE PILENI,    Department of Chemistry, Laboratorie SRSI, URA CNRS 1662, Universite P. et M. Curie (Paris VI), BP52, 4 Place Jussieu, 75231 Paris Cedex 05, France

DR. RYAN RICHARDS,    Dept. of Chemistry, Max Planck Institute, Kaiser Wilhelm Platz 1, 45470 Mulheim an der Ruhr, Germany

PROFESSOR GUNTER SCHMID,    Institute fur Anorganische Chemie, Universitat Essen, Essen, Germany

PROFESSOR CHRIS SORENSEN,    Dept. of Physics, Cardwell Hall, Kansas State University, Manhattan, KS 66506

DR. SLAWOMIR WINECKI,    Nanoscale Materials, Inc., 1500 Hayes Drive, Manhattan, KS 66502

# Index

# 1   Introduction to Nanotechnology

KENNETH J. KLABUNDE

Department of Chemistry, Kansas State University, Manhattan, Kansas and Nanoscale
Materials, Inc., Manhattan, Kansas

## 1.1   INTRODUCTION TO THE NANOWORLD

It has been said that a nanometer is "a magical point on the length scale, for this is the point where the smallest man-made devices meet the atoms and molecules of the natural world."[1]

Indeed, "nanotechnology mania" is sweeping through essentially all fields of science and engineering, and the public is becoming aware of the quote of the chemist and Nobel Laureate, Richard Smalley: "Just wait—the next century is going to be incredible. We are about to be able to build things that work on the smallest possible length scales, atom by atom. These little nanothings will revolutionize our industries and our lives."[2]

In a recent report of the National Science Foundation to the President's Office of Science and Technology Policy it was stated that "Nanoscience and technology will change the nature of almost every human-made object in the next century."[3]

So what are these "nanothings" that are going to change our lives? Perhaps the best way to begin to convey the possibilities is to list topical areas that nano-technology promises to affect.

*Pharmacy*    It may be possible to create biomolecules that carry out "pharmacy in a cell,"[1] that could release cancer-fighting nanoparticles or chemicals in response to a distress signal from an afflicted cell.

*Therapeutic Drugs*    It is now possible to produce new solid state medicines by simply producing them in nanoparticle form. The high surface areas of these small particles allow them to be solubilized into the bloodstream where normal micro

**1**

particles or larger particles cannot.[3] Since over 50% of new drug formulations are never brought to market because of solubility problems, this simple transformation into a nano-form opens up broad new possibilities for drug synthesis and utilization.[3]

*Tagging of DNA and DNA Chips*    Nanoparticle assay of DNA has been possible by coating gold nanoparticles with DNA strands. When these are exposed to complementary DNA, binding (hybridization) occurs, and this causes the colloidal gold particles to aggregate, and as a result a color change takes place.[4,5]

Microarrays to detect and help identify DNA samples have been built by creating devices with up to 100,000 different known DNA sequences. When the unknown target DNA sequences match with any of the DNA chip arrays, then binding (hybridization) occurs and the unknown sequence is identified by its position on the array.[3]

*Information Storage*    Ultrafine dye particles often yield higher quality inks in terms of color, coverage, and color-fastness.[6] Also, "nanopens" (atomic force microscope tips) can write letters with features as small as 5 nm.[1]

Actually, nanoparticles have already found their way into modern audio and videotapes and disks, which are dependent on magnetic and optical properties of fine particles. Further advances will be made with smaller and smaller sizes and with control of magnetic coercivity and optical absorption, so that much denser storage media should be possible.[6]

*Refrigeration*    On a small scale it has been demonstrated that an entropic advantage can be gained in magnetic particle field reversal. Thus, upon application of a magnetic field, the entropy of a magnetic species changes, and if adiabatic conditions are maintained, the application of the field will result in a temperature change. This $\Delta T$ is the magnetocaloric effect, and the magnitude of this effect depends on the size of the magnetic moment, heat capacity, and temperature dependence of the magnetization. If nanoparticles with large magnetic moments and adequate coercivity can be obtained, the magnetocaloric effect may allow refrigeration on a practical scale.[7]

The promise of magnetic nanoparticle refrigerators, with no need for refrigeration fluids (Freons, HFC, etc.), has enticed many researchers, and success would mean tremendous benefits for society and the environment.

*Chemical/Optical Computers*    Organized two-dimensional or three-dimensional arrays of metal or semiconductor nanoparticles exhibit special optical and magnetic properties. These materials hold promise in numerous applications in the electronics industry, including optical computers.[8,9]

*Improved Ceramics and Insulators*    The compression of nanoscale ceramic particles yields more flexible solid objects, apparently because of the multitude of grain boundaries that exist.[3,10] After further development of compression techniques, so

that highly densified nonporous materials can be prepared, these new materials may find uses as replacements for metals in many applications.

*Harder Metals*   Nanoparticulate metals when compressed into solid objects exhibit unusual surface hardness, sometimes as high as five times that of the normal microcrystalline metal.[3,10]

*Film Precursors*   Similar to their use in inks, nanoqueous metallic colloidal solutions have proven useful as precursors for thin metallic film formation when used as spray paint.[11] In particular, gilding of silver artifacts with gold has been accomplished with gold–acetone colloids.[12,13]

*Environmental/Green Chemistry*

- *Solar Cells*. Semiconductor nanoparticles, with size-tunable bandgaps, hold the potential for more efficient solar cells for both photovoltaics (electricity production) and water splitting (hydrogen production).[14,15]
- *Remediation*. Photoexcitation of fine particles of semiconductors leads to electron–hole pairs that are useful for both oxidation and reduction of pollutants, for use in decontaminating water.[14–16]
- *Water Purification*. Reactive metal fine powders (Fe, Zn) show high reactivity toward chlorocarbons in an aqueous environment. These results have led to the successful implementation of porous metal powder–sand membranes for groundwater decontamination.[17]
- *Destructive Adsorbents*. Nanoparticulate metal oxides exhibit high intrinsic surface reactivities and high surface areas, and strongly chemisorb acidic gases and polar organics. Since dissociative chemisorption is usually observed , these new materials have been dubbed "destructive adsorbents," and are finding use in anti-chemical/biological warfare,[18] in air purification,[19] and as an alternative to incineration of toxic substances.[20]

*Catalysts*   Successful catalytic processes developed over the last six decades have led to a vital industry that contributes to the economy at least 20% of the GDP.[21]

What is significant in the context of nanostructural materials in chemistry is that heterogeneous catalysis is dependent on nanoparticles of metals, and research on the effect of particle size (percent dispersion as a measure of the fraction of metal atoms on the surface and thus available to incoming reactants) and shape (crystal faces, edges, corners, defects that lead to enhanced surface reactivity) has been and continues to be a vigorous field.

*Sensors*   Porous aggregates of semiconductor nanoparticles can be prepared by low-load compression. These materials maintain their high surface areas, and when they undergo adsorption of various gases, their electrical conductivity changes. Since more of the gas to be detected (such as sulfur dioxide) is adsorbed per unit

mass compared with normal compressed powders, the electrical changes are more pronounced. Thus, the use of nanoparticles yields a considerable advantage in sensor technology.

*Defect-tolerant Chemically Assisted Architectures* Size reduction of electronic devices, if continued apace, will reach the size of *molecules* in a few decades. However, when entering the molecular scale or nanoscale, the fact that these are quantum mechanical objects means that the physics upon which the devices are based will be dramatically changed. Manufacturing processes will also have to change dramatically. One concept of making such a dramatic shift is through molecular electronics; molecules will have to serve as quantum electronic devices, and be synthesized and allowed to self-assemble into useful circuits. Recent efforts have shown some promise; for example, electrical properties of a single immobilized benzene-1,4-thiol molecule have been measured.[22] Also, a molecular switch based on the rotaxane molecule has been experimentally demonstrated.[9,23]

*Nanostructured Electrodes* Nanoscale metal crystallites can be grown by rapid electrodeposition due to very high nucleation rates and thereby reduced crystallite (grain) growth. Magnetic metals such as iron can then form dense magnetic solids with soft magnetic properties (low coercivity and high saturation magnetization). These materials are useful for transformers.[24,25]

*Improved Polymers* There are almost magical effects produced when nanopowders are added to polymer matrices. The nanopowders can be in the form of fine particles, needlelike structures, or platelets. There is a reinforcing effect such that strength of the composite is greatly increased.

The mechanism by which this reinforcement takes place is poorly understood at present. However, with further work and better understanding, the potential outcomes of improved polymers and plastics are easy to imagine. Stronger, lighter materials, wear-resistant tires, tougher coatings, replacements for body parts, flame-retardant plastics, replacements for metals, and more can be imagined.[3]

*Self-cleaning and Unusual Coloring in Paints* It has been demonstrated that when paints are doped with light-absorbing nanoparticles, such as $TiO_2$, the paints are self-cleaning.[3] The mechanism by which this happens is related to photooxidation of contaminants by $TiO_2$ in water discussed earlier. Organic greasy materials that adhere to paint can be oxidized by the electron–hole pair formed when $TiO_2$ nanoparticles absorb sunlight. Thus, the organic materials are cleaned off the paint film. It is perhaps surprising that the paint itself is not attacked by this powerful oxidation/reduction couple, and it may be found that such paints are not as long-lived as those that are not doped with $TiO_2$ nanoparticles.

Another interesting development is the use of gold nanoparticles to give paints a beautiful metallic reddish color, due to the special optical properties of such particles.[26]

*Smart Magnetic Fluids*  Ferrofluids are colloidal solutions containing small magnetic particles stabilized with surfactant ligands. These have been known since the 1960s and are important as vacuum seals, viscous dampers, and contamination exclusion seals. With improvements, other applications may become important, such as their use as cooling fluids, nanoscale bearings, magnetically controlled heat conductors, and magnetic acids in separation of ores in mining and scrap metal separation.[3,27]

*Better Batteries*   Nanostructural materials in lithium ion batteries have proven to be very advantageous. For example, researchers at Fuji found that by placing nano-crystalline tin (7–10 nm) within an amorphous glass-forming matrix yielded nano-crystalline islands of tin enclosed by an amorphous oxide network. Electrical conductivity can be maintained within such an electrode. The advantage of such a nanostructural material is that the rather open structure of the glass helps to accommodate strain associated with the volume expansion during insertion and removal of lithium from tin. Also, it is believed that the nanocrystalline nature of the tin precludes formation of bulk phases of Li–Sn alloys, which are deleterious to the battery.[3,28]

Other advantages have been gleaned from nanostructural materials, such as the rapid reaction of $Li_2CO_3$ and NiO to form a desired mixed oxide.[29] Dragieva and coworkers have prepared a series of nickel–metal–hydride (Ni–M–H) batteries through the preparation of nickel nanoparticles by borohydride reduction in water.[30]

In general, the ability to prepare metallic nanocrystals that can be consolidated into high-surface-area electrodes has certain inherent advantages, and further progress is sure to come.

*Improved National Security*   The use of high-surface-area reactive nanoparticles as destructive adsorbents for decontamination of chemical and biological warfare agents has proven quite effective, and allows rapid response with few logistical problems.[31,32]

Sensors for toxic airborne and waterborne materials are also possible through the unique adsorbent properties of consolidated nanocrystals. Indeed, there appear to be numerous areas where national security can be improved through advances in nanotechnology in electronics, optics, catalysts, and sorbents.[3]

*Summary*   It is quite apparent that there are innumerable potential benefits for society, the environment, and the world at large. Some of them have been briefly described, but the list is longer still.[3]

Before presenting greater detail, as Chapters 2–9 will do regarding nanomaterials in chemistry and related fields, it is appropriate now to describe in a more academic sense why nanoparticles are so unique.

## 1.2   A NEW REALM OF MATTER THAT LIES BETWEEN CHEMISTRY AND SOLID STATE PHYSICS

After considering the current interest in nanotechnology, it seems appropriate to place the nanoworld in the context of basic sciences. Chemistry is the study of atoms and molecules, a realm of matter of dimensions generally less than one nanometer, while condensed matter physics deals with solids of essentially an infinite array of bound atoms or molecules of dimensions greater than 100 nm. A significant gap exists between these regimes. Figure 1.1 illustrates this gap, which deals with particles of 1 to 100 nm, or about 10 to $10^6$ atoms or molecules per particle.[33,34]

In this nanoscale regime neither quantum chemistry nor classical laws of physics hold.[2] In materials where strong chemical bonding is present, delocalization of valence electrons can be extensive, and the extent of delocalization can vary with the size of the system. This effect, coupled with structural changes with size variation, can lead to different chemical and physical properties, *depending on size*. Indeed, it has now been demonstrated that a host of properties depend on the size of such nanoscale particles, including magnetic properties, optical properties, melting points, specific heats, and surface reactivity. Furthermore, when such ultrafine particles are consolidated into macroscale solids, these bulk materials sometimes exhibit new properties (e.g., enhanced plasticity).

It is clear that a huge new field of science has been born. Think of the multitude of combinations of two, three, or more elements with particles of varying sizes! Each change in composition or size can lead to different physical and chemical properties. It is evident that an almost infinite number of possibilities present themselves. And this new field of clusters/nanophase materials, lying between the traditional fields of chemistry and solid-state physics, touches upon disciplines such as electronics, astronomy, mathematics, and engineering. Therefore, interdisciplinary research is required for progress to be made. The most important aspects are synthesis, physical properties, and chemical properties, but the most important of these at this time is *synthesis*. The nanoparticles of interest are almost always prepared in the laboratory (as opposed to occurring naturally), are sometimes reactive with oxygen and water, and are difficult to produce in a monodisperse (one size only) form. Thus creative synthesis schemes that lead to gram or kilogram quantities of pure materials are absolutely essential before this new field of science can be developed for the benefit of humankind.

| Atoms/<br>Molecules | Nanoscale<br>Particles | | Condensed<br>Matter | |
|:---:|:---:|:---:|:---:|:---:|
| 1 | 125 | 70,000 | $6\times10^6$ | $\infty N^o$Atoms |
| | 1 | 10 | 100 | $\infty$ Diameter (nm) |
| Quantum<br>Chemistry | **?** | | Solid State<br>Physics | |

**FIGURE 1.1**   Size relationships of chemistry, nanoparticles, and condensed matter physics.

Another way to calibrate the nanocrystalline size range is to compare it with other small things in our world. Figure 1.2 compares the size of bacteria, viruses, nanocrystals, and the Buckminsterfullerene molecule. Note that bacteria are huge in comparison and it is helpful to realize that the volume of one *Bacillus cereus* bacterium could hold a million 5 nm nanoparticles.

These illustrations help make the point that nanocrystals, particularly in the 1–10 nm range (100 to 70,000 atoms) serve as bridges from molecules to condensed matter. In this size range intrinsic properties change due to size alone. For semiconductors such as ZnO, CdS, and Si, *bandgaps* (the energy needed to promote an electron from the valence band to the conduction band) change. In some cases, for bandgaps in the visible spectrum, this means that colors can change with size change in the 1–10 nm range. Furthermore, *melting points* change in this size regime, and *specific heats* change. For magnetic materials such as Fe, Co, Ni, $Fe_3O_4$, and others, magnetic properties are size-dependent. In particular the coercive force (or "magnetic memory") needed to reverse an internal magnetic field within the particle is size-dependent. Further, the strength of a particles' internal magnetic field can be size-dependent.

Of particular importance for chemistry, surface energies and surface morphologies are also size-dependent, and this translates to enhanced intrinsic surface reactivities. Added to this are huge surface areas for nanocrystalline powders, and this also affects their chemistry in substantial ways. Consider, for example, that a 3 nm iron particle has 50% of its atoms on the surface, whereas a 10 nm particle has just 20% on the surface, and a 30 nm particle only 5%. There are several important ramifications of large fractions of surface atoms, not the least of which is the fact that such materials can chemically react as nearly stoichiometric reagents.
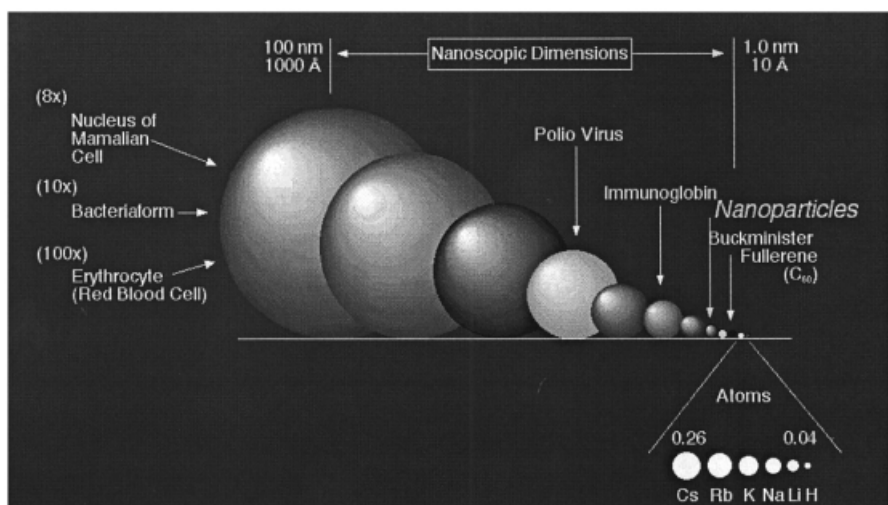


**FIGURE 1.2**    Size comparisons of nanocrystals with bacteria, viruses, and molecules.

## 1.3    HISTORICAL PERSPECTIVE ON NANOMATERIALS

As mentioned above, heterogeneous catalysis can be considered as one of the first uses of nanoscale materials. However, the broad field of colloid chemistry can also be viewed as an early integral part of nanotechnology.[35] Indeed, several decades have passed since catalysts and colloids were the true pioneering aspects of nano-technology. So why is it that this topic has "heated up" only in recent years?

The answer undoubtedly lies in the invention of numerous techniques for characterization and analysis of such materials. It is now possible to actually see atoms, a development that was hard even to imagine only a few years ago. In fact there are numerous technological developments that tend to amaze even scientists working in this area of investigation. Some of these developments are briefly described below.

*High-resolution Transmission Electron Microscopy (HRTEM)*    A high-voltage electron beam passes through a very thin sample, and the sample areas that do not allow the passage of electrons allow an image to be presented. Due to advances in electronics, computers, and sample preparation techniques, modern high-voltage instruments have resolution in the 0.1 nm range; thus is possible to image heavy atoms in some cases, and nanoparticle sizes and shapes are easily imaged. Sample preparation is crucial, and usually involves placing very dilute particle suspensions onto carbon-coated copper grids. Another useful technique is imbedding the particle in a solid organic polymer, slicing very thin sections, and passing the electron beam through the section.

*Scanning Probe Microscopy (SPM; also called Scanning Tunneling Microscopy, STM) and Related Atomic Force Microscopy (AFM)*[36]    Discovery of the SPM technique took place in the 1980s. It involves dragging a very sharp needlelike probe across a sample very close to the sample surface. For conducting samples a tunneling current between the sample and probe tip can be monitored and held constant. As the probe approaches an elevated portion of the sample, the probe moves up and over, and by rastering over an area of the sample, a surface map can be produced. With proper sample preparation and using a high-quality instrument in a vibration-free environment, it is sometimes possible to image down to atomic resolution. In fact, it has been possible to probe electronic structure and single atoms by Scanning Tunneling Microscopy (STM).[37]

When the sample is nonconducting, the atomic force (AFM) mode can be used, where the probe tip is essentially touching the surface, and the surface can be mapped by the weak interaction force between tip and sample. In the AFM mode, resolution is substantially poorer than for the tunneling mode. There continue to be developments in this area, and magnetic mapping is also possible.

*Powder X-Ray Diffraction (XRD)*    Although XRD has been useful for crystalline powders for several decades, modern improvements in electronics, computers, and X-ray sources have allowed it to become an indispensable tool for identifying nanocrystalline phases as well as crystal size and crystal strain. Other aspects include

small angle X-ray scattering to characterize particle sizes in nano-, micro-, and macroscale in compressed powders.[38,39]

*Differential Scanning Calorimetry (DSC)* Heating nanostructured materials can lead to crystal growth by amalgamation (exothermic), melting (endothermic), or crystal phase changes (exo- or endothermic). When the nanoparticles are ligated—for example, thiol coatings on gold—chemical reactions and ligand displacements can occur, which can be exo- or endothermic. By use of DSC, these transformations can be monitored and the extent of exo- or endothermicity determined, which can be very helpful in characterization.

*Superconducting Quantum Interference (SQUID) Magnetometry* For magnetic nanomaterials, the very sensitive SQUID can yield information on blocking temperatures, Néel temperatures, coercivity, saturation magnetization, ferro-magnetism, and superparamagnetism. The device is cooled with liquid helium, and the sample can be studied at near liquid helium temperature or up to well above room temperature.

*Laser Desorption Fourier Transform Ion Cyclotron Resonance Mass Spectrometry (LD-FTICR-MS)* The field of mass spectrometry is in rapid transition with the development of numerous new sample ionization techniques, better electronics, and data processing. Electrospray ionization now allows very high mass "molecules" to be analyzed. In addition, laser desorption coupled with ion cyclotron resonance allows probing of surface compositions and structure of surface adsorbed species.[40]

*Brunauer–Emmett–Teller Gas Adsorption Surface Area Measurement and Pore Structure Analysis (BET Method)* Another technique that has been well known for many decades is the determination of surface areas of powders by nitrogen gas adsorption at near liquid nitrogen temperature. Physisorption of a monolayer of $N_2$ allows calculation of surface area, by plotting pressure versus gas uptake. In recent years great improvements have allowed not only rapid surface area determinations but also pore size distributions, pore volumes, and in general the ability to more thoroughly characterize morphologies and even fractal dimensions.[41]

This brief summary of important characterization technqiues for nanostructural materials is far from complete. Advances in scanning electron microscopy (SEM), dynamic light scattering, surface techniques for obtaining IR and UV–visible spectra, X-ray photoelectron spectroscopy, Auger spectroscopy, and many more are of considerable importance as well.

In addition to advances in characterization methods, there have also been striking advances in the synthetic arena. Perhaps it is obvious that nanostructural materials are for the most part synthetic chemicals, and their synthesis has to precede everything else.

How, in a chronological way, the field of nanomaterials was born is an interesting story, and has been treated earlier.[33,42] Basically it seems to have begun from the "bottom up," where the study of the chemistry of free atoms (metal atom–vapor chemistry, and matrix isolation spectroscopy) led to the study of small aggregates of atoms (produced by pulsed cluster beams, continuous flow cluster beams, ionized cluster beams, solvated metal atom dispersion/aggregation, and other metal vaporization/clustering/aggregation methods). This was followed by the advance of chemical methods of producing small metal aggregates (reduction of metal ions by alkali metals or borohydrides, radiolysis, thermal or sonocative decomposition of metal carbonyls and other compounds).

These developments, which were initially concerned with *metal* nanoparticles, led to the realization that essentially all solid materials in nanoscale would be of interest. Thus, synthetic routes to metal oxides, sulfides, and other binuclear materials were developed or improved (sol-gels, aerogels, aerosol spray pyrolysis, inverse micelle methods, reactive evaporation of metals, zintyl salts, and others).

All of these pioneering synthetic approaches have been invaluable in establishing the new field of exciting scientific endeavor: *nanostructured materials*. These and other synthetic advances will be described in much more detail in the following chapters.

## 1.4   CLASSIFICATIONS OF NANOMATERIALS

If we consider that the periodic table of the elements is "a puzzle that has been given to us by God"[43] that holds a huge treasure chest of new solid materials, think of what this means in the realm of nanoparticles. Every known substance and every material yet to be discovered will yield a new set of properties, dependent on size. Optical properties, magnetic properties, melting points, specific heats, and crystal morphologies can all be influenced because nanomaterials serve as a bridge between the molecular and condensed phases. The likelihood of new discoveries and new applications is extremely high.

The thousands of substances that are solids under normal temperatures and pressures can be subdivided into metals, ceramics, semiconductors, composites, and polymers. These can be further subdivided into biomaterials, catalytic materials, coatings, glasses, and magnetic and electronic materials. All of these solid substances, with their widely variable properties, take on another subset of new properties when produced in nanoparticle form. The possibilities are endless. But synthesis of the nanomaterials is the first prerequisite. Purity, monodispersity, ligation, and other chemical properties and manipulations are important. Therefore, chemistry and chemists must take a leadership role if this new field is to prosper.

As a final point, as the field of nanostructured materials has evolved, many names and labels have been used. It is important that some strict definitions be presented.

*Cluster*   A collection of units (atoms or reactive molecules) of up to about 50 units. Cluster *compounds* are such moieties surrounded by a ligand shell that allows isolation of a molecular species (stable, isolable, soluble).

*Colloid*   A stable liquid phase containing particles in the 1–1000 nm range. A colloidal particle is one such 1–1000 nm sized particle.

*Nanoparticle*   A solid particle in the 1–1000 nm range that could be noncrystalline, an aggregate of crystallites, or a single crystallite.

*Nanocrystal*   A solid particle that is a single crystal in the nanometer size range.

*Nanostructured or nanoscale material*   Any solid material that has a nanometer dimension; three dimensions → particles; two dimensions → thin films; one dimension → thin wire.

*Nanophase material*   The same as nanostructured material.

*Quantum dot*   A particle that exhibits a size quantization effect in at least one dimension.

After this introduction, it is appropriate that the topic of nanostructured materials in chemistry is considered in more detail, which is taken up in the following chapters. First, important chapters on the three major materials—metals, semiconductors, and ceramics—are presented. The final chapters deal more specifically with properties— optical, magnetic, chemical, and physical. Finally, a chapter on current applications is presented. In all these chapters, the approach is mainly that which deals with chemistry. However, condensed matter physicists, chemical engineers, and materials scientists will also find much that is interesting to them.

## REFERENCES

1. Eugene Wong, quoted by R. S. Boyd, Knight Rider Newspapers, *Kansas City Star*, Monday, November 8, **1999.**

2. R. Smalley, Congressional Hearings, Summer, **1999**.

3. M. C. Roco, R. S. Williams, P. Alivisatos (editors), *Interagency Working Group in Nanoscience Engineering and Technology (IWGN) Workshop Report: Nanotechnology Research Directions; Vision for Nanotechnology R and D in the Next Decade*, Published by Int. Tech. Research Institutes, WTEC Division, Loyola College, **1999**, pp. xxv, 58, 118, 67, xxvii, 70, 7, 102, 103.

4. C. A. Merkin, R. L. Lestinger, R. C. Mucic, J. J. Storhoff, *Nature*, **1996**, *382*, 607–609.

5. A. P. Alivasatos, K. P. Johnson, X. Peng, T. E. Wilson, C. J. Loweth, P. G. Schultz, *Nature*, **1996**, *382*, 609.

6. (a)  D. E. Bugner, Conference on Nanotechnology, Rochester American Chemical Society Meeting, Rochester, NY, October 15–16, **1998**.
   (b)  E. Matejivic, *Annu. Rev. Mater. Sci.*, **1985**, *15*, 483.
   (c)  E. Matejivic, *MRS Bulletin*, 18 (Dec. 1989).

7. (a) R. D. Shull, R. D. McMichael, L. J. Swartzendruber, L. H. Bennett, in *Studies of Magnetic Properties of Fine Particles and Their Relevance to Materials Science*, J. J. Pormann, D. Fiorani (editors), Elsevier Publishers, Amsterdam, **1992**, pp. 161–169.
   (b) R. D. McMichael, R. D. Shull, L. J. Swartzendruber, L. H. Bennett, *J. Magn. Mater.*, **1992**, *111*, 29.

8. N. Herron, *Chem. Technol.*, **1989**, *542*.

9. J. R. Heath, P. J. Kuekes, G. S. Snider, R. S. Williams, *Science*, **1998**, *280*, 1716–1721.

10. R. P. Andres, R. S. Averback, W. L. Brown, L. E. Brus, W. A. Goddard, A. Kaldor, S. G. Louie, M. Moskovits, P. S. Percy, S. J. Riley, R. W. Siegel, F. Spaepon, Y. Wang, *J. Mater. Res.*, **1989**, *4*, 704.

11. K. J. Klabunde, G. Youngers, E. J. Zuckerman, B. J. Tan, S. Artrim, P. M. A. Sherwood, *Eur. J. Inorg. Solid State*, **1992**, *29*, 227.

12. G. Cardenas-T., K. J. Klabunde, *Bol. Soc. Chil. Quim.*, **1988**, *33*, 1634.

13. B. S. Rabinovitch, R. H. Horner, K. J. Klabunde, P. Hooker, *Metalsmith*, **1994**, *14*, 41–43.

14. (a) J. Kiwi, M. Grätzel, *Angew. Chemie; Int. Ed. Engl.*, **1979**, *18*, 624.
   (b) G. Riegel, R. J. Bolton, *J. Phys. Chem.*, **1995**, *280*, 1716–1721.

15. A. Kay, R. Humphrey-Baker, M. Grätzel, *J. Phys. Chem.*, **1994**, *98*, 952.

16. J. Fan, J. T. Yates, Jr., *J. Phys. Chem.*, **1994**, *98*, 952.

17. T. Boronina, K. J. Klabunde, G. B. Sergeev, *Environ. Sci. Technol.*, **1995**, *29*, 1511–1517.

18. (a) Y. X. Li, K. J. Klabunde, *Langmuir*, **1991**, *7*, 1388.
   E. Lucas, K. J. Klabunde, *Nanostructured Materials*, **1999**, *12*, 179–182.

19. A. Khaleel, P. Kapoor, K. J. Klabunde, *Nanostructured Materials*, **1999**, *11*, 459–468.

20. O. Koper, I. Lagadic, A. Volodin, K. J. Klabunde, *Chem. Mater.*, **1997**, *9*, 2468–2480.

21. V. Haensel, R. Burwell, *Sci. Am.*, **1971**, *225*, 46.

22. M. A. Reed, J. M. Tour, T. P. Burgen, C. Zhou, C. J. Miller, *Science*, **1997**, *278*, 252.

23. C. P. Collier, E. W. Wong, M. Belohradsky, F. M. Raymo, J. F. Stoddart, P. J. Kuekes, R. S. Williams, J. R. Heath, *Science*, **1999**, *285*, 391–394.

24. M. L. Trudeau, J. Ying, *Nanostructured Materials*, **1996**, *7*, 245.

25. M. L. Trudeau, Conference on Processing and Catalytic/Chemical Properties of Nano Structural Materials, Maui, Hawaii, January 16–21, 2000, United Engineering Foundation, Inc., New York.

26. T. Kobayashi, H. Kamo, H. Ishibashi, Abstract 62, Materials Secretariat, American Chemical Society, 216th National Meeting August 23–27, **1998**.

27. R. E. Rosensweig, *Ferrohydrodynamics*, Cambridge University Press, New York, **1985**.

28. H. Li, X. Huang, L. Chen, *Electrochemical and Solid State Letters*, **1998**, *1*, 241–243.

29. C. C. Chang, P. N. Kumta, M. A. Sriram, "Cathode Materials for Lithium-ion Secondary Cells," U.S. patent application, **1997**.

30. M. Mitov, A. Popov, I. Dragieva, *Colloids and Surfaces. A. Physicochem. Eng. Agents*, **1999**, *149*, 413–419.

31. O. Koper, E. Lucas, K. J. Klabunde, *J. Appl. Toxicol.*, **1999**, *19*, 559–570.

32. (a) G. Wagner, P. W. Bartram, O. B. Koper, K. J. Klabunde, *J. Phys. Chem.*, **1999**, *103*, 3225–3228.

(b) G. W. Wagner, O. B. Koper, E. Lucas, S. Decker, K. J. Klabunde, *J. Phys. Chem. B.*, **2000**, *104*, 5118–5123.

33. K. J. Klabunde, *Free Atoms, Clusters, and Nanoscale Particles*, Academic Press, San Diego, **1994**, pp. 2, 36.

34. K. J. Klabunde, C. Mohs, in *Chemistry of Advanced Materials: An Overview*, L. V. Interrante, M. J. Hampden-Smith (editors), Wiley-VCH, New York, **1998**, p. 271.

35. P. C. Hiemenz, *Principles of Colloid and Surface Chemistry*, J. J. Lagowoski (editor), Marcel Dekker, New York, **1977**, pp. 453–466.

36. C. Joachim, S. Gauthrier (editors), *Scanning Probe Microscopy: Beyond the Images*, les editors de physique, B.P. 112, F-91944 Le Ulis Cedex A, France, **1999**.

37. A. Yazdani, B. A. Jones, C. P. Lutz, M. F. Crommie, D. M. Eigler, *Science*, **1997**, *275*, 1767–1770.

38. C. N. R. Rao, B. Raveau, *Transition Metal Oxides Structure, Properties, and Synthesis of Ceramic Oxides*, 2nd edition, Wiley-VCH, **1998**, p. 4.

39. T. P. Rieker, A. Hanprasopwattana, A. Datye, P. Hubbard, *Langmuir*, **1999**, *15*, 638.

40. Y. Li, J. Huang, R. T. McIver, Jr., J. C. Hemminger, *J. Am. Chem. Soc.*, **1992**, *114*, 2428–2432.

41. S. J. Gregg, K. S. W. Sing, *Adsorption, Surface Area and Porosity*, 2nd edition, Academic Press, London, **1982**.

42. K. J. Klabunde, *Chemistry of Free Atoms and Particles*, Academic Press, New York, **1980**.

43. I. Amato, *Science*, **1991**, *252*, 644, writing about materials synthesis in the laboratories of F. Desalvo and J. D. Corbitt.

# 2  Metals

GUNTER SCHMID

University of Essen, Essen, Germany

## 2.1  INTRODUCTION

### 2.1.1  Structure and Bonding

About two-thirds of the chemical elements are metals, which means that the electronic situation found in a metal is very common. Nonmetals preferably form covalent bonds between each other, especially between atoms of the same element, with the aim of achieving a noble gas electronic configuration. In some cases the combination of only two atoms is sufficient to achieve that state, as in $H_2$, $N_2$, $O_2$, $F_2$, etc. Other elements, such as carbon and phosphorus, build up infinite lattices to produce a stable electronic configuration, as is known from graphite and diamond or red and black phosphorus. We understand these elementary structures and bonding situations as the most economical way to attain noble gas configurations. However, the fewer valence electrons an atom has the more difficult it is to find a simple solution. Boron is an illustrative example of how complicated the relationship between identical atoms may become if the formation of simple covalent $\sigma$- and $\pi$-bonds does not result in noble gas-like situations. Two boron atoms will never be able to form a stable combination. Complicated electron deficiency bonds in $B_{12}$ icosahedra are the result of a kind of "compromise" to generate a stable structure.

The heavier homologues of these elements, for example, aluminum, tin, lead, bismuth, behave very differently from their lighter relatives. Why is this? Owing to their increased distance from the nucleus, the outer valence electrons can easily be removed from the atom. This increased electropositivity is characteristic for all heavier main group elements and especially for all transition elements: they form metals. The formation of a metallic state can best be illustrated by considering the interaction of, for instance, 2, 6, 10, etc. and finally of an infinite number of lithium atoms having only a single electron in the 2s orbital. Using the molecular orbital
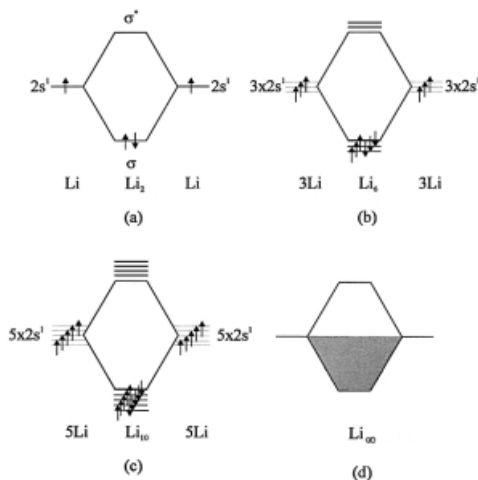
**FIGURE 2.1**   Formation of a metallic state, exemplified by lithium.

(MO) description, as is usual for covalently bonded atoms in molecules, the generation of a metal can be simply understood as the formation of an infinitely extended molecular orbital. Figure 2.1 illustrates this process in a simplified manner.

Two lithium atoms combine via their $2s^1$ electrons to form a doubly occupied binding molecular orbital (Figure 2.1a). This situation is directly comparable with the formation of an $H_2$ molecule by two $1s^1$ orbitals. The decisive difference, however, is that $H_2$ is stable due to its He configuration, whereas $Li_2$ has in addition $2 \times 3$ (not shown) unoccupied $p$-orbitals. $Li_2$ molecules indeed exist in the gas phase, but not under more usual conditions. $2 \times 3$ Li atoms (b) behave in principle the same, as do $2 \times 5$ Li atoms (c). However, continuing this thought-experiment we will end up with, say, 1 mole of Li atoms combining, with 1 mole of bonding and 1 mole of antibonding molecular orbitals. $6 \times 10^{23}$ MOs cannot further be strictly separated from each other; instead they form what we call an energy band, consisting of $6 \times 10^{23}$ quasi-equivalent doubly occupied MOs, followed by the same number of unoccupied antibonding levels. This is the situation in a typical metal, responsible for all its well-known properties. The situation in lithium is relatively simple compared with that in heavier metals, especially of transition metals where $s$, $p$, $d$, and even $f$ electrons may participate in the metallic bond. However, it does not seem necessary to extend these basic considerations to these elements for an enhanced understanding. The lithium situation describes the principles sufficiently.

To transform Figure 2.1d into a more descriptive image, a metal can also be described as consisting of a regular lattice of positively charged metal ions, embedded in a gas of quasi-delocalized electrons. Most of these lattices consist of cubic or hexagonal close packings; others form cubic centered structures, completed by a few specialties such as gallium and mercury. (For details see appropriate text

books.) Most of the properties of a metal can be deduced from this simple description. It should be noted, however, that much more knowledge is necessary for understanding of properties such as magnetism and conductivity in detail.

Before discussion of some of the properties of bulk metals, a more quantitative insight into the electronic situation might be useful.

The relation between the MO description of a finite molecular system and the "infinite" situation in a bulk metal is that the highest occupied molecular orbital (HOMO) is now called the Fermi energy $E_F$ of the free electron model. $E_F$ depends only on the density $\rho = N/V$ of the electrons ($N =$ number of electrons, $V =$ volume). Thus, $E_F$ is independent of the particle size. Assuming that all levels up to $E_F$ are occupied by a total of $N$ electrons, it can be roughly estimated that the average level spacing $\delta \cong E_F/N$. Consequently, $\delta$ is inversely proportional to the volume $V = L^3$ ($L =$ side length of the particle) or $\delta \propto E_F(\lambda_F/L)^3$, with $\lambda_F$ the wavelength of the electron of energy $E_F$. $\lambda_F$ is of the order of interatomic distances. These considerations assume the wave character of the electron, including the fact that the allowed values for the wavelength $\lambda$ are quantized; that is, for the model of an electron in a "box" of side $L$ the ratio $2L/\lambda$ is an integer or, in other words, only discrete values for the energy are allowed. The separation values $\delta$ become larger the smaller the value of $L$. The development of the density of states (DOS) $\delta$ as a function of energy from a molecular system to a bulk $d$-metal is shown in Figure 2.2.[1] This illustration corresponds in some respects to that in Figure 2.1, but now the understanding is based on the relation between the Fermi energy $E_F$ and the density of states.

The typical band structure in Figure 2.2c originates from a nondifferentiated infinite number of $s$ and $d$ electrons, whereas in (a) only well-separated energy levels are present. The highest occupied molecular orbital (HOMO) corresponds to $E_F$. The situation in (b) will later become most important, when the electronic situation of nanosized particles will be discussed. At this point it suffices to mention that (b) represents one of the most exciting situations with respect to materials properties. Before we deal with these near-degenerate electronic levels in detail, the following section briefly summarizes some of the most important properties of bulk metals, deriving from their electronic characteristics.

## 2.1.2  Properties

The most important property of a metal is, without doubt, its ability to transport electrons: the property of conductivity. To understand what conductivity is based on, we have again to consider the relation between occupied and nonoccupied electronic bands.

Electrons can only become mobile if the energy band of which they are part is not fully occupied. In the case of lithium the occupied and the nonoccupied parts of the total $s$-band fulfill that condition: the $s$-band in bulk lithium is only half occupied, so that electrons can move freely. The situation changes if we consider the next element in the periodic system, beryllium. Its electron configuration is $2s^2$, that is, the $s$-band is completely occupied. Why is beryllium a conducting metal, in spite of this? It is a
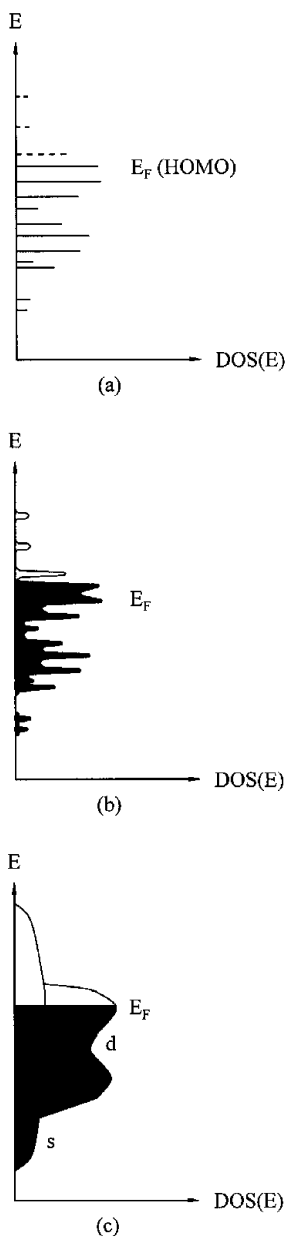
**FIGURE 2.2**  Formation of a band structure (a) from a molecular state, (b) from a nanosized particle with broadened energy states, and (c) the fully developed band structure consisting of $s$ and $d$ band. $E_F$ = Fermi energy; DOS = density of states. In (a) $E_F$ corresponds to the highest occupied molecular orbital (HOMO).
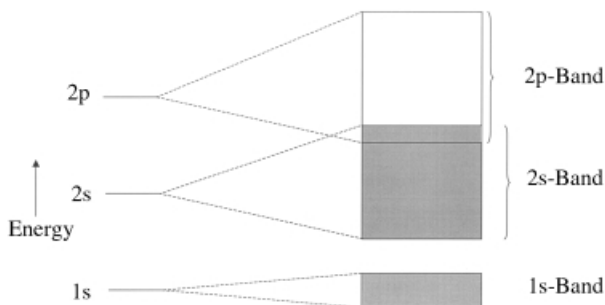
**FIGURE 2.3**  Overlap of the fully occupied 2$s$ band with the empty 2$p$ band in beryllium is responsible for the metallic behavior.

conductor because of the proximity of the empty $p$-band, as illustrated in Figure 2.3. Electrons from the fully occupied $s$-band can easily move into the $p$-band and so become mobile.

Most of the transition metals of the $d$-type are characterized by only partially filled $d$-orbitals so that incompletely filled bands result in any case. $d^{10}$ elements such as palladium, platinum, or gold have nearby $s$-bands that can be used for electron transport.

In addition to electronic conductivity, magnetism is another unique property, at least of some metals. The so-called ferromagnetism of iron, cobalt, and nickel is well known. Among many different kinds of magnetism, which do not form the subject of this chapter, ferromagnetism is not only the best known but is the most important kind of magnetism for practical reasons. In a magnetic metal the DOS at the Fermi level in the $d$-band is partly unoccupied. The resulting $d$-holes are responsible for the magnetism. Nonmagnetic metals like gold, palladium, or platinum have fully occupied states with only spin-paired electrons. The existence of unpaired electrons is a condition for magnetism; however, only the uniform orientation of free spins over a larger area (Weiss area) results in ferromagnetism. Nonoriented free spins produce paramagnetic materials. The properties of magnetism will be discussed again later in connection with nanometer-sized particles.

Except for copper and gold, the only colored metals, all others look "silvery" if they have smooth surfaces. Finely dispersed metals, even copper and gold, are dark brown or black. The silvery lustre and the dark appearance are not colors in the classical sense, but are caused by the total reflection of light in the first case, and by the total absorbtion of light in the latter. Color in the classical sense is caused by the partial absorbtion of light by electrons in matter, resulting in the visibility of the complementary part of the light. If, as on smooth metal surfaces, light is totally reflected by the high density of electrons, no color results; instead we observe a mirrorlike appearance. Finely dispersed metal particles have very large surfaces at which incoming light is fully absorbed through repeated reflection. The light energy is quantitatively transformed into heat.

If metal particles become very small, reaching the nanometer size scale, true color may occur, however. This is a typical size-dependent property and will also be discussed later as a phenomenon of nanomaterials.

## 2.2    REDUCTION OF SIZE

### 2.2.1    General

The development of a metallic band structure requires a minimum number of electronic levels, which have to be very similar in energy so that electrons can move inside the particle by only thermal activation. All properties that we know for a bulk metal derive from the existence of such a band: the electrical conductivity as well as the specific heat, the metallic lustre, or the ductility, to cite just a few typical metallic characteristics.

Let us make another thought-experiment. In the previous section we developed the metallic band structure using molecular orbitals with a few atoms up to a mole of lithium atoms. Conversely, we now ask how small a metal particle has to become to lose the band structure to such an extent that the effect can be observed. This situation corresponds to Figure 2.2b, where the unstructured s- and d-bands in (c) are beginning to be split but without forming truly discrete levels as in (a). It can be assumed that one mole of metal atoms, (i.e. $6 \times 10^{23}$ atoms) has a completely developed band structure. Assemblies of many fewer atoms also do, as we know from experience. Any metal particle that we can observe by naked eye or even under a light microscope can be considered to behave in a bulklike way. This is not surprising, because even such a small particle as, say, a $1\,\mu m^3$ cube of gold still consists more than $10^{10}$ atoms! There is no doubt that $10^{10}$ atoms are able to form a band structure. But how far do have we to go in miniaturization to reach the borderline between bulk and molecule?

Before presenting practical examples, we can give a general answer to this question. Electrons in a three-dimensionally extended metal spread as waves of various wavelengths, usually called the "de Broglie wavelength," referring to the French physicist Duc de Broglie. He first interpreted the relation between the wavelength and the mass of an electron through the formula $\lambda = h/(mv)$ ($\lambda =$ electronic wavelength, $h =$ Planck's constant, $m =$ mass of the electron, $v =$ speed of the electron). Delocalization of electrons in the conductivity band of a metal is possible as long as the dimension of the metal particle is a multiple of the de Broglie wavelength $\lambda$. From this it follows that the smallest metal particles must have a dimension of the order of $\lambda$ or some multiple of it. Smaller particles have electrons localized between atomic nuclei; that is, they behave as typical molecules. It is to be assumed, however, that there is no sharp borderline between these two fundamental situations, but that this transition will be continuous and is, as will be discussed, also temperature-dependent. The description of bulk materials is made by means of the laws of classical physics. If we reach a size range where, in the case of metals, the band structure is beginning to disappear and discrete energy levels are becoming dominant, quantum mechanical rules have to replace those of classical physics. Quantum mechanics is a well-established theory for describing the electronic situation in molecules and atoms. So far, there is nothing new; however, in relation to small particles, the use of quantum mechanics is somewhat special as we still talk about parts of a material, not about atoms or small molecules.

The model of the "electron in a box", normally used for atoms, helps to describe simply the situation in small metal particles when size restrictions begin to influence electronic behavior (Figure 2.4).

If $L$ is the diameter of a metal particle, the situation at $n = 0$ corresponds to that of an $s$ orbital in an atom. A metal particle of this "smallest size" therefore has an electronic ground state comparable with that of an atomic $s$ orbital or, in other words, a metal cluster; such small particles can now also be considered as very large metal atoms! Excited states, such as $n = 1$, can then be compared with $p$ orbitals, and so on. This is what makes a metal cluster different from the bulk where $L$ is "infinitely" large, hosting an infinite number of electronic waves $\lambda$.

In treating such mesoscopic systems quantitatively, formidable problems arise for particles consisting of only a few thousand atoms. They are too small to be considered as bulk, owing to strong size-effects; on the other hand, they are far too large to be handled as molecules. It would be considerably beyond the scope of this chapter to describe these problems in more detail. For more detailed overviews of the electronic energy level structures of clusters, see for example de Jongh.[1]

With decreasing size of metal particles, the percentage of surface atoms increases. This is an important point to be considered when one discusses cluster properties. As a result of the reduction of the numbers of neighboring atoms, surface atoms have narrower $d$-bands, so that the density of states can vary considerably. Another surface effect is equally important: Metal clusters in general are provided with a protective shell of ligand molecules. Otherwise we would not be able to prepare them by chemical methods and especially to isolate and to investigate them as individual particles. The ligation of clusters will be considered in detail in Section 2.3. Ligand–metal interactions dramatically influence the electronic nature of the metal atoms involved. Both the reduction of coordination numbers and, in the case of ligand-protected clusters, the metal–ligand bonds have to be considered when specific properties are discussed. As is known from numerous investigations, the ligation effects are short-ranged, so that inner-core atoms can be roughly separated from surface atoms for the purposes of discussion. Of course, the influence of surface
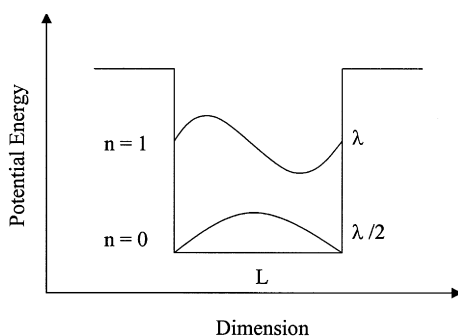


**FIGURE 2.4**   Particle in a box. In the ground state ($n = 0$), $\lambda/2$ ($\lambda =$ de Broglie wavelength) corresponds to the diameter of the nanoparticle. In the first excited state ($n = 1$), the size of the nanoparticle corresponds to $\lambda$.

atoms becomes more important the smaller the particle is. Physical measurements that give averaged information on the total particle are therefore always to be considered in this light, whereas methods distinguishing between differently bound atoms allow a more detailed description. Strictly speaking, only the inner-core atoms represent a minute piece of the bulk with strong quantum size effects. Assuming a Fermi energy of 5 eV, the level spacing $\delta \cong E_F/N$ for a 100-atom inner-core would be 100 K, a remarkable value compared with that for $\sim 10^5$ atoms with a $\sigma$ value of only 1 K.[1] The restriction of the quasi-freely mobile electrons in a piece of bulk metal can be reached not only by reduction of the volume to the minute size of a "zero-dimensional" (0D) quantum dot but can also be gained by reducing the dimensionality from 3 to 2 or 1. If a piece of metal is reduced by making it thinner and thinner until the electrons can only move in two instead of three dimensions, we have performed a two-dimensional (2D) quantum confinement, called a "quantum well." Further reduction in dimensionality finally ends in a "quantum wire" (1D), where the electrons can move in only one direction.

Quantum wells can be prepared almost routinely by physical vapor deposition (PVD) or by chemical vapor deposition (CVD). In PVD atoms from the gas phase are deposited on a substrate atom by atom and layer by layer. For CVD processes chemical compounds are evaporated and decomposed on hot substrates. All components except the metal must be volatile, so that ultrathin layers of metals can be generated.

Quantum wires are much more difficult to prepare and there is still no routine method. Some promising attempts have been described and these will be discussed in Section 2.3. Figure 2.5 summarizes the relations between bulk, 2D, 1D, and 0D situations with respect to the change of electronic characteristics. There is of course a relationship with Figure 2.2, where a bulk volume is directly reduced to a quantum dot, without considering the special situations of 2D and 1D. The intermediate state (b) in Figure 2.2, though still of the 3D type, shows similar quantum size behavior as do 2D and 1D arrangements.
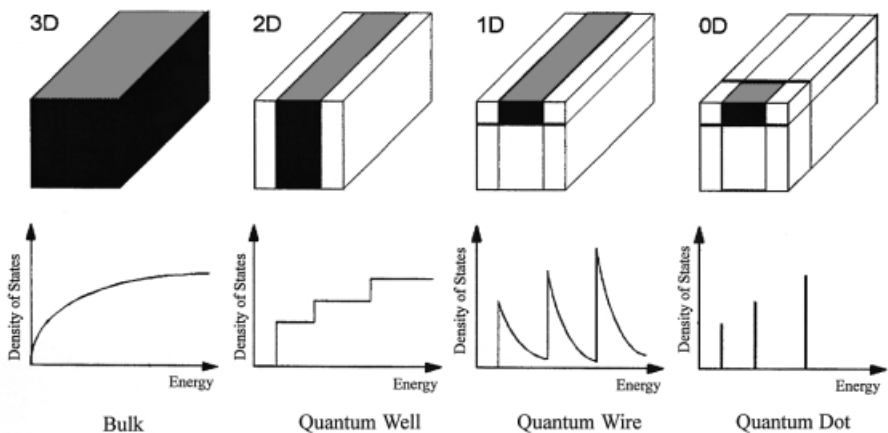


**FIGURE 2.5** Formation of a zero-dimensional (0D) quantum dot by the formal reduction of dimensions, correlating with the continuing discretization of the energy states.

Typical quantum dot behavior is reached only in the region of a few nanometers. Roughly how many atoms we need to reach the 0D conditions will be shown in the following section.
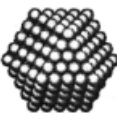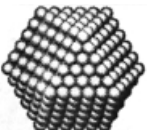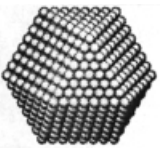
### 2.2.2   Size-dependent Properties

To demonstrate quantum size effects experimentally, appropriate materials are needed. In the course of the last 10–15 years there has been remarkable progress in preparing metal clusters in the size range of less than one nanometer up to dozens of nanometers.[2] It can be assumed that somewhere in this range quantum size behavior should be observable, giving hints at the very end (or the beginning) of metallic behavior. The preparation of nanosized metal particles will be the subject of Section 2.3. Here, only some selected examples are given that have turned out to exhibit well-established size-dependent properties.

***2.2.2.1   Melting points***   Let us first consider a property that is not directly dependent on the electronic situation in the particles, but is rather a consequence of the averaged coordination number of the participating atoms. By far the majority of metals form hexagonal or cubic close-packed structures with coordination numbers of 12, except for surface atoms when it is 9 or smaller, depending on whether faces, and which kind of faces, edges, or corners are considered. However, it is typical for bulk materials that the surface atoms form a negligible part of the total number of atoms. The smaller a particle becomes, the more the proportion of surface atoms increases. Table 2.1 contains some information on the percentage of surface atoms in close-packed full-shell clusters of different sizes. Full-shell clusters are built up by hexagonal (hcp) or cubic (ccp) close-packed atoms, as is the case in most bulk metals consisting of a central atom that is surrounded by 1, 2, 3, ... dense-packed shells. The number of atoms per shell is $\sum = 10n^2 + 2$, where $n$ = number of shell. The smallest full-shell cluster consists of $1 + 12 = 13$, the next of $13 + 42 = 55$ atoms, and so on.

A spherical particle of 50 nm in diameter has only about 6% of surface atoms, so that for micrometer-sized or even millimeter-sized particles these atoms can indeed be neglected with respect to their contribution to the average coordination number. The melting point of a solid is reached when the order of the lattice is beginning to be destroyed. For a distinct solid this is a physical constant, but only so long as the surface is negligibly small in comparison with the total volume—that is, for a typical bulk material. If percentages are reached as given in Table 2.1, the number of surface atoms becomes equal to or even exceeds the number of inner-core atoms. As the coordination number of surface atoms is 9 or smaller, these atoms are more easily rearranged than those in the center of the particle: the melting process starts earlier. In Figure 2.6 the relation between particle size and melting point of gold particles is shown, calculated by the method of Reifenberger.[3] As can be seen, there is a dramatic decrease of melting points for particles smaller than 3–4 nm.

**TABLE 2.1   The relation between the total number of atoms in full shell clusters and the percentage of surface atoms**

| Full-shell Clusters | | Total Number of Atoms | Surface Atoms (%) |
|---|---|---|---|
| 1 Shell | | 13 | 92 |
| 2 Shells | | 55 | 76 |
| 3 Shells | | 147 | 63 |
| 4 Shells | | 309 | 52 |
| 5 Shells | | 561 | 45 |
| 7 Shells | | 1415 | 35 |
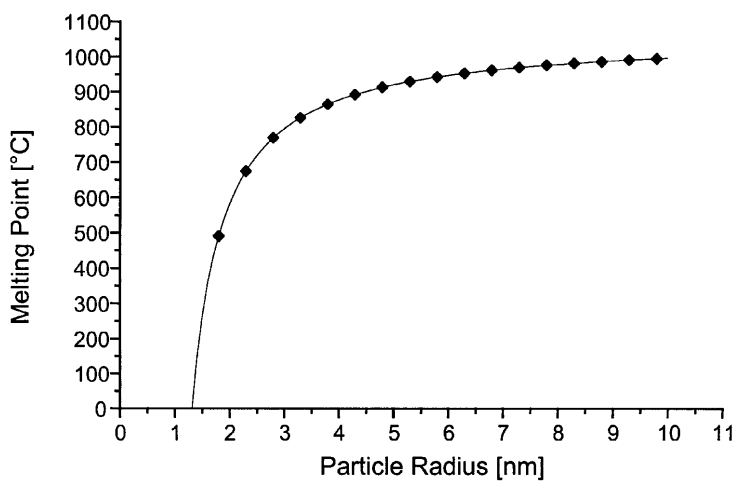


**FIGURE 2.6**   Relation between the size of gold particles and their melting point.

   In conclusion, we can see that even thermodynamic properties of matter, which classically described are natural constants, change with the dimension of the material. More interesting with respect to the "birth" of a metal are the electronic properties. The next section will deal with those.

*2.2.2.2  Magnetism*   Diamagnetic materials have only spin-paired electrons. However, in practice it cannot be assumed that a macroscopic piece of a diamagnetic metal does not have one or more unpaired electrons. This can in no way be measured because of the effectively infinite number of atoms and electrons. However, if the particle size were small enough to make one unpaired electron measurable, the predicted so-called odd–even effect should become visible: Among small diamagnetic metal particles there should be a 50 : 50 distribution of odd and even numbers of electrons.

   A series of palladium clusters of different sizes has been used to verify this prediction. Palladium clusters of 2.5, 3.0, 3.6, and 15 nm, all stabilized by the same kinds of ligand molecules, have been investigated with respect to their temperature-dependent susceptibility.[4] Figure 2.7 shows the experimental results. All samples
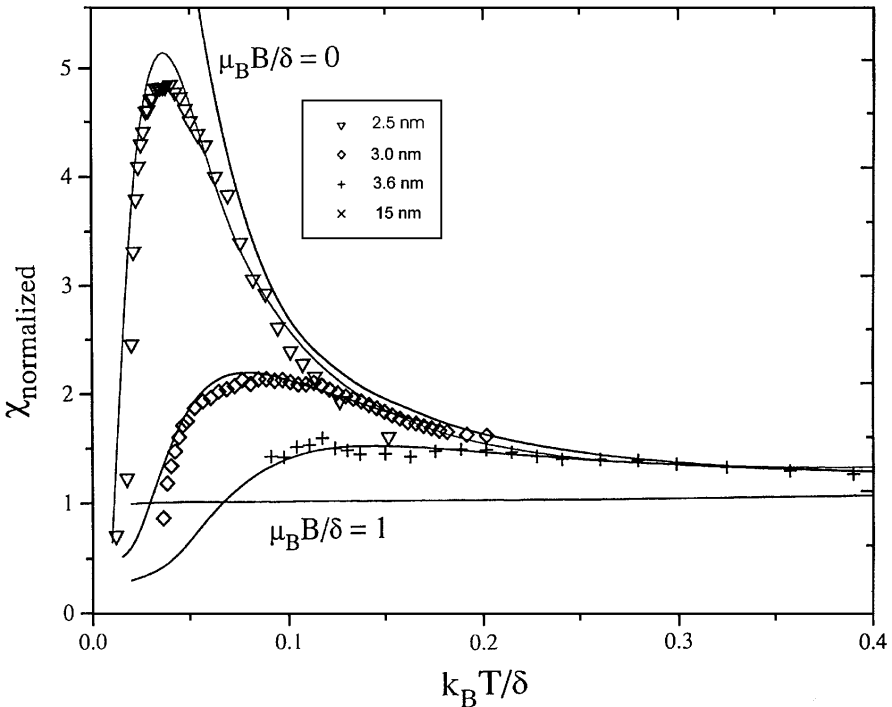


**FIGURE 2.7**   Electronic magnetic susceptibility of palladium clusters of different sizes. Interactions between spins on neighboring clusters increase with decreasing size. The temperature is scaled by the average energy gap value $\delta$ appearing in the theory. Solid curves are fits to theory.

show diamagnetic behavior like that of bulk palladium down to temperatures of about 1 K. Below 1 K, however, there is a distinct difference. Whereas the 15 nm Pd particles behave in a more or less bulklike manner, the smaller clusters show an increasing maximum of susceptibility with decreasing size. The 2.5 nm clusters exhibit the strongest signal, indicating that the 50% of particles with an odd number of electrons can indeed be visualized.

In conclusion, metal particles between $\sim$2 and 4 nm do indeed show size-dependent properties, in this case the susceptibility; however, they do so only at extremely low temperatures.

***2.2.2.3 Mössbauer spectroscopy*** The Mössbauer effect, also called nuclear resonant fluorescence, is based on the transition between a low-lying nuclear level and the ground state, linked with the absorption or emission of a photon that is a $\gamma$-ray of some few tens of keV. In the case of gold, the energy difference between the excited state and ground states is 77.34 keV, with a nuclear spin of $I = \frac{1}{2}$ for the excited and of $I = \frac{3}{2}$ for the ground state. A synchroton $\gamma$-ray beam, covering a range of energies, is used to obtain an absorption spectrum. The resonant energy is absorbed and is isotropically reemitted. $^{197}$Pt is the relevant isotope that decays into the $^{197}$Au excited state by $\beta^-$ elimination. On its return to the ground state it emits the required $\gamma$-ray of 77.34 eV. The sample to be investigated contains the Mössbauer isotope in its ground state, in the case of gold the only stable isotope, $^{197}$Au. There is a complication to overcome to produce an absorption spectrum, as the absorption and emission energy in the solid are approximately of the same size. To differentiate between them one uses the Doppler effect to give one of the two lines, for example, the emission line, a continuous range of energies. Usually the Mössbauer source is moved toward and away from the absorber at $-15$ to $+15$ mm s$^{-1}$. Thus the region of interest can be scanned. The information one can get from a Mössbauer absorption spectrum is mainly based on the *s*-electron density difference between source and absorption. The absorption line observed is shifted from the zero-velocity position. This is the so-called isomer shift (IS) or chemical shift (CS). In addition, quadrupole splitting (QS) may be observed. This happens if one or both nuclear levels carry a quadrupole moment and the nucleus is in an electric field gradient. The spin $-\frac{3}{2}$ ground state of gold has such a quadrupole moment, so that in the case of gold Mössbauer spectroscopy IS and QS may be observed, both giving valuable information on the different gold sites in metal clusters. The data are compared with those of bulk gold to get information on quantum size effects in clusters. The advantage of Mössbauer spectroscopy is the detailed information on different atoms in a cluster rather than averaged information resulting from the methods described above.

The first example that demonstrates this perfectly is the investigation of the four-shell cluster Pt$_{309}$ by Mössbauer spectroscopy.[5] This cluster has a diameter of 1.8 nm and is protected by phen* ligands; phen* is a derivative of 1,10-phenanthroline substituted at the 4,7 positions by *p*-C$_6$H$_4$SO$_3$Na functions. In addition to phen* ligands, the cluster surface is partially covered by O$_2$ molecules, resulting in the formula Pt$_{309}$phen*$_{36}$O$_{30\pm10}$. Figure 2.8 shows the bare cluster and its different surface atoms. These can be differentiated into those coordinated by the N atoms of
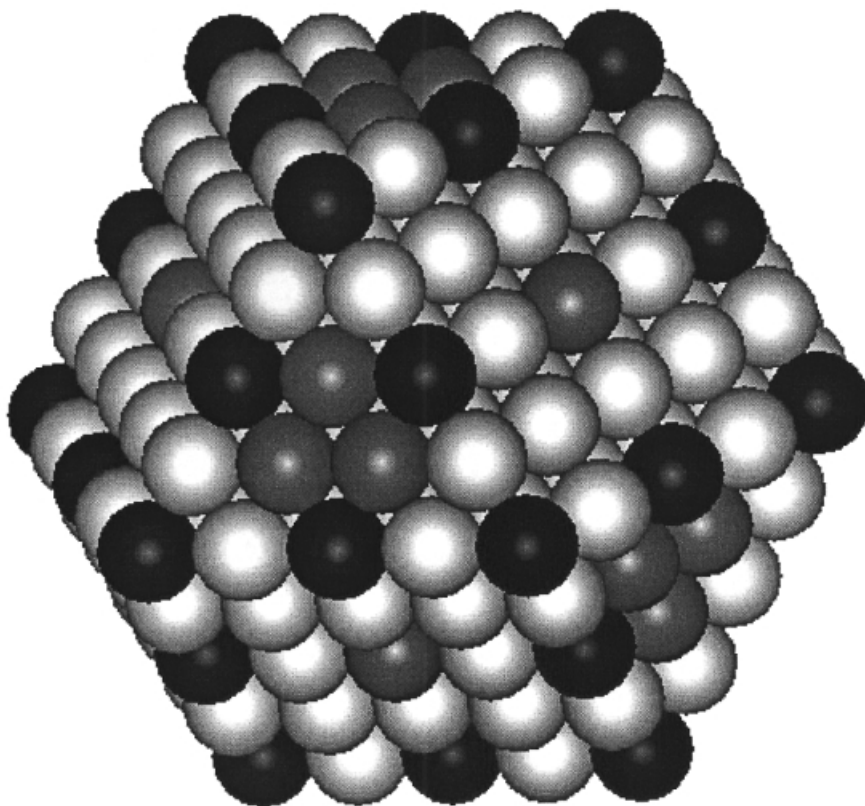
**FIGURE 2.8**   Sketch of a $Pt_{309}$ cuboctahedral cluster. Black spheres symbolize platinum atoms coordinated by phen*, dark grey spheres bind $O_2$ molecules, light spheres are bare.

phen* and those coordinated by oxygen, and those that are free of ligand molecules. A fourth type of platinum atom forms the inner core of the cluster, consisting of 147 atoms (three-shell cluster).

As platinum does not have a Mössbauer-active nucleus, this cluster was irradiated by thermal neutrons. The resulting $^{197}Pt$ nucleus then follows the same decay processes as described before. Of course, it is not possible to transfer the platinum atoms quantitatively to gold. However, because even a single activated platinum atom per cluster statistically occupies all different positions, a composition $Pt_{308}Au_1$ is sufficient for a successful investigation. This is indeed what has been produced by neutron activation. The result is remarkable: One can not only differentiate between the three types of surface atoms, which are not of much interest in this connection, but one can explore the behavior of the 147 inner-core atoms. Both the isomer shift and the quadrupole splitting are exactly the same as that for $^{197}Au$ in bulk metallic platinum, namely zero.

The information from these investigations is very valuable. The most important is that a $Pt_{147}$ core, surrounded by a shell of platinum atoms that are partially chemically bound, behaves in a bulklike manner with respect to the $6s$ electron density in the participating nuclei. This is no contradiction of what we discussed in the preceding section regarding the susceptibility of the larger palladium clusters that all exhibited quantum size behavior up to 3.6 nm. The odd-even phenomenon was found below 1 K: the Mössbauer spectra were recorded at 40 K. Furthermore, it is reasonable that different methods give different information. Only the use of as many different methods as possible will give sufficient information.

The Mössbauer data of the cluster compound $Au_{55}(PPh_3)_{12}Cl_6$ as well as those of some derivatives with other ligands also exhibit different gold sites for the surface and the 13 inner-core atoms.[6–9] The line for the $Au_{13}$ nucleus shows an isomer shift of $-1.4 \pm 0.1$ mm s$^{-1}$ which is very similar to that of bulk gold of $-1.2 \pm 0.1$ mm s$^{-1}$, but not identical. The negative shift can be explained by a loss of $s$-electron density, shifted to the narrowed $d$-bands of surface atoms. This effect may even be supported by the interaction of some of the surface atoms with the ligands.

Concluding this section, we can say that inner-core atoms of ligand-stabilized clusters behave in a very bulklike manner, because these atoms have coordination numbers of 12. They represent the real "metal-part" of the cluster. Investigations that cannot distinguish between the different kinds of metal atoms give information only on the electronic behavior of the particle as a whole. As we will see, for their use as quantum dots the latter property is decisive, not that of a part of the cluster. The similarity of 13 inner-core atoms of $Au_{55}$ clusters to bulk gold is, however, of principal importance.

*2.2.2.4 Colors* Metals can be polarized by electromagnetic irradiation exciting electrons. Considering the ideal case of an undamped oscillation of free electrons in a defect-free metal lattice, the solution of the wave equation results in an expression for the complex refractive index $n$:[10]

$$n^2 = 1 - \frac{e^2 N_E}{\varepsilon_0 m_e v^2} \tag{2.1}$$

where $N_E =$ the density of electrons, $m_e =$ electronic mass, $v =$ frequency of the electromagnetic irradion, $\varepsilon_0 =$ dielectric constant of vacuum.

The refractive index is related to the reflectivity $R_v$ of a metal by the Beer equation

$$R_v = \frac{(n' - 1)^2 + k^2}{(n' + 1)^2 + k^2} \tag{2.2}$$

where $k =$ absorption coefficient, $n' =$ real part of the complex refractive index.

If $v$ is small enough $n^2$ becomes smaller than 0 and $n$ then consists of only the imaginary part $n''$. With $n' = 0$, the reflectivity $R$ is 1, which means that metals reflect electromagnetic irradiation totally. Higher frequencies cause a real part of the complex refractive index $n' > 1$ with $k = 0$ and in the case of nonabsorbing metals $n$ approximates to 1 and $R$ to 0. This means that ideal metals under these conditions become transparent, for instance alkali metals in the near UV-region.

The limiting or plasma frequency $v_P$ for the transition $R = 0 \rightarrow R = 1$ for free electrons is

$$v_P = \sqrt{\frac{e^2 N_E}{\varepsilon_0 m_e}} \tag{2.3}$$

In real metals, collision processes at defects induce damping of the oscillation. In addition to this source of damping in real lattices, the migration of electrons is also not free because, owing to the oscillation of the electrons, a damped dipole is caused in the field of the atomic nucleus. This leads to a dispersion of the refractive index and to a maximum in the spectral absorption. Metals also deviate from the ideal model if their particle size is so reduced that the mean free path of the electrons exceeds the particles' radius.[11] In this case electrons can be excited by visible light to perform fluidlike plasmon oscillations (Mie theory). The dipole and higher multipole moments are caused by surface charging, which is especially effective for spherical shapes (Figure 2.9)

Figure 2.10 shows some typical absorbance spectra of silver and gold clusters of different sizes.[12] As can be seen from Figure 2.10, the varying intensity of the plasmon resonances depends on the cluster size. Due to the increasing damping with decreasing particle size, the electronic relaxation after electromagnetic excitation is accelerated. The reduced lifetime of the plasma excitation causes a broadening of the lines. Furthermore, plasmon frequency is affected by the surrounding medium. Induced dipoles lead to further damping of the electron oscillation, observed as a red-shift of the plasmon resonance in the absorption spectra.[13] For instance, the resonance of 5 nm gold clusters in water is at 520 nm; the same particles in $\alpha$-$Al_2O_3$ cause absorption at 565 nm. Deviations from the ideal spherical geometry also give rise to a change of optical properties, due to anisotropy.

Not all metal particles show plasmon resonances. Although in silver and gold nanoparticles the Mie resonances are well expressed, other metals such as iron, palladium, and platinum do not show resonances because of lifetime broadening via
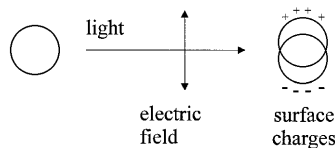


**FIGURE 2.9** Formation of surface charges on a metal particle by the electric field of light.

Ag-clusters:                    Au-clusters:



(a)                              (b)

wavelength(nm)
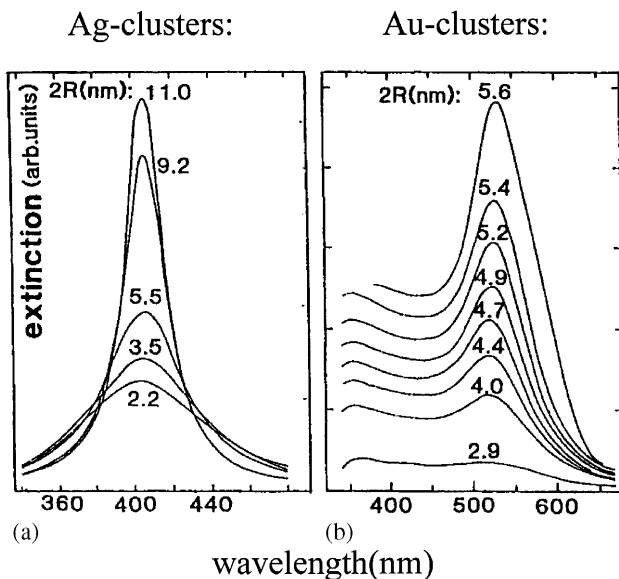
**FIGURE 2.10**   Absorbance spectra of (a) silver and (b) gold clusters of different sizes. Reprinted with permission from *Handbook of Optical Properties*, Vol. II (ed Hummel and Wissmann) **1997**. Copyright CRC Press, Boca Rata, Florida.[12]

strong plasmon decay channels. Strong conduction electron relaxation, radiation dumping, as well as transformation of the collective excitation into electron–hole pair excitation are obvious reasons for this behavior.

The above-mentioned optical properties refer to isolated nanoparticles. In practice, however, the particles often cannot be considered as independent from each other. Aggregates of clusters effect shifts of the plasmon resonances depending on their topologies. The packing of otherwise identical samples dramatically influences the optical behavior. Details of these phenomena cannot be discussed here. The principle of optical behavior of connected nanoparticles is elucidated in Figure 2.11. The orientation of the dipoles of connecting particles results in two individual vibrations of the optical excitation. Excitation along the row causes a long-wave shift, whereas perpendicular excitation results in a high-energy shift. The optical properties of such particle arrangements are a complex combination of properties of the particles, of the electronic environment, and of dispersion and arrangement.



(a)                              (b)
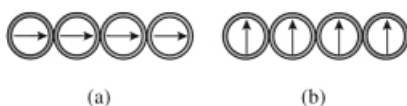
**FIGURE 2.11**   Eigenmodes of an idealized chain of colloids. (a) longitudinal eigenmode, (b) transverse eigenmode.

***2.2.2.5   Conductivity***   Electrical conductivity of metals is based on their band structure. If the so-called conduction band is only partially occupied by electrons, they can move in all directions without resistance, provided there is a perfect metallic crystal lattice. They are not scattered by the regular building blocks, owing to the wave character of the electrons. The mobility of electrons is best described by the expression

$$\mu = \frac{e\lambda}{4\pi\varepsilon_0 m_e V_F} \tag{2.4}$$

where $\lambda$ = mean free path of the electrons between two collisions, $m_e$ = effective mass of the electron in the lattice, $V_F$ = speed of the electrons (Fermi speed), $\varepsilon_0$ = dielectric constant of vacuum. $\lambda/V_F$ can be interpreted as the mean time $\tau$ between two collisions of electrons owing to defects in real metals. Some examples for copper at room temperature are $V_F = 1.6 \times 10^6 \, \mathrm{m\,s^{-1}}$, $\lambda = 4.3 \times 10^{-8} \, \mathrm{m} = 43 \, \mathrm{nm}$, $\tau = 2.7 \times 10^{-14} \, \mathrm{s}$. Two scattering mechanisms participate in any metal: (1) scattering by lattice defects (foreign atoms, vacancies, interstitial positions, grain boundaries, dislocation, stacking disorders, etc.), and (2) scattering at thermal vibrations of the lattice, called phonons. The first contribution is more or less independent of temperature, the second is independent of lattice defects. The rule of Matthiessen, $\rho = \rho_s + \rho_T(T)$, says that the specific resistance of a metal $\rho$ consists of the temperature-independent part of the lattice defects $\rho_s$ and the temperature-dependent part of the lattice vibrations $\rho_T$. At elevated temperature $\rho_T$ increases linearly with the temperature. This linear increase of the specific resistance is a typical property of bulk metals. At low temperatures the phonon contribution to the resistance disappears by the 5th power of temperature.

A collective motion of electrons (current $I$) in a bulk metal is induced by applying a voltage $U$. Ohm's law describes the linear relation between $U$ and $I$ by $U = RI$ ($R$ = resistance of the material).

All relations described above depend on the existence of a band structure, that is, the presence of freely mobile electrons in the lattice. As already discussed with reference to Figures 2.2 and 2.5, the band structure begins to change if the dimension of a metal particle becomes small enough. Discrete energy levels finally dominate and, as a consequence, Ohm's law is no longer valid. How does the current–voltage behavior change if we approach a zero-dimensional metal particle?

To answer this, single nanoparticles have to be investigated with respect to their $I - V$ characteristics. This is a big challenge! In principle individual particles have to be positioned between two electrodes to which an increasing/decreasing voltage can be applied. However, to observe electronic details, direct contact between electrodes and metal particles has to be avoided. Instead, two capacitances (non-conducting materials) between electrodes and object are used. Figure 2.12 illustrates the experimental conditions.

If an electron is transferred to the particle, its Coulomb energy $E_C$ increases by $E_C = e^2/(2C)$, where $C$ is the capacitance of the particle. Thermal motion of the atoms in the particle can initiate a change of the charge and of the Coulomb energy, so that further electrons may tunnel uncontrolled. To produce single electron
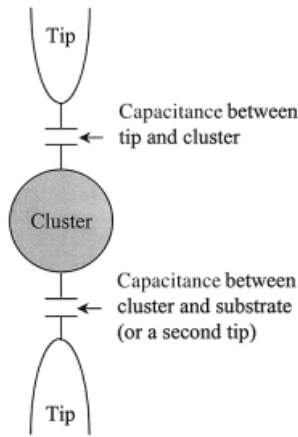
**FIGURE 2.12** Experimental conditions for recording a current (*I*)–voltage (*U*) characteristic of a single nanoparticle. The capacitances between tips and cluster are formed by the ligand shell.

tunneling (SET) processes, the thermal energy of the particle must be much smaller than the Coulomb energy, in order to keep the energy on the particle $kT \ll e^2/(2C)$. With an additional charge, a voltage $U = e/C$ is produced, leading to a tunneling current $I = U/R_T = e/(R_T C)$ (where $R_T$ = tunnel resistance). The resulting additional charge on the particle has a mean lifetime $\tau = R_T C$. The related Heisenberg uncertainty of energy $\delta E = h/\tau = h/(R_T C)$ leads to unexpected tunneling if it exceeds the Coulomb energy. This is quantum mechanically described by the quantum Hall resistance $R_{QH}$ and the capacity of the particle (quantum dot):[14]

$$E_{C,QH} = \frac{h}{R_{QH}C} \tag{2.5}$$

Thus a second condition for SET effects is $R_{QH} \ll R_T$.

The current–voltage characteristic for an ideal quantum dot shows no current up to

$$U_{Coulomb} = \pm\frac{e}{2C} \quad \text{(Coulomb blockade)} \tag{2.6}$$

If this value is reached, an electron can be transferred. Following this an electron tunneling process occurs if the Coulomb energy of the quantum dot is compensated by an external voltage of $U = \pm ne/(2C)$.[15] An idealized "staircase", resulting from the repeated tunneling of single electrons, is shown in Figure 2.13. The step height $\Delta I$ corresponds to $e/(RC)$ and the width $\Delta U$ to $e/(2C)$. It thus becomes possible to charge and to discharge a quantum dot in a quantized manner, which is a condition for use of such particles in future generations of computers.
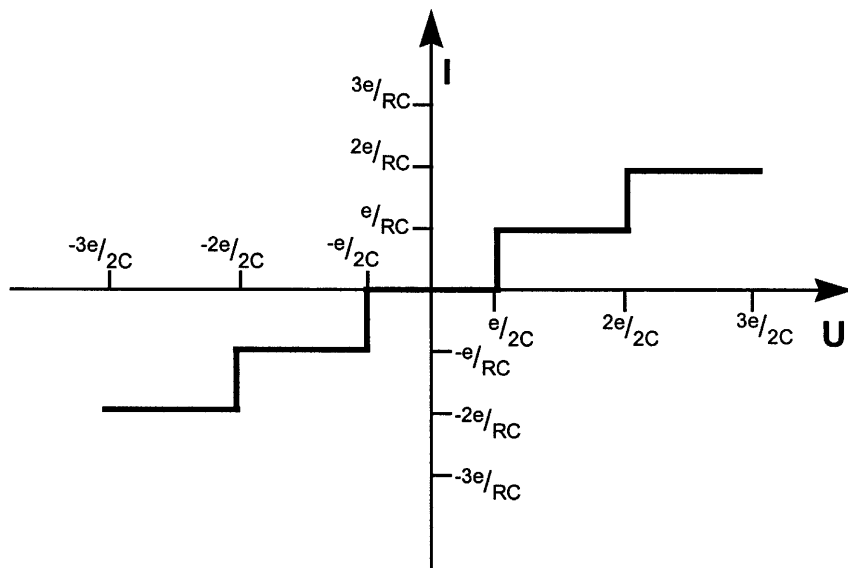
**FIGURE 2.13**    *I–U* characteristic of ideal single electron transport.

In Figure 2.14 a scanning electron microscopic (SEM) image of an experiment is shown in which a 17 nm palladium particle is trapped between two platinum tips, separated from them by a thin shell of organic molecules ($p$-$H_2N$–$C_6H_4$–$SO_3Na$).[16]

Figure 2.15 shows the *I–U* characteristic of this relatively large particle at two different temperatures. At 295 K there is a linear relation between *I* and *U*, corresponding to Ohm's law. At 4.2 K, however, a typical Coulomb gap of ∼55 mV is observed, indicating that the condition $kT \ll e^2/(2C)$ is fulfilled. In other words: a 17 nm palladium particle behaves in a bulklike manner at room temperature but as a quantum dot at liquid helium temperature. To make quantum size behavior of small metal particles available at room temperature we have to further reduce their size, as the capacitance *C* of the particles depends directly on their diameter.

Indeed, the gold cluster compound $Au_{55}(PPh_3)_{12}Cl_6$, the core diameter of which is only about one-tenth of that of the palladium particle discussed above, shows typical Coulomb blockade even at room temperature, as can be seen from Figure 2.16.[17]

Compared with transport of $10^7$ electrons in 1970 and $10^4$ electrons at present required to switch a silicon-based transistor, the one-electron switch being made possible by use of such quantum dots would revolutionize computer techniques.

In addition to the single experiments described above, the function of $Au_{55}$ clusters as quantum dots in a three-dimensional collective has been demonstrated by impedance measurements. Figure 2.17 illustrates the electronic situation in such a cluster.[18,19] It was found that, due to the extremely small size of these particles, discrete energy levels are formed. The electronic ground state is occupied by two electrons and is described by $\lambda_0/2 = 1.4$ nm ($\lambda_0 =$ de Broglie wavelength). The
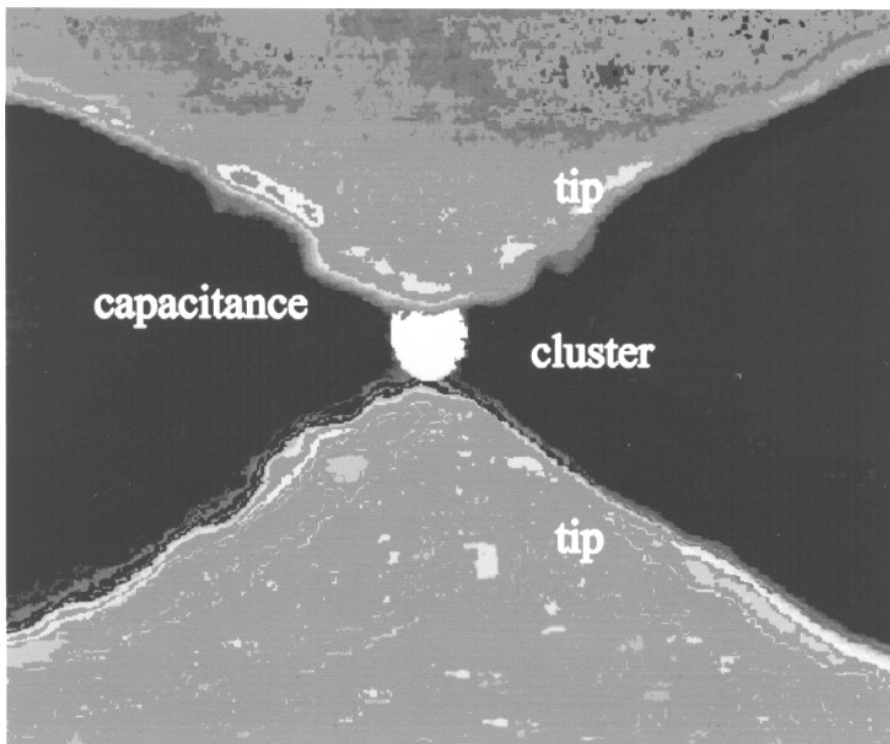
**FIGURE 2.14**   Scanning electron microscopic image of a 17 nm ligand-stabilized palladium cluster, trapped between two platinum tips. Reprinted with permission from *Appl. Phys. Lett.*, **1997**, *71*, 1273. Copyright The American Institute of Physics.[16]
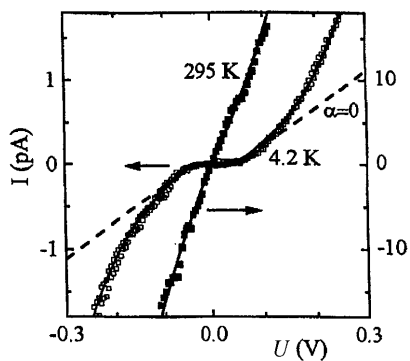


**FIGURE 2.15**   *I–U* characteristics of the 17 nm palladium cluster shown in Figure 2.14. At 295 K it behaves in a bulklike manner, following Ohm's law. At 4.2 K a pronounced Coulomb blockade is observed. Reprinted with permission from *Appl. Phys. Lett.*, **1997**, *71*, 1273. Copyright The American Institute of Physics.[16]
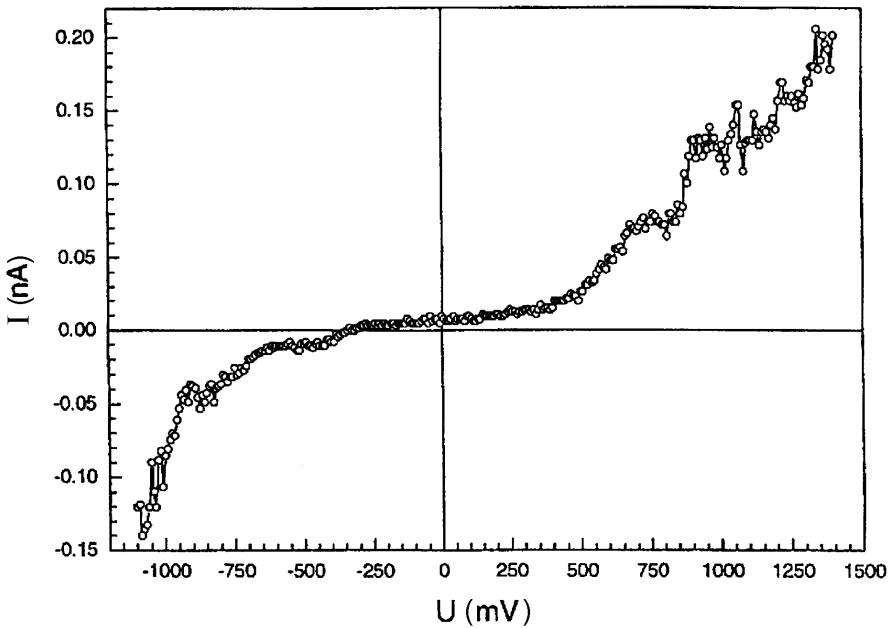
**FIGURE 2.16** *I–U* characteristic of a ligand-stabilized $Au_{55}$ cluster (diameter of the cluster core = 1.4 nm) at room temperature, showing a distinct Coulomb blockade. Reprinted with permission from *Appl. Phys. A*, **1998**, *66*, 189–190. © 1998 Springer Verlag.[17]

electronic conductivity of many clusters in a row results from tunneling processes between them through the ligand shells, leading to electronic intercluster bands by resonant tunneling. Figure 2.18 elucidates the situation.[18,19] The first excited state is characterized by the tunneling of an electron onto the first cluster in a row. Owing to the intercluster band structure, the electron is one-dimensionally delocalized. Such a "cluster-wire" should therefore conduct electrons without resistance.

This behavior has been observed in three-dimensional $Au_{55}(PPh_3)_{12}Cl_6$ cluster arrangements with 1.4 nm $Au_{55}$ nuclei separated from each other by $2 \times 0.35$ nm ligand shells. Whereas in the ground state the material behaves more or less as a nonconducting system, it becomes conductive when the electrons are elevated to the first excited state. If the distances are extended by thicker ligand shells or by spacer molecules, the activation energies increase. This can be seen from Figure 2.19.[20,21]

The use of such clusters or similar clusters as quantum dots demands their regular two-dimensional arrangements instead of a three-dimensional architecture. This is why many groups around the world are very active in trying to achieve simple and easily reproducible two-dimensional arrangements of quantum dots. Initial progress will be reported in Section 2.4.2.
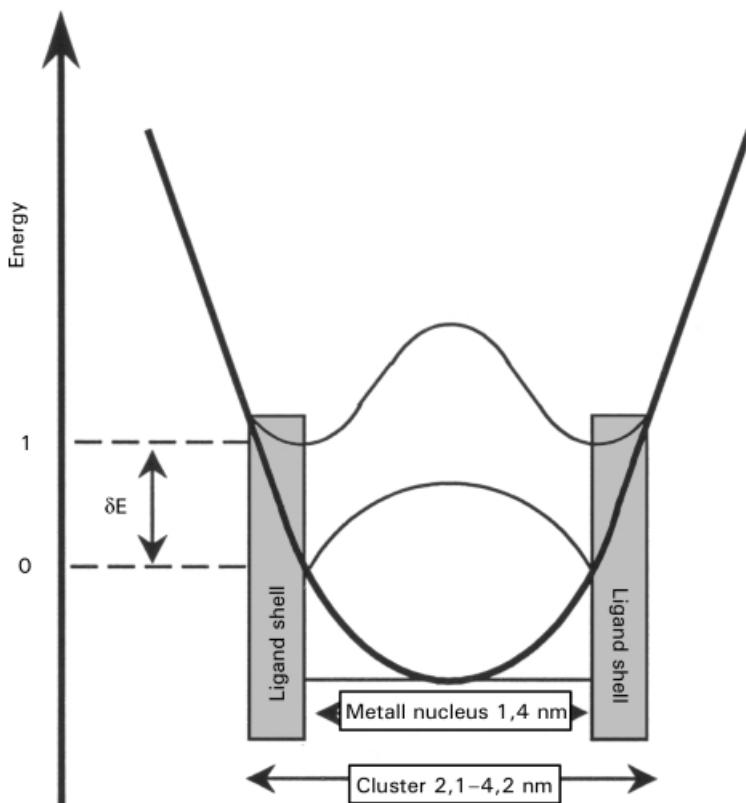
**FIGURE 2.17**    Scheme of the energy levels of a $Au_{55}(PPh_3)_{12}Cl_6$ cluster. In the ground state the diameter of the 1.4 nm $Au_{55}$ core corresponds to $\lambda/2$ ($\lambda =$ de Broglie wavelength). The excited state enables electron tunneling through the ligand shell.
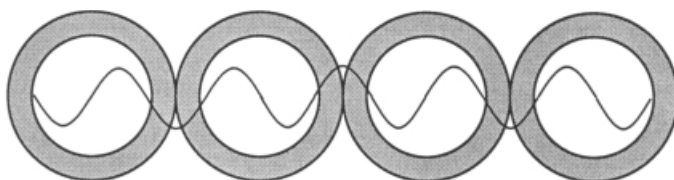


**FIGURE 2.18**    Idealized cluster wire with tunneling conditions.

### 2.2.3    Applications

**2.2.3.1    Colors**    Applications of nanosized particles have already been made in different fields and are to be foreseen in many future developments. A very obvious property of nanoparticles, at least of some metals, is their specific color (see Section 2.2.2.4). This is why the easily available gold colloids have been used since antiquity to color glasses. The well-known ruby-glass contains finely dispersed gold colloids,
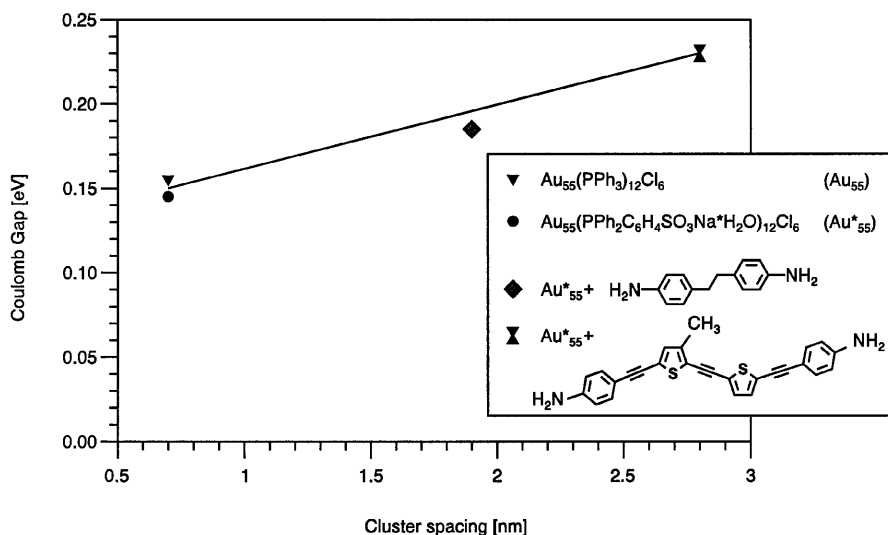
**FIGURE 2.19**  Correlation between cluster spacing and Coulomb gap of variously ligated $Au_{55}$ clusters.

generated during the glass-production process. No dramatic change has occurred subsequently in the making of red glasses, although the range of colors has, of course, been extended considerably up to the present time. Other metals such as silver and copper have also been discovered to give attractive colors in glassy materials. The use of alloys in particular has broadened the availability of nano-metals for coloring transparent materials.

**2.2.3.2  Catalysis**  The use of nanosized metals in heterogeneous catalysis is well established. The increasing proportion of surface atoms with decreasing particle size, compared with bulk metals, makes small metal particles become highly reactive catalysts, as surface atoms are the active centers for catalytic elementary processes. Among the surface atoms, those sitting on edges and corners are more active than those in planes. The percentage of edge and corner atoms also increases with decreasing size (see Table 2.1) and this is why very small metal particles are preferred as catalysts.

Catalysts based on the activity of metal nanoparticles can only be of the heterogeneous type. For industrial processes the particles are generated on supports such as alumina, silica, or charcoal by impregnating these substrates with solutions of the corresponding metal salt. Appropriate reduction processes follow, trans-forming the salts into zero-valent nanoparticles. Such procedures produce particles of various sizes. Since the larger particles will be less active than smaller ones, only a portion of the metal particles actually contribute to the catalytic process. Routes to uniform nanoparticles are therefore a research goal. This can be achieved if the particles are synthesized not on the support but in separate procedures. As will be discussed in section 2.3, such syntheses result in ligand-protected clusters and

colloids. Ligand shells on the particles surface may be a disadvantage, as the ligand molecules occupy catalytically active sites. On the other hand, ligand-protected particles can be used to tune a catalyst with respect to optimized selectivity. As ligand molecules never cover a particle surface completely, there exist enough channels to allow reactants and products to reach the metal surface and to desorb after the catalytic process. Figure 2.20 elucidates the principle of this type of catalytic system.[22–24]

Two practically studied catalytic processes illustrate how ligand molecules can influence catalytic activity and selectivity. Palladium is known as a good hydrogenation catalyst. On the other hand, hydrogenation of unsaturated compounds is often required not to proceed to the fully saturated state but only to partially hydrogenated products; the so-called semihydrogenation of alkynes to alkenes is an example. A good catalyst should not only enable semihydrogenation but in addition should selectively determine *cis-* or *trans*-configuration of the resulting alkene. The semihydrogenation of 2-hexyne to *cis*-2-hexene (Equation 2.7) is used to demonstrate a well-tuned catalyst. Other possible products such as *trans*-2-hexene, hexane, and olefinic isomers should be avoided.

$$CH_3-C{\equiv}C-CH_2-CH_2-CH_3 \xrightarrow[H_2]{catal.}$$

2-hexyne                                                    *cis*-2-hexene

(2.7)
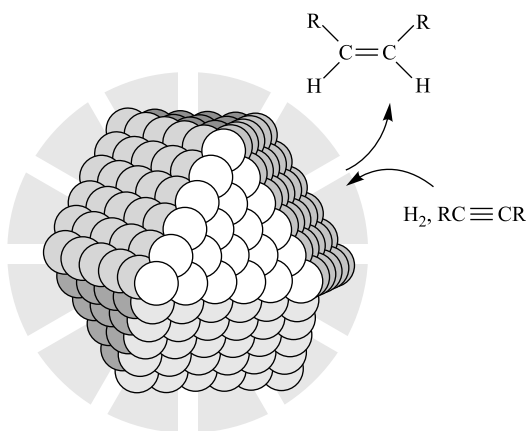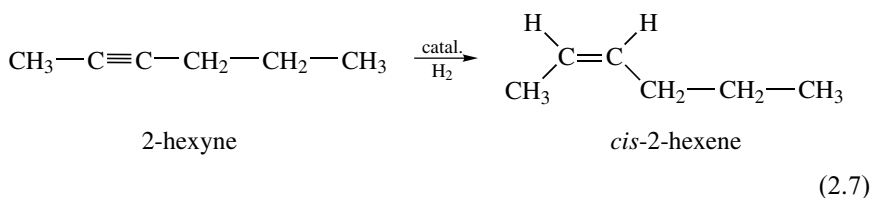


**FIGURE 2.20**   Sketch of a ligand-stabilized metal cluster indicating channels between ligand molecules admit reactants and allow products to leave. *J. Chem. Soc.*, *Dalton Trans.*, **1996**, *5*, 589–595. Reproduced by permission of the Royal Society of Chemistry.[22]

Palladium particles of 3–4 nm, protected by phenanthroline ligands in one case and by 2-*n*-butylphenanthroline ligands in the other, clearly show the different influence on activity and selectivity.

1,10-Phenanthroline            2-*n*-butylphenanthroline
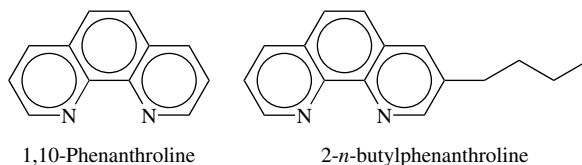
Figure 2.21 shows the course of the catalysis. In both cases TiO$_2$ was used as support, loaded by 0.5 weight% of the catalysts. The reactions were carried out at room temperature and 1 atm of H$_2$ pressure. Using unsubstituted phenanthroline, the maximum of *cis*-2-hexene formation is reached after ∼75 min. The selectivity is about 95%. After reaching the maximum, the product is immediately transferred to other compounds, mainly to *trans*-2-hexene. In contrast, using 2-*n*-butylphenan-throline, the activity of the catalyst is dramatically reduced: 500 min is the time required to reach the maximum. However it reaches 100% and, most significantly, the formation of other compounds is virtually unobservable. Only after ∼1500– 2000 min are small amounts of *trans*-2-hexene formed. Evidently, the butyl-tail of the ligands creates conditions on the particles surface such that semihydrogenation occurs exclusively.

### 2.2.3.3  *Nanoelectronics*   Whereas manipulation of colors and catalytic activity of nanometallic particles has already formed part of established practices, the most valuable electronic properties of small metal particles, as discussed in section 2.2.2.5, have not yet been realized in working systems. However, it can be foreseen that metal clusters behaving as quantum dots will become of decisive importance in future nanoelectronics. This is simply due to their ability to enable single-electron storage and tunneling. As has been shown before, ligand-stabilized 1.4 nm clusters can be charged by a single electron, which is then stored in the particle until the corresponding voltage is applied to move it to the counterelectrode. Thus these particles behave ultimately as miniaturized transistors, working at room temperature! There are still tremendous scientific and technical problems to be solved: for instance, there is still no way to address these incredibly small dots and electrical connections of the same size range must be developed. Furthermore, the quantum dots must be specifically arranged on suitable substrates. Modern microtransistors are lithographically generated on silicon surfaces. They are large enough to be mechanically contacted (∼200 nm) and their arrangement on the silicon wafer is performed by the lithographic process itself. Individual nanoclusters must be orga-nized, fixed, and contacted. In spite of these huge challenges it can be assumed that appropriate solutions will be found. The advantages of using single-electron tran-sistors instead of traditional semiconductor structures are so manifold and evident that their development and use is inevitable. An actual transistor unit on a silicon
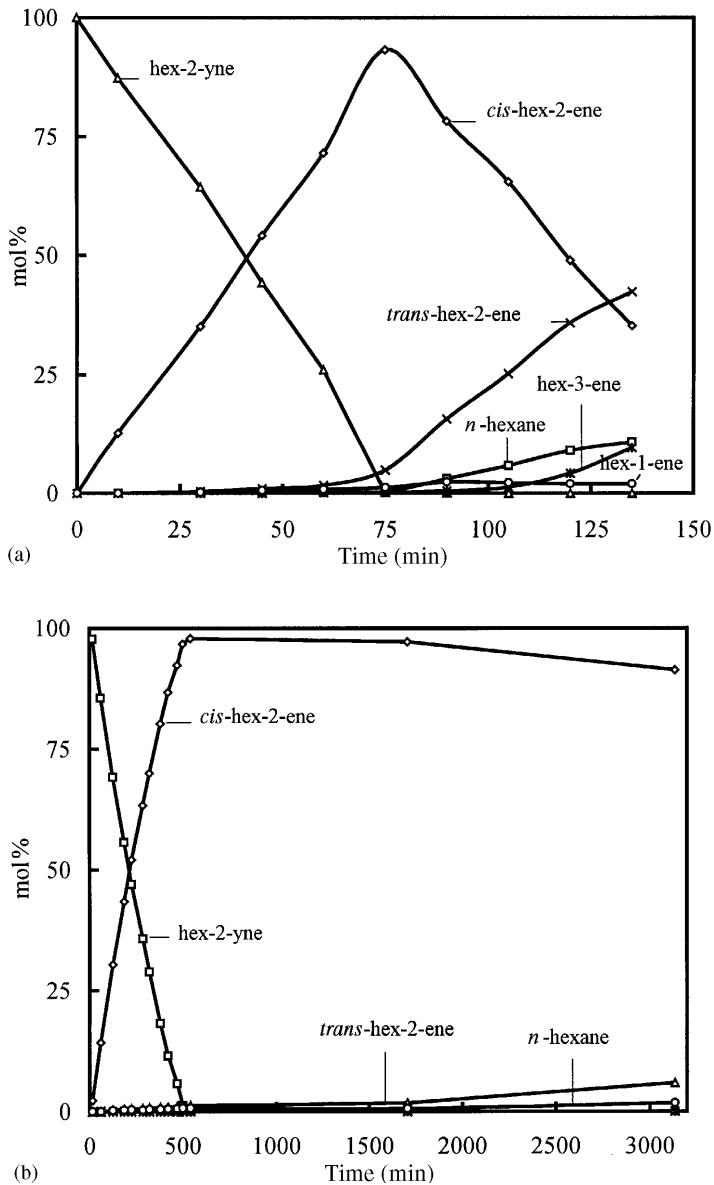
**FIGURE 2.21**    (a) Course of the semihydrogenation of hex-2-yne to *cis*-hex-2-ene with phenanthroline-stabilized palladium clusters as catalysts on TiO$_2$ as a support. (b) The same reaction with 2-butylphenanthroline as ligands on the same palladium clusters. Compared with the reaction in (a) the activity has decreased dramatically, whereas the selectivity has increased 100%. Formation of other products starts after ~25–30 hours. *J. Chem. Soc., Dalton Trans.*, **1996**, *5*, 589–595. Reproduced by permission of the Royal Society of Chemistry.[22]

wafer works with $\sim 10^4$ electrons per action. Its dimensions of $\sim 200\,nm$ are tremendous compared with a 1.4 nm cluster. A simple comparison shows that a contemporary silicon transistor could be substituted by about 1000 cluster quantum dots.

Many efforts have been initiated to solve the first of the various problems, namely, to find ways to routinely arrange clusters on surfaces in a well ordered manner. Section 2.4 will deal with these problems and illustrate some very promising first successes.

## 2.3   SYNTHESES OF METAL NANOPARTICLES AND STRUCTURES

### 2.3.1   General

There are generally two routes to preparation of nanosized metal particles: top-down and bottom-up. Top-down methods reduce macroscopic particles to the nano size scale. This route is usually not very well suited to preparing uniformly shaped particles; very small sizes are especially difficult to realize. Top-down routes will not be considered further. Bottom-up procedures are much better suited to generating uniform particles, often of distinct size, shape, and structure, as will be shown in the following sections. Bottom-up methods start with atoms that aggregate in solution or even in the gas phase to form particles of definite size, if appropriate experimental conditions are applied.

### 2.3.2   Gas Phase Syntheses

Figure 2.22 shows a schematic drawing of a so-called cluster-beam generator. It consists of a heating unit where metal targets are evaporated by simple heating or, better, by laser irradiation. The flow of atoms then passes variously constructed slits to focus the beam. Modern techniques use mass spectrometric units to separate different particles according to mass, leading to fractions of very uniform particles. The disadvantage of cluster-beam generated particles is the lack of a protecting skin for the clusters. Bare metal particles immediately aggregate to polycrystalline powders, owing to the thermodynamically preferred metal–metal bonding, and aggregation of particles means loss of individuality. Solutions to this problem include the deposition of the particles on supports; a more recent promising method uses the spontaneous reaction of bare particles with ligand molecules in solution.[25] The naked particles of a cluster-beam react with molecules, covering their surface faster than they react with each other. This procedure is similar to chemically based methods that have been known for decades for preparing stabilized nanoparticles in gram amounts. Chemical approaches to nanosized metals are therefore the much more suitable alternative. Some principles will be discussed in the following.
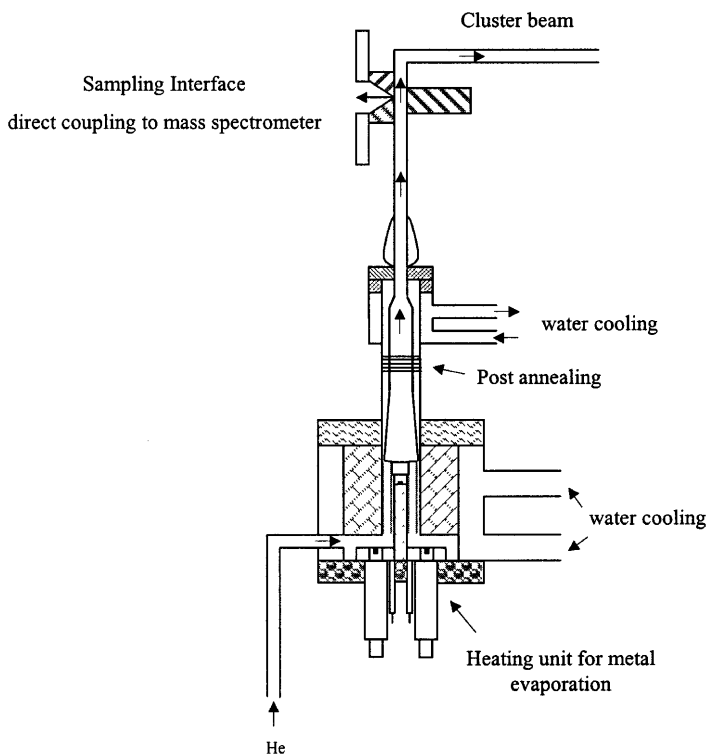
**FIGURE 2.22**   Simplified sketch of a cluster beam generator on the basis of a generator described in reference 25.

### 2.3.3   Chemical Syntheses

All chemically based synthetic routes to nanosized metal particles start with the reduction of positively charged metal atoms, either as simple ions or as centers of complexes in solution.[2] Solvents can vary from water to very nonpolar media such as hydrocarbons, depending on the nature of the salt or the complex used. The nature of the metal compound also determines the kind of reducing agent to be applied. Gaseous hydrogen, hydridic compounds, reducing organics like alcohols, and many other species have been successfully applied. In any case it is essential to generate the particles in the presence of suitable molecules that will cover their surface. This is an essential, but also the most serious and complicated step in cluster formation: if the ligand molecules are already present when reduction starts, formation of larger particles can be prevented by blocking of growth. If the ligands are added subsequently, it is difficult to determine the right moment for stopping cluster growth; in practice it involves the interplay between the generation of metallic precipitates or mirrors on the one hand and the formation of mono- or oligonuclear complexes on the other hand. Figure 2.23 shows a highly simplified scheme of the principal steps of nanosized particle formation in solution. Some specific syntheses will be discussed in the following to show the wide field of preparative possibilities for nanosized particles based on chemical processes.
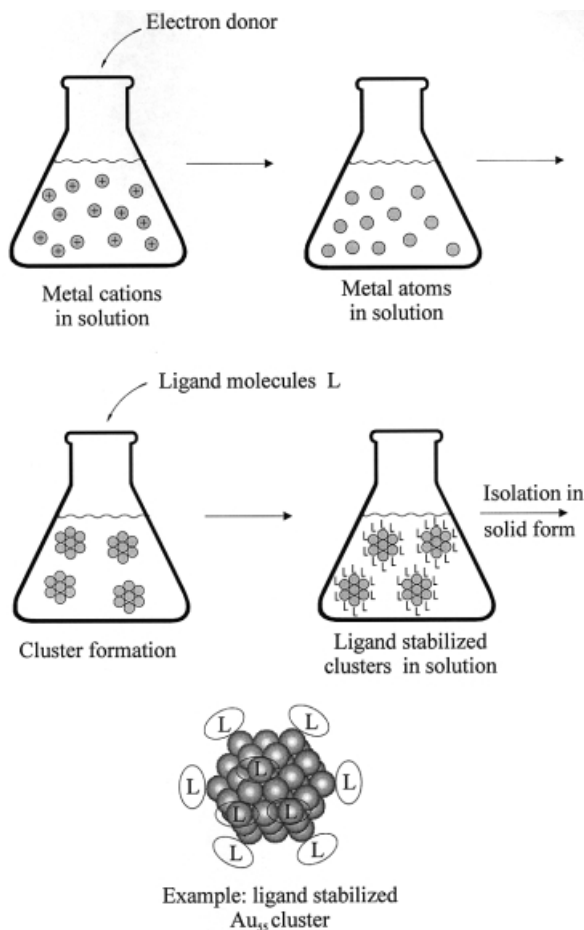
**FIGURE 2.23**   Schematic procedure of cluster synthesis.

The generation of larger metal particles, usually called colloids, can be traced back to Michael Faraday in the mid-nineteenth century.[26] Faraday studied the formation of deep red colloidal gold solutions in water. Even today it is a very convenient procedure to generate gold colloids by Faraday's method using the reduction of $[AuCl_4]^-$ by citric acid. Nowadays numerous additional recipes exist for the preparation of mainly noble metal colloids in dilute solution.[27–29] It has been known since Faraday's time that such solutions can be of considerable stability without the addition of stabilizing ligand molecules if impurities are excluded. Why do these large particles not precipitate owing to coalescence processes? As an example, we consider the classical gold sols, prepared by the above-mentioned reduction of $[AuCl_4]^-$ by sodium citrate. The particles formed are surrounded by an electric double layer arising from adsorbed citrate and chloride ions and by the corresponding cations. The resulting Coulomb repulsion between the particles prevents aggregation and coalescence. Figure 2.24 illustrates the situation between
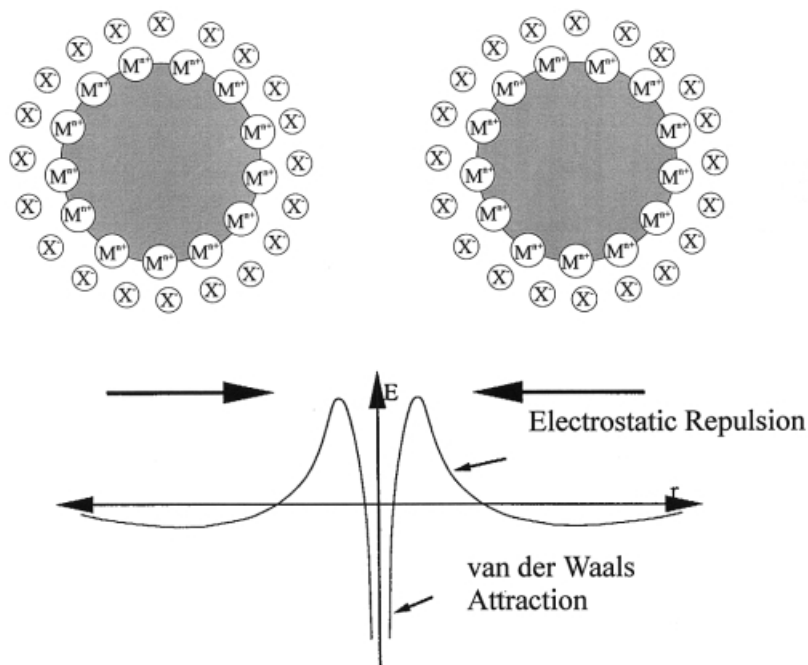
**FIGURE 2.24** Electrostatic stabilization of metal colloids. Van der Waals attraction and electrostatic repulsion compete with each other.[27]

two particles having electric double layers. The Coulomb repulsion between the particles decays approximately exponentially with the particle distance. The weak minimum in the potential energy defines a stable situation. Thus, if the electric potential resulting from the double layers is high enough, electrostatic repulsion prevents aggregation. The surface charge can be reduced if the adsorbed anions are displaced by strong ligand molecules. This enables the formation of colloid patterns as can be seen in Figure 2.25.

In contrast to the charge-stabilization of colloids, the protection of colloidal particles and of other nanosized metal particles by strongly binding molecules improved their stability and enabled their use for a variety of purposes.

Colloidal particles can be generated by very different methods. *Salt reduction* is one of the most frequently used routes; alcohols have proved very successful reducing agents, due to their $\alpha$-hydrogen atom;[30,31] for example,

$$RhCl_3 + \tfrac{3}{2}R^1R^2CHOH \rightarrow Rh_{coll} + \tfrac{3}{2}R^1R^2C{=}O + 3HCl \qquad (2.8)$$
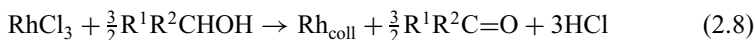
Palladium is another metal that is preferably synthesized in colloidal state using alcohols.[32–34] Gold is probably the most famous metal with respect to the colloidal state. Faraday prepared it first by using phosphorus vapor to reduce $[AuCl_4]^-$ in aqueous solution. Subsequently, a variety of other compounds have been success-
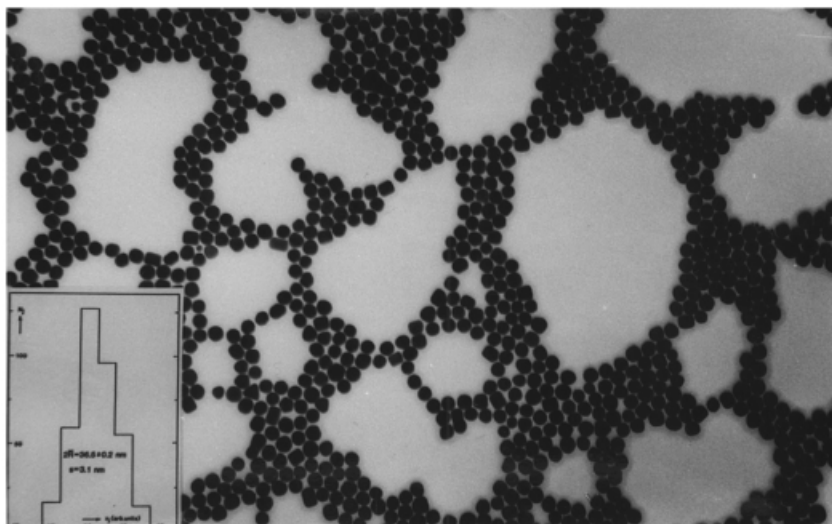
**FIGURE 2.25** Pattern of ligand-stabilized 36 nm gold colloidal particles. The inset shows the particles' size distribution.

fully introduced for making gold colloids; the best-known reducing agent for gold is sodium citrate. Turkevitch and coworkers, in particular, have developed gold colloid syntheses on a broad scale.[28] Citrate is also well-suited to make platinum hydrosols. Another very powerful reducing component for noble metal salts is hydrogen, and borohydrides, hydroxylamine hydrochloride, formaldehyde, carbon monoxide, and other compounds have also been applied successfully.[35]

The formation of metal nanoparticles is not limited to the reduction of cations to the zero-valent state; it can also occur by *thermal decomposition* of organometallic compounds.[27] However, this technique is fairly limited and has not become as important as salt reduction. The same applies to so-called *ligand reaction and displacement* from organometallics. Complexes like $Pd(dba)_2$, $Pd_2(dba)_3$, $Pt_2(dba)_3$ (dba = dibenzylideneacetone) react with hydrogen or carbon monoxide under mild conditions to give free ligands and zero-valent metals as nanoparticles.[27,36] Finally, *photolysis and radiolysis* should also be mentioned as methods that have never achieved the importance of the salt reduction. However, they are used with advantage in some special cases. In principle, the photolytic method has a long tradition in photography, where silver halides are decomposed to silver nuclei and halogen by light. Radiolytic methods start with metal ions and produce solvated electrons that reduce the cations to neutral atoms, for instance,[27,37]

$$Cu^{2+} \xrightarrow{e^-_{solv}} Cu_2 \xrightarrow{e^-_{solv}} Cu_{coll} \tag{2.9}$$

The generation of metal particles on the nanoscale, independently of the method used, affords their stabilization by a protecting envelope. Without protection, the particles will exist only in diluted solution, weakly stabilized for instance by a shell of electrically charged species. This charge-stabilization, however, will not allow

isolation of the particles in solid state and the solutions can be concentrated only to a limited extent. If the water of a "Faraday-sol" is evaporated, precipitates of poly-crystalline gold or gold mirrors are formed.

The protective enveloping of nanoparticles may be achieved by various routes. A very common method is the use of organic polymers such as poly(vinyl pyrroli-done), poly(vinyl alcohol), or poly(methyl vinyl ether). Using these or related functionalized polymers in liquid form, the nanoparticles can be generated directly in the polymer to give liquid composites that are used for catalytic purposes. Such systems, still relatively dilute, cannot be used for physical investigations of the particles, so various procedures have been developed to protect the particles' surface with strongly bonded molecules. Various syntheses have been devised to make well-defined clusters. Colloids, in this chapter on metallic nanoparticles as polycrystalline species with a more or less defined size distribution, are usually generated only as charge-stabilized particles and must be protected after their formation. Clusters, that is, monocrystalline particles of distinct size, shape, and architecture, are often found in the presence of ligands. Ligand exchange reactions allow derivatization of the clusters. As the solubility of clusters is exclusively determined by the chemical nature of the ligand molecules, ligand exchange reactions open the possibility of producing clusters of identical metal cores but of completely different solubility, in solvents ranging from nonpolar hydrocarbons to water.

As an example we illustrate the generation of some $Au_{55}$ clusters, starting with the synthesis of $Au_{55}(PPh_3)_{12}Cl_6$ and some of its derivatives, available by ligand exchange (Figure 2.26).[38,39]

## 2.4   ROUTES TO ARRANGEMENTS

Several aspects make metal nanoparticles interesting objects of research. As described in earlier sections, an especial one is future applications in diverse nanoelectronic devices, owing to the quantum size behavior of nanoclusters. In addition there is their use as powerful catalysts on different supports, as well as their magnetism, their colors, and many other properties that already have relevance in modern technologies. However, the most valuable property of metal nanoparticles, namely the electronic quantum confinement, can be used practically only under certain conditions: the quantum dots must be regularly arranged, either three- (3D), two- (2D), or one-dimensionally (1D). Otherwise communication between them, storage of information, and so on, will not be possible. For this reason we conclude this chapter on nanosized metal particles with a description of current knowledge of their 3D, 2D, and 1D arrangements.

### 2.4.1   Three Dimensions

Nature prefers three-dimensional ordering of atoms, ions, and molecules and the crystallinity of the inorganic world belongs to our everyday life. Except in the biosphere and in liquids material tends to organize three-dimensionally. The 3D habit of nanosized metals should be quite obvious, but is not. Why not?
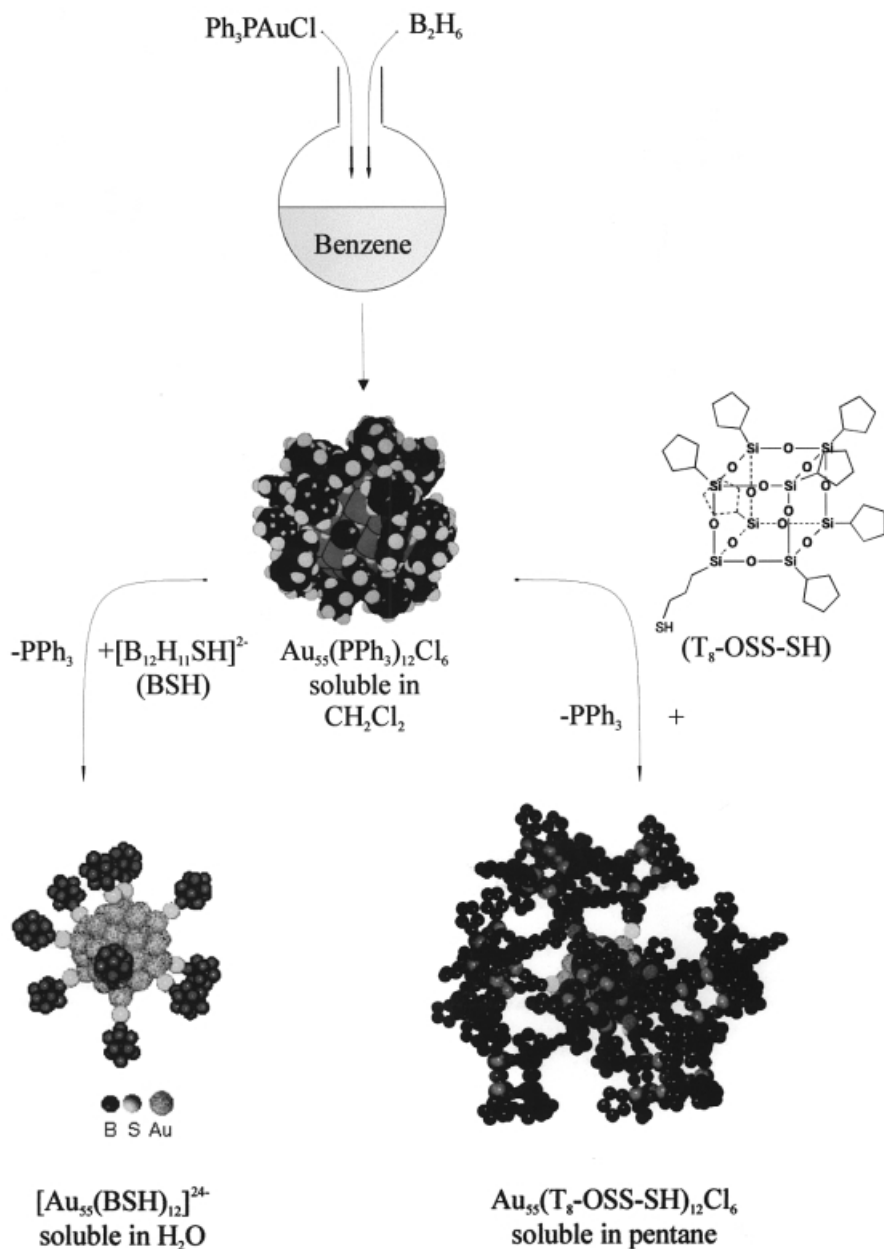
**FIGURE 2.26** Synthetic routes to $Au_{55}(PPh_3)_{12}Cl_6$ and two derivatives by ligand exchange.

One of the main reasons is probably the size distribution and the disagreement in structure of particles in the nanometer regime. Crystals usually consist of periodically positioned identical building blocks. Metal particles, say 10 or 20 nm in size, differ in size by at least 10%. Smaller clusters are of identical size and shape, but a second difficulty arises from the unavoidable protective ligand shell on the particle's surface, making them spherelike. These circumstances prevent or at least complicate formation of 3D crystals of nanosized metal particles. In spite of these hindrances, various groups have succeeded in generating small 3D arrangements of colloidal particles and of nanoclusters. On the other hand, 3D assemblies will probably be less important for future applications than 2D and perhaps 1D arrangements. The addressing of individual dots in a 3D crystal appears almost impossible, and controlled communication between the building blocks is probably equally difficult. Artificial neuronal networks, still a distant prospect, may profit from such 3D nanoarchitectures. Some nice examples of 3D superstructures have been described in the last few years. Silver nanoparticles, protected by dodecanethiol, have been self-assembled layer by layer. Crystals with edge length of some micrometers and up to 17 layers (~100 nm) have been obtained. The silver nanocrystals forming such 3D assemblies were 4–5 nm in size. [25,40,41] Figure 2.27 illustrates the packing principle of the truncated octahedra via the thiol ligands.

The procedure for depositing silver nanoclusters two- and finally three-dimensionally from the gas phase seems complicated compared with crystallization from solution as is usual in chemistry. The well-defined cluster $Au_{55}(PPh_3)_{12}Cl_6$ and some of its derivatives can be crystallized from solution under very simple conditions in preparative amounts. Crystals of some micrometers in size are easily formed if the solvent in a cluster solution, for instance $Au_{55}(PPh_3)_{12}Cl_6$ in dichloromethane, is removed in vacuum. The black residue consists exclusively of microcrystals. Slow crystallization from solution does not work, due to the continuous decomposition of
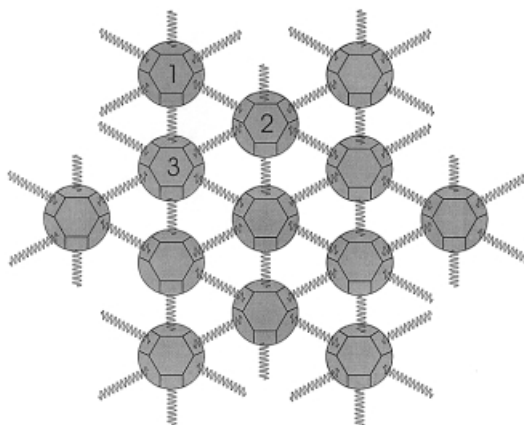


**FIGURE 2.27**    Sketch of a $[\bar{1}1\bar{1}]$ image of thiol-linked truncated octahedral silver particles. The particles labeled 1, 2, 3 represent the first, second, and third layers from the bottom.

the clusters in solution. The clusters form mostly hexagonally shaped crystals with fcc-packed clusters as can be seen from Figure 2.28.[42]

The structural arrangement of the gold clusters was studied by high-resolution electron microscopy of thin crystals and by wide-angle (WAXS) and small-angle (SAXS) X-ray crystallography. The reason these small clusters form 3D super-structures by such a simple process can be seen in the uniformity of size and shape in contrast to less well defined larger colloids.

3D assemblies of 6 nm nanoparticles of $Fe_{50}Pt_{50}$ have been achieved in very good quality and with surprisingly high stability with respect to temperature.[43] The advantage of such ferromagnetic nanoparticles is obvious. $Fe_{48}P_{52}$ nanocrystals of 4 nm have been used for high-density magnetization reversal transitions.
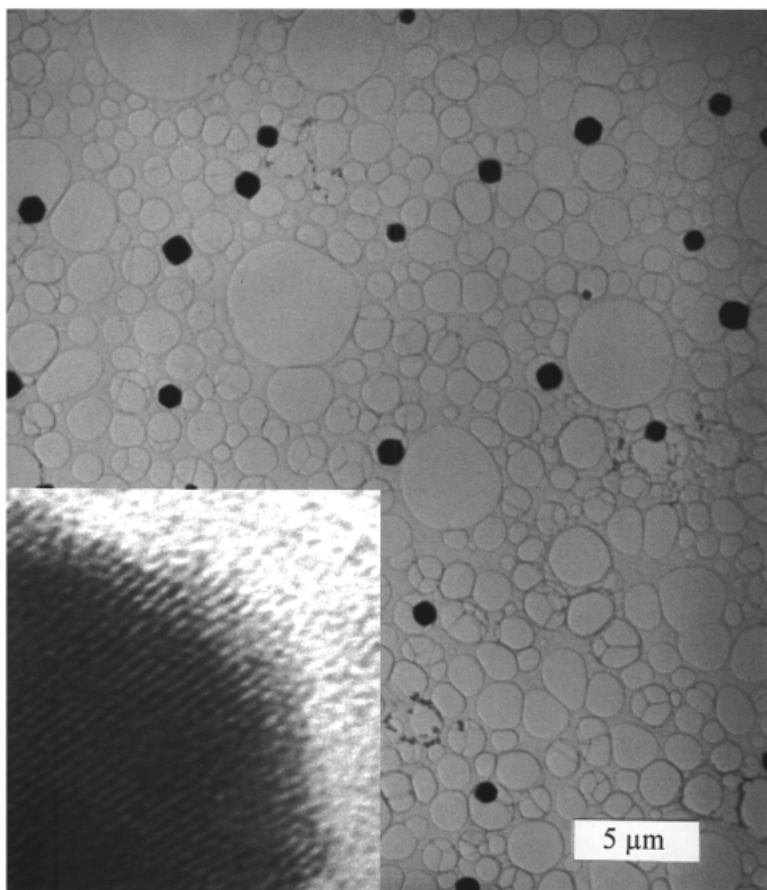


**FIGURE 2.28** Microcrystals of $Au_{55}(PPh_3)_{12}Cl_6$. The inset shows a TEM image of a thin crystal edge, indicating rows of fcc packed clusters. Reprinted from *Chem. Comm.*, **1999**, 1303–1304. Reproduced by permission of the Royal Society of Chemistry.[42]

### 2.4.2 Two Dimensions

As already mentioned, 2D assemblies of nanoparticles will probably play a much more important future role than do 3D microcrystals. A surface covered with ordered quantum dots that can be addressed individually is a prerequisite for future chip generations.

Two different routes have been developed for depositing metallic nanoparticles onto surfaces: one is the use of regularly ordered micelles in diblock copolymer films as nanoreaction vessels to produce the particles inside, followed by a quantitative oxidation of the organic material in an oxygen plasma.[44–47] The micelles are filled by the corresponding metal salt, followed by a reduction step forming the nanoparticles. The other route is based on self-assembly processes. Very often such regular two-dimensional arrays formed accidentally under appropriate conditions on the carbonated copper grid used for electron microscopy. These results do not promise attractive applications because they cannot easily be reproduced, and the 2D lattices cannot be transferred to surfaces where they are needed.

A first approach aiming at a particular result used molecularly linked metal clusters for 2D ordering.[48] Gold colloids encapsulated by a shell of alkyl thiols were used to form a close-packed monolayer on a flat substrate, followed by the addition of bifunctional dithiols linking the particles to give a 2D network (Figure 2.29).

A novel approach to 2D superlattices formed by quantum dots recently developed[49,50] is of particular interest because ligand-stabilized $Au_{55}$ clusters have been used as building blocks. As described in earlier sections, these clusters can be used for single-electron storage and tunneling even at room temperature. Hexagonally ordered and primitive square planar arranged $Au_{55}(Ph_2PC_6H_4SO_3H)_{12}Cl_6$ clusters self-assemble on a poly(ethyleneimine) (PEI)-covered surface of a carbonated



10 nm
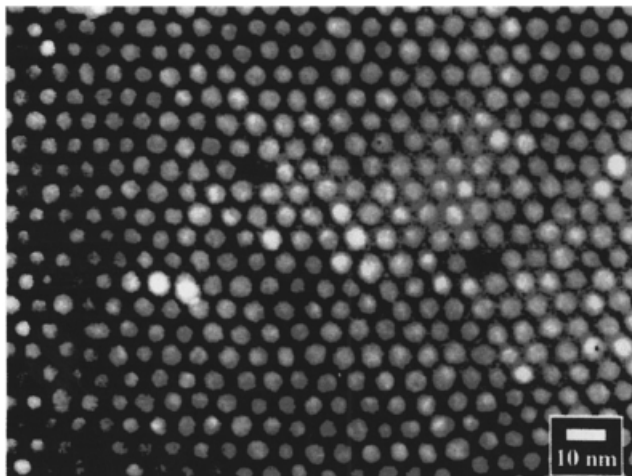
**FIGURE 2.29** Hexagonally close-packed monolayer of gold nanoparticles linked by dithiols.

copper grid. Acid–base reactions take place between the NH groups of the PEI and the $SO_3H$ functions on the cluster surface. However, this procedure only works if molecularly flat surfaces are available.

An alternate procedure guarantees absolutely smooth surfaces for the 2D network formation: the phase boundary between two liquids. It can be used to assemble $Au_{55}(PPh_3)_{12}Cl_6$ clusters with the help of amphiphilic molecules or, even better, amphiphilic polymers. Figure 2.30 illustrates the procedure generally. Thiolated cyclodextrins, poly(vinylpyrrolidone) and poly(phenylene-ethynylene) work best and as amphiphiles give very good results, as can be seen from Figures 2.31 and 2.32. Figure 2.33 shows a cutout of a simple square-planar ordering of clusters, illustrating the perfect arrangements of clusters touching each other via their ligand shells.

These are only initial steps toward nanostructured surfaces for nanoelectronic purposes. The next aim is to vary the distances between the clusters so as to change the activation barriers between the quantum dots.
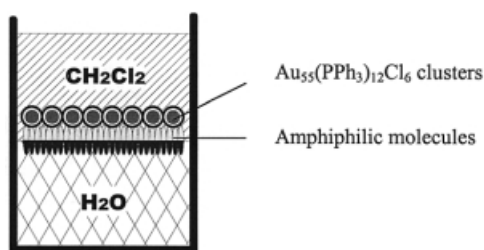


**FIGURE 2.30**   Illustration of the self-assembly of a $Au_{55}(PPh_3)_{12}Cl_6$ monolayer at the phase boundary between water and dichloromethane.
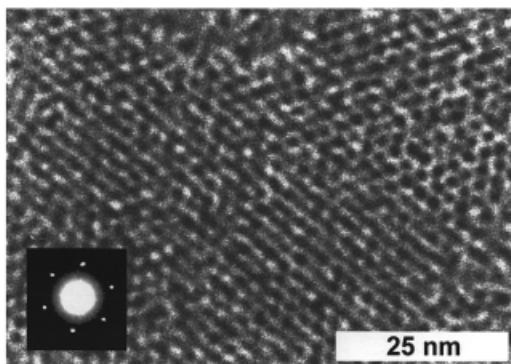


**FIGURE 2.31**   TEM image of a hexagonal $Au_{55}(PPh_3)_{12}Cl_6$ monolayer on poly-(vinylpyrrolidone). The inset shows the electron diffraction pattern. Reprinted with permission from *Eur. J. Inorg. Chem.*, **2000**, 835–837. © Wiley-VCH.[50]
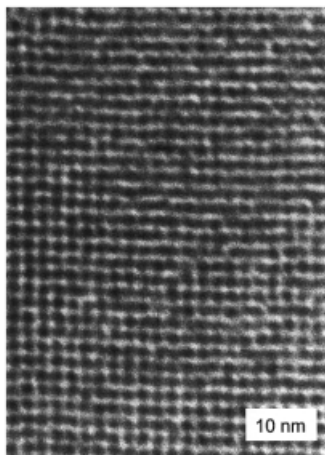
**FIGURE 2.32** TEM image of a $Au_{55}(PPh_3)_{12}Cl_6$ monolayer, arranged as squares on poly(ethyleneimine). Reprinted with permission from *Angew. Chem.*., **2000**, 181. © 2000 Wiley-VCH.[49]
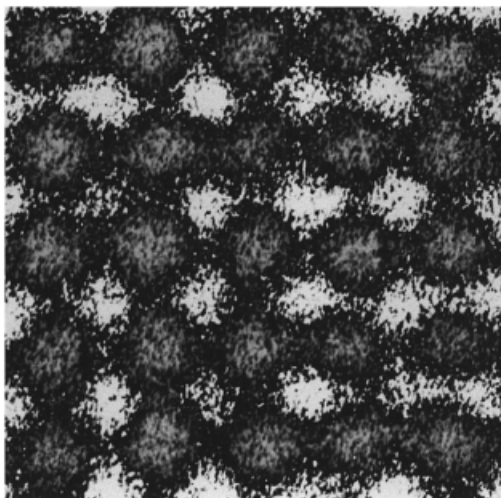


**FIGURE 2.33** Magnified cutout of the monolayer shown in Figure 2.32. Reprinted with permission from *Angew. Chem.*., **2000**, 181. © 2000 Wiley-VCH.[49]

### 2.4.3 One Dimension

The routine fabrication of one-dimensionally arranged metal nanoclusters has not yet been achieved. However, based on some accidental formations of particle chains, there are indications that with the help of appropriate templates 1D nanocluster assemblies can be prepared selectively and reproducibly.

The following templates have been shown to be useful tools for 1D arrangements of nanoparticles:

*Defined steps on crystalline surfaces*      The particles tend to self-assemble predominantly along crystallographically well-defined steps, due to the increased surface activity (Figure 2.34). This technique requires very particular instrumentation and crystalline materials. A routine technique for fabricating series of parallel quantum dot wires for nanoelectronic devices is in principle possible, but is difficult.

*Channels and pores*   Channels and pores of appropriate dimensions can be filled with particles. The quality of the 1D cluster wires depends on the quality of the matrices. The problem at present is the lack of adequate pores and channels only a few nanometers in diameter. The usual technique for generating channels is electron beam lithography. However, with this technique it is hardly possible to get below 20–30 nm, far too wide to be filled with a single chain of 2–4 nm clusters.

Nanoporous alumina membranes seem to fulfill the conditions required to make huge bundles of nanowires. Alumina films with nanopores, running almost parallel through the transparent and glassy films, can easily be prepared by anodizing
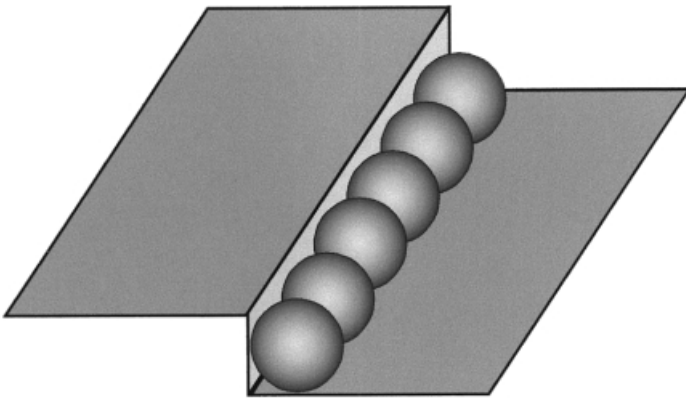


**FIGURE 2.34**   One-dimensional arrangement of nanoparticles at a surface step.
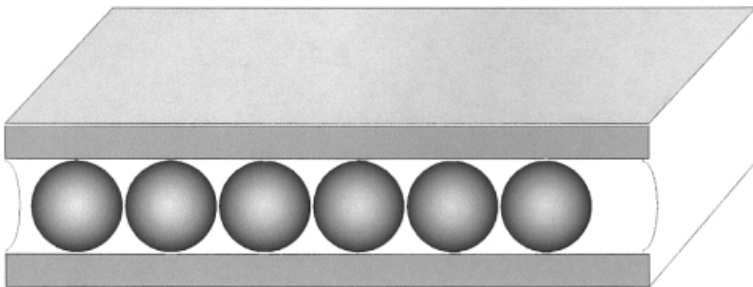


**FIGURE 2.35**   One-dimensional arrangement of nanoparticles in a channel of a nanoporous matrix.

alumina plates in oligoprotic acids.[51–55] The pore widths can be varied between ~5 and 200 nm. Figure 2.36a shows an atomic force microscopy (AFM) image of an alumina surface with perfectly ordered pore entrances. Figure 2.36b gives a view into the membrane by means of transmission electron microscopy (TEM).

Different methods have been tried for filling such pores. The simplest and most effective is the vacuum induction of cluster solutions, followed by evaporation of the solvent. However, the order of the particles that remain is usually not very good. Electrophoretic filling works better as the particles are deposited from the bottom of the pores. Figure 2.37a shows a TEM image of a single pore of 7 nm in diameter, filled with $Au_{55}$ clusters with a bulky ligand shell that increases their diameter from 1.4 nm to 4.2 nm. This is still too small for a 7 nm pore and leads to the observed helical cluster arrangement shown in Figure 2.37b.[55] Only a few of the $10^9$–$10^{11}$ pores per $cm^2$ could be filled in such a pseudo-1D manner and most of them show defects, due to missing clusters in a row.

Another strategy using a given texture for generating 1D cluster assemblies is based on wetting instabilities, observed when monolayers are transferred onto solid substrates. Figure 2.38 shows an SFM (dynamic scanning force microscopy) image of a monolayer of L-α-dipalmitoylphosphatidylcholine (DPPC), formed from a Langmuir–Blodgett film on water by transfer onto mica.[56] The channels have a width of about 200 nm, much too large for nanoparticles of interest. However, in contact with ligand-stabilized $Au_{55}$-clusters, dissolved in 1-phenyloctane, quasi-one-dimensional cluster-arrays in the channels can be generated, although the DPPC layer is obviously free of clusters. The height of the assemblies of ~4 nm corresponds well with the cluster diameter, except for a few instances. Figure 2.38 shows
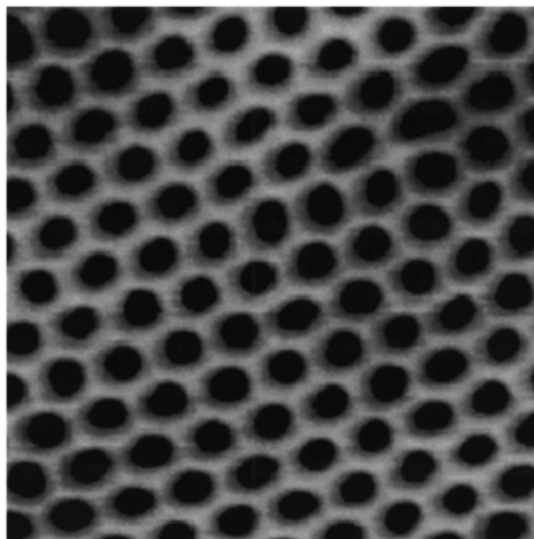


(a)

**FIGURE 2.36**    (a) AFM image of an alumina surface with hexagonally ordered 60 nm pores.
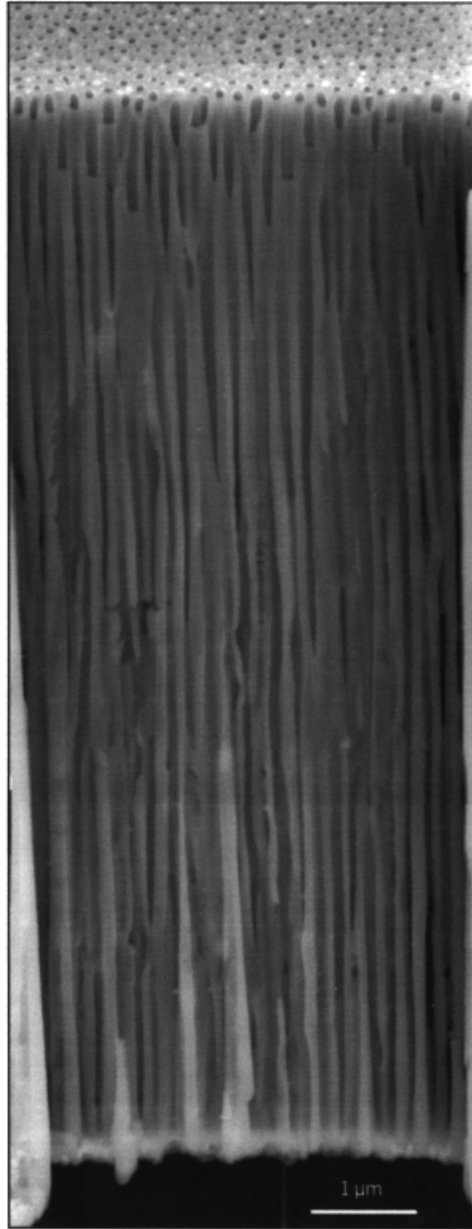
(b)

**FIGURE 2.36** (b) TEM image of the alumina membrane sectioned perpendicular to the surface. The parallel pores can be seen.
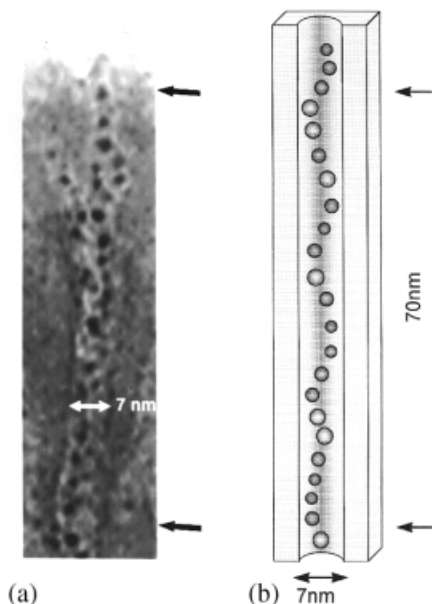
**FIGURE 2.37** (a) Wire of $Au_{55}(T_8\text{-OSS})_{12}Cl_6$ (diameter $= 4.2$ nm) clusters in a 7 nm pore. (b) Model of the wire indicating the helical ordering due to the discrepancy between cluster diameter and pore width. $T_8$-OSS is the silsesquioxane ligand shown in Figure 2.26. Reprinted with permission from *Chem. Eur. J.,* **1997**, *3,* 1951–1956. © Wiley-VCH.[50]
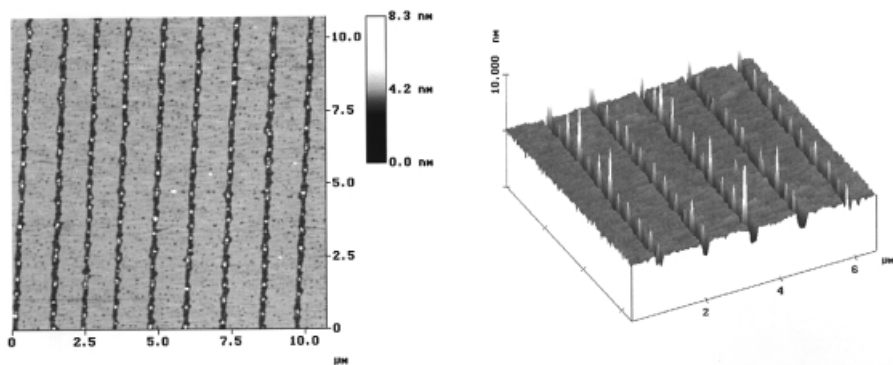


**FIGURE 2.38** SFM image of $Au_{55}(T_8\text{-OSS})_{12}Cl_6$ cluster islands in 200 nm channels of a monolayer of L-$\alpha$-dipalmitoylphosphatidylcholine. $T_8$-OSS is the silsesquioxane ligand shown in Figure 2.26. Reprinted with permission from *Nature,* **2000**, *403,* 173–175. © 2000 Macmillan Magazines Ltd.[56]
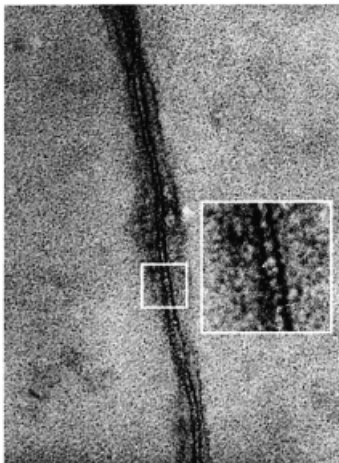
**FIGURE 2.39** One-dimensional arrangement of $Au_{55}(PPh_3)_{12}Cl_6$ clusters along a poly(1,4-phenylene-ethynylene) molecule.

an SFM image of cluster islands in the channels, the diameter of which is in the range of the channel's width, i.e. 200 nm, corresponding to about 50 clusters per island. This example shows principally that clusters can be arranged one-dimensionally in a parallel manner, if appropriate channels are available. Here, we observe cluster disks in a row.

*Long-chain polymers*  A third method that may become of interest if initial results can be developed further is the use of long-chain stiff molecules (polymers), which are able to interact with clusters to marshall them in rows. The first experiments with poly(phenylene-ethynylene) and $Au_{55}(PPh_3)_{12}Cl_6$ clusters in very dilute solutions (to avoid 2D layer formation) give perfect 1D cluster arrangements. It can be foreseen that one-dimensional quantum dot arrangements will become available routinely and in perfect order. Further research and development is necessary to optimize the conditions.

   To summarize this section on 3D, 2D, and 1D quantum dot organizations, 3D and 2D arrangements of a series of nanoparticles are already available and can be used for further development. 1D structures are not yet as far developed, but there are several promising procedures. In other words, after two decades of synthetic work we are now on the way to using metal nanoparticles for the most valuable applications, namely in nanoelectronics. The problems of positioning will be solved.

## REFERENCES

1. J. de Jongh (editor), *Physics and Chemistry of Metal Cluster Compounds*, Kluwer Academic Publishers, Dordrecht, **1994**.

2. G. Schmid (editor), *Clusters and Colloids. From Theory to Applications*, VCH, Weinheim, **1994**.

3. T. Castro, R. Reifenberger, E. Choi, R. P. Andres, *Phys. Rev. B.*, **1990**, *13*, 8548.

4. Y. Volokitin, J. Sinzig, L. J. de Jongh, G. Schmid, I. I. Moiseev, *Nature*, **1996**, *384*, 621.

5. F. M. Mulder, T. A. Stegink, R. C. Thiel, L. J. de Jongh, G. Schmid, *Nature*, **1994**, *367*, 716.

6. A. H. A. Smit, R. C. Thiel, L. J. de Jongh, G. Schmid, N. Klein, *Solid State Commun.*, **1988**, *65*, 915.

7. F. M. Mulder, E. A. v. d. Zeeuw, R. C. Thiel, G. Schmid, *Solid State Commun.*, **1993**, *85*, 93.

8. H. H. A. Smit, P. R. Nugteren, R. C. Thiel, J. de Jongh, *Physica B*, **1988**, *153*, 33.

9. R. C. Thiel, R. E. Benfield, R. Zanoni, H. H. A. Smit, M. W. Dirken, *Structure and Bonding*, **1993**, *81*, 1.

10. R. E. Hummel (editor), *Electronic Properties of Materials*, 2nd edition, Springer, Heidelberg, **1992**.

11. U. Kreibig, M. Vollmer (editors), *Optical Properties of Metal Clusters*, Springer, Heidelberg, **1995**.

12. R. E. Hummel, P. Wissmann (editors), *Handbook of Optical Properties*, Vol. II, *Optics of Small Particles, Interfaces and Surfaces*, CRC Press, Boca Raton, FL, **1997**.

13. L. M. Liz-Marzán, M. Giersig, P. Mulvaney, *Chem. Commun.*, **1996**, *731*.

14. K. von Klitzing, D. Dora, M. Pepper, *Phys. Rev. Lett.*, **1980**, *45*, 494.

15. H. Grabert, M. H. Devoret, *Physikal. Blätter* **1994**, *50*, 231.

16. A. Bezryadin, C. Dekker, G. Schmid, *Appl. Phys. Lett.* **1997**, *71*, 1273.

17. L. F. Chi, M. Hartig, T. Drechsler, Th. Schwaack, C. Seidel, H. Fuchs, G. Schmid, *Appl. Phys. A.*, **1998**, *A66*, 187.

18. G. Schön, U. Simon, *J. Colloid Polymer Sci.*, **1995**, *273*, 101.

19. G. Schön, U. Simon, *J. Colloid Polymer Sci.*, **1995**, *273*, 202.

20. U. Simon, R. Flesch, H. Wiggers, G. Schön, G. Schmid, *J. Mater. Chem.*, **1998**, *8*, 517.

21. G. Schmid, *Prog. Colloids Polymers*, **1998**, *111*, 52.

22. G. Schmid, V. Maihack, F. Lantermann, St. Peschel, *J. Chem. Soc., Dalton Trans.*, **1996**, *589*.

23. G. Schmid, S. Emde, V. Maihack, W. Meyer-Zaika, St. Peschel, *J. Mol. Catal. A*, **1996**, *107*, 95.

24. G. Schmid, in *Metal Clusters in Chemistry*, P. Braunstein, L. A. Oro, P. R. Raithly (editors), Wiley-VCH, Weinheim, **1999**, Vol. 3, p. 1325.

25. S. A. Harfenist, Z. L. Wang, M. M. Alvarez, I. Vezmar, R. L. Whetten, *Adv. Mater.*, **1997**, *9*, 817.

26. M. Faraday, *Phil. Trans. Roy. Soc.*, **1857**, *147*, 145.

27. J. S. Bradley, in *Clusters and Colloids. From Theory to Applications*, G. Schmid (editor), VCH, Weinheim, **1994**, p. 459.

28. J. Turkevich, P. C. Stevenson, J. Hillier, *Discuss. Faraday Soc.*, **1951**, *11*, 55.

29. J. Turkevich, *Gold Bulletin*, **1985**, *18*, 86.

30. H. Hirai, Y. Nakao, N. Toshima, *J. Macromol. Sci.-Chem.*, **1978**, *A12*, 1117.

31. H. Hirai, *J. Macromol. Sci.-Chem.*, **1979**, *A13*, 633.

32. J. S. Bradley, J. M. Millar, E. W. Hill, *J. Am. Chem. Soc.*, **1991**, *113*, 4016.

33. J. S. Bradley, E. W. Hill, S. Behal, C. Klein, B. Chaudret, A. Duteil, *Chem. Mater.*, **1992**, *4*, 1234.

34. F. Porta, F. Ragaini, S. Cenini, G. Scari, *Chim. Ital.*, **1992**, *122*, 361.

35. P. R. van Rheenen, M. J. McKelvey, W. S. Glaunsinger, *J. Solid State Chem.*, **1987**, *67*, 151.

36. O. Vidoni, K. Philippot, C. Amiens, B. Chaudret, *Angew. Chem. Int. Ed.*, **1999**, *38*, 3736.

37. B. G. Ershov, E. Janata, M. Michaelis, A. Henglein, *J. Phys. Chem.*, **1991**, *95*, 8996.

38. G. Schmid, R. Pugin, W. Meyer-Zaika, U. Simon, *Eur. J. Inorg. Chem.*, **1999**, *11*, 2051.

39. G. Schmid, R. Pugin, J.-O. Malm, J.-O. Bovin, *Eur. J. Inorg. Chem.*, **1998**, *6*, 813.

40. Z. L. Wang, *Adv. Mater.*, **1998**, *10*, 13.

41. Z. L. Wang, S. A. Harfenist, I. Vezmar, R. L. Whetten, J. Bentley, N. D. Evans, K. B. Alexander, *Adv. Mater.*, **1998**, *10*, 808.

42. G. Schmid, R. Pugin, Th. Sawitowski, U. Simon, B. Marler, *Chem. Comm.*, **1999**, 1303.

43. S. Sun, C. B. Murray, D. Weller, L. Folks, A. Moser, *Science*, **2000**, *287*, 1989.

44. J. P. Spatz, A. Roescher, M. Möller, *Adv. Mater.*, **1996**, *8*, 337.

45. J. P. Spatz, S. Mössner, M. Möller, *Chemistry Eur. J.*, **1996**, *2*, 1552.

46. S. T. Sehan, J. P. Spatz, H.-A. Klok, M. Möller, *Adv. Mater.*, **1998**, *10*, 132.

47. J. P. Spatz, T. Herzog, S. Mössner, P. Ziemann, M. Möller, *Adv. Mater.*, **1999**, *11*, 149.

48. R. P. Andres, J. D. Bielefeld, J. I. Henderson, D. B. Janes, V. R. Kolagunta, C. P. Kubiak, W. J. Mahoney, R. G. Osifchin, *Science*, **1996**, *273*, 1690.

49. G. Schmid, M. Bäumle, N. Beyer, *Angew. Chem., Int. Ed.*, **2000**, *39*, 181.

50. G. Schmid, N. Beyer, *Eur. J. Inorg. Chem.*, **2000**, *835*.

51. J. W. Diggle, T. C. Downie, C. W. Goulding, *Chem. Rev.*, **1969**, *69*, 365.

52. J. P. O'Sullivan, G. C. Wood, *Proc. Roy. Soc. London*, **1970**, *317*, 511.

53. M. M. Lohrengel, *Mater. Sci. Eng.*, **1993**, *6*, 241.

54. H. Masuda, H. Yamada, M. Satoh, H. Asoh, M. Nakao, T. Tamamura, *Appl. Phys. Lett.*, **1997**, *79*, 2270.

55. G. L. Hornyak, M. Kröll, R. Pugin, Th. Sawitowski, G. Schmid, J.-O. Bovin, G. Karsson, H. Hofmeister, S. Hopfe, *Chem. Eur. J.*, **1997**, *3*, 1951.

56. M. Gleiche, L. F. Chi, H. Fuchs, *Nature*, **2000**, *403*, 173.

# 3   Semiconductor Nanocrystals

M. P. PILENI

Laboratoire LM2N, ESA CNRS 1070, Université P. et M. Curie, Paris, France

## 3.1   INTRODUCTION

The fabrication of assemblies of perfect nanometer-scale crystallites (quantum crystals), identically replicated in unlimited quantities in such a state that they can be manipulated and understood as pure macromolecular substances, is an ultimate challenge of modern materials research with outstanding fundamental and potential technological consequences. These potentialities are mainly due to the unusual dependence of the electronic properties on the particle size, for metal,[1–4] or semiconductor[1,5–18] or diluted magnetic semiconductor[19–26] particles, in the 1 to 10 nm range.

Nanometer-sized crystals exhibit behavior intermediate between that of bulk material and molecules. Their sizes range from smaller than to a few times larger than the effective Bohr diameter of an exciton in bulk crystal. These systems have been given special attention because of their unique size-dependent properties, which include optical properties such as absorption and third-order nonlinearity, as well as their potential applications in solar energy. Because the size dependence of the band levels of semiconductor particles results in a shift of the optical spectrum, quantum mechanical descriptions of the shift have been carried out by several researchers.[6–8,14–19,27]

## 3.2   BACKGROUND ON QUANTUM DOT SEMICONDUCTORS[28]

In a typical molecular solid, the intermolecular interactions are much weaker than the intramolecular bonding, so the properties of a molecular solid can be analyzed as the sum of individual molecular contributions with small perturbations from the intermolecular forces. Such weak intermolecular interactions rarely extend beyond

the nearest neighbors and the electronic properties of a molecular crystal are usually independent of the size of the crystal. Inorganic semiconductors consist of a network of ordered atoms with no discernible "molecular" unit. For a semiconductor crystal, electronic excitation involves a loosely bound electron–hole pair, usually delocalized over a length much longer than the lattice constant. As the diameter of the semiconductor crystallite approaches this exciton Bohr diameter, its electronic properties start to change. This is the so-called quantum size effect, which can be observed as a blue-shift in the optical bandgap or exciton energy. For CdS, the quantum size effect occurs when crystallite diameter is comparable to or below the exciton diameter of 5–6 nm (3000–4000 atoms). Many terms have been used to describe these ultrasmall particles, such as quantum dots, nanocrystals, Q particles, clusters, and other terms. For nanocrystals in such a small size regime, a large percentage of the atoms are on or near the surface. For example, a 5 nm CdS nanocrystal has 15% of the atoms on the surface. The existence of this vast interface between the nanocrystal and the surrounding medium can have a profound effect on the nanocrystal properties. For nanocrystals having imperfect surfaces, electron and/or hole traps are observed upon optical excitation. The presence of these trapped electrons and holes can in turn modify the optical properties of the particles.

## 3.3 BACKGROUND ON REVERSE MICELLAR SOLUTION[29]

Reverse micelles are water-in-oil droplets. Water is readily solubilized in the polar core, forming a so-called "water pool," characterized by $w$, the water/surfactant molar ratio ($w = [H_2O]/[S]$) . We make no distinction between swollen micelles or microemulsions because there is none. However, some groups call "reverse micelles" aggregates containing a low amount of water ($w < 15$), reserving "microemulsion" for larger water content.

Assuming that water-in-oil droplets are spherical, the radius of a sphere is expressed as $R = 3V/\Sigma$, where $R$, $V$, and $\Sigma$ are the radius, the volume, and the surface of the sphere. Assuming that the volume and the surface of the droplets are governed by the volume of the water molecules and by the area of the surfactant molecules (all located at the interface), respectively, the water pool radius, $R_w$, is similar to the sphere radius ($R = R_w$) and can be expressed as

$$R_w = \frac{3V_{aq}[H_2O]}{\sigma[S]}$$

where $V_{aq}$, $\sigma$, and [S] are the volume of water molecules, the head polar group area, and the surfactant concentration, respectively.

One of the surfactants often used to form reverse micelles is sodium diethyl sulfosuccinate, usually called Aerosol OT or Na(AOT). From the geometrical model developed above, the water pool radius follows the relation

$$R_w(A) = 1.5w$$

For Na(AOT)–water–isooctane solutions, various experiments[30] confirm the linear variation of the water pool radius with the water content and, at a given water content, the invariance of the water pool radius with the polar volume fraction. These droplets exchange their water contents by collision and again form two independent droplets.

The phase diagram of a divalent metal ion diethyl sulfosuccinate, $M(AOT)_2$, usually called functionalized surfactant, may change markedly compared from that for Na(AOT). When the metal is Fe(II), Cd(II), or Cu(II) the phase diagram of $M(AOT)_2$–isooctane–water does not drastically change. Thorough quantitative studies of these phases diagrams have been described elsewhere.[31,32]

## 3.4 SYNTHESES

Mixed reverse micelles are used to make CdS, CdTe, $Cd_{1-y}Zn_yS$, $Cd_{1-y}Mn_yS$, and $Ag_2S$ nanocrystals. It should be noted that functionalized surfactants are needed. When cadmium ions are solubilized in water-in-oil droplets, the crystallinity of the resultant particles is rather low and the size distribution of the nanocrystals is very wide. For alloy nanocrystals, solubilization of reactive ions in the water-in-oil droplet induces formation of a mixture of various nanocrystals and not the alloys; with $Ag_2S$ there is a mixture of silver and $Ag_2S$.

The composition, $y$, of prepared samples is determined by energy dispersion spectroscopy (EDS), and the nanocrystal structure is determined by electron diffraction. The particle size, determined from the transmission electron microscopy pattern, is controlled by the size of the water droplets in which syntheses are made. Similar behavior has been observed for various nanoparticles.[1]

### 3.4.1 Syntheses of Spherical Nanocrystals

Semiconductors are synthesized using reverse micelles.[1,2] Coprecipitation takes place. Two procedures can be used.

*Mixed reversed micelles*   Two micellar solutions having the same water content, $w = [H_2O]/[AOT]$ are mixed: 0.1 M Na(AOT) containing either $S^{2-}$ or $Te^{2-}$ ions, and a mixed micellar solution made of Na(AOT) and reactants such as $Cd(AOT)_2$, $Zn(AOT)_2$, $Mn(AOT)_2$, or Ag(AOT). The syntheses are made at various $x$ ratios, where $x = ([Cd^{2+}] + [Mn^{2+}])/[Te^{2-}]$ or $x = ([Cd^{2+}] + [Mn^{2+}])/[S^2])$.

After mixing of the two micellar solutions, the procedures differ as follows:

*Procedure I.* Dodecanethiol is immediately added to the micellar solution having a given water content, $w$. This results in a selective surface reaction between the thio derivative and cadmium and manganese ions. The particles are extracted immediately from micelles and the surfactant is removed by addition of ethanol. The nanocrystallites coated by dodecanethiol are dispersed in a mixture of two solvents (isopentane–methylcyclohexane, 3 v/v, forming an optically clear glass at low temperature. The average size of coated particles

increases with increase in the water content in the medium in which the particles are synthesized.

*Procedure II.* The particles are left in the micellar solution for 48 hours. Dodecanethiol is then added and the particles are immediately extracted.

*Procedure III.* Immediately after synthesis, dodecanethiol is added and the nanocrystallites remain in the micellar solution for 48 hours. The particles are then extracted from micelles using the same procedure as described above.

*Procedure IV.* Nanocrystallites are kept in the micellar solution for 90 minutes and then dodecanethiol is added and the particles are extracted as described above.

### 3.4.2   Synthesis of triangular nanocrystals

The colloidal self-assembly of $Cd(AOT)_2$–isooctane–$H_2O$ is used to make CdS nanocrystals. The water content ($w$) and the surfactant concentration are kept constant ($w = 30$; $[Cd(AOT)_2] = 5 \times 10^{-2}$ M). A mixture of $H_2S$ and $N_2$ produces cadmium with a sulfide coprecipitation reaction at a molar fraction of $1/3$. The gas flow is around $0.05 \, cm^3 \, s^{-1}$. The solution is stirred during the chemical reaction. At the end of the reaction, dodecanthiol ($0.5 \, \mu l \, ml^{-1}$) is added to the micellar solution. Procedure II is then used.

## 3.5   CADMIUM TELLURIDE NANOCRYSTALS[33]

Cadmium telluride (CdTe) is an important II–VI semiconductor quantum dot because of its large exciton Bohr diameter (15 nm). It has received some attention and its bandgap shift with cluster size has been well mapped. CdTe quantum dots are usually made by RF magnetron sputtering in a glass matrix.[34–41]

Syntheses are made at various contents under procedures I and II. To prevent the oxidation of telluride, the syntheses were done in the presence of an excess of cadmium ($x = ([Cd^{2+}])/[Te^{2-}] = 2$). Procedure I permits a change in the particle size from 2.6 nm to 3.4 nm, whereas it is from 3.4 to 4.1 nm by procedure II. The size distribution[42] is close to 13%. As expected, the CdTe absorption spectrum is red-shifted with increasing water content and with increasing the particle size. This is attributed to quantum size effects.[6–8,14–19,27–41]

The energy bandgap increases with decreasing CdTe particle size. For a given particle size, the value of the energy bandgap is constant. However, the excitonic peak is better defined for particles produced by procedure II than for those from procedure I.

Photoluminescence (PL) spectra change markedly with the procedure used. Particles made with procedure I (where nanocrystals are extracted from reverse micelles immediately after the synthesis) show a long-tail PL spectrum. This is due to the recombination of charge carriers in the surface traps.[38,43] At the opposite
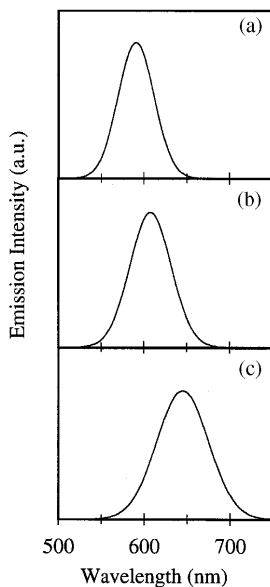
**FIGURE 3.1**   Photoluminescence spectra of CdTe nanocrystals made by procedure II and recorded at 77 K: (a) $d = 3.4$ nm; (b) $d = 3.8$ nm; (c) $d = 4.1$ nm. $x = [Te^{2-}]/[Cd^{2+}] = 1/2$.

extreme, under procedure II (where the nanocrystals age inside the micellar solution before extraction), Figure 3.1 shows well-defined peaks centered at higher energies. The energy bandgap and the maximum of photoluminescence are similar. This permits the photoluminescence to be attributed to the direct recombination of free electron and hole. A red-shift is observed in the maximum of the PL spectrum due to the direct transition on increasing the particle size. This is due to a quantum size effect. The relative fluorescence quantum yield of the direct transition, $\Phi_{PL}$, decreases with increase in the particle size. Comparing the photoluminescence spectra obtained with particles differing in their sizes and their fabrication mode, it is concluded that the aging of the crystals permits observation of the direct transition. This can be explained by formation of a passivated layer due to Oswald ripening, which allows a decrease in the surface defects and then in the trap emissions. These data have to be related to those obtained previously with CdSe nanoparticles produced through inorganic syntheses at 280°C. A direct transition is observed, at room temperature, when the particles are coated with ZnS. This has been explained through a decrease in the number of CdSe defects with shell formation. Similarly, direct transition has been observed by addition of adsorbate at the particle interface. The procedure described permits observation of the direct transition without addition of external adsorbate.

## 3.6 CADMIUM SULFIDE NANOCRYSTALS

### 3.6.1 Spherical Nanocrystals

In our previous work[9,4,18,27] the synthesis of CdS was carried out using procedure I. In these cases no direct fluorescence was observed. To check whether the direct fluorescence of CdS could be observed using procedure II and in the presence of an excess of cadmium ($x = ([Cd^{2+}])/[S^{2-}] = 2$), syntheses of CdS nanocrystals were performed in the same experimental conditions as described above (syntheses at various water contents). As expected, a shift toward low energy was observed when the average particle size increased. As observed with CdTe, the excitonic peak was better resolved when the particles were aged. This is probably due to better crystallinity. Photoluminescence spectra of CdS nanocrystals differing in size and mode of fabrication are very broad and correspond to CdS defect states.[9,18,5,44,45] Hence, contrary to what is observed with CdTe, aging does not permit observation of the direct fluorescence of CdS. However we know that carrying out the syntheses in an excess of cations increases the sulfur vacancies and the trap emission. To prevent the presence of sulfur vacancies, syntheses have been made in the presence of an excess of sulfur ($x = ([Cd^{2+}])/[S^{2-}] = 1/2$). A large PL spectrum results due to the trap emission. However, a peak is observed at lower energy and can be attributed to the direct transition. Hence, aging permits observation of the direct transition of CdS nanocrystals that are sulfur-rich.

### 3.6.2 Triangular CdS Nanocrystals[46]

The transmission electron microscopy (TEM) pattern (Figure 3.2a) shows that a triangular shape with an average side length of 10 nm characterizes most of the particles. To determine the structure of isolated triangular nanocrystals, high-resolution transmission electron microscopy (HRTEM) experiments and image processing by the square Fourier transform (power spectrum, PS)[47] are performed. A large collection of triangular nanocrystals is used and the obtained data are highly reproducible. The HRTEM image of the triangular nanocrystals shows several lattice planes (Figure 3.2b). The PS shows several well-defined sharp spots: the inner three pairs are characterized by an interplane distance of 3.626 Å. The second order is well defined. Another series of spots corresponds to a distance of 2.1094 Å with a 60° angle between the spots.

These experimental data are compared to the calculated single-crystal diffraction patterns[48] oriented in [111] and [001] planes for cubic (zincblende) and hexagonal (wurtzite) structures, respectively. For the cubic phase, the first-order external diffraction spots are observed. Conversely, for the hexagonal phase, all the spots are present (inner and external). Table 3.1 compares the calculated and experimental data for the interplanar distances and shows rather good agreement between them. The spots corresponding to 100, 110 and 200 diffraction of the hexagonal structure (wurtzite) are shown in Figure 3.2c. From this, it can be concluded that isolated triangular nanocrystals are crystallized in a wurtzite structure. The well-defined
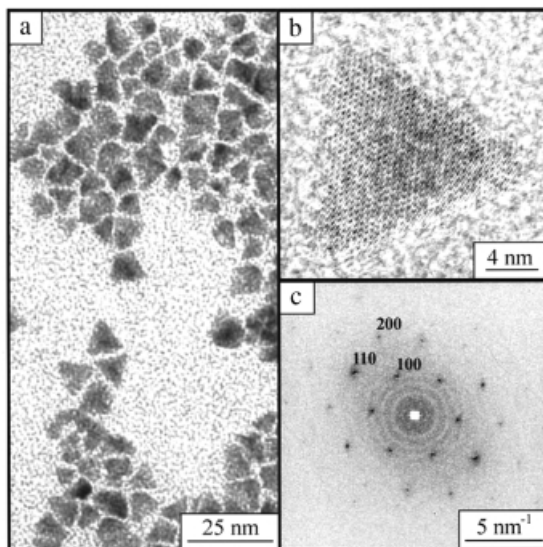
**FIGURE 3.2** (a) TEM image of CdS triangular-shaped nanocrystals. (b) HR-TEM of a nanocrystal. (c) Power spectrum of this nanocrystal.

**TABLE 3.1 Calculated single-crystal diffraction for the [001] plane of wurtzite CdS with electron radiation $\lambda = 0.025\,08$ Å compared to the experimental results**

|  | Diffraction | | |
| --- | --- | --- | --- |
|  | 100 | 110 | 200 |
| $d$ (Å) calculated | 3.5861 | 2.0705 | 1.7931 |
| $d$ (Å) experiment | 3.626 | 2.094 | 1.810 |

second-order of diffraction spots indicates a high crystallinity of the flat equilateral triangular particles. The triangular shape of PS spots (Fourier transform form factor) indicates a highly homogeneous surface.

Thus at the scale of a few nanometers, it can be concluded that the isolated, flat, equilateral triangular particles are highly crystallized in a hexagonal structure with a homogeneous surface.

At this stage in the study another question arises: Are the nanocrystals flat triangles or pyramids? Tilt experiments are performed to determine this. Figure 3.3 shows on the left the TEM images of nanocrystals tilted by five various angles; in the center the simulation of a flat, equilateral-triangular particle; and on the right the simulation of a pyramidal particle. These calculations are performed using Cerius software.[48] The TEM and simulated patterns show the following.

- At 0° tilt angle, the classical picture is obtained, with formation of equilateral nanocrystals (each angle of the triangle is 60°). No distinction can be made between flat equilateral triangular and pyramidal shapes.

- At −30° and +30° the experimental and the simulated images do not change significantly compared to those obtained at 0°.

- At +54° and −58°, the top angle of the sample is close to 90° instead of 60° at 0° tilt. Similar behavior is observed in the simulation of flat, equilateral
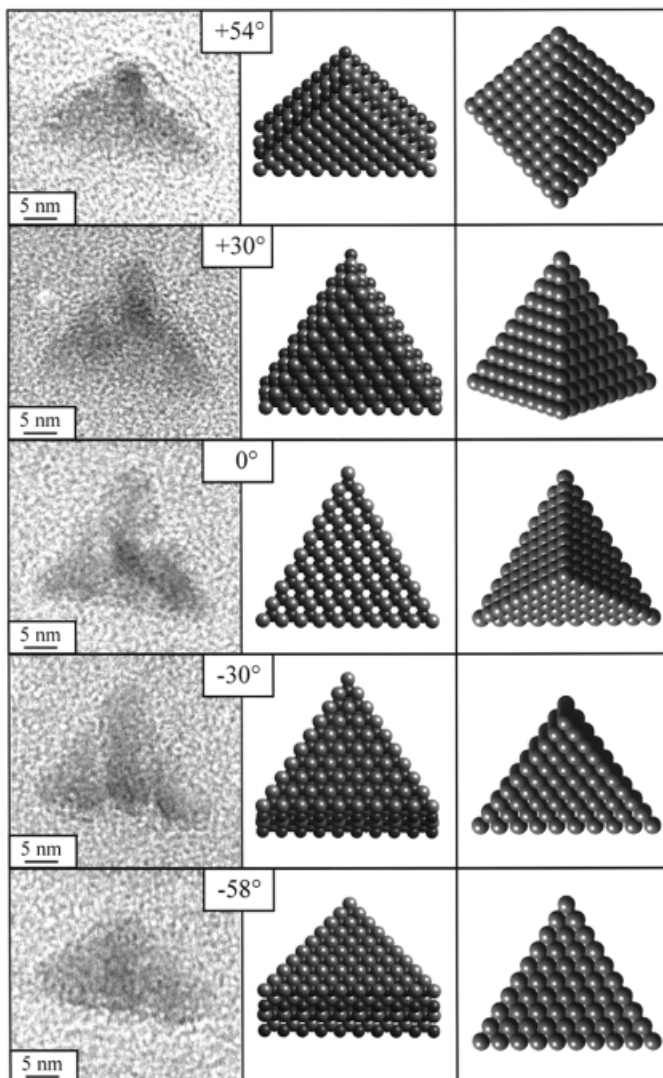


**FIGURE 3.3**    TEM image of nanocrystals tilted at five different angles (left); simulation of a triangular flat particle (center); and simulation of a pyramidal particle (right side).

particles (center). Furthermore, the overall particle shapes of simulated and experimental patterns are similar (left and center). Comparison between the TEM image obtained at a large tilt angle (left side) and the simulation of triangular pyramids (right) shows marked differences. At $+54°$ the experimental and simulated particle shapes differ drastically. The experimental pattern is rectangular (top angle around $90°$), whereas the simulated pattern is characterized by a rhombohedrical shape (with a top angle of $103°$). At $-58°$ the TEM pattern remains the same as that observed at $+54°$, but the simulated triangular pyramid (right) evolves from a rhombohedrical shape (at $+54°$) to an equilateral triangle at $-58°$.

It is concluded from these considerations that the pyramidal structures can be rejected.

According to the confinement properties of quantum dots, because of the low thickness of the flat, equilateral triangle, we would expect to observe a blue-shift in the absorption spectrum of CdS nanocrystals. As assumed, the absorption spectrum has an excitonic peak. It is blue-shifted compared to the bulk phase with onset at 510 nm (for the bulk phase it is 520 nm). The bandgap deduced from the Wang formula[49] ($E_g = 2.49$ eV) is shifted compared to that of the bulk phase ($E_g = 2.42$ eV).[50] To evaluate the average thickness of the triangular nanocrystals, the Nosaka theory[51] developed for spherical particles is used. According to this theory, the bandgap energy decreases with increase in the particle size to reach that of the bulk phase for 10 nm spherical particles.[50] The bandgap energy 2.49 eV corresponds to spherical particles with 6 nm average diameter. With spherical particles, it has been well demonstrated[51] that the bandgap shift is due to particles having a smaller radius than the Bohr radius. Assuming that such behavior applies for flat triangles, the average thickness of flat, equilateral triangle nanocrystals is 6 nm.

A minimum value of the thickness can be evaluated by taking account of the total number of atoms needed to make 6 nm spherical particles (i.e., 4500). Assuming that the equilateral triangle, characterized by an average side of 10 nm, consists of 4500 atoms, the thickness deduced is 3 nm. Of course this is a minimum value. From photoabsorption spectroscopy it is concluded that the thickness of the flat triangles is in the range of 3 to 6 nm.

Hence high crystallinity and a rather homogeneous surface characterize the triangular particles, of 10 nm size and around 5 nm thickness.

## 3.7 ALLOY SEMICONDUCTORS

### 3.7.1 Solid Solution of $Cd_{1-y}Zn_yS$[52–54]

As expected, the absorption spectrum of $Cd_{1-y}Zn_yS$ particles made under procedure I and having the same composition, $y$, is red-shifted with increasing particle size. At fixed size, a red-shift in the absorption spectrum is observed with increasing $y$. This is due to changes in the solid-phase composition. The energy bandgap, determined

from the excitonic peak, increases smoothly with increasing composition from ZnS to CdS.[52] Similar behavior was observed for the bandgap variation of bulk $Cd_{1-y}S$.[55] Solid solution is obtained when the syntheses are made in the presence of an excess of sulfur ($x = ([Cd^{2+}] + [Zn^{2+}])/[S^{2-}] = 1/2$).

### 3.7.2    II–VI Diluted Magnetic Semiconductors[56–61]

Type II–VI diluted magnetic semiconductors (DMS)[62] are semiconductors in which host cations (II) are randomly substituted by magnetic ions, $Mn^{2+}$. The presence of localized magnetic ions in a semiconductor alloy leads to exchange interactions between $sp$ band electrons and the $Mn^{2+}$ $d$ electrons. This $sp-d$ exchange interaction constitutes a unique interplay between semiconductor physics and magnetism. It plays a double role in determining optical properties: (1) the bandgap of the compound is altered depending upon the concentration of manganese ions; and (2) the $3d$ levels of transition metal ions are located in the bandgap region and $d$–$d$ transitions dominate the spectrum.

In the nanometer-sized crystallites of semimagnetic semiconductors, many of these properties are expected to be influenced by the quantum confinement of the electronic states and to be different from those of the bulk crystals. Due to the quantum dot's unique properties, these nanostructures have a great potential for a variety of applications. Recent work on manganese-doped nanocrystals suggests that doped nanocrystals represent a new class of materials.[21]

The direct bandgap is determined from the absorption onset. For a given composition, there is an increase in the band edge energy with decreasing particle size. This is due to the quantum size effect. For a given particle size, the bandgap does not vary monotonically with composition, as is observed for most semiconductor alloys: it decreases and then increases (Figure 3.4). Similar behavior has been observed in the bulk phase[62] and films.[63] With nanocrystals, the minimum is more pronounced and its depth increases with decreasing particle size (Figure 3.4). It has been demonstrated that appearance of the minimum in the energy bandgap with increasing composition, $y$ is not due to chemical disorder.[56] It is usually attributed to a shift of the energy levels due to statistical fluctuations of the crystal potential in an alloy and is called bandgap bowing.

In the bulk phase,[64] the bandgap energy minimum has been attributed to $s$–$d$ and $p$–$d$ exchange interactions. An exchange interaction is known to occur in the bulk magnetic II–VI semiconductor between the $d$ electrons of the $Mn^{2+}$ and the band electrons. The energy bandgap is related to temperature and susceptibility by:[64]

$$E_g(y, T) = E_g(CdS)\frac{AT^2}{T + B} + y\,\Delta E - b\chi(y, T)T \qquad (3.1)$$

where $E_g(CdS)$, $\Delta E$, $\chi(y, T)$, and $T$ are the band edge energy without $Mn^{2+}$, the linear variation of bandgap energy between CdS ($E_g(CdS) = 2.45$ eV) and MnS ($E_g(MnS) = 3.4$ eV),[63] the susceptibility of the material, and the temperature, respectively. The constraints $A$ and $B$ depend on the material, whereas constant $b$
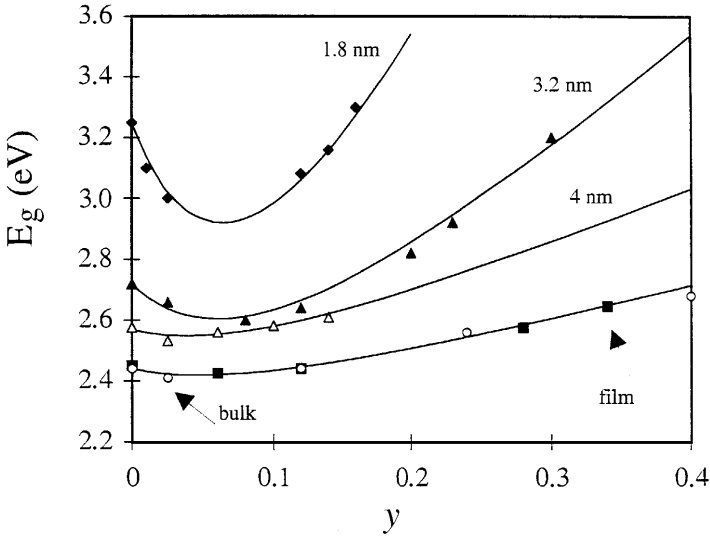
**FIGURE 3.4**   Variation of the bandgap energy, $E_g$, with comparison, $y$, for various particles sizes, bulk, and thin film. The line is obtained from the best fit between experimental data and Equation (3.1).

takes into account the exchange interactions between the $Mn^{2+}$ $d$ electrons and band electrons. The $A$ and $B$ values are determined from the energy bandgap variation, at a given composition, with temperature. They are size-independent and equal to $5.6 \pm 0.7 \times 10^{-4}$ eV $K^{-1}$ and $256 \pm 14$ K, respectively. These values are close to those obtained in the bulk phase.[65] This probably indicates that the electron–phonon interactions do not markedly depend on the dot size in $Cd_{1-y}Mn_yS$ nanocrystals.

To determine the value of $b$ from Equation (3.1), the magnetic susceptibility, $\chi(y, T)$, in the nanoscale range and at various compositions has to be known. Unfortunately, for experimental reasons, it is impossible to determine $\chi(y)$ at 298 K. Using a SQUID (superconducting quantum interference device), the magnetic susceptibility, $\chi(y, T)$, is measured at various temperatures, from 3 K to 180 K. This is done for various particle sizes and compositions. As in the bulk phase, above 60 K, the magnetic susceptibility follows the Curie–Weiss law:

$$\chi(y, T) = \frac{C_0 y}{T + \Theta_0 y} \tag{3.2}$$

where $C_0 y$ and $\Theta_0 y$ are the $Cd_{1-y}Mn_yS$ Curie constant and temperature, respectively.

At a given particle size and composition, the $C_0$ and $\Theta_0$ values are deduced by plotting $\chi(T, y)^{-1}$ versus $T$. Table 3.2 gives the $C_0$ and $\Theta_0$ values determined for various particle sizes. Taking these values into account, the magnetic susceptibility is calculated at 298 K (Equation 3.2).

**TABLE 3.2 $C_0$ and $\Theta_0$ values derived from $\chi^{-1}$ extrapolation and variation of the parameter $b$, derived from simulation of bandgap evolution by Equation (3.4) and experimental linewidth, $\Delta H_{pp}$, of $Cd_{0.9}Mn_{0.1}S$ nanoparticles for different sizes**

| | Particle size | | | |
|---|---|---|---|---|
| | 1.8 nm | 3.2 nm | 4 nm | Bulk |
| $C_0$(K) | 0.015 | 0.025 | 0.03 | 0.03 |
| $\Theta_0$ (emu g K$^{-1}$) | 700 | 630 | 409 | 280 |
| $b$ (eV g Oe emu$^{-1}$K$^{-1}$) | 1250 | 440 | 150 | 120 |
| $\Delta H_{pp}$ (G) | 400 | 250 | 182 | |

The value of $b$ is then deduced from the best fit (full line) between experimental data and calculation obtained from Equation (3.2). Table 3.2 shows a drastic increase in the value of $b$ with decreasing particle size. This indicates an increase in the exchange interactions. Indeed, the value of $b$ is directly related to the interaction strength between manganese ions and conduction and valence band electrons:

$$C_0 = \frac{N_0(g\mu B)^2 S(S+1)}{2k_B}, \qquad \Theta_0 = -\frac{(2/3)S(S+1)ZJ}{k_B} \qquad (3.3)$$

where $N_0$, $g$, $\mu B$, $S$, $k_B$, $Z$, and $J$ are respectively the number of cations per unit volume (to a first approximation $N_0$ does not depend on $y$ in the range $0 < y < 0.3$); the Landé factor; the Bohr magneton, $S = 5/2$; the Boltzmann constant; the number of nearest neighbors ($Z = 12$ for zincblende DMS); and the nearest-neighbor exchange integral ($J/k_B = -4$ K for $Cd_{1-y}Mn_yS$).[61] Table 3.2 gives the calculated $C_0$ and $\Theta_0$ values and the $b$ value is deduced from the same procedure as described above. Table 3.2 shows a drastic increase in the values of $b$ obtained with nanocrystals.

From these data, it is concluded that with decreasing particle size there is an increase in the exchange interactions between the $d$ electrons of $Mn^{2+}$ and the band electrons. It is well established that the $Mn^{2+}-Mn^{2+}$ interactions occur through a superexchange process[66] which implicates the CdS band electrons. As demonstrated above, the increase in the $b$ factor with decreasing particle size involves interactions between $d$ electrons of $Mn^{2+}$ and the band electrons. From magnetization measurements, the magnetic susceptibilities, $\chi(y, T)$, of $Cd_{1-y}Mn_yS$ nanocrystals differing in size and composition is measured at 30 K and compared to those obtained in the bulk phase. It is demonstrated that the $Mn^{2+}-Mn^{2+}$ interactions increase with decreasing particle size. This is confirmed from EPR (electron paramagnetic resonance) experiments performed at various sizes and compositions (Table 3.2). It is concluded that the magnetic interactions increase with decreasing particle size. These abnormal interaction variations are confirmed for different sizes of nanocrystals (1.8–3.2–4 nm) at various compositions ($0.006 < y < 0.2$).

The increase in the depth of the minimum of the bandgap with variation in composition is due to strong interactions between manganese ions and the band

electrons. The magnetic interactions increase markedly with decreasing particle sizes.

The photoluminescence (PL) spectra of $Cd_{0.95}Mn_{0.05}S$ nanocrystals made under procedure I, in the range of sizes from 1.8 to 3.2 nm and recorded at 77 K, are shown in Figure 3.5. For 1.8 nm particles, the PL spectrum has a large band centered at 600 nm. This luminescence is homothetic to that obtained without $Mn^{2+}$ ions included in the CdS matrix and is attributed to CdS defect states.[9,18,5,43,44] The photoluminescence excitation (PLE) spectrum of trap emission shows a well-resolved excitonic peak (Figure 3.5). A slight shift in the PLE spectra with the emission wavelength is obtained. This is due to the size distribution.

Similar behavior is observed for 3.2 nm crystallites, with good correlation between the bandgap energy determined from absorption and PLE spectra. As expected,[64] the CdS trap emission is red-shifted when the particle size increases. The bandgap energies are derived from the PLE spectra, and compared to those obtained from absorption spectra at the same temperature (77 K). Rather good agreement between these two techniques is observed. Hence, by using procedure I the PL spectra are attributed to trap emissions of CdS nanocrystals. The presence of $Mn^{2+}$ inside the CdS matrix does not perturb the PL spectra. This result is in total disagreement to those previously obtained.[19–21] To explain such differences between our experimental data and those published previously,[19–23] the synthesis modes are changed.
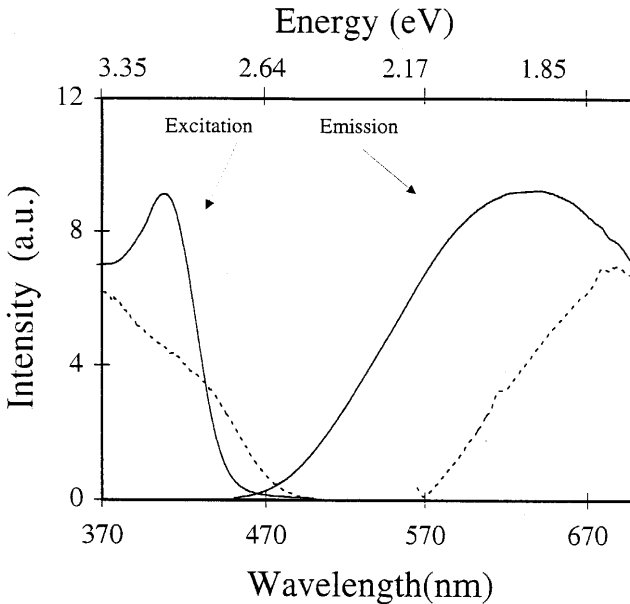


**FIGURE 3.5** PL ($\lambda_{ex} = 400$ nm) and PLE ($\lambda_{em} = 600$ nm) spectra recorded at 77 K, of $Cd_{0.95}Mn_{0.05}S$ nanoparticles of various sizes prepared by procedure I: solid curve, 1.8 nm particles; broken curve, 3.2 nm particles.

When using procedure III to make 4 nm particles ($w = 40$), the PL and PLE spectra of particles differing in composition are recorded at 77 K: Without $Mn^{2+}$ included in CdS matrices, the luminescence band is broad and is attributed to CdS trap emission (Figure 3.6a). When $Mn^{2+}$ ions are included in a CdS matrix, a new luminescence band appears with a sharp peak centered at 580 nm (Figures 3.6b and
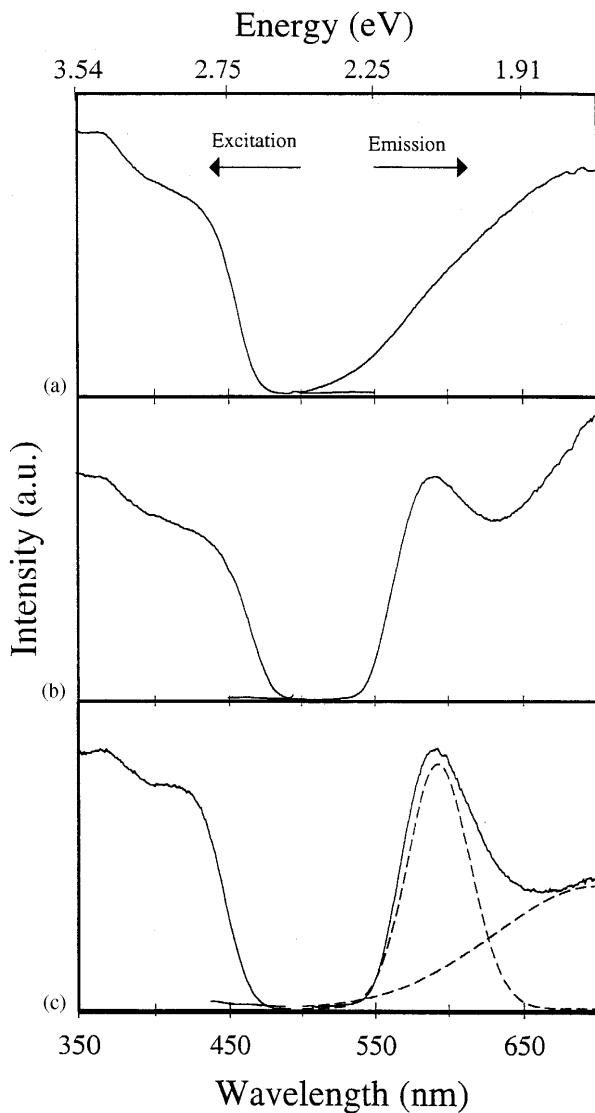


**FIGURE 3.6**   PL ($\lambda_{ex} = 400$ nm) and PLE ($\lambda_{em} = 580$ nm) spectra, recorded at 77 K, for various compositions: (a) $y = 0$; (b) 0.05( $j$); (c) 0.1. The average particle diameter is 4 nm. The particles were prepared by procedure III.

3.6c). This is attributed to $Mn^{2+}$ emission in a tetrahedral coordination (transition $4T_1$ to $6A_1$).[65,67] The PL spectrum is fitted by assuming two Gaussian curves and two spectra are derived: The spectrum designated 1 in Figure 3.6c is characterized by a maximum centered at 585 nm and attributed to the isolated $Mn^{2+}$ PL spectrum.[26] The simulated half-width of $Mn^{2+}$ luminescence is 0.23 eV, which is in good agreement with that determined for $Mn^{2+}$ luminescence in the bulk phase[26] and in $Zn_{1-y}Mn_yS$ nanoclusters.[6,7,62,66] This indicates formation of isolated manganese ions in tetrahedral sites. To confirm this, EPR measurements are performed at various compositions. The EPR spectrum is recorded at 103 K for $y = 0.006$. The hyperfine structure is deduced from the difference between the experimental spectrum and the Lorentzian fit and shows six well-defined intense lines, and between each of them two weaker lines corresponding to forbidden transitions with a nuclear hyperfine splitting of 69 G. This is characteristic of isolated manganese ions in the CdS matrix. Hence from the PL spectrum and the hyperfine structure it is clearly demonstrated that isolated $Mn^{2+}$ are present in the CdS matrix.

We now concentrate on the behavior of isolated $Mn^{2+}$ ions in the CdS matrix with composition $y$. The increase in the PL intensity due to isolated $Mn^{2+}$ with increasing composition is followed by a decrease for compositions above 0.1. A plot of the relative ratio of the simulated PL spectrum (1) centered at 580 nm to that of (2) 700 nm with composition (contribution of the emission due to CdS at $y = 0$ is extracted) shows the appearance of a maximum at $y = 0.1$. This is related to the number of isolated $Mn^{2+}$ (without any interactions). The number of these $Mn^{2+}$, $y_{eff}$, with composition $y$, has been calculated by Kreitman *et al.*[68] The variation of $y_{eff}$ with composition has a maximum around 0.1. However, the shape of the relative intensity variation with composition differs from that for $y_{eff}$.

EPR spectroscopy is performed in the same experimental conditions. The integral of the hyperfine structure and that of the total signal are calculated from experimental data at various compositions ($0.006 < y < 0.2$). The ratio, $X$, of these integrals, determined at various compositions, increases with increasing composition and reaches a maximum around $y = 0.05$. The number of isolated $Mn^{2+}$, $N_{Is}$, is the product of $X$ with composition $y$ and the number of cations included in the CdS particle. The last term is estimated from the calculation of Lippens *et al.*[11] $N_{Is}$ increases with increasing composition, $y$, and reaches a maximum at $y = 0.1$. Figure 3.7 shows similar variation of $N_{Is}$ with $y$ as for $\Phi_{580}/\Phi_{700}$. The good correlation between the EPR hyperfine structure and the PL data shown in Figure 3.7 clearly confirms that the PL is due to isolated manganese ions in a tetrahedral coordination. Hence, using procedure III, isolated $Mn^{2+}$ appears in tetrahedral sites, whereas with procedure I that is not observed.

At the nanoscale therefore, Figure 3.7 shows a progressive increase in the fluorescence yield due to isolated manganese, reaching a maximum at 0.1 and then a decrease. Such behavior differs markedly from that observed in the bulk phase where the PL[64,65] and hyperfine structure[68] of isolated $Mn^{2+}$ ions in tetrahedral coordination are observed at low composition ($y < 0.01$).[68] The increase in $Mn^{2+}$ content induces a disappearance in the PL intensity and a broadening of the hyperfine structure lines to produce a single line. These phenomena have been attributed to
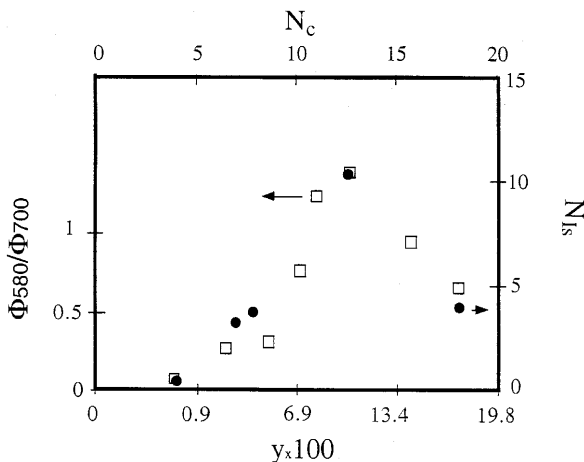
**FIGURE 3.7**    Variation with composition ( $y$ ) and $N_c$ of the relative luminescence quantum yield $\Phi_{580}/\Phi_{700}$ ($\square$) and of the number of isolated $Mn^{2+}$ per particle ($\bullet$) of particles prepared by procedure III.

$Mn^{2+}$–$Mn^{2+}$ energy transfer and interactions, respectively. Hence, the maximum of the PL yield due to isolated $Mn^{2+}$ ions in a tetrahedral site is reached at $y < 0.01$ in the bulk phase, whereas it is at $y = 0.1$ in quantum dots. Furthermore, the relative PL quantum yield of aged particles differs markedly with aging time.

To explain these differences in the behavior we take into account the process used to make the particles and particularly the resulting size and composition: As described above, for a given ratio of reactants ($[Mn(AOT)_2]/([Mn(AOT)_2] + [Cd(AOT)_2]$)), the composition, $y$, detected by EDS is always larger for particles made under procedure I than for those from III. To simplify the following, we denote particles I and II those made under procedures I and III. The slopes deduced by plotting composition, $y$, versus $[Mn(AOT)_2]/([Mn(AOT)_2] + [Cd(AOT)_2]$ are 0.86 and 0.51 for particles I and III, respectively. Particles I contain a larger amount of manganese ions compared to particles III (and particles I are smaller). Hence the aging induces an increase in the particle size and a decrease in the $y$ composition is determined by EDS. Assume that particle III ($D = 4$ nm) is made of particle I ($D = 3.2$ nm) surrounded by an external layer that grows during aging (Figure 3.8). Hence, particle I forms the internal core with an external shell of 0.4 nm thickness. Because of the difference in composition between the particles I and III, the external phase will contain a smaller number of manganese ions and this could be responsible for the presence of isolated $Mn^{2+}$ in tetrahedral sites. From the Lippens method,[11] the total number of atoms per nanocrystal is 740 and 1400 atoms for particle I (internal core) and particle III, respectively. Then the cation numbers are 370 and 700 atoms, respectively. For a given ratio of reactants with which the synthesis is made, the compositions of particle I and of particle III are measured by EDS. This permits calculation of the number of manganese ions in particles I and III. Hence, the number of manganese ions in the external layer of particle III, $N_c$, is deduced from
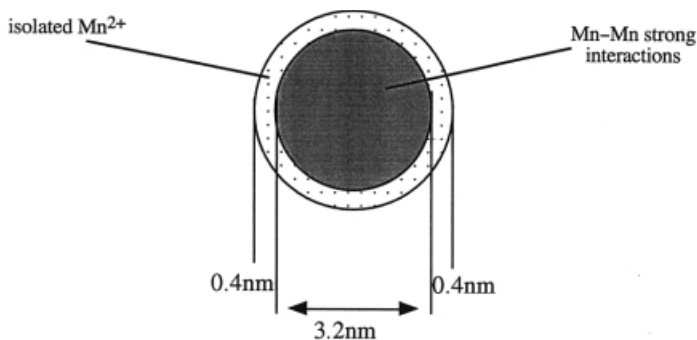
**FIGURE 3.8**    Model of particles.

the difference between the number of manganese ions in particles III and I. The $N_c$ value is then calculated at various compositions, $y$. Plotting $\Phi_{580}/\Phi_{700}$ and $N_{IS}$ versus the number of manganese ions in the external shell, $N_c$, a maximum is reached at $N_c = 12$ (Figure 3.7). This corresponds to a composition of particle III, $y = 0.1$. The variation of luminescence and hyperfine structure with composition, $y$, and with the calculated number of isolated $Mn^{2+}$ in the external layer, $N_c$, strongly supports the model shown in Figure 3.8. Of course we could expect an increase in the $Mn^{2+}-Mn^{2+}$ interactions in the external layer with increasing composition. As observed in Figure 3.7, above $y = 0.1$ and/or $N_c = 12$ the PL and hyperfine structure disappears. Hence, assuming that all the $Mn^{2+}$ atoms are isolated in the layer we would expect to observe a straight line (dashed line) on plotting the number of isolated $Mn^{2+}$ determined by EPR versus the number of manganese atoms in the layer, $N_c$. Two distinct regions are observed: (1) below a number of manganese atoms, $N_c$, of 12 $Mn^{2+}$ atoms in the external shell are isolated in a tetrahedral site; (2) above $N_c = 12$, the $Mn^{2+}-Mn^{2+}$ interactions are predominant and induce a decrease in the number of isolated $Mn^{2+}$ as observed by PL and from the hyperfine structure.

A model may be proposed to explain the appearance of isolated $Mn^{2+}$ ions in the CdS matrix at high manganese composition compared to that observed in the bulk phase. The appearance of the PL spectrum due to isolated $Mn^{2+}$ in the CdS matrix is due to formation of particles having an internal core rich in manganese ions that interact strongly with an external shell that is manganese poor and arranged in a tetrahedral structure. This is strongly supported by taking into account the variation of the luminescence and the hyperfine structure of isolated $Mn^{2+}$ with the number of atoms in the external layer formed during the aging of the particles.

## 3.8   2D AND 3D SUPERLATTICES OF SILVER SULFIDE NANOCRYSTALS

With the use of a dilute solution of dodecanethiol coated $Ag_2S$ nanocrystallites (particle volume fraction $\phi = 0.01\%$), monolayers of nanocrystals[69–73] are formed. When particles are deposited on a TEM grid covered by amorphous carbon, drop by drop with time for solvent evaporation before adding another droplet, large domains

of monolayers are observed. Most of the TEM grid surface is covered by the nanocrystals. The monolayer domain is very large and forms long ribbons. This is obtained for various nanocrystal sizes (from 2 to 6 nm)[71] and in all the experimental conclusions the ribbons are almost larger than 100 μm. The nanocrystals are self-arranged in a compact hexagonal network, with 1.8 nm as the average distance between them. Similar behavior is observed on replacing amorphous carbon by cleaved graphite (HOPG). With 5.8 nm nanocrystals deposited on a TEM grid covered by amorphous carbon (Figure 3.9a), very large domains of monolayer are observed. At higher silver nanocrystal concentration ($10^{-3}$ M), the solution remains optically clear. TEM images reveal the formation of large aggregates (Figure 3.9b) over large areas. To ensure that these aggregates are due to self-organization of nanoparticles into 3D superlattices, Tapping–atomic force microscopy (TM–AFM) experiments (Figure 3.9c) were carried out on these aggregates, which show similar size and average distribution of the islands to those observed by TEM (Figure 3.9b).
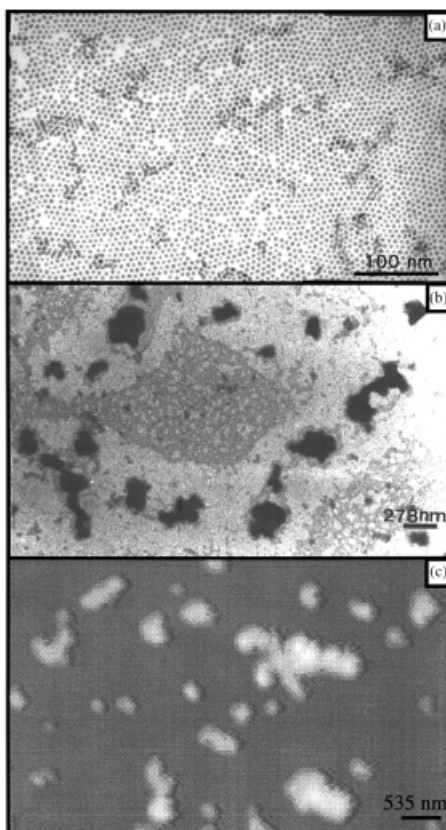


**FIGURE 3.9**   Silver sulfide nanocrystals of 5.8 nm. (a) Monolayer of 5.8 nm silver sulfide nanocrystals deposited on amorphous carbon. (b) TEM pattern on amorphous carbon. (c) Atomic force microscopy pattern on HOPG pattern.

The cross-section of these islands shows formation of a large aggregate having a truncated pyramid form. The similarity between patterns obtained by TEM (Figure 3.9b) and TM–AFM (Figure 3.9c) indicates the formation of a three-dimensional superlattice.

The TEM contrast of the patterns obtained on large aggregates (Figure 3.9b) compared with those observed from a monolayer (Figure 3.9a) confirms the three-dimensional superlattices. Magnification of one of these islands shows that they are made of highly oriented nanosized particles with a fourfold symmetry (Figure 3.10), attributed to the orientation of the particles in the {001} plane of face-centered cubic (fcc) structure. The core-to-core distance between two particles in the [010] direction of the superlattice of particles is ∼11 nm, which corresponds to the cell parameter of the pseudo-fcc crystal formed by $Ag_2S$ particles. The average particle diameter is about 5.8 nm, while the shortest distance between particles is 7.8 nm. This gives a calculated spacing between two particles of 2 nm, in good agreement with the average distance between particles (2 nm) obtained from the monolayer observation (see Figure 3.9a). The superlattice is still maintained after several months.

As already demonstrated,[1,2] it is possible to make particles differing in their sizes. Using the same procedure, 3D "supracrystals" made of nanocrystals having an average size of either 3 nm or 4 nm are produced. These aggregates are very similar to those formed with particles with an average size of 5.8 nm (Figure 3.10) and fourfold symmetry attributed to fcc stacking.

Instead of coating the nanocrystals with dodecanethiol, alkyl chain lengths varying from $C_8$ to $C_{14}$ are used, with procedure I. A drop of the solution of coated nanocrystals is deposited on an amorphous carbon grid. In most of the cases, monolayers made from particles differing in size are observed (see exceptions in reference 72). The nanocrystals are self-organized in hexagonal network over a large domain. The average distance between particles arranged in a hexagonal network increases with the thiol chain length (Table 3.3). The all-*trans* zigzag conformation length of the alkylthiol tail, $L$, can be evaluated from the empirical equation given by
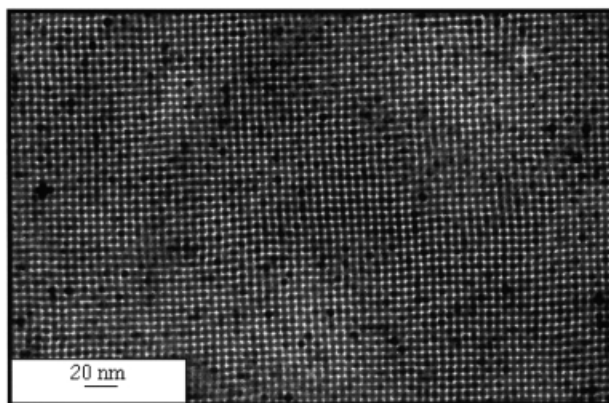


**FIGURE 3.10**    High-resolution image of an aggregate observed in Figure 3.9b.

Bain et al.,[74] $L$ (nm) $= 0.25 + 0.127n$, where $n$ is the number of $CH_2$ groups. The $L$ values for $C_8$, $C_{10}$, $C_{12}$, and $C_{14}$, are 1.27, 1.52, 1.77, and 2.03 nm, respectively. The edge–edge core spacings, $d_{p-p}$, are considerably shorter than twice the length of the alkanethiolate chains. For $C_8$ and $C_{10}$ derivatives, the edge–edge core is slightly longer than one chain length (Table 3.3) and corresponds to a *trans* zigzag configuration length equal to $C_9$ and $C_{11}$ respectively. For $C_{12}$ it is equal to one chain length, whereas it is shorter for $C_{14}$.

For $C_8$ and $C_{10}$, the edge–edge core spacing, $d_{p-p}$, is longer than one chain, whereas it is equal to one for $C_{12}$ and shorter for $C_{14}$ (Table 3.3). This behavior can be explained by the change in the chain length conformation and the various defects that depend on the chain length.[75] The amount of near-surface *gauche* defects decreases with increasing chain length, whereas that of chain-end *gauche* increases. Hence, when the alkyl chains are short, they behave as free alkanes in the liquid state. The increase in the chain length favors the order with predominantly the all-*trans* zigzag conformation. The chains are then densely packed, and less space is available for molecular reorientations and the *trans–gauche* bond isomerization is restricted. For $C_{12}$ the adjacent particles are separated by one chain length. This suggests that ordering arises from interdigitation of chains on neighboring particles. A cooperative chain-melting process occurs. The alkylated nanoparticles can serve as a highly dispersed analogue to the much-studied planar self-assembled mono-layers. The increase in the alkyl chain to $C_{14}$ induces an increase in the end *gauche* defects that cause the pseudo-rotational motion of individual chain segments about the long axis of the thiol derivative. This explains why the edge–edge core spacing is smaller than one chain length in the all-*trans* zigzag configuration. The edge–edge core spacing, $d_{p-p}$, is independent of the particle size. This is not so surprising. Because of the particle curvature, a relatively small number of alkyl chains parti-cipates in the interdigitation. The $d_{p-p}$ value depends on (1) the alkyl chain length, and (2) the chain's ability to bind to the surface. For a short alkyl chain ($C_6$, $C_8$), the average distance between particles cannot be reduced because of the large alkyl chain number of *gauche* defects and their ability to behave as a free alkane in the liquid state.[76] This prevents 2D self-organization. Hence, contrary to what has been claimed elsewhere,[76] in 2D self-assemblies the average distance between particles cannot be drastically changed.

Whatever the particle size, and with rather large numbers of $Ag_2S$ particles ($6 \times 10^{18}$ per ml) deposited on amorphous carbon, large aggregates are obtained. Nanocrystals coated with $C_8$ (Figure 3.11a) and $C_{10}$ (Figure 3.11b) alkyl chains form well-faceted aggregates over a very large domain with a fourfold symmetry as

**TABLE 3.3   Variation of the average distance $d_{p-p}$ between nanocrystals organized in a hexagonal network, and coated with thiol derivatives differing in their chain length ($C_4$–$C_{14}$)**

| Chain length | C8 | C10 | C12 | C14 |
|---|---|---|---|---|
| $d_{p-p}$ (nm) | 1.4 | 1.6 | 1.75 | 1.8 |

observed above with $C_{12}$. With $C_{14}$, aggregates are formed but are not arranged in a well-defined structure (Figure 3.11c). This difference in the behavior of aggregate structure from replacing $C_8$, $C_{10}$, and $C_{12}$ with $C_{14}$ is related to the edge–edge core spacing, $d_{p-p}$ value, observed when monolayers of nanoparticles are close-packed. With the various alkyl chains ($n < 14$), the $d_{p-p}$ value is either similar to ($n = 12$) or slightly longer than ($8 < n < 12$) the calculated length of a *trans* zigzag confor- mation. This imposes dense packing of the alkyl chain and there is maximum chain interdigitation and/or folding. With $C_{14}$ the experimental $d_{p-p}$ value is 1.8 nm, whereas the calculated length of one chain for the *trans* zigzag conformation is 21.03 nm. This difference is rather large and is due to the end *gauche* defects of the alkyl chains. This markedly reduces the packing of the chain, which prevents the growth of monolayers in 3D superlattices. The formation of the aggregates observed is due to attractive interactions between particles when they are dispersed in solution. Hence with $n < 14$, the interactions between particles are rather large and favor the interdigitation of the alkyl chains. With $C_{14}$ derivatives, the interactions remain large, with a very poor interdigitation due to the defect in the long chain.
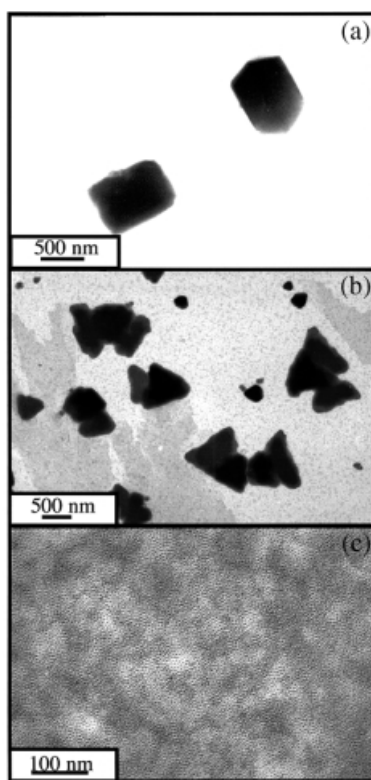


**FIGURE 3.11** Aggregates of silver sulfide nanocrystals coated with various alkyl chains. (a) Face-centered cubic "supracrystal" obtained with $C_8$. (b) Face-centered cubic "supra- crystal" obtained with $C_{10}$. (c) Aggregates obtained with $C_{14}$.

It can be concluded that, to obtain well-organized 3D superlattices in an fcc structure, the two parameters, interaction between particles and chain packing have to be taken into account.

## 3.9 CONCLUSION

It has been shown that reverse micelles can be used to make semiconductor nano-crystals differing in size and composition. Direct fluorescence can be obtained when the particles are passivated. The technique enables alloys to be made that exhibit specific properties. Increase in particle size induces a decrease in the magnetic interactions. Furthermore, the fluorescence due to isolated manganese in its tetra-hedral site depends on the preparation mode (aging process).

Self-organization is observed in hexagonal compact (2D) and fcc structured (3D) silver sulfide nanocrystals. The interparticle distance can be controlled.

## REFERENCES

1. M. P. Pileni, *Langmuir*, **1997**, *13*, 3266.
2. M. P. Pileni, *J. Phys. Chem.*, **1993**, *97*, 6961.
3. I. Lisiecki, M. P. Pileni, *J. Amer. Chem. Soc.*, **1993**, *115*, 3887.
4. C. Petit, P. Lixon, M. P. Pileni, *J. Phys. Chem.*, **1993**, *97*, 12974.
5. L. Motte, C. Petit, P. Lixon, L. Boulanger, M. P. Pileni, *Langmuir*, **1992**, *8*, 1049.
6. L. E. Brus, *J. Chem. Phys.*, **1983**, *79*, 5566.
7. R. Rossetti, J. L. Ellison, J. M. Bigson, L. E. Brus, *J. Chem. Phys.*, **1984**, *80*, 4464.
8. A. J. Nozik, F. Williams, M. T. Nenadocic, T. Rajh, O. I. Micic, *J. Phys. Chem.*, **1985**, *89*, 397.
9. C. Petit and M. P. Pileni, *J. Phys. Chem.*, **1988**, *92*, 2282.
10. Y. Kayanuma, *Phys. Rev. B.*, **1988**, *38*, 9797.
11. P. E. Lippens, M. Lannoo, *Phys. Rev. B.*, **1989**, *39*, 10935.
12. C. Petit, P. Lixon, M. P. Pileni, *J. Phys. Chem.*, **1990**, *94*, 1598.
13. Y. Z. Hu, M. Lindberg, S. W. Koch, *Phys. Rev. B.*, **1990**, *42*, 1713.
14. Y. Wang, N. Herron, *Phys. Rev. B.*, **1990**, *41*, 6079.
15. M. G. Bawendi, M. L. Steigerwald and L. E. Brus, *Annu. Rev. Phys. Chem.*, **1990**, *41*, 477.

16. M. V. Rama Krishna, R. A. Friesner, *J. Chem. Phys.*, **1991**, *95*, 8309.

17. J. Nosaka, *J. Phys. Chem.*, **1991**, *95*, 5054.

18. M. P. Pileni, L. Motte, C. Petit, *Chem. Mater.*, **1992**, *4*, 338.

19. Y. Wang, N. Herron, K. Moller, T. Bein, *Solid State Commun.*, **1991**, *77*, 33.

20. R. N. Bhargava, D. Gallagher, T. Welker, *J. Lumin.*, **1994**, *60 & 61*, 275.

21. R. N. Bhargava, D. Gallagher, X. Hong, A. Nurmikko, *Phys. Rev. Lett.*, **1994**, *72*, 416.

22. R. N. Bhargava, *J. Lumin.*, **1996**, *70*, 85.

23. K. Sooklal, B. S. Cullum, S. M. Angel and C. J. Murphy, *J. Phys. Chem.*, **1996**, *100*, 4551.

24. A. A. Khosravi, M. Kundu, B. A. Kuruvilla, G. S. Shekhawat, R. P. Gupta, A. K. Sharma, P. D. Vyas, S. K. Kulkarni, *Appl. Phys. Lett.*, **1995**, *67*, 2506.

25. K. Yanata, K. Susuki, Y. Oka, *Jpn. J. Appl. Phys.*, **1993**, *32* (3, suppl.), 384.

26. Y. Oka, K. Yanata, *J. Lumin.*, **1996**, *70*, 35.

27. L. Motte, C. Petit, L. Boulanger, P. Lixon, M. P. Pileni, *Langmuir*, **1992**, *8*, 1049.

28. L. Brus, *J. Phys. Chem.*, **1986**, *90*, 2555.

29. M. P. Pileni (editor) *Reactivity in Reverse Micelles*, Elsevier, Amsterdam, **1989**.

30. M. Zulauf, H. F. Eicke, *J. Phys. Chem.*, **1979**, *83*, 480.

31. I. Lisiecki, P. André, A. Filankembo, C. Petit, J. Tanori, T. Gulik-Krzywicki, B. W. Ninham, M. P. Pileni, *J. Phys. Chem. B.*, **1999**, *103*, 9168.

32. I. Lisiecki, P. André, A. Filankembo, C. Petit, J. Tanori, T. Gulik-Krzywicki, B. W. Ninham, M. P. Pileni, *J. Phys. Chem.*, **1999**, *103*, 9176.

33. D. Ingert, N. Feltin, L. Levy, P. Gouzert, M. P. Pileni, *Adv. Mater.*, **1999**, *11*, 220.

34. B. G. Potter, H. Simmons, *J. Appl. Phys.*, **1990**, *68*(3), 1218.

35. B. G. Potter, H. Simmons, *Phys. Rev. B.*, **1991**, *43*(3), 2234.

36. B. G. Potter, H. Simmons, P. Kumar, C. J. Stanton, *J. Appl. Phys.*, **1994**, *75*(12), 8039.

37. B. G. Potter and H. Simmons, *Sol. Stat. Commun.*, **1996**, *98*(8) 717.

38. C. R. M. Oliveira, A. M. Paula, F. O. Plentz Filho, J. A. Medeiros Neto, L. C. Barbosa, O. L. Alves, E. A. Menezes, J. M. M. Rios, H. L. Fragnito, C. H. Brito Cruz, C. L. Cesar, *Appl. Phys. Lett.*, **1995**, *66*(4), 439.

39. A. M. Paula, L. C. Barbosa, C. H. B. Cruz, O. L. Alves, J. A. Sanjurjo, C. L. Cesar, *Appl. Phys. Lett.*, **1996**, *69*(3), 357.

40. L. C. Barbosa, V. C. S. Reynoso, A. M. Paula, C. R. M. Oliveira, O. L. Alves, A. F. Craievich, R. E. Marotti, C. H. Brito Cruz, C. L. Cesar, *J. Non-Cryst. Sol.*, **1997**, *219*, 205.

41. Y. Msumoto, K. Sonobe, *Phys. Rev. B.*, **1997**, *56*(15), 9734.

42. The size distribution is deduced by fitting a Gaussian curve obtained by plotting the percentage of particles having a given size.

43. Y. Wang, N. Herron, *J. Phys. Chem.*, **1991**, *95*, 525.

44. N. A. Kotov, F. C. Meldrum, C. Wu., J. H. Fendler, *J. Phys. Chem.*, **1994**, *98*, 2735.

45. J. L. Coffer, S. R. Bigham, R. F. Pinizzotto, H. Yang, *Nanotechnology*, **1992**, *3*, 69.

46. N. Pinna, K. Weiss, J. Urban and M. P. Pileni, *Adv. Hat.*, **2001**, *16*, 200.

47. Semper version 6 was used to perform power spectra (PS), and image processing of electron diffraction.

48. Cerius version 5 was used to perform single crystal diffraction calculations and structure simulation.

49. Y. Wang, N. Herron, *J. Phys. Chem.*, **1991**, *95*, 525.

50. Y. Nosaka, *J. Phys. Chem.*, **1991**, *95*, 5054.

51. L. E. Brus, *J. Chem. Phys.*, **1984**, *80*, 4403.

52. J. Cizeron, M. P. Pileni, *J. Phys. Chem.*, **1995**, *99*, 17410.

53. J. Cizeron, M. P. Pileni, *Nanostruct. Mater.*, **1997**, *8*, 419.

54. J. Cizeron, M. P. Pileni, *J. Phys. Chem.*, **1997**, *101*, 8887.

55. L. G. Suslina, E. L. Danasyuk, S. G. Konnikov, D. L. Federov, *Fiz. Tekh. Poluprovodn.*, **1976**, *10*, 1830.

56. L. Levy, J. F. Hochepied, M. P. Pileni, *J. Phys. Chem.*, **1996**, *100*, 18332.

57. L. Levy, N. Feltin, D. Ingert, M. P. Pileni, *J. Phys. Chem.*, **1997**, *101*, 9153.

58. L. Levy, D. Ingert, N. Feltin, M. P. Pileni, *Adv. Mater.*, **1998**, *10*, 53.

59. N. Feltin, L. Levy, D. Ingert, M. P. Pileni, *J. Phys. Chem.*, **1999**, *103*, 4.

60. N. Feltin, L. Levy, D. Ingert, M. P. Pileni, *Adv. Mater.*, **1999**, *11*, 398.

61. L. Levy, N. Feltin, D. Ingert, M. P. Pileni, *Langmuir*, **1999**, *15*, 3386.

62. J. K. Furdyna, J. Kossut, *Semiconductors and Semimetals*, Vol. 25, Academic Press, New York, **1998**.

63. C. T. Tsai, S. H. Chen, D. S. Chuu, W. C. Chou, *Phys. Rev. B.*, **1996**, *54*, 11555.

64. R. B. Bylsma, W. M. Becker, J. Kossut, U. Debska, *Phys. Rev. B.*, **1986**, *33*, 8207.

65. J. K. Furdyna, *J. Appl. Phys.*, **1988**, *64*, R29.

66. M. Ikeda, K. Itoh, S. Hisano, *J. Phys. Soc. Jpn.*, **1968**, *25*, 455.

67. T. Dannhauser, M. O'Neil, K. Johansson, D. Whitten, G. McLendon, *J. Phys. Chem.*, **1986**, *90*, 6074.

68. M. M. Kreitman, D. L. Barnett, *J. Chem. Phys.*, **1965**, *43*, 364.

69. L. Motte, F. Billoudet, M. P. Pileni, *J. Phys. Chem.*, **1995**, *99*, 16425.

70. L. Motte, F. Billoudet, E. Lacaze, M. P. Pileni, *Adv. Mater.*, **1968**, *8*, 1018.

71. L. Motte, F. Billoudet, E. Lacaze, J. Douin, M. P. Pileni, *J. Phys. Chem. B.*, **1997**, *101*, 138.

72. L. Motte, M. P. Pileni, *J. Phys. Chem. B.*, **1998**, *102*, 4104.

73. L. Motte, E. Lacaze, M. Maillard, M. P. Pileni, *Langmuir*, **2000**, *16*, 3803.

74. C. D. Bain, E. B. Troughton, Y. T. Tao, J. Evall, G. M. Whitesides, R. G. J. Nuzzo, *Am. Chem. Soc.*, **1989**, *111*, 321.

75. M. J. Hostetler, J. J. Stokes, R. W. Murray, *Langmuir*, **1996**, *12*, 3604.

76. J. R. Heath, C. M. Knobler, D. V. Leff, *J. Phys. Chem. B.*, **1997**, *101*, 189.

# 4 Ceramics

ABBAS KHALEEL and RYAN M. RICHARDS

Department of Chemistry, Kansas State University, Manhattan, Kansas

## 4.1 INTRODUCTION

Developments in the field of nanoparticles have produced very significant and interesting results in all areas investigated. The science of ceramic nanoparticles is no exception, and has been under investigation for many years with much success in several areas including synthesis, surface science, texturology, destructive adsorption, catalysis, etc. This field of nanoscience is facilitated by the fact that many of the systems of interest have been studied extensively in the bulk and therefore provide ready comparisons with nanoparticulate systems.

Materials can be separated into metals, semiconductors, and insulators. With metals and semiconductors, which possess strong metallic or covalent bonds, changes of properties with size are well documented and appreciated for what these changes represent: progression from "quantum behavior" (a near continuum of energy states). However, in the case of insulator particles, quantum size effects are less obvious and so far are generally related to changed surface chemistry.[1] Of course, some metal oxides are semiconductors—ZnO and $TiO_2$ for example—the semiconductor properties of which are covered in depth elsewhere in this book.

The insulating oxides are made up of the metals from the left and right sides of the periodic table; typical examples of insulating oxides include MgO, CaO, $Al_2O_3$, and $SiO_2$. The oxides of the metals in the middle of the periodic table (Sc to Zn) make up the semiconducting or metallic oxides; typical examples include ZnO, $TiO_2$, NiO, $Fe_2O_3$, and $Cr_2O_3$.

It is now well known that within the intermediate region of 2–10 nm, neither quantum chemistry nor classical laws of physics hold. In spherical nanoparticles, for example, at a size of 3 nm, 50% of the atoms or ions are on the surface, allowing the possibility of manipulation of bulk properties by surface effects and allowing near-stoichiometric reaction chemistry.[1] When strong chemical bonding is present,

delocalization can vary with size; this in turn can lead to different chemical and physical properties.[2]

In choosing materials for study, MgO and CaO have been found to be attractive because they are highly ionic and have a high melting point, and it would be expected that samples of very small particle size might be stable and isolable. Furthermore, reactive surface sites on these oxides have been studied extensively, especially for MgO crystals and powders.

The refractory nature of most of the metal oxides actually facilitates the formation of ultrasmall particles. The highly ionic nature of some materials, especially MgO, $Al_2O_3$, $ZrO_2$, and $TiO_2$, allows the formation of many stable defect sites, including edges, corners, and anion/cation vacancies.

It should also be noted that aerogel prepared materials have very low densities, can be translucent or transparent, and have low thermal conductivities and unusual acoustic properties. They have found various applications, including detectors for radiation, superinsulators, solar concentrators, coatings, glass precursors, catalysts, insecticides, and destructive adsorbents. It has been shown that nanoparticles of ceramic materials can be compressed at relatively low temperatures into solids that possess better flexibility and malleability than traditional ceramics.[2]

Taking a closer look at the insulator metal oxides, it will be noted that there have been numerous studies of their surfaces in an attempt to clarify the type of defect sites that can exist.[3–6] The most common defects are coordinatively unsaturated ions due to the presence of planes, edges, corners, anion/cation vacancies, and electron excess centers. Such sites are often considered the active sites for many useful and interesting reactions, including methane activation,[7] $D_2-CH$ exchange,[8] CO oligomerization,[9] and oxygen exchange in $CO_2$[10] and $H_2O$.[11]

It should also be noted that nanoparticles of crystalline substances have about $10^{19}$ interfaces per $cm^3$ and range in surface area up to 800 $m^2\ g^{-1}$. Upon compaction, but without growth of the nanocrystals, solids with multitudinous grain boundaries are formed. In the cases of $CaF_2$[12] and $TiO_2$,[13] solid samples are obtained that undergo plastic deformation at room temperature, presumably by diffusional creep. It has been proposed that further work in the area of consolidated nanophase materials may lead to ceramics with increased flexibility, less brittleness, and perhaps greater strength.[2] It may also be possible to form materials with a large fraction of atoms at grain boundaries, perhaps in arrangements that are unique. It may also be possible to produce binary materials of normally immiscible compounds or elements.

The methods of sample preparation are of course the determining factors in producing different morphologies.[1] For example, burning magnesium in oxygen (MgO smoke) yields 40–80 nm cubes and hexagonal plates, whereas thermal decomposition of $Mg(OH)_2$, $MgCO_3$, and especially $Mg(NO_3)_2$ yields irregular shapes often exhibiting hexagonal platelets. Surface areas can range from 10 $m^2\ g^{-1}$ (MgO smoke) to 250 $m_2\ g^{-1}$ for $Mg(OH)_2$ thermal decomposition, but surface areas of about 150 $m^2\ g^{-1}$ are typical. In the case of calcium oxide, surface areas can range from 1 to 100 $m^2\ g^{-1}$ when prepared by analogous methods, but generally about 50 $m^2\ g^{-1}$ is typical.

Modifications to the traditional aerogel method have been used to produce numerous ceramic nanoparticles. One modification has involved addition of large amounts of aromatic hydrocarbons to alcohol–methoxide solutions before hydrolysis and alcogel formation. This was done to further reduce the surface tension of the solvent mix and to facilitate solvent removal during the alcogel–aerogel transformation.[1,14,15] This led to two interesting developments:[16,17] higher surface areas and smaller crystallite sizes for MgO, CaO, $TiO_2$, and $ZrO_2$ (here referred to as AP samples for "aerogel prepared").

It has been proposed that as particles become smaller in size they may take on different morphologies that may alter their surface chemistry and adsorption properties in addition to increasing the surface area.[18] One of the most intriguing observations was that nanocrystals prepared by the altered aerogel approach exhibited higher surface chemical reactivities than more conventionally prepared samples (precipitation of hydroxides followed by vacuum dehydration, herein referred to as CP samples).[18] For example, in the reaction of $2CaO + CCl_4 \rightarrow 2CaCl_2 + CO_2$, AP samples demonstrated reaction efficiencies twice those of CP samples and 30 times higher than those of commercial samples.[1,19] AP MgO adsorbed three times as much $SO_2$ per $nm^2$ as did CP MgO.[20] For the destructive adsorption of $CH_3(CH_3O)_2PO$, the reaction efficiency was four times higher for AP MgO than for CP MgO and 50 times higher than that for CM MgO.[21] This high reactivity, observed both at room temperature and at high temperatures, for numerous reactions demonstrates that this is not an effect of higher surface area alone. The nanoparticles (especially the AP samples) have been shown to possess a much greater number of defect sites per unit surface area, which are believed to be responsible for the observed chemistry.

Nanoscale MgO and CaO particles exhibit unusual surface morphologies and possess more reactive surfaces due to the presence of high concentrations of edge/corner sites and other defects. This allows such particles to exhibit unique surface chemistry, as demonstrated by room temperature adsorptions. Morphological studies indicate that the nanocrystals are more polyhedral and thus possess more defects.[2] Such defects could be of the Frenkel or Schottky type (vacancies) or may be manifested as unusual configurations of edges, corners, or crystal planes. MgO and CaO are particularly interesting in nanoparticulate form. It has been possible to synthesize MgO with surface areas $> 500 \ m^2 \ g^{-1}$ with crystallite sizes $< 4$ nm.[14] The high surface areas of MgO and CaO dictate that 30–40% of the MgO (CaO) moieties are on the surface, thus allowing surface gas reactions to approach the stoichiometric range.

## 4.2 SYNTHESIS

The synthesis of nanoscale particles has received considerable attention in view of the potential for new materials and unique properties. The novel properties and the numerous applications of nanophase materials, especially ceramic powders, have

encouraged many researchers to invent and explore the methods, both chemical and physical, by which such materials can be prepared.

Several physical aerosol methods have been reported for the synthesis of nanosize particles of ceramic materials. These include gas condensation techniques,[22–29] spray pyrolysis,[30–37] thermochemical decomposition of metal-organic precursors in flame reactors,[38–41] and other aerosol processes named after the energy sources applied to provide the high temperatures during gas–particle conversion.

On the other hand, liquid phase chemistry has been attracting the attention of many chemistry and materials researchers and has been recognized as another potential route to better materials and ceramics. This increasing interest in chemical processing of nanoscale particles of ceramics and other materials is clearly indicated by the number of reports and reviews on this subject.[15,42–49,72–79] This interest reflects mounting evidence that chemical processing allows for better ceramics and will have a lasting role in advanced materials. The most common and widely used liquid phase chemistry method has been the sol-gel processing. Other wet chemistry methods including novel microemulsion techniques and precipitation from solutions have also been used. Mechanochemical synthesis methods involving solid state chemistry reactions have also been investigated as an alternative chemical route to nanosize materials including ceramics.

## 4.2.1 Physical/Aerosol Methods

***4.2.1.1 Vapor Condensation Methods***    Gas condensation techniques to produce nanoparticles directly from a supersaturated vapor of metals are among the earliest methods for producing nanoparticles. They generally involve two steps: First, a metallic nanophase powder is condensed under inert convection gas after a supersaturated vapor of the metal is obtained inside a chamber. A high pressure of inert gas is usually needed to achieve supersaturation. Frequent collisions with the gas atoms decrease the diffusion rates of atoms away from the vapor source region and also cool the atoms. Limiting the diffusion rates of atoms helps avoid the deposition of individual atoms or very small clusters of atoms on the collecting surface. Second, the powder is oxidized by allowing oxygen into the chamber. This postoxidation is a critical step and very often it is necessary that it be done slowly. Due to the highly exothermic reaction, particles heat up for short times (usually less than 1 s) to temperatures as high as 1000°C resulting in their agglomeration into large particles by rapid diffusion processes. A subsequent annealing process at higher temperature is often required to complete the oxidation.

The general process was described in 1976 by Ganqvist and Buhrman.[51] A more recent description was reported by Ichinose *et al.*[52] The system consists of a vapor source inside a vacuum chamber containing a mixture of an inert gas, usually argon or helium, mixed with another gas that is selected on the basis of the material to be prepared. Oxygen is mixed with the inert gas to produce metal oxides;[23] ammonia is usually used to prepare metal nitrides,[24] and an appropriate alkane or alkene, as a source of carbon, is usually used to prepare metal carbides.[23,25] Nanoparticles are formed when supersaturation is achieved above the vapor source. A collection

surface, usually cooled by liquid nitrogen, is placed above the source. The particles are transported to the surface by a convection current or by a combination of a forced gas flow and a convection current that is set up by the difference in the temperature between the source and the cold surface.[53] The process was later improved by adding a way to scrape the nanoparticles from the cold collection surface so that the particles would fall into a die, and a unit where they can be consolidated into pellets (Figure 4.1).[53–55]

A more recent development of this technique involved the use of forced flowing gas with high velocity in a technique named the FGE (flow gas evaporation) tech-
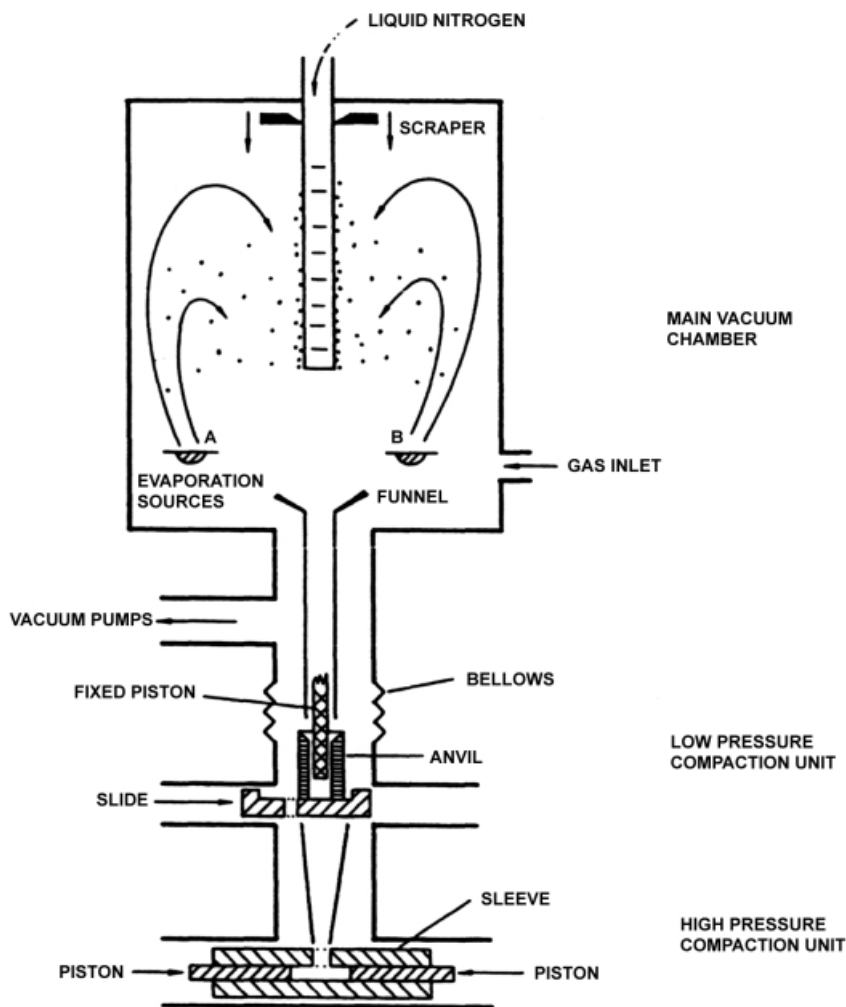


**FIGURE 4.1**  Typical apparatus for producing nanoparticles from supersaturated vapor.[53] Reprinted with permission from A S Edelstein and R C Cammarato, (eds), *Nanoparticles: Synthesis, Properties and Applications*, IOP Publishing, Philadelphia, (1996).

nique.[56] The advantage of this new technique is that the formation of the vapor zone and particle growth zone along the flow of inert gas can be controlled by the inert gas species and the flow velocity. By traveling in the gas flow, the particles grow by coalescence. This technique has been used to prepare nanoparticles of metals and can be extended for metal oxides and ceramics. It allows the formation of ultrafine particles with a narrow size distribution.

A schematic presentation of the system is shown in Figure 4.2. It consists essentially of a cylindrical chamber (9 cm inner diameter and 150 cm long), two Knudsen cells as the evaporation source, and the gas flowing system. Samples for electron microscopy were collected on grids positioned at different locations A, B, and C in the chamber.

Supersaturated vapor has been achieved by many different vaporization methods. The most common techniques include thermal evaporation, sputtering, and laser methods.

*Thermal Evaporation* Thermal evaporation, using different types of heat sources, was the earliest method used for achieving supersaturated vapor. Preparation of nanoparticles from supersaturated vapor produced by thermal evaporation was first established in 1930 to prepare nanoparticles of elements.[56–59] Oxides were later prepared by the same method by introducing oxygen to the metal vapor.[60–63]

*Sputtering* Sputtering is a more convenient method of evaporation and has some advantages over thermal evaporation techniques. First, it can be used for a wide variety of materials. Second, the evaporation conditions are very stable and easily controlled by the current. Both DC and RF magnetron sputtering have been used to prepare several types of nanoparticles and clusters.[22,26,64,65] The typical apparatus is similar to that shown in Figure 4.1, except that the evaporation source consists of a
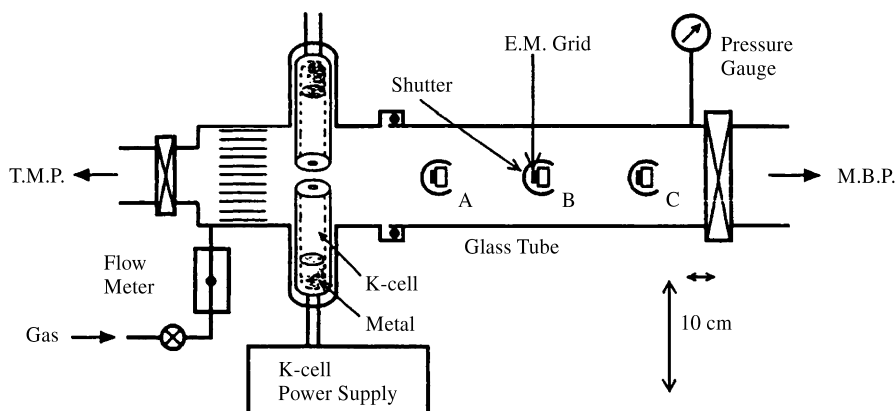


**FIGURE 4.2** A schematic of the apparatus used in the flow gas evaporation (FGE) technique. Used with permission from *Mesoscopic Materials and Clusters, Their Physical and Chemical Properties*, ed. T. Arai, K. Mihama, K. Yamamoto, S. Sugano, Kodansha and Springer, New York, **1999**, pp. 275–283.[56]

sputter source, with an appropriate sputter target, positioned normal to the cold surface axis. As an example, nanocrystalline $ZrO_2$ powder was synthesized using a sputter source that has a zirconium target of 75 mm diameter positioned 100 mm from the cold surface.[64]

Metal oxide ceramics can be prepared in two ways. In the first method, the metal particles prepared by DC sputtering using an argon atmosphere are allowed to react with oxygen (postoxidation). The second method involves reactive RF sputtering of a metal target using various $Ar/O_2$ gas mixtures. In this case, oxygen should be continuously added to the sputter chamber to replace the amount consumed. This second method is usually preferred since it avoids the high particle temperature agglomeration that normally occurs during postoxidation.[64,65]

*Laser Methods*    Laser vaporization is achieved by focusing a high-energy pulsed laser onto the metal target of interest. The temperature at the focusing spot can exceed 10,000 K and can vaporize any substance.[28] The hot metal atoms are then allowed to react with oxygen or ammonia inside the chamber to form vapor phase metal oxide or metal nitride molecules and clusters. A variety of nanoscale metal oxides have been prepared using laser vaporization techniques, including ZnO, $SiO_2$, $TiO_2$, $ZrO_2$, $Al_2O_3$ and MgO.[23] Metal carbide nanoparticles have also been prepared by means of laser vaporization in the presence of an appropriate source of carbon such as methane, ethylene, or isobutene. As an example, nanoparticles of SiC and different titanium carbides were prepared by laser vaporization of silicon or titanium in a mixture of helium and isobutene.[23,25] A detailed description of the system can be found in several references.[23,28]

Gas condensation methods for preparing nanoparticles directly from super-saturated vapor have many advantages over other techniques, including versatility, ease of performance and analysis, and high-purity products. They can also be employed to produce films and coatings. Furthermore, laser vaporization techniques allow for the production of high-density, directional, and high-speed vapor of any metal within an extremely short time. In spite of the success of these methods, they have the disadvantage that the production cost is still high because of low yields and the difficulty in scaling up. Heating techniques have other disadvantages, which include the possibility of reactions between the metal vapors and the heat-source materials. Also, the operating temperature is limited by the choice of the source material and as a result the technique cannot be used to make a wide variety of materials. For further discussion on supersaturation, particle nucleation and growth, and the transport and collection of the particles, see reference 53.

**4.2.1.2  Spray Pyrolysis**    Spray pyrolysis is another useful method for the synthesis of high-purity homogeneous ceramic powders.[30–37] This technique has been known by several other names, including solution aerosol thermolysis,[34] evaporative decomposition of solutions,[35] plasma vaporization of solutions,[36] and aerosol decomposition.[37] The starting materials in this process are chemical precursors, usually appropriate salts, in solution, sol, or suspension. The process involves the generation of aerosol droplets by nebulization or "atomization" of the starting solution, sol, or suspension. The droplets generated undergo evaporation with solute

condensation within the droplet, drying, thermolysis of the precipitate particle at higher temperature to form a microporous particle, and finally, sintering to form a dense particle. Figure 4.3 shows a schematic representation of a spray pyrolysis apparatus.

Various techniques for atomization have been employed, including pressure, two-fluid, electrostatic, and ultrasonic atomizers.[32,33] These atomizers differ in droplet size (2–15 μm), rate of atomization, and droplet velocity (1–20 m s$^{-1}$). These factors affect the heating rate and residence time of the droplet during spray pyrolysis which, in turn, affect some of the particle characteristics, including particle size. For a specific atomizer, the particle characteristics, including particle size distribution, homogeneity, and phase composition depend on the type of precursor, solution concentration, pH, viscosity, and the surface tension.[31–33]

Aqueous solutions are usually used because of their low cost, safety, and the availability of a wide range of water-soluble salts. A wide variety of ceramic materials have been prepared using this technique, including MgO, $Al_2O_3$, and $ZrO_2$. Metal chloride and nitrate salts are commonly used as precursors because of their high solubility. Precursors that have low solubility or those that may induce impurities, such as acetates that lead to carbon in the products, are not preferred.[32,35]

The transformation of the aerosol droplets into particles involves various processes, including solvent evaporation, precipitation of dissolved precursor, and thermolysis of precipitated particles. All of these processes take place in one step, which represents an advantage of this method. Other advantages include the production of high-purity nanosize particles; the homogeneity of the particles as a result of the homogeneity of the original solution; and the facts that each droplet/particle undergoes the same reaction conditions and that no subsequent milling is necessary. Disadvantages of spray pyrolysis include the large amounts of solvents necessary and the difficulty of scaling up the production. The use of large amounts of nonaqueous solvents increases the production expense as a result of the high cost of pure solvents and the need for proper disposal.

### 4.2.1.3 Thermochemical/Flame Decomposition of Metal-Organic Precursors

Flame processes have been widely used to synthesize nanosize powders of ceramic materials. This is another type of gas condensation technique, with the starting material being a liquid chemical precursor. The process is referred to as chemical vapor condensation (CVC). Chemical precursors are vaporized and then oxidized in a combustion process using a fuel–oxidant mixture such as propane–oxygen or methane–air.[39] The process combines the rapid thermal decomposition of a precursor–carrier gas stream in a reduced pressure environment with thermophoretically driven deposition of the rapidly condensed product particles on a cold substrate.[41] The flame usually provides a high temperature (1200–3000 K), which promotes rapid gas phase chemical reactions.[38]

Several types of flame reactors have been used.[38–41,66–69] One example of these reactors is a diffusion flame reactor in which the combustion processes are mainly determined by the rate of interdiffusion of the oxidant and the fuel. The maximum flame temperature usually occurs at the tip of the flame where agglomerates fuse and
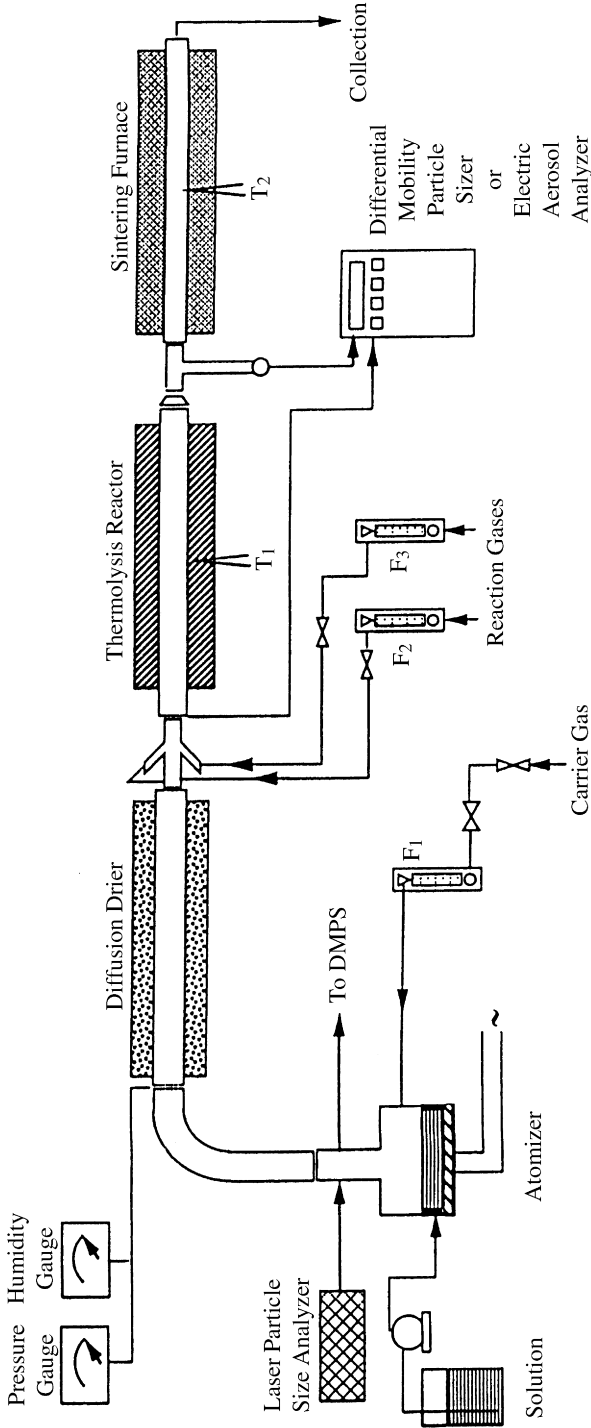
**FIGURE 4.3** Schematic representation of spray pyrolysis apparatus. Reproduced with permission of *J. Am. Ceramic Society*, **1993**, *76(11)*, 2707. The American Ceramic Society, Ohio.[33]

leave the flame. As they leave the flame, the flame temperature drops quickly and particles continue to coagulate without sintering, resulting in large agglomerates of primary particles. A variety of ceramic nanoparticles have been successfully prepared by this method, including $TiO_2$ and $SiO_2$.[38] The advantage of a diffusion flame reactor is that it provides a stable flame over a wide range of operation conditions.

Another example is the recent development of a low-pressure flat flame combustion reactor (Figure 4.4). Advantages of this method over previously used hot-wall reactors include an increase in the production rate and the fact that pyrolysis and condensation occur in the gas phase, which precludes impurity entrainment from the reactor walls. Nanoparticles of several ceramic oxides have been successfully prepared using this reactor, including titanium oxide, silicon oxide, and aluminum oxide.[41,66]

A variety of chemical precursors have been used, including metal chlorides such as $TiCl_4$ to prepare $TiO_2$ and $SiCl_4$ to prepare $SiO_2$;[31,39] metal-alkyl precursors;[40] metal alkoxides;[41] and gaseous metal hydrides, such as silane as a source of silicon to prepare silica.[70,71] Chlorides have been the most widely used precursors in the industry and the process is sometimes referred to as "chloride process." The high
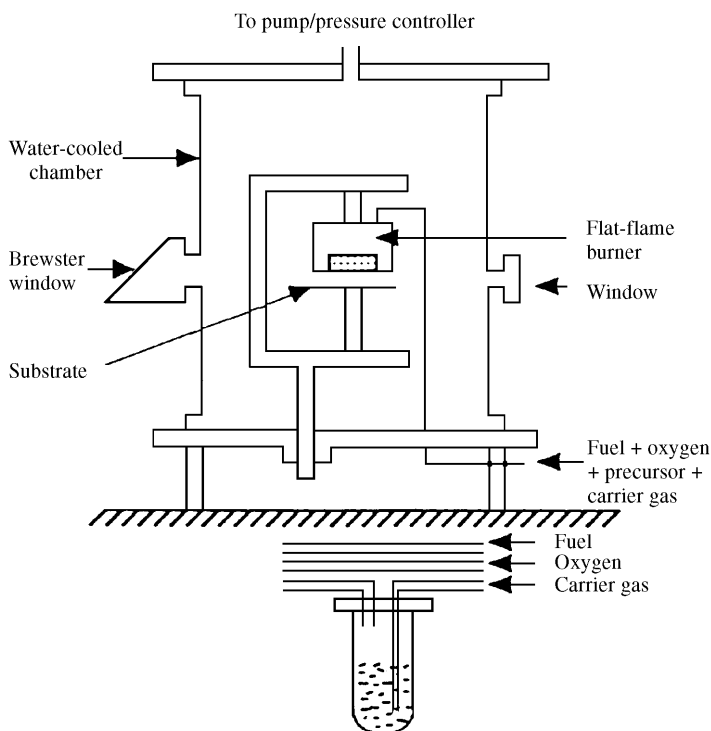


**FIGURE 4.4**   A schematic of a flat-flame combustion reactor. Reprinted from *Acta Materia 1a* (formerly *Nanostructured Materials*), Skanadan, G., Chen, Y-J., Glumac, N., and Kear, B. H., p.149, copyright **1999**, with permission from Elsevier Science.[41]

vapor pressure of chlorides and the fact that they can safely be stored and handled make them excellent potential precursors. The disadvantages of using chloride precursors are the formation of acidic gases and contamination of the products with halide residues. Flame processes are used industrially to produce commercial quantities of ceramic particulates, such as silica, titania, etc. This is because of the low cost of production as compared to all other methods. The disadvantage of flame synthesis is that the control of particle size (both primary particle and aggregate size), morphology, and phase composition is difficult and limited.

## 4.2.2 Chemical Methods

### 4.2.2.1 Sol-gel Technique

The role of sol-gel processing, as well as the role of chemistry in general, in materials fabrication has been growing rapidly. The development of sol-gel processing of materials, and especially of ceramics, has been described in several books and reviews.[15,42–48,72–79]

The process is typically used to prepare metal oxides via the hydrolysis of reactive metal precursors, usually alkoxides in an alcoholic solution, resulting in the corresponding hydroxide. Condensation of the hydroxide molecules by elimination of water leads to the formation of a network of metal hydroxide. When all hydroxide species are linked in one networklike structure, gelation is achieved and a dense porous gel is obtained. The gel is a polymer of a three-dimensional skeleton surrounding interconnected pores (see Figure 4.5). Removal of the solvents and appropriate drying of the gel results in an ultrafine powder of the metal hydroxide. Further heat treatment of the hydroxide leads to the corresponding ultrafine powder of the metal oxide. Since the process starts with a nanosized unit, and undergoes reactions on the nanometer scale, it results in nanometer materials. A flow chart of typical sol-gel processing of nanoscale metal oxides is shown in Figure 4.5.

In a recent study,[42] a sol-gel processing technique was developed to produce porous spheres of $\gamma$-Al$_2$O$_3$. The aluminum hydroxide sol was gelated by using a chemical dehydrating agent, 2-ethylhexanol, along with the surfactant SPAN-80. To obtain the gelated material in spherical form, the process was carried out in a glass column as shown in Figure 4.6. The sol was injected by nozzle, which permits the formation of near-perfect spherical droplets. The flow rate in the injection system was optimized to control the diameter of the spheres. The column allowed the sol droplets to proceed downward against an upward stream of the dehydrating agent. The flow rate of the dehydrating agent allowed sufficient time for the sol droplets to gelate. The gelated spheres were then dried and calcined at 400°C in air, leading to $\sim 0.5$ mm diameter porous $\gamma$-Al$_2$O$_3$ spheres composed of 4–5 nm crystallites.

Hydrolysis and drying are two key steps in determining the properties of the final product in sol-gel processing.

*Hydrolysis and Condensation of Metal Alkoxides*   Hydrolysis of metal alkoxides $(M(OR)_z)$ involve nucleophilic reactions with water as follows:

$$M(OR)_z + xH_2O \rightleftharpoons M(OR)_{z-x}(OH) + xROH$$
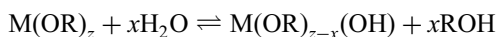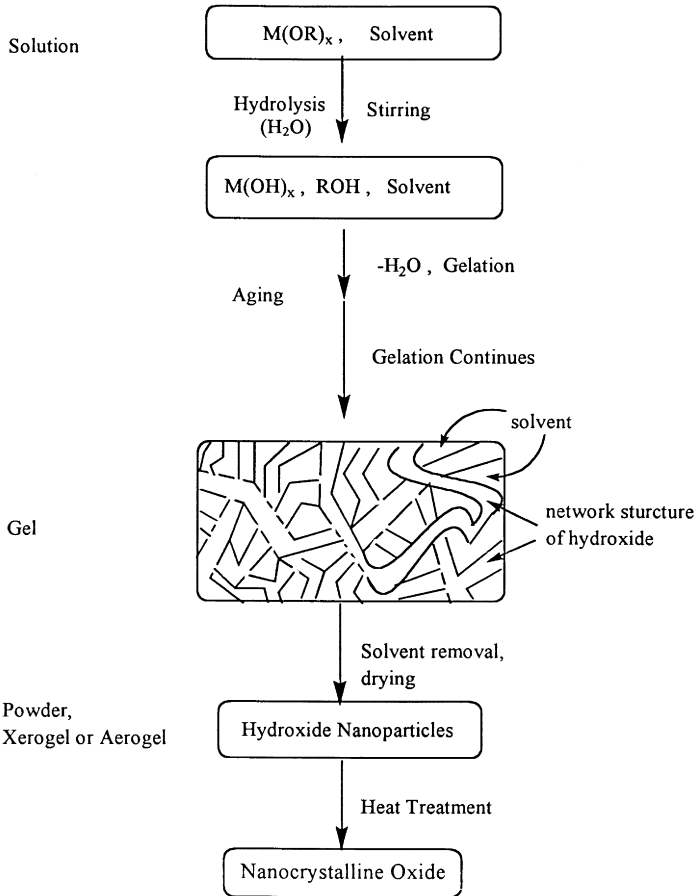
**FIGURE 4.5**   A flow chart of a typical sol-gel process for preparing nanoscale metal oxide powders.

The mechanism of this reaction involves the addition of a negatively charged $HO^{\delta-}$ group to the positively charged metal center ($M^{\delta+}$). The positively charged proton is then transferred to an alkoxy group followed by the removal of ROH:

$$\begin{array}{ccccc} H & & {}^+H & & H \\ \diagdown & & \diagdown & & \diagdown \\ O^{\delta-} + M^{\delta+}-O^{\delta=}-R & \rightleftharpoons & O-M-O^{\delta=}-R & \rightleftharpoons & HO-M-O^+ \\ \diagup & & \diagup & & \diagdown \\ H & & H & & R \end{array}$$

$$\rightleftharpoons \quad HO-M + ROH$$
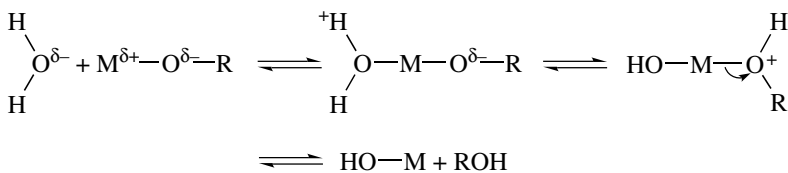
Condensation occurs when the hydroxide molecules bind together as they release water molecules and a gel/network of the hydroxide is obtained as shown in the following scheme:

$$\begin{array}{c}\diagdown \\ \diagup\end{array}\!\!M{-}OH + HO{-}M\begin{array}{c}\diagup \\ \diagdown\end{array} \rightleftharpoons \begin{array}{c}\diagdown \\ \diagup\end{array}\!\!M{-}O{-}M\begin{array}{c}\diagup \\ \diagdown\end{array} + H_2O$$

The rate of hydrolysis and condensation are important parameters that affect the properties of the final product. Slower and more controlled hydrolysis typically leads to smaller particle sizes and more unique properties. Hydrolysis and condensation rates depend on the following factors:

- The electronegativity of the metal atom and its ability to increase its coordination number: This factor is supported by the mechanism shown above. The hydrolysis rate of $Ti(OEt)_4$, as an example, is about five orders of magnitude greater than that of $Si(OEt)_4$. Consequently, the gelation times of silicon alkoxides are much longer (on the order of days) than those of titanium alkoxides (few seconds or minutes).[43]
- Steric hindrance of the alkoxy groups: The sensitivity of metal alkoxides toward hydrolysis decreases as the OR group size increases. Smaller OR groups lead to higher reactivity of the corresponding alkoxide toward water
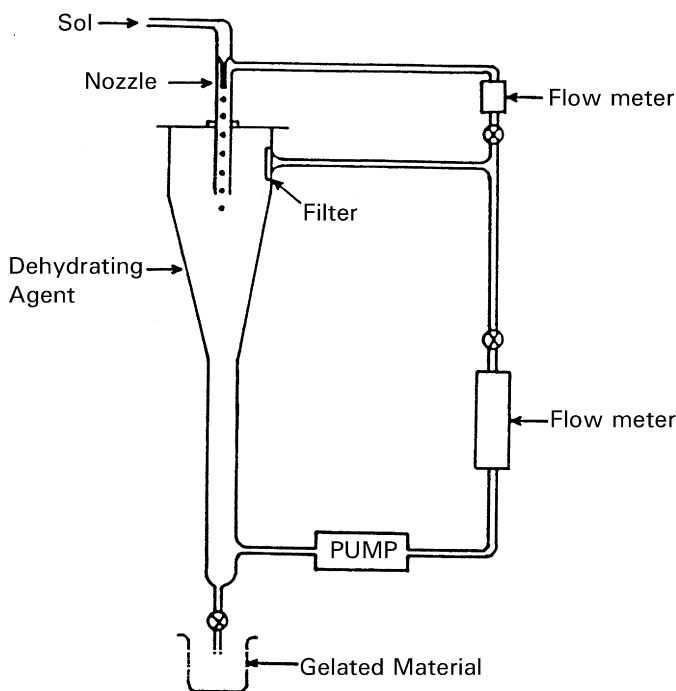


**FIGURE 4.6** Glass column used in the sol-gel process to obtain spherical gelated materials. Reprinted from *Nanostruct. Mater.*, **11**(3), VR Palkar, p. 370, ©1999, with permission from Elsevier Science.[42]

**TABLE 4.1 Gelation time of different silicon alkoxides**[43]

| Alkoxide | Gelation time (h) |
|----------|-------------------|
| $Si(OMe)_4$ | 44 |
| $Si(OEt)_4$ | 242 |
| $Si(OBu)_4$ | 550 |

and in some cases result in uncontrolled precipitation of the hydroxide. Table 4.1 shows the gelation time of different silicon alkoxides. This makes the choice of solvents in sol-gel processes important because alcohol interchange reactions are possible. As an example, when silica gel was prepared from $Si(OMe)_4$ and heated to 600°C, the surface area was 300 m$^2$ g$^{-1}$ with mean pore diameter of 29 Å if EtOH was used as a solvent. However, the surface area dropped to 170 m$^2$ g$^{-1}$ and the mean pore diameter increased to 36 Å if MeOH was used.

- Molecular structure of the metal alkoxides: The higher the coordination number around the metal center in the alkoxide, the slower the hydrolysis. Consequently, alkoxides that tend to form oligomers usually show slower rates of hydrolysis, and hence, are easier to control and handle. $n$-Butoxide (O-Bu$^n$) is currently preferred as a precursor to different oxides, including $TiO_2$ and $Al_2O_3$, because it is the largest alkoxy group that does not prevent oligomerization.[44]

Most metal alkoxides are highly reactive toward water, and they require careful handling in dry atmospheres to avoid rapid hydrolysis and uncontrolled precipitation. For alkoxides that have low rates of hydrolysis, acid or base catalysts can be used to enhance the process. Acids protonate the relatively negative alkoxides, creating a better leaving group and eliminating the need for proton transfer in the transition state. Bases provide better nucleophiles (OH$^-$) for hydrolysis. On the other hand, deprotonation of metal hydroxide groups enhances their condensation rates.

*Solvent Removal and Drying* When drying is achieved by evaporation under normal conditions, the gel network shrinks as a result of capillary pressure, and the hydroxide product obtained is referred to as xerogel. However, if supercritical drying is applied using a high-pressure autoclave reactor at temperatures higher than the critical temperatures of solvents, less shrinkage of the gel network occurs as there is no capillary pressure and no liquid–vapor interface, which better protects the porous structure. The hydroxide product obtained is referred to as an aerogel. Aerogel powders usually exhibit higher porosities and larger surface areas than analogous xerogel powders. Aerogel processing has been very useful in producing highly divided powders of various metal oxides.[15]

Sol-gel processes have been useful for preparing only metal oxides as a result of the presence of metal–oxygen bonds in the corresponding alkoxide precursor, and the derived gels are essentially metal hydroxides or oxides. However, some studies have shown that sol-gel processing can be used to prepare nonoxide powders from organometallic precursors other than alkoxides[49,50] Monodispersed spherical $\beta$-SiC have been prepared using a methanol solution of phenyltriethoxysilane ($C_6H_5Si(OC_2H_5)_3$) and tetraethyl orthosilicate ($Si(OC_2H_5)_4$).[49] Heat treatment of the gel product at 1500°C in argon atmosphere resulted in 0.6 µm spherical agglomerates that consisted of primary particles of 40 nm in diameter.

Sol-gel processes have several advantages over other techniques for synthesizing nanopowders of metal oxide ceramics. These include the production of ultrafine porous powders and the homogeneity of the product as a result of homogeneous mixing of the starting materials on the molecular level. Also, sol-gel processing holds strong promise for employment industrially on large scales. Successful efforts have recently resulted in scaling up the production of several metal oxide nano-particles.[80]

### 4.2.2.2 *Reverse Microemulsions/Micelles Method* 

The reverse micelle approach is one of the recent promising routes to nanocrystalline materials. Several recent studies have shown that this approach is a potential candidate to synthesize nanocrystalline ceramic powders with well defined and controlled properties.[81–88]

Surfactants dissolved in organic solvents form spheroidal aggregates called reverse micelles. In the presence of water, the polar head groups of the surfactant molecules organize themselves around small water pools ($\sim 100$ Å), leading to dispersion of the aqueous phase in the continuous oil phase as shown in Figure 4.7.[89–91]

Reverse micelles are used to prepare nanoparticles by using a water solution of reactive precursors that can be converted to insoluble nanoparticles. Nanoparticle synthesis inside the micelles can be achieved by various methods, including hydrolysis of reactive precursors, such as alkoxides, and precipitation reactions of metal salts.[82,83] Solvent removal and subsequent calcination lead to the final product. A variety of surfactants can be used in these processes, such as pentadeca-oxyethylene nonyl phenyl ether (TNP-35),[83] decaoxyethylene nonyl phenyl ether (TNT-10),[83] poly(oxyethylene)$_5$ nonyl phenol ether (NP5),[88] and many others that are commercially available. Several parameters, such as the concentration of the reactive precursor in the micelle and the mass percentage of the aqueous phase in the microemulsion, affect the properties, including particle size, particle size distribution, agglomerate size, and phases of the final ceramic powders. There are several advantages to using this method, including the preparation of very small particles and the ability to control the particle size. Disadvantages include low production yields and the need to use large amount of liquids.

### 4.2.2.3 *Low-Temperature Wet-Chemical Synthesis; Precipitation from Solutions* 

One of the conventional methods for preparing nanoparticles of metal oxide ceramics is the precipitation method.[92–94] This process involves dissolving a salt

**FIGURE 4.7**  Microstructure of monodisperse spherical $\beta$-SiC.[49]

precursor, usually a chloride, oxychloride, or nitrate; for example, $AlCl_3$ to make $Al_2O_3$, $Y(NO_3)_3$ to make $Y_2O_3$, and $ZrCl_4$ to make $ZrO_2$. The corresponding metal hydroxides usually form and precipitate in water on addition of a base solution such as sodium hydroxide or ammonium hydroxide solution. The resulting chloride salts—NaCl or $NH_4Cl$—are then washed away and the hydroxide is calcined after filtration and washing to obtain the final oxide powder. This method is useful in preparing ceramic composites of different oxides by coprecipitation of the corresponding hydroxides in the same solution. It has even been employed to prepare ceramic composites containing metal carbides. Nanocomposites of 5 wt% SiC–15 wt% $ZrO_2-Al_2O_3$ were prepared from aqueous suspensions of nano-SiC and aqueous solutions of zirconium oxychloride, aluminum chloride, and ammonia.[92]

Solution chemistry has also been used to prepare nonoxide ceramics or preceramic precursors that were converted to ceramics upon pyrolysis. Several ceramic nanoscale materials such as carbides, nitrides, and borides have been prepared by low-temperature nonaqueous phase reactions.[95] For example, $W_2C$ and $Mo_2C$ carbide were synthesized by the room temperature reduction of THF (tetrahydrofuran) suspensions of $WCl_4$ and $MoCl_4(THF)_2$ with $LiBEt_3H$.[95a] Particle sizes of 1–2 nm were obtained as micrometer-sized agglomerates. It was proposed that $LiBEt_3H$ and not the solvent was the source of carbon. This conclusion was based on two considerations: First, the decomposition of the solvent is more likely to lead to metal oxide formation; second, the reduction of the same precursors under the same reaction conditions using $LiBH_4$ as the reducing agent did not give the corresponding carbides. Using a similar procedure, $TiB_2$ ultra-fine powder was prepared from the precipitation reaction of $TiCl_4$ and $NaBH_4$.[95b]

Nanostructured AlN powder was also prepared via chemical synthesis as follows. Aluminum chloride hexahydrate and urea in equimolar ratio were dissolved in deoxygenated water. Ammonia was bubbled through the solution under vigorous stirring. Heating the reaction solution gradually (24 h) to 363 K resulted in a white gel that was aged at 393 K for 24 h. Removal of the solvent under vacuum, followed by pyrolysis of the gel precursor at 1373 K under a continuous flow of anhydrous ammonia, resulted in nanocrystalline powder (AlN) with an average crystallite size of ∼ 50 nm.[95c]

One disadvantage of this method is the difficulty in controlling the particle size and size distribution. Fast (uncontrolled) precipitation often takes place, resulting in large particles.

### 4.2.2.4 Chemical Synthesis of Preceramic Polymers Coupled with Physical Processing Techniques

This method involves the use of molecular precursors that facilitate the synthesis of nanomaterials containing phases of desired composition.[96–99] Using chemical reactions to prepare the preceramic polymer not only allows for control of phase compositions but also overcomes the limitation of low production yields of physical methods. This method has been very useful in preparing nonoxide ceramics such as silicon carbide and silicon nitride. The conversion of an organometallic precursor into a ceramic depends on different parameters such as the molecular structure of the precursor and the pyrolysis conditions (temperature, duration, atmosphere). Metal carbides and metal nitrides have been obtained by pyrolysis of polymers containing the appropriate metal such as silver or aluminum and carbon or nitrogen (preceramic polymers).[43] A considerable amount of free carbon from the thermolysis process is very often a problem. Silicon carbide (SiC) and silicon nitride ($Si_3N_4$) are the most-studied ceramic materials prepared via this route. They are usually synthesized by the pyrolysis of polycarbosilanes and polysilazanes, for which general formulas are shown below, at temperatures between 1000 and 1200°C.

$$\left[ \begin{array}{c} | \\ Si-CH_2 \\ | \end{array} \right]_n \qquad \left[ \begin{array}{c} | \\ Si-C\equiv C \\ | \end{array} \right]_n$$

Polycarbosilanes

$$\left[ \begin{array}{c} | \qquad | \\ Si-N \\ | \end{array} \right]_n$$
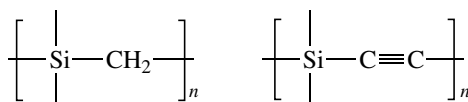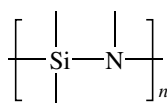
Polysilazanes

Nanoscale silicon nitride powders were prepared from the reaction of $SiCl_4$ and $NH_3$ in n-hexane.[96] The initial products of this reaction were $Si(NH)_2$ (silicon diimide) and $NH_4Cl$. The product mixture (precipitate) was heated at 360°C,

resulting in the sublimation of $NH_4Cl$ and polymerization of $Si(NH)_2$. Thermal pyrolysis of polymerized $Si(NH)_4$ led to ultrafine particles of $\alpha\text{-}Si_3N_4$. These reactions are summarized below:

$$SiCl_4(l) + 6NH_3(g) \xrightarrow[0°C]{n\text{-}C_6H_{14}} Si(NH)_2 + 4NH_4Cl$$

$$Si(NH)_2 \xrightarrow{polym.} [Si(NH)_2]_n \xrightarrow{heat} \alpha\text{-}Si_3N_4$$
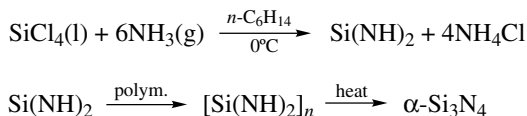
In another example, chemical synthesis was coupled with ultrasonic atomization and laser techniques to prepare nanoparticles of $Si_3N_4/SiC$ composite.[98] Liquid silazane monomeric precursor was prepared by the reaction of methyldichlorosilane $(CH_3SiHCl_2)$ with ammonia in diethyl ether at 0°C.[99] The product was mainly cyclic $[CH_3SiHNH]_x$, with $x = 3$ or 4, as well as some linear structures with the component of $x = 4$ being the major one. This liquid monomeric precursor was converted into intermediate polymeric preceramic containing $Si-C-N$ nanoparticles. This was achieved by laser-induced polycondensation and crosslinking reactions using ultrasonic injection of the liquid precursor into the beam of a high-power industrial $CO_2$ laser. When the amorphous pre-ceramic powder was annealed at 1100°C in ammonia, it resulted in nanocrystalline (40–60 nm) powder of $Si_3N_4/SiC$. A schematic of the apparatus is shown in Figure 4.8.

Other techniques that have been employed to prepare nonoxide ceramics include laser-induced gas-phase reactions[100] and plasma chemical methods. A radio-frequency (RF) plasma,[101] a direct current (DC) arc jet,[102] and a hybrid plasma (superposition of RF plasma and a DC arc jet[103] have been used to prepare several ceramic ultrafine powders, especially silicon nitride, silicon carbide, and their composites. For preparing nanoparticles of SiC or $Si_3N_4$, the reactants are usually $SiH_4$ and $C_2H_4$ or $NH_3$. For composites of both materials, $C_2H_4$ and $NH_3$ have been used with $SiH_4$. $SiCl_4$ vapor can also be used instead of $SiH_4$.[101–103]

**4.2.2.5  *Mechanochemical Synthesis***  Mechanochemical synthesis involves mechanical activation of solid state displacement reactions. This process has been used successfully to make nanoparticles of a number of materials, including ceramics such as $Al_2O_3$ and $ZrO_2$.[104–109] It involves the milling of precursor powders (usually a salt and a metal oxide) to form a nanoscale composite structure of the
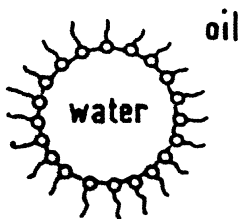


**FIGURE 4.8**    Schematic representation of an inverse micelle.

starting materials that react during milling and subsequent heating, if necessary, to form a mixture of dispersed nanocrystals of the desired oxide within a soluble salt matrix. Nanoparticles of $Al_2O_3$, for example, were prepared by milling $AlCl_3$ with CaO powders. A nanocomposite mixture of CaO particles embedded within an amorphous $AlCl_3$ matrix was obtained. Subsequent heating at 300°C led to nano-particles of $\gamma$-$Al_2O_3$ within a $CaCl_2$ matrix as a result of the following reaction:

$$2AlCl_3 + 3CaO \rightarrow \gamma\text{-}Al_2O_3 + 3CaCl_2$$
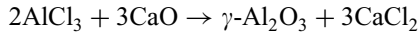
Pure $\gamma$-$Al_2O_3$ particles (particle sizes of 10–20 nm) were isolated after removal of $CaCl_2$ by-product.[106] In another example, $ZrO_2$ was synthesized as an ultrafine powder by milling and subsequent heat treatment of $ZrCl_4$ and CaO powders. Nanoparticles of $ZrO_2$ formed in a $CaCl_2$ matrix according to the following reaction:

$$ZrCl_4 + 2CaO \rightarrow ZrO_2 + 2CaCl_2$$
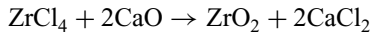
The by-product, $CaCl_2$, was removed by simple washing, resulting in pure particles of $ZrO_2$ of $\sim$5 nm in size.[105]

## 4.3   BONDING

### 4.3.1   General

Metal oxides crystallize in a variety of structures, and bonding in these materials can range from ionic (MgO, $Fe_{1-x}O$) to metallic (TiO, $ReO_3$).[110] The structures of many oxides have been obtained through use of new crystallography techniques for single crystals and for powders by employing methods of X-ray, electron, and neutron diffraction.

An understanding of not only the crystal structure and bonding but also the local structure or microstructures that are due to defects is necessary for understanding the structure of complex transition metal oxides. Of course, on the nanoparticulate scale the number of defects due to edges, corners, f-centers, and other surface imper-fections is greatly enhanced by the large surface area.

Five types of crystals can be defined based on bonding considerations: covalent, ionic, metallic, molecular (van der Waals), and hydrogen-bonded. Ionic crystals are formed when highly electronegative and highly electropositive elements are combined in a lattice. The ionic model is a poor approximation for crystals containing large anions and small cations (e.g., oxides and sulfides) where the covalent contribution to bonding becomes significant.[110] Van der Waals interactions play a crucial role in many transition metal oxides, especially those with layered structures. In many oxide hydrates or hydroxy oxides, hydrogen bonding also contributes to the cohesive energy. In most transition metal oxides the bonding is only partly ionic; in other words, there is a considerable overlap between the orbitals

of the cations and anions. However, there are several examples that are mainly ionic, such as MgO and CaO. Many transition metal oxides also exhibit metallic properties.

Inorganic compounds of the formula AB can have the rock salt (B1), CsCl (B2), zincblende (B3), wurzite (B4), or NiAs (B8) structure.[111] Alkaline earth metal oxides such as MgO and monoxides of $3d$ transition metals as well as lanthanides and actinides such as TiO, NiO, EuO, and NpO exhibit the rock salt structure with the 6:6 octahedral coordination.

## 4.3.2   Defects

Because of the number of atoms at the surface and the limited number of atoms within the lattice, the chemistry and bonding of ceramic nanoparticles is greatly affected by the defect sites present. Point defects in crystals, such as vacancies and interstitials described by Schottky and Frenkel, account for the transport properties of ionic solids.[111] However, it appears that the point defect model is valid only when the defect concentration (or the deviation from stoichiometry) is extremely small. The defects that occur in the ionic solids are called point, linear, planar, and volumetric defects. Point defects are due to the absence of one of the constituent atoms (or ions) on the lattice sites or their presence in interstitial positions. Foreign atoms or ions present in the lattice represent another type of point defect. Point defects cause displacements on neighboring atoms or ions because of polarization in the surrounding region. A cationic vacancy in an ionic solid will have an electronegative charge, causing displacements of neighboring anions.[110] The energy of formation of a point defect depends mainly on the atomic arrangement in the immediate neighborhood of the corresponding rows of atoms that do not possess the right coordination. Boundaries between small crystallites (grain boundaries), stacking faults, crystallographic shear planes, twin boundaries, and antiphase boundaries are planar defects. Three-dimensional volumetric defects are a result of segregating point defects.

The common point defects in ionic solids are Schottky pairs (pairs of cation and anion vacancies) and Frenkel defects (cation or anion interstitial plus a vacancy).[111] When there is a large concentration of Schottky pairs, the measured pyknometric density of the solid is considerably lower than the density calculated from the X-ray unit cell dimensions (e.g., VO).[110] Creation of defects is generally an endothermic process. Thus, the formation energies of vacancies in ionic solids are generally 2 eV or more. The intrinsic defect concentration in these solids is therefore extremely low even at high temperatures. The intrinsic defect concentration in binary solids around $0.8T_m$ is $\sim 10^{-5}$.[110]

The surface of a crystal constitutes a planar, two-dimensional defect. The environment of atoms or ions on the surface of a crystal is considerably different from that in the bulk. In polycrystalline materials there are grain boundaries between the particles. The interface between two solid phases is an important factor in determining the course of reactions, crystal growth, and so on. An interface may be coherent, incoherent, or semicoherent. It is coherent when the interface matches

perfectly between the contact planes of two solid planes. Epitaxial growth occurs when there is considerable mismatch (semicoherent interface).

One often encounters stacking faults in close-packed solids. For example in a solid with cubic close packing, ABC ABC ABC, there can be a fault such as ABC AB ABC. Other types of planar defects include tilt boundary (array of period space or edge dislocations), twist boundary (array of screw dislocations), twin boundary (a layer with mirror plane symmetry with respect to the rotation of one part of the crystal, on a specific plane, with respect to another), and antiphase boundary (across which the sublattice occupation becomes interchanged).

The radius of the oxide anion (1.44 Å) given by Shannon and Prewitt is larger than that for most cations.[112] However, the ionic radii correspond to free ions not to ions in crystals. The anions in crystals are subjected to a positive Madelung potential, which gives rise to a contraction of the charge cloud, while cations are subjected to negative potential, causing an opposite effect.[110]

Phase purity is generally hard to achieve, especially for phases containing more than one cation.[110] Often phase segregation occurs, so that the particles are a mixture of other possible phases derivable from the precursors.

### 4.3.3 Metal Oxides

One of the most intensively studied nanoparticulate systems is that of the metal oxides, in particular MgO and CaO. Two types of nanocrystalline oxides have been prepared and thoroughly studied; a "conventional preparation" (CP), and an "aerogel preparation" (AP).[1,14–16]. Nanocrystalline MgO was prepared by a modified aerogel procedure, yielding a fine, white powder of 400–500 $m^2$ $g^{-1}$ and 4 nm average crystallite size. High-resolution TEM imaging of a single crystallite indicated a polyhedral structure, suggesting the presence of high surface concentrations of edge/corner sites, and various exposed crystal planes (such as 002, 001, 111).[113]

If intrinsic surface chemistry differences due to size are to be uncovered, consider that in bulk MgO the effective ionic charges are close to +2, whereas the MgO molecule is much more covalent with effective charges close to +1.[1] Lower-coordination surface ions such as $Mg_{3c}^{2+}$, $Mg_{4c}^{2+}$, $O_{3c}^{2-}$, and $O_{4c}^{2-}$ are expected to have effective charges between +1 and +2. Surface sites on crystalline and powdered MgO have been probed by theoretical as well as experimental efforts. *Ab initio* calculations with $H_2$ have been used to probe perfect crystal surfaces and various defect sites. On the perfect (100) MgO surface, $H_2$ has a small adsorption energy and does not dissociate. However, temperature-programmed desorption methods have shown that polycrystalline samples do dissociate $H_2$, probably on $O_{3c}$–$Mg_{3c}$ sites. These sites are apparently very active for heterolytic $H_2$ dissociation. The microfaceted (111) surface of MgO is particularly reactive, and steps, kinks, and point defects (ion vacancies and substitutions) are also important. Indeed, the unique catalytic properties of defective MgO surfaces also depend on a plethora of unusual coordination sites.

Electron microscopy at low magnification shows the presence of porous weblike aggregates in the size region of about 1400 nm (Figure 4.9a) that exist in the as-prepared powder.[113] These are formed by interaction of the 4 nm (average) crystallites, and their overall size distribution is surprisingly narrow (Figure 4.9b).

Further investigation of the as-prepared powder samples by high-resolution TEM revealed why these porous networks form on the nanoscale.[113] Figure 4.10 shows a micrograph at essentially atomic resolution, revealing the lattice planes for Mg and O ions. Note the "cubelike" crystallites that aggregate into polyhedral structures with numerous corner/edge sites, and the embryonic formation of pores between those crystalline structures. Plates of the crystalline lattice show a lattice spacing of 2.1 Å corresponding to the (002) plains of MgO. Cubic nanocrystals are shifted along the (001) coalescence faces. This results in the appearance of many steps of
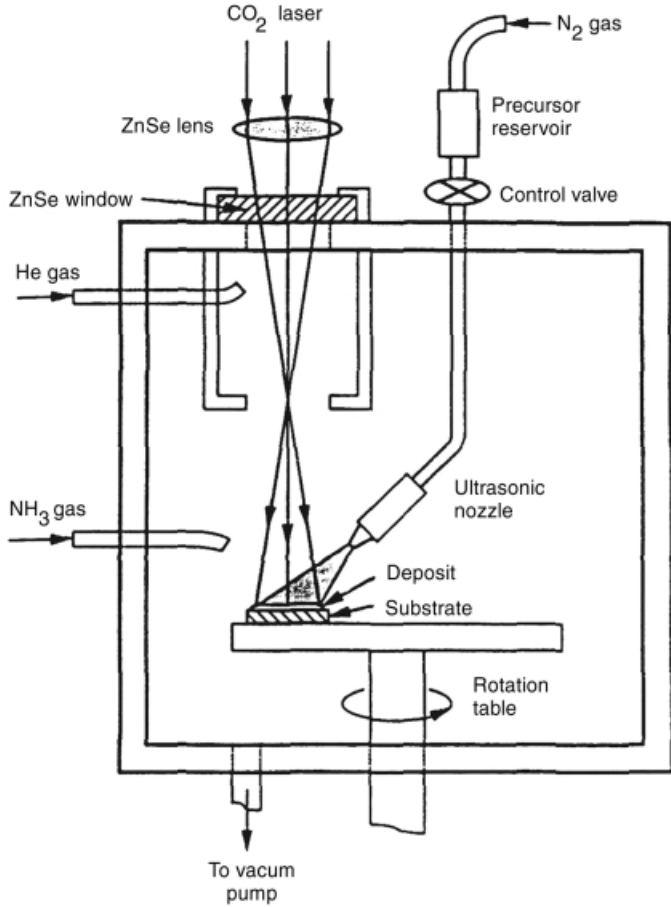


**FIGURE 4.9** Schematic diagram of laser processing chamber. Reprinted with permission from KE Gonsalves, PR Strutt, TD Xio, PG Klemens, *J. Mater Sci*, **1992**, *27*, 323, Kluwer.[98]

(a)

(b)

size (micrometers)
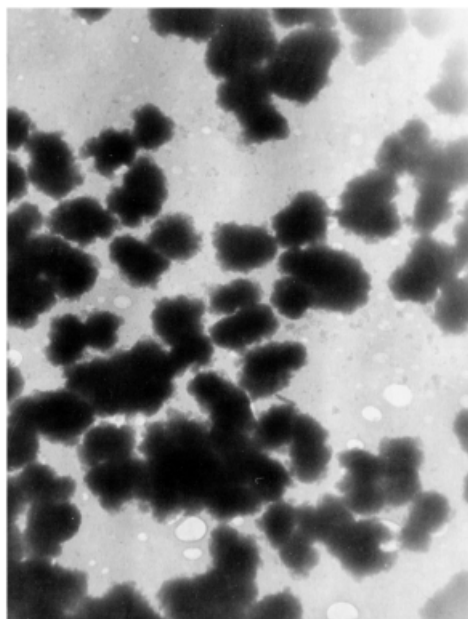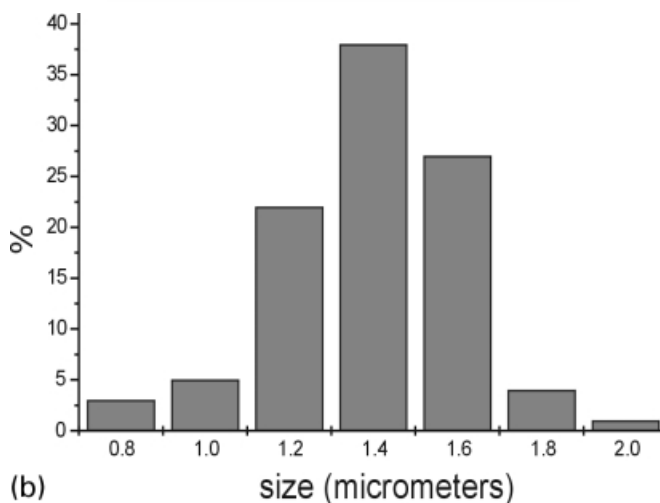
**FIGURE 4.10** (a) TEM image of AP-MgO porous aggregates that exist in the as-prepared powder. These are formed from interactions of 4 nm crystallites. (b) Bar graphs showing observed size distributions of weblike porous aggregates. Reprinted with permission from *J. Am. Chem. Soc.*, **2000**, *122*, 4921–4925. Copyright 2000 American Chemical Society.[113]

subatomic size on the surface of the "cubes" with the egress of the edges and corners of the cubic particles to the external surface. The particular size distribution histogram indicates 10–30 Å cubic crystals and, in this photograph, about 20 Å

average size [although powder X-ray diffraction (XRD) broadening indicates an average of 40 Å (4 nm)].

There have also been studies of the Lewis acid and base sites of metal oxide nanoparticles using a variety of techniques. Through the use of probe molecules, electron spin resonance (ESR) can be used to quantify the numbers of each type of site available for each sample.[114] For samples of AP MgO the number of Lewis base sites has been determined to be $5 \times 10^{18}$ sites per gram. Surprisingly, AP MgO was also found to adsorb TEMPON (2,2,6,6-tetramethyl-piperidine-1-oxyl). From this it is concluded that the surface of the oxide has Lewis acid sites that possess sufficiently high adsorption heats for TEMPON for the room temperature equilibrium to be shifted to the right:

$$TEMPON + Lewis\ acid \rightarrow (Lewis\ acid\ TEMPON)$$
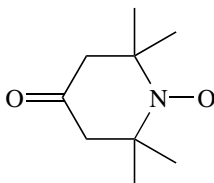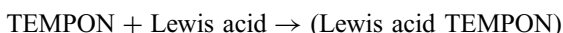


This is very interesting, since MgO is typically not associated with acid catalysis and it is believed that this is the first observation of this type of Lewis acid activity on MgO.



**FIGURE 4.11**   High-resolution TEM of AP-MgO. Note the cubelike nanocrystals that amalgamate into polyhedral structures with many corner/edges, and the embryonic pore structure. Reprinted with permission from *J. Am. Chem. Soc.*, **2000**, *122*, 4921–4925. Copyright 2000 American Chemical Society.[113]

### 4.3.4 SiC, SiN

Nanocrystalline SiC prepared in an inductively coupled plasma using $C_2H_4$ and $SiH_4$ as reactants formed particles with a mean crystallite size of 42 nm.[115] HRTEM images show {111} lattice planes with 0.25 nm spacing, as well as an amorphous surface layer that may be composed mainly of carbon. Samples of SiC prepared by plasma chemical vapor deposition were identified to be $\beta$-SiC with a particle size of 16 nm.[101] Upon sintering at 2200°C, graphite was crystallized and some $\alpha$-SiC transformed from $\beta$-SiC.

It has been shown that crystalline SiN exists in two forms, $\alpha$ and $\beta$, which are built from three-dimensional networks of $SiN_4$ tetraheda.[116] The strong covalent bonds and the rigid structure endow this material with extraordinary hardness, durability, and mechanical strength. The crystal structure of $\beta$-$Si_3N_4$, which is built from a $Si_6N_8$ unit cell, is shown in Figure 4.12. Channels with a pore diameter of about 0.15 nm play a certain role in the diffusion of atoms. Also shown in Figure 4.12 is the crystal structure of $\alpha$-$Si_3N_4$, which is built up from a $Si_{12}N_{16}$ unit cell. Diffusion is much more difficult in this structure because there are no channels. Recent data supports the concept that $\alpha$- and $\beta$-$Si_3N_4$ are polymorphic modifications. $\alpha$-$Si_3N_4$ is the low-temperature modification, as evidenced by the increasing $\alpha$ content as synthesis temperature decreases and the fact that the $\alpha-\beta$ conversion occurs only at temperatures exceeding 1650°C. It is believed that kinetics are the reason that a $\beta \rightarrow \alpha$ transition has not yet been observed. It has been reported that the presence of oxygen and carbon in surface layers of different $Si_3N_4$ nanoparticles is respectively 2–20 and $10^2-10^3$ times higher than the bulk.[117]

Thermal decomposition of silicon diimide, $Si(NH)_2$, in vacuum resulted in very high-purity, fine particle size amorphous $Si_3N_4$ powders.[118] Examination of XRD patterns demonstrated a gradual transition from an amorphous material to a crystalline $\alpha$-phase occurring at 1200°C. As the temperature was raised above 1450°C, the crystalline $\beta$-phase was observed.

### 4.3.5 TiO$_2$

Titania produced by controlled thermal decomposition of metal-organic precursors consisted of a mixture of anatase and rutile phases (approximately 30% rutile and
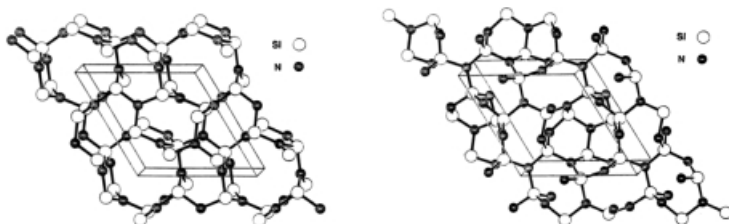


**FIGURE 4.12** Crystal structure of (a) $\beta$-$Si_3N_4$ and (b) $\alpha$-$Si_3N_4$. Used with permission from H. Lange, G. Wottig and G. Winter, *Angewandte Chemie*, International Edition England, *30*, 1579, **1991**, John Wiley and Sons.[116]

70% anatase).[119] HRTEM shows that the lattice planes extend up to the surface of the particle, clearly indicating that the particles are fully crystalline and do not have an amorphous coating on the surface. $TiO_2$ particles with two different average particle sizes were obtained in the experiments. The particles with the smaller average particle size were found to contain a higher volume fraction of the anatase phase. This demonstrates that the crystal structure is a function of particle size and that there is a threshold diameter at which the metastable phase is formed in nanoparticles. The authors were unfortunately unable to identify this threshold particle size. It should be noted that the anatase phase is preferred for applications in gas sensors and catalysis, while the rutile phase has a higher ultraviolet scattering effect. It was found that above 800°C the anatase phase transforms completely to rutile. This, however, is not the desired method for obtaining rutile phase because it leads to the formation of incipient necks between the particles. It is known that the activation energy for the transformation from anatase to rutile is on the order of $40\,kJ\,mol^{-1}$, so rutile is more stable than anatase.[120] The crystal pattern for rutile has much closer atomic packing and the transformation from anatase to rutile involves a volume contraction and a cooperative movement of titanium and oxygen ions, which increases with increasing temperature. It was also found that analogous experiments with silica and alumina produced $SiO_2$ with an amorphous structure and $Al_2O_3$ in the $\gamma$-phase. Subsequent annealing of the nanoparticulate $Al_2O_3$ powder transformed the $\gamma$-phase to the $\alpha$-phase.

The effects of doping on the characteristics of titania particles made by oxidation of $TiCl_4$ in diffusion flames have also been investigated.[120] It was found that introduction of $Si^{4+}$ inhibited the anatase to rutile transformation as well as decreasing the primary particle size. The addition of $Al^{3+}$ had the opposite effect, presumably because $Si^{4+}$ entered the lattice interstitially while $Al^{3+}$ entered substitutionally into the titania lattice.

### 4.3.6 Others

Lead zirconate–titanate (PZT), a solution of ferroelectric $PbTiO_3$ ($T_c = 490°C$) and antiferroelectric $PbZrO_3$ ($T_c = 230°C$), belongs to the ferroelectric family of perovskite structure with a general formula $ABO_3$ (where A = mono- or divalent, and B = tri- to hexavalent ions).[121]. Nanoscale PZT particles (25 nm) were synthesized using an *in situ* method. Powder XRD studies of these particles found the sample to be X-ray amorphous and single-phase PZT was produced after heating at 500°C.

Nanophase powders of $Y_x Zr_{1-x} O_{2-x/2}$ have been prepared from a mixture of commercially available $ZrO_2$ and $Y_2O_3$ powders.[122] It was found that, depending on the starting powder mixture composition, the yttrium content in the nanophases can be controlled and the tetragonal or cubic phases can be obtained. Tetragonal or a mixture of tetragonal and cubic were observed for low yttria content (3.5 mol% yttria), and cubic for higher yttria contents (19, 54, and 76 mol% yttria). These powders were found to have a most probable grain radius of about 10–12 nm and the grains appeared as isolated unstrained single crystals with polyhedral shapes. The

grain shapes appeared to be polyhedral and not too anisotropic. Lattice fringes were parallel to the surfaces, showing that (100) and (111) faces dominate.

## 4.4 SELECTED PROPERTIES

The properties of nanoparticles are usually size-dependent. When prepared in nanometer-sized particles, materials exhibit unique chemical and physical properties that are remarkably different from those of the corresponding bulk materials. The study of physical and chemical properties of nanoparticles is of great interest as a way to explore the gradual transition from atomic or molecular to condensed matter systems.

As the size of a particle decreases, the percentage of atoms residing on the surface increases. As an example, a study on different samples of MgO nanoparticles has revealed that for particles ∼4 nm in diameter about 30% of the atoms are surface atoms.[15] Of course, surface atoms/ions are expected to be more reactive than their bulk counterparts as a result of coordinative unsaturation. Because of this and the fact that the surface-to-volume ratio is large, it is not unusual to see unique behavior and characteristics for nanoparticles. This particle size effect is a characteristic of different nanomaterials, including insulating metal oxides and other ceramic materials.

In this section we will briefly discuss some selected properties of nanophase ceramics that have shown significant size dependence.

### 4.4.1 Chemical Properties

***4.4.1.1 Acid–Base Behavior of Insulating Metal Oxide Surfaces*** Generally, insulating oxides are hard acids or bases, so they catalyze acid–base chemistry. Several insulating oxides and oxide composites have been found to be potential catalysts for a variety of important reactions as a result of their surface basicity or acidity.[123–127] Some selected reactions commonly carried out on insulating oxides are shown in Table 4.2.

**TABLE 4.2 Examples of reactions commonly carried out on insulating metal oxides (solid acids and bases)**

| Reaction Type | Example |
| --- | --- |
| Dehydration of alcohols | Butanol → butene |
| Cracking | $[(CH_3)_2CH(C_6H_5)]$ → benzene + propylene |
| Isomerization of olefins | 1-Butene → 2-butene |
| Isomerization of parrafins | $n$-Octane → isooctane |
| Alkylation | $CH_3(C_6H_5) + CH_3OH \rightarrow CH_3CH_2(C_6H_5) + H_2O$ |
| Esterification | Acetic acid + butanol → butylacetate |

Acidity and basicity behavior vary from one metal oxide to another. Several metal oxides exhibit surface basic behavior, such as MgO, CaO, and SrO, while others are considered to be acidic solids that possess more and stronger acidic sites on their surfaces, such as $Al_2O_3$. Acid–base behavior and the presence of several types of deficiencies in the lattice and on the surface are two major driving forces for surface reactivity of metal oxides. On the other hand, when metal oxides are prepared in nanostructures, the percentage of coordinatively unsaturated ions, especially on edges and corners, increases significantly. Consequently, surface chemistry effects, which are barely noticeable in large particle systems, become overwhelming in nanoparticle systems. These effects are demonstrated by enhanced surface reactivities and catalytic potentials possessed by many nanoparticle systems of metal oxides.[128–132]

***4.4.1.2    Unusual Adsorptive Properties***    One of the great promises that nanoparticles of metal oxides hold in chemical applications is their remarkable ability to chemically adsorb a wide variety of molecules, especially organic molecules that are of concern as environmental hazards. Compared to their conventionally prepared and commercial counterparts, nanoparticles of several metal oxides exhibit a significantly enhanced ability to chemically adsorb and dissociate a variety of organic molecules on their surfaces.

Several oxides have shown promise in this field, including MgO, CaO, $Al_2O_3$, $SiO_2$, and ZnO. A wide range of molecules, including chlorinated hydrocarbons, phosphorus compounds, alcohols, aldehydes, ketones, and amines, have been found to strongly adsorb and chemically decompose on the surfaces of these oxides.[133–141] Details and examples on this subject are discussed in Chapter 7.

## 4.4.2    Physical/Mechanical Properties

Many physical properties of nanophase ceramics are also size-dependent. Most of the physical properties are dominated by those of the surface, which differ from the bulk due to the different bonding geometry. Several systems of nanophase ceramics have exhibited quite interesting and potentially useful mechanical properties, which creates the necessity for much more work on exploring their physical properties.

***4.4.2.1    Improved Sintering and Hardness Properties***    Ceramics produced from nanophase powders have shown unique consolidation and compaction properties. A ceramic is processed from nanophase powders by first compacting a powder composed of individual ceramic particles (usually less than 50 nm in size) into a raw shape (often called a green body). This compacted powder is then heated at elevated temperatures. Densification occurs as a result of diffusion of vacancies out of pores (to grain boundaries), which leads to shrinkage of the sample. This process is referred to as pressureless sintering. Fortunately, nanophase powders were found to compact as easily as their analogous submicrometer particles. To avoid particle size growth, samples have to be sintered at the lowest possible temperature for a time sufficient to remove the residual porosity and establish coherent grain boundaries.

Successful sintering enhances the hardness of materials. If hardness decreases with sintering, then only grain growth is occurring.[142]

Experimental evidence shows that nanophase powders densify at faster rates than do commercial (submicrometer) particles. Slow densification of commercial samples is a result of their larger grain and pore sizes. It has also been found that faster densification rates allow a given density to be achieved at smaller grain sizes before serious growth takes place. As a result of their small particle and pore sizes, nanocrystalline powders sinter to much greater densities than their conventional analogues at the same temperature. This also establishes that nanocrystalline powders, as compared to conventional powders, reach the same density at much lower temperatures. This, of course, eliminates the need for very high temperatures. This has been well established experimentally, as shown in Figure 4.13 as an example.[141–145]

One disadvantage that can accompany fast densification, though, is inhomogeneous heating, when the outside layers of the particles densifies into a hard impervious shell that constrains the inside of the sample from normal shrinking leading to some cracking as a result of strain incompatibility. This problem can be avoided in several ways. The most efficient is to heat the samples slowly to reduce the shrinkage in the outer shell while heat is transported to the inner regions.[146]
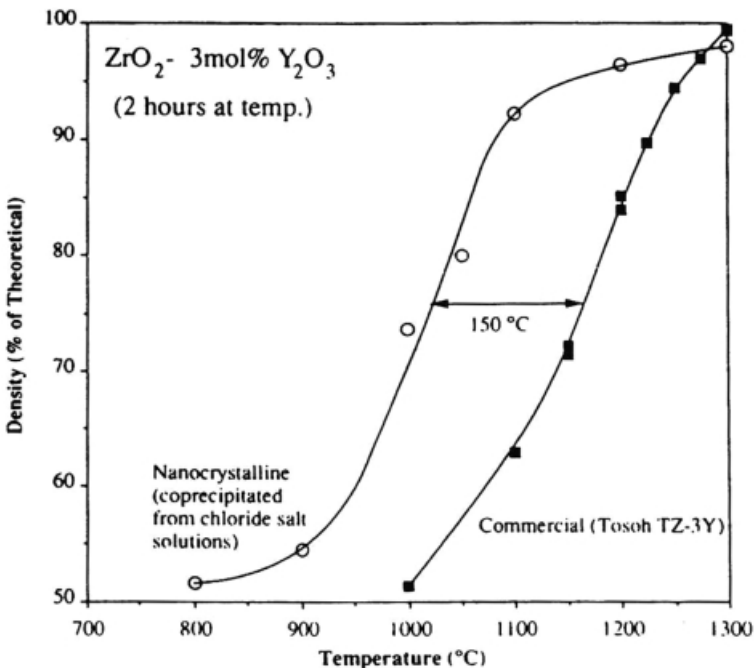


**FIGURE 4.13**   Comparison of the densification behavior of nanocrystalline (15 nm) and commercial (0.17 μm) $ZrO_2 - 3 \, mol\% \, Y_2O_3$ as a function of temperature.[142] Reprinted with permission from A S Edelstein and R C Cammarato (eds), *Nanoparticles: Synthesis, Properties and Applications*, IOP Publishing, Philadelphia, (1996).

Alternatively, high-density nanostructured ceramic systems including $Y_2O_3$, $TiO_2$ and $ZrO_2$ have been achieved by means of pressure-assisted sintering. Applying some pressure during sintering can increase the densification rate and suppress the particle growth.[147,148]

Nanoscale powders of nonoxide ceramics such as metal carbides and nitrides have shown similar behavior. Conventional SiC, as an example, is difficult to sinter. Addition of some additives such as boron or carbon, is often necessary for densification of SiC. Ultrafine powder of SiC was found to sinter at lower temperatures and to densify without additives.[101]

#### 4.4.2.2 Reduced Brittleness and Enhanced Ductility and Superplasticity

Superplasticity and ductility refer to the capability of some polycrystalline materials to undergo extensive tensile deformation without necking or fracture. Theoretical and experimental results provide evidence for the possibility that traditional brittle materials can be ductilized by reducing their grain sizes. When made from nanocrystals, brittle ceramics can be superplastically deformed at modest temperatures and then heat-treated at higher temperatures for high-temperature strengthening. The great interest in this property stems from the fact that brittle fracture is a technical barrier in the use of ceramics in load-bearing applications. This interest in superplasticity of ceramic materials has been growing since it was experimentally demonstrated in 1986 that yttria-stabilized tetragonal zirconia polycrystals could be elongated over 100% in tension.[148–150] Similar behavior was later demonstrated for other nanophase ceramic systems involving $Al_2O_3$, $TiO_2$, and ZnO.[151–159]

All of these studies have established the capability to synthesize superplastic ceramic materials. They have shown that nanocrystalline ceramics deform at faster rates, lower stresses, and lower temperatures.

One important use of superplasticity in ceramics is diffusion bonding, in which two ceramic parts are pressed together at moderate temperatures and pressures to form a seamless bond through diffusion and grain growth across the interface. Diffusion bonds form more easily in nanocrystalline ceramics than in larger-grained ceramics as a result of both the enhanced plastic flow of nanocrystalline ceramics and the larger number of grain boundaries they provide for diffusional flux across the interface.[160,161]

Other properties of ceramics that are size-dependent include electrical and optical properties. An increase in the electrical resistance and dielectric constant has been observed for nanophase ceramic materials as a result of their small particle sizes.[121,162] An effect on optical properties of ceramic materials has also been found due to their nanometer particle sizes. As an example, nanoparticles of $TiO_2$ were found to become more efficient UV absorbers.[163] In conclusion, nanophase ceramic powders and metal oxides hold great promise for better materials with unique and desirable properties and for potential applications as compared to their large-grained counterparts.

# REFERENCES

1. K. J. Klabunde, J. V. Stark, O. Koper, C. Mohs, D. G. Park, S. Decker, Y. Jiang, I. Lagadic, D. Zhang, *J. Phys. Chem.*, **1996**, *100*, 12142–12153.

2. K. J. Klabunde, C. Mohs, in *Chemistry of Advanced Materials*, L. V. Interrante, M. J. Hampden-Smith (editors), Wiley-VCH, New York, **1998**, Chap. 7, p. 317.

3. H. Liu, L. Feng, X. Zhang, O. Xue, *J. Phys. Chem.*, **1995**, *99*, 332.

4. K. Tanabe, *Solid Acids and Bases*, Academic Press, San Diego, CA, **1970**.

5. M. Utiyama, H. Hattori, K. Tanabe, *J. Catal.*, **1978**, *53*, 237.

6. R. M. Morris, K. J. Klabunde, *Inorg. Chem.*, **1983**, *22*, 682.

7. D. J. Driscoll, W. Martin, J. X. Wang, J. H. Lunsford, *J. Am. Chem. Soc.*, **1985**, 107.

8. M. F. Hoq, K. J. Klabunde, *J. Am. Chem. Soc.,* **1986**, *108*, 2114.

9. (a) R. M. Morris, K. J. Klabunde, *J. Am. Chem. Soc.*, **1983**, *105*, 2633.
   (b) M. A. Nygren, L. G. M. Pettersson, Z. Barandiaran, L. Siejo, *J. Phys. Chem.*, **1994**, *100*, 2010.
   (c) T. Tashiro, J. Ito, R. B. Sim, K. Miyazawa, E. Hamada, K. Toi, H. Kobayashi, T. Ito, *J. Phys. Chem.*, **1995**, *99*, 6115.

10. H. Tsuji, T. Shishido, A. Okamura, Y. Gao, H. Hattori, H. Kita, *J. Chem. Soc., Faraday Trans.*, **1994**, 803.

11. Y. X. Li, K. J. Klabunde, *Chem. Mater.*, **1992**, *4*, 611.

12. J. Karch, R. Birringer, H. Gleiter, *Nature*, **1987**, *330*, 556.

13. R. W. Siegel, S. Ramasamy, H. Hahn, L. Zonqquan, L. Timg, R. Grosky, *J. Mater. Res.*, **1988**, *3*, 1367.

14. S. Utampanya, K. J. Klabunde, J. R. Schlup, *Chem. Mater.*, **1991**, *3*, 175.

15. H. Itoh, S. Utampanya, J. V. Stark, K. J. Klabunde, J. R. Schlup, *Chem. Mater.*, **1993**, *5*, 71.

16. K. J. Klabunde, J. V. Stark, O. Koper, C. Mohs, A. Khaleel, G. Glavee, D. Zhang, C. M. Sorensen, G. C. Hadjipanayis, in *Nanophase Materials*, G. C. Hadjipanayis, R. W. Siegel (editors), Kluwer Academic Publishers, Dordrecht, **1994**, pp. 1–21.

17. A. Bedilo, K. J. Klabunde, *Chem. Mater.*, **1993**, *5*, 500.

18. O. Koper, I. Lagadic, A. Volodin, K. J. Klabunde, *Chem. Mater.*, **1997**, *9*, 2468.

19. Y. X. Li, O. Koper, M. Atteya, K. J. Klabunde, *Chem. Mater.*, **1992**, *4*, 323.

20. (a) J. V. Stark, D. G. Park, I. Lagadic, K. J. Klabunde, *Chem. Mater.*, **1996**, 1904.
    (b) J. V. Stark, K. J. Klabunde, *Chem. Mater.*, **1996**, *8*, 1913.

21. Y. X. Li, K. J. Klabunde, *Langmuir*, **1991**, *7*, 1388.

22. R. W. Siegel, S. Ramasamy, H. Hahn, L. Zongquan, L. Ting, R. Gronsky, *J. Mater. Res.*, **1988**, *3*, 1367.

23. M. S. El-Shall, W. Slack, W. Vann, D. Kane, D. Hanely, *J. Phys. Chem.*, **1994**, *98*(12), 3067.

24. H. Xu, S. Tan, N. T. Leo, *Trans. Nonferrous Met. Soc. China*, *2*(1), 58–60 (English) **1992**.

25. M. I. Baraton, M. S. El-Shall, *Nanostruct. Mater.*, **1995**, *6*, 301.

26. A. S. Edelstein, G. C. Hadjipanayis, R. W. Siegel (editors), *Nanophase Materials*, Kluwer Academic Publishers, Dordrecht, **1994**, pp. 73–80.

27. M. Y. Huh, S. H. Kim, J. P. Ahn, J. K. Park, B. K. Kim, *Nanostruct. Mater.*, **1999**, *11*(2), 211.

28. G. M. Cow, K. E. Gonsalves (editors), *Nanotechnology, Molecularly Designed Materials*, American Chemical Society, Washington, D.C., **1996**, pp. 79–99.

29. A. Rouanet, G. Pichelin, C. Roucan, E. Snoeck, C. Monty, in G. C. Hadjipanayis, R. W. Siegel (editors), *Nanophase Materials*, Kluwer Academic Press, Dordrecht, **1994**, pp. 85–88.

30. Kodas, T. T., *Adv. Mater.*, **1989**, *6*, 180.

31. Hadjipanayis, G. C., Siegel, R. W. (editors), *Nanophase Materials*, Kluwer Academic Publishers, Dordrecht, **1994**, pp. 109–116.

32. Dj. Janackovic, V. Jokanovic, Lj. Kostic-Gvozdenovic, D. Uskokovic, *Nanostruct. Mater.*, **1998**, *10*(3), 341.

33. G. L. Messing, S. C. Zhang, G. V. Jayanthi, *J. Am. Ceram. Soc.*, **1993**, *76*(11), 2707.

34. G. V. Jayanthi, S. C. Zhang, G. L. Messing, *J. Aerosol Sci. Technol.*, **1993**, *19*(4), 478.

35. G. L. Messing, T. J. Gardner, *Am. Ceram. Soc. Bull.*, **1984**, *64*, 1498.

36. J. P. Pollinger, G. L. Messing, *J. Aerosol Sci. Technol.*, **1993**, *19*(4), 217.

37. T. T. Kodas, A. Datye, V. Lee, E. Engler, *J. Appl. Phys.*, **1989**, *65*, 2149.

38. G. M. Cow, K. E. Gonsalves (editors), *Nanotechnology, Molecularly Designed Materials*, American Chemical Society, Washington, D.C., **1996**, pp. 64–78.

39. G. D. Ulrich, J. W. Riehl, *J. Colloid Interface Sci. Technol.*, **1982**, *87*, 257.

40. D. Lindackers, C. Janzen, B. Rellinghaus, E. F. Wassermann, P. Roth, *Nanostruct. Mater.*, **1998**, *10*(8), 1247.

41. G. Skanadan, Y.-J. Chen, N. Glumac, B. H. Kear, *Nanostruct. Mater.*, **1999**, *11*(2), 149.

42. V. R. Palkar, *Nanostruct. Mater.*, **1999**, *11*(3), 369.

43. L. V. Interrante, M. J. Hampden-Smith (editors), *Chemistry of Advanced Materials: An Overview*, Wiley-VCH, New York, **1998**.

44. E. A. Barringer, H. K. Bowen, *J. Am. Ceram. Soc.*, **1982**, *65*, C-199.

45. H. D. Gesser, P. C. Gosswami, *Chem. Rev.*, **1989**, *89*, 765.

46. D. L. Bourell, *J. Am. Ceram. Soc.*, **1993**, *76*, 705.

47. M. Chatry, M. Henry, J. Livage, *Mater. Res. Bull.*, **1994**, *29*, 517.

48. H. Kumazawa, T. Inoue, E. Sasa, *Chem. Eng. J.*, **1994**, *55*, 93.

49. F. Hatekeyama, S. Kanzaki, *J. Am. Ceram. Soc.*, **1990**, *73*(7), 2107.

50. D. A. White, S. M. Oleff, J. R. Fox, *Adv. Ceram. Mater.*, **1987** *2*(1), 53.

51. C. G. Granqvist, R. A. Burhman, *J. Appl. Phys.*, **1976**, *47*, 2200.

52. N. Ichinose, Y. Ozaki, S. Kashu, *Superfine Particle Technology*, Springer, London, **1992**.

53. A. S. Edelstein, R. C. Cammarato (editors), *Nanoparticles: Synthesis, Properties and Applications*, Institute of Physics Publishing, Philadelphia, **1996**, pp. 13–54.

54. H. Gleiter, *Prog. Mater. Sci.*, **1989**, *33*, 223.

55. R. Birringer, U. Herr, H. Gleiter, *Trans. Japan. Inst. Met. Suppl.*, **1986**, *27*, 43.

56. T. Arai, K. Mihama, K. Yamamoto, S. Sugano (editors), *Mesoscopic Materials and Clusters. Their Physical and Chemical Properties*, New York, Kodansha and Springer, New York, **1999**, pp. 275–283.

57. (a) A. H. Pfund, *Phys. Rev.*, **1930**, *35*, 1434.

(b)  H. C. Burger, P. H. van Cittert, *Z. Phys.*, **1930**, *66*, 210.

58. L. Harris, D. Feffries, B. M. Siegel, *J. Appl. Phys.*, **1948**, *19*, 791.

59. R. Uyeda, *J. Cryst. Growth*, **1974**, *24*, 69.

60. P. Chaudhari, J. W. Matthews, *Appl. Phys. Lett.*, **1970**, *17*, 115.

61. C. Kaito, K. Fujita, H. Shibahara, M. Shiojiri, *Japan. J. Appl. Phys.*, **1977**, *16*, 697.

62. C. M. Kaito, *Japan, J. Appl. Phys.*, **1978**, *17*, 601.

63. A. Rouanet, H. Solmon, G. Pichelin, C. Rouicau, F. Sibieude, C. Monty, *Nanostruct. Mater.*, **1995**, *6*(1–4), 283.

64. H. Hahn, R. S. Aberback, *Appl. Phys. Lett.*, **1990**, *67*, 1113.

65. M. J. Mayo, R. W. Siegel, A. Narayanasamy, W. D. Nix, *J. Mater. Res.*, **1990**, *5*, 1073.

66. A. Singhal, G. Skandan, A. Wang, N. Glumac, B. H. Kear, R. D. Hunt, *Nanostruct. Mater.*, **1999**, *11*(4), 545.

67. M. K. Wu, R. S. Windeler, C. K. R. Steiner, S. K. Friedlander, *Aerosol Sci. Technol.*, **1993**, *19*, 527.

68. D. Lindackers, M. G. D. Strecker, P. Roth, C. Janzen, S. E. Pratsinis, *Combust. Sci. Technol.*, **1997**, *123*, 287.

69. N. G. Glumac, Y. J. Chen, G. Skandan, B. Kear, *Mater. Lett.*, **1998**, *34*, 148.

70. M. R. Zacharia, D. Chin, H. G. Semerjian, J. L. Katz, *Combust. Flame*, **1989**, *78*, 287.

71. C. H. Hung, J. L. Katz, *J. Mater. Res.*, **1992**, *7*, 1861.

72. L. L. Hench, J. K. West, *Chem. Rev.*, **1990**, *90*, 33.

73. G. Yi, M. Sayer, *Ceram. Bull.*, **1991**, *70*, 1173.

74. D. Avnir, *Acc. Chem. Res.*, **1995**, *28*, 328.

75. C. D. Chandler, C. Roger, M. J. Hampden-Smith, *Chem. Rev.*, **1993**, *93*, 1205.

76. C. J. Brinker, C. W. Scherer, *Sol-Gel Science*, Academic Press, San Diego, CA, **1990**.

77. D. Segal, *Chemical Synthesis of Advanced Ceramic Materials*, Cambridge University Press, Cambridge, **1989**.

78. L. Klein, (editor), *Sol-Gel Optics: Processing and Applications*, Kluwer, Boston, **1993**.

79. C. K. Narula, *Ceramic Precursor Technology and Its Applications*, Marcel Decker, New York, **1995**.

80. Personal Contact with Nanoscale Materials, Inc., Manhattan, Kansas, USA.

81. H. Herrig, R. Hempelmann, *Mater. Lett.*, **1996**, *27*, 287.

82. Ch. Bruch, J. K. Kruger, H. G. Unruh, *Ber. Bunsenges, Phys. Chem.*, **1997**, *101*(11), 1761.

83. W. Hartl, C. Beck, M. Roth, F. Meyer, R. Hempelmann, *Ber. Bunsenges. Phys. Chem.*, **1997**, *101*(11), 1714.

84. L. M. Gan, H. S. O. Chan, L. H. Zhang, C. H. Chew, B. H. Loo, *Mater. Chem. Phys.*, **1994**, *37*, 263.

85. L. M. Gan, L. S. Zhang, H. S. O. Chan, C. H. Chew, B. H. Loo, *J. Mater. Sci.*, **1996**, *31*, 1071.

86. J. Wang, S. E. Lee, S. C. Ng, L. M. Gan, *Mater. Lett.*, **1997**, *30*, 119.

87. J. K. Lim, J. Wang, S. C. Ng, L. M. Gan, *Mater. Lett.*, **1996**, *28*, 431.

88. J. Fang, J. Wang, S. C. Ng, C. H. Chew, L. M. Gan, *Nanostruct. Mater.*, **1997**, *8*(4), 499.

89. H. L. Rosano, M. Claussen, *Microemulsion Systems*, Marcel Decker, New York, **1987**.

90. S. Martellucci, A. N. Chester (editors), *Progress in Microemulsions*, Plenum Press, New York, **1989**.

91. M. P. Pileni, *J. Phys. Chem.*, **1993**, *97*, 6961.

92. L. Gao, H. Z. Wang, J. S. Hong, H. Miyamoto, K. Miyamoto, Y. Nishikawa, S. D. D. L. Torre, *Nanostruct. Mater.*, **1999**, *11*(1), 43.

93. Z. Qian, J. L. Shi, *Nanostruct. Mater.*, **1998**, *10*(2), 235.

94. R. M. Rao, K. Rao, A. V. Prasada, S. Komameni, *Mater. Lett.*, **1996**, *1*(28), 463.

95. (a) J. Ding, T. Tsuzuki, P. G. McCormick, *J. Am. Ceram. Soc.*, **1996**, *79*, 2958.
    (b) R. L. Axelbaum, S. E. Bates, W. E. Buhro, C. Frey, K. F. Kelton, S. A. Lawton, S. M. Sastry, in *Abstracts for First International Conference on Nanostructured Materials*, Academia Mexicana, Cancun, **1992**.
    (c) T. D. Xiao, K. E. Gonsalves, P. R. Strutt, *J. Am. Ceram. Soc.*, **1993**, *76*, 987.

96. K. S. Mazdiasni, C. M. Cooke, *J. Am. Ceram. Soc.*, **1973**, *56*, 628.

97. D. Bahloul, M. Pereira, P. Goursat, N.S. C. K. Yive, R. J. P. Corriu, *J. Am. Ceram. Soc.*, **1994**, *76*(5), 1156.

98. K. E. Gonsalves, P. R. Strutt, T. D. Xio, P. G. Klemens, *J. Mater. Sci.*, **1992**, *27*, 3231.

99. D. Seyferth, G. H. Wiseman, *J. Am. Ceram. Soc.*, **1984**, *67*, C-132.

100. X. Li, Y. Nakata, H. Nagai, M. Suzuki, *Nanostruct. Mater.*, **1998**, *10*(7), 1173.

101. K. Kijima, H. Noguchi, M. Konishi, *J. Mater. Sci.*, **1989**, *24*, 2929.

102. G. P. Vissokov, L. B. Brakalov, *J. Mater. Sci.*, **1983**, *18*(7), 2011.

103. H. J. Lee, K. Eguchi, T. Yoshida, *J. Am. Ceram. Soc.*, **1990**, *73*(11), 3356.

104. D. Zeng, M. J. Hampden-Smith, *Chem. Mater.*, **1992**, *4*, 968.

105. J. Ding, T. Tsuzuki, P. G. McCormick, *Nanostruct. Mater.*, **1997**, *8*(1), 75.

106. J. Ding, W. F. Miao, P. G. McCormick, R. Street, *Appl. Phys. Lett.*, **1995**, *67*, 3804.

107. J. Ding, T. Tsuzuki, P. G. McCormick, R. Street, *J. Phys. D: Appl. Phys.*, **1996**, *29*, 2365.

108. J. Ding, T. Tsuzuki, P. G. McCormick, *Nanostruct. Mater.* **1997**, *8*(6), 739.

109. P. Matteazzi, D. Basset, F. Miani, *Nanostruct. Mater.* **1993**, *2*(3), 217–270.

110. C. N. R. Rao, B. Raveau, *Transition Metal Oxides, Structure, Properties, and Synthesis of Ceramic Oxides*, 2d edition, Wiley-VCH, New York, **1998**, p. 4.

111. D. F. Shriver, P. W. Atkins, C. H. Langford, *Inorganic Chemistry*, W. H. Freeman, New York, **1990**.

112. R. D. Shannon, C. T. Prewitt, *Acta Crystallogr.*, **1969**, *B25*, 925.

113. R. Richards, W. Li, S. Decker, C. Davidson, O. Koper, V. Zaikovski, A. Volodin, T. Rieker, K. J. Klabunde, *J. Am. Chem. Soc.*, **2000**, *122*(20), 4921.

114. R. Richards, A. Volodin, K. J. Klabunde, in preparation.

115. P. Tartaj, M. Reece, J. S. Moya, *J. Am. Ceram. Soc.*, **1998**, *81*(2), 389–394.

116. H. Lange, G. Wotting, G. Winter, *Angew. Chem., Int. Ed. Engl.*, **1991**, *30*, 1579.

117. R. A. Andrievski, *Nanotechnology, Particulate Nanostructured $Si_3N_4$ and TiN*, **1996**, pp. 294–301.

118. K. S. Mazdiyasni, C. M. Cooke, *J. Am. Ceram. Soc.*, **1973**, *56*, 628.

119. G. Skanadan, Y-J. Chen, N. Glumac, B. H. Kear, *Nanostruct. Mater.*, **1999**, *11*(2), 149.

120. W. Zhu, S. E. Pratsinis, *Nanotechnology*, **1996**, Chapter 4, p. 64.

121. R. N. Das, P. Pramanik, *Nanostruct. Mater.*, **1998**, *10*(8), 1371–1377.

122. A. Rouanet, G. Pichelin, C. Roucau, E. Snoeck, C. Monty, in *Nanophase Materials*, G. C. Hadjipanayis, R. W. Siegel (editors), Kluwer Academic Publishers, Dordrecht, **1994**, pp. 85–88.

123. R. Philipp, K. Omata, A. Aoki, K. Fujimoto, *J. Catal.*, **1992**, *134*, 422.

124. T. Ito, J.-X. Wang, C.-H. Liu, J. H. Lunsford, *J. Am. Chem. Soc.*, **1985**, *107*, 5062.

125. D. J. Driscoll, W. Martir, J.-X. Wang, J. H. Lunsford, *J. Am. Chem. Soc.*, **1985**, *107*, 58.

126. X. D. Peng, D. A. Richards, P. C. Stair, *J. Catal.*, **1990**, *121*, 99.

127. A. Yu. Stakheev, E. S. Shapiro, J. Apijok, *J. Phys. Chem.*, **1993**, *97*, 5668.

128. M. J. Mayo, J. R. Seidensticker, D. C. Hague, A. H. Carim, *Nanostruct. Mater.* **1999**, *11*(2), 271.

129. B. Vishwanathan, B. Tanka, L. Toyoshima, *Langmuir*, **1986**, *2*, 113.

130. N. Sun, K. J. Klabunde, *J. Am. Chem. Soc.*, **1999**, *121*, 5587.

131. N. Sun, K. J. Klabunde, *J. Catal.*, **1999**, *185*, 506.

132. Y. Jiang, S. Decker, C. Mohs, K. J. Klabunde, *J. Catal.*, **1998**, *180*, 24.

133. K. J. Klabunde, A. Khaleel, D. Park, *High Temp. Mater. Sci.*, **1995**, *33*, 99.

134. A. Khaleel, K. J. Klabunde, in *Nanophase Materials*, G. C. Hadjipanayis, R. W. Siegel (editors), Kluwer Academic Publishers, Dordrecht, **1994**, pp. 785–788.

135. K. J. Klabunde, Y. Li, A. Khaleel, in *Nanophase Materials*, G. C. Hadjipanayis, R. W. Siegel (editors), Kluwer Academic Publishers, Dordrecht, **1994**, pp. 757–769.

136. A. Khaleel, W. Li, K. J. Klabunde, *Nanostruct. Mater.*, **1999**, *12*, 463.

137. A. Khaleel, P. N. Kapoor, *Nanostruct. Mater.*, **1999**, *11*(4), 459.

138. O. B. Koper, E. A. Wovchko, J. A. Glass, J. T. Yates, Jr., K. J. Klabunde, *Langmuir*, **1995**, *11*, 2054.

139. G. W. Wagner, P. W. Bartram, O. Koper, K. J. Klabunde, *J. Phys. Chem. B*, **1999**, *103*, 3225.

140. R. I. Masel, *Principles of Adsorption and Reaction on Solid Surfaces*, Wiley, New York, **1996**.

141. V. Henrich, P. A. Cox, *Metal Oxides*, Cambridge University Press, New York, **1994**.

142. A. S. Edelstein, R. C. Cammarato (editors), *Nanoparticles: Synthesis, Properties, and Applications*, Institute of Physics Publishing, Philadelphia, **1996**, p. 170.

143. J. Karch, R. Birringer, *Ceram. Int.*, **1990**, *16*, 291.

144. P. Apte, B. H. Suits, R. W. Siegel, *Nanostruct. Mater.*, **1997**, *9*(1–8), 501.

145. M. J. Mayo, *J. Mater. Res.*, **1990**, *5*(5), 1073.

146. D.-J. Chen, M. J. Mayo, *Nanostruct. Mater.*, **1993**, *2*, 469.

147. H. Hahn, G. C. Hadjipanayis, R. W. Siegel, *Nanophase Materials, Synthesis–Properties–Applications*, Kluwer Academic Publishers, London, **1994**, pp. 263–273.

148. H. Hahn, R. S. Averback, *Mater. Res. Soc. Symp.*, **1991**, *206*, 561.

149. F. Wakei, S. Sakaguchi, Y. Matsuno, *Adv. Ceram. Mater.*, **1986**, *1*, 259.

150. T. G. Nieh, J. Wadsworth, *Acta. Metall. Mater.*, **1990**, *38*, 1121.

151. F. Wakai, H. Kato, *Adv. Ceram. Mater.*, **1988**, *3*, 71.

152. T. G. Nieh, C. M. McNally, J. Wadsworth, *Scr. Metall.*, **1989**, *23*, 457.

153. J. Karch, R. Birringer, H. Gleiter, *Nature*, **1987**, *330*, 556.

154. H. Hahn, R. S. Aberback, *J. Am. Ceram. Soc.*, **1991**, *74*, 2918.

155. M. J. Mayo, R. W. Siegel, Y. X. Liao, W. D. Nix, *J. Mater. Res.*, **1992**, *7*, 973.

156. C. C. Koch, D. G. Morris, K. L. Lu, A. Inoue, *Mater. Res. Bull.*, **1999**, *24*(2), 54.

157. T. G. Nieh, C. M. McNally, J. Wadsworth, *J. Met.*, **1989**, 31.

158. Y. Maehara, T. G. Langdon, *J. Mater. Sci.*, **1990**, *25*, 2275.

159. T. J. Nieh, J. Wadsworth, F. Wakai, *Int. Mater. Rev.*, **1991**, *36*, 146.

160. T. H. Cross, M. J. Mayo, *Nanostruct. Mater.*, **1994**, *3*, 163.

161. J. R. Weertman, D. Farkas, K. Hemker, H. Kung, M. Mayo, R. Mitra, H. V. Swygen-hoven, *Mater. Res. Bull.*, **1999**, *24*(2), 44–50.

162. S. Saito, *Fine Ceramics*, Elsevier, New York, Ohmsha Ltd., Tokyo, **1985**.

163. Gleiter, H., *Nanostruct. Mater.*, **1995**, *6*, 3.

# 5 Metal Nanoparticles: Double Layers, Optical Properties, and Electrochemistry

PAUL MULVANEY

Max-Planck-Institut für Kolloid- und Grenzflächenforschung, Potsdam-Golm, Germany

## 5.1 INTRODUCTION

The history of metal particles is a long and illustrious one. Gold and silver particles have found their way into glasses for over 2000 years, usually as nanoparticles. They have most frequently been employed as colorants, particularly for church windows. In 1685 Andreas Cassius and Johan Knuckel described a mixture of tin dioxide and gold that was found to have an intense purple color, a royal purple color in fact, and this "Purple of Cassius" was used to color glasses and even garments. The preparation involved the reduction of gold salts by Sn(II) present in the tin dioxide to form small, impregnated gold particles.[1] The actual purple color may have been due to the agglomerated state of the gold particles, but may equally have been caused by the high refractive index of the tin dioxide, something we will discuss later in this chapter. For it is the colors of metal sols that have long fascinated researchers. The first so-called "scientific" study of gold particles took place in 1831, when Michael Faraday investigated the ruby red colloids of gold, and announced that the color was due to the small size of the metal particles and was not attributable to some peculiar state of the gold metal.[2]

A milestone in the development of metal particle science was Mie's theoretical considerations of the colors of colloidal metals, and in particular those of gold.[3] He explained the colors "quantitatively" by solving the fundamental problem of the absorption and scattering of light by small spheres. The solution to this generic problem now bears his name unofficially, though Debye carried out a similar independent investigation for completely different reasons at about the same time.[4]

One of the many key results of Mie's 70-page tour de force was that materials with negative values of the real part of the dielectric function will show an anomalous peak in the absorption spectrum when in the form of small particles.

Since Mie's work, numerous researchers have investigated the properties of metal particles because of their unusual optical properties. As we will see, gold, silver, and copper are very attractive subjects for these investigations, while the *d*-band metals such as platinum, iridium, and rhodium are optically less exciting but are catalytically far superior.

In this chapter on nanoparticles, we attempt to unite the optical and electronic properties of small metal particles. To do this we will utilize a link between the electron density in the particle and the optical and double layer response. This allows us to understand how normal chemical spectroscopy can be utilized to follow fundamental chemical processes at metal nanoparticle surfaces. The static charge on a metal particle is also of fundamental importance since this is often responsible for the colloid stability. This charge may be ionic and/or electronic. To begin, we will review the elements of electrical double layer theory relevant to metal nanoparticles. Section 5.2 will highlight the basic equations needed to understand how charge is distributed around the particles, and how this controls colloid stability and electron transfer. We will then examine the basic equations that determine electrode kinetics and how they can be applied to small particles in section 5.3. To use spectroscopy to monitor these reactions, we will need some equations that link the electron density to the optical properties of the particles. This will be covered in section 5.4. Finally, in section 5.5, we will look at charge transfer between metal colloid particles and a metal electrode.

## 5.2   COLLOID STABILITY

### 5.2.1   The Electrical Double Layer around Colloid Particles

Most chemistry occurs at interfaces of some form or another. In these first sections, we will consider the basic structure of the electrical double layer around colloid particles. The equations will be couched in terms that allow the treatment to be applied both to metal colloids, the basic theme of the chapter, and to semiconductor and other small particles, considered elsewhere in this book. The primary difference between metals and metal oxides or insulators is how the electrical charge on the surface is manipulated.

For semiconductors or insulators, the amount of electronic charge that can be exchanged with a solution redox couple is much less than for metals, since the mobile charge is due only to impurities. As a consequence, it is usually the preferential loss of lattice cations and anions, or the adsorption of charged species from solution, that determines the amount of surface charge on a semiconductor particle. For example, when a metal oxide surface is created in solution, the adsorption of hydroxyl ions or protons leads to the generation of a surface charge, and an electric potential develops between the surface and the bulk solution.

Provided the surface activity of these so-called "potential determining" ions ($H^+$, $OH^-$) remains constant, the surface potential of a metal oxide particle in aqueous solution is given by the familiar Nernst equation:

$$\psi_0 = -0.059(\text{pH} - \text{pH}_{\text{pzc}}) \tag{5.1}$$

where $\text{pH}_{\text{pzc}}$ refers to the pH at which there is equal adsorption of potential-determining cations and anions at the surface. The value of the $\text{pH}_{\text{pzc}}$ is readily determined by electrophoresis of the colloid at different pH values.

When a conductor is placed into water, the steady state charge that builds up on the solid is usually due to charge transfer between the metal and solution. The potential is generally controlled by the dominant redox couple in solution. Hence we add a redox couple to fix the electrochemical potential at a desired value:

$$E_{\text{redox}} = E_{\text{redox}}^0 + \frac{0.0592}{z} \log_{10} \frac{[\text{Ox}]}{[\text{Red}]} \tag{5.2a}$$

The surface potential is usually referred to the normal hydrogen electrode (NHE). If a metal electrode is connected to such a reference electrode, then the potential between them can be adjusted. At a certain potential, the metal electrode will have a zero surface charge. This particular potential is termed the potential of zero charge, and can be denoted by "pzc" or "$E_{\text{pzc}}$." It is normally determined from the minimum in the interfacial capacitance, which can be readily determined for a bulk metal electrode. In this case, we can write

$$E_{\text{surf}} = E_{\text{redox}} - E_{\text{pzc}} \tag{5.2b}$$

where both potentials on the right-hand side are measured relative to a reference electrode. We have used $E$ to indicate that these potentials are measured electrochemically. (Note that the surface potential is caused by several different effects, including the spatial inhomogeneities in the charge distribution near the surface, surface dipoles, dielectric saturation of the solvent, and other less direct factors. We concentrate here on purely electrostatic contributions.) For metal colloid particles, determination of the pzc is much harder to determine because we cannot measure the particle redox potential directly, nor the particle capacitance. In principle, the charge can be determined from electrophoresis as with metal oxide or other nonmetallic particles, but it is difficult to sweep the redox potential of the solution over a large range. It is often found experimentally that ionic adsorption from solution may contribute significantly to the final charge density on metal particles. Conversely, for most nonmetallic colloids, the surface potential is adjustable through changes in pH, which allows the surface potential to be swept through about 600 mV. In what follows we will assume that the surface potentials of metal and nonmetallic particles are controllable and measurable. It will be assumed that the surface potential is Nernstian and for that any colloid it is given by

$$\psi_0 = -0.059(\text{pH} - \text{pH}_{\text{pzc}}) \tag{5.1}$$

or

$$\psi_0 = E_{\text{redox}} - E_{\text{pzc}} \tag{5.2b}$$

Most of the theory of colloid double layers is built upon the models developed to explain the electrical properties of the dropping mercury electrode double layer. This research began with Helmholtz in 1879, and in 1947 Grahames's research culminated in the "complete" classical model, which incorporated and modified the ideas of Helmholtz, Stern, Gouy, and Chapman.

In response to the adsorbed surface charge and the creation of an electric potential at the particle surface, there will be a local excess of counterions around the particle. These counterions form a diffuse layer around the particle, and cause the electric potential to slowly decay to zero as one moves away from the particle surface toward the bulk solution, as shown schematically in Figure 5.1. However, some of these ions may be strongly adsorbed, forming a plane of bound countercharge, which will lower the electric potential immediately adjacent to the particle surface. This region is called the Helmholtz or Stern layer, and is made up of both strongly polarized water molecules and desolvated ions, as shown in Figure 5.2. The adsorption plane is
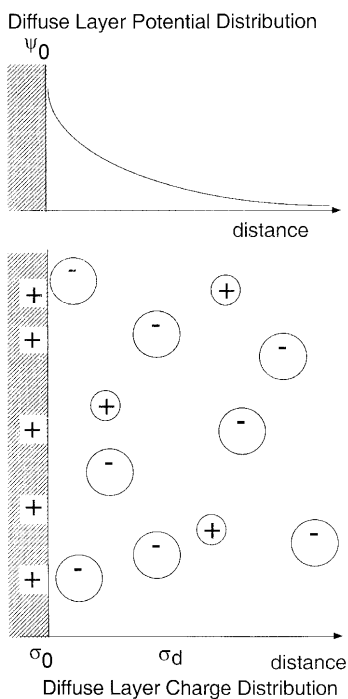


**FIGURE 5.1**  Model illustrating the distribution of ions in the diffuse layer around a small colloid particle. The model shows both the charge distribution and the potential decay near the surface.

Diffuse Layer and Stern Layer
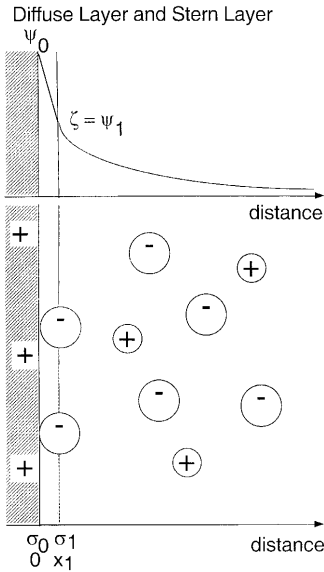


**FIGURE 5.2**   Model illustrating the idea of a Stern plane or Helmholtz layer in which some ions are bound at a well-defined distance $x_1$ from the surface. The diffuse layer starts at $x_1$ where the potential is $\psi_1$. This plane is usually assumed to be close to the shear plane, and the potential at this plane is taken to be the observed zeta potential, $\zeta$, measured by electrophoresis.

located at a distance $x_1$ from the actual surface, and the relative permittivity in the region $0 < x < x_1$ is taken to be $\varepsilon_1$; $\varepsilon_1$ has a value between 2 and 6, compared with 78 in bulk water. The drastic decrease is due to the loss of rotational polarization for the aligned water molecules. Since the distance of these ions from the surface is only $3\,\text{Å}$ or so, the surface charge and countercharge may be treated as a parallel condenser with a capacitance per unit surface area given by

$$K_{\mathrm{I}} = \frac{\sigma_0}{\psi_0 - \psi_1} = \frac{\varepsilon_1 \varepsilon_0}{x_1} \tag{5.3}$$

where $\varepsilon_1 \varepsilon_0$ is the permittivity of the layer and $\sigma_0$ is the surface charge density. Consequently, the potential at $x_1$ is reduced to

$$\psi_1 = \psi_0 - \frac{\sigma_0}{K_{\mathrm{I}}} = \psi_0 - \frac{\sigma_0 x_1}{\varepsilon_1 \varepsilon_0} \tag{5.4}$$

Normally the ions adsorbed electrostatically at the Helmholtz plane will not completely neutralize the surface charge, but if there is, in addition, a chemical driving energy for adsorption, the adsorbed countercharge may exceed that of the "true" surface charge, and the overall charge on the particle may be reversed. This is
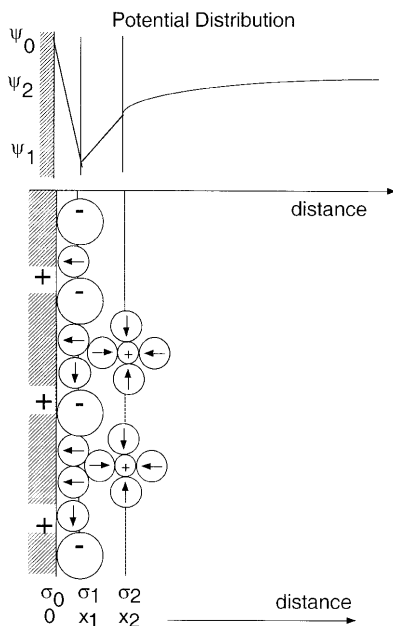
**FIGURE 5.3** Model showing the idea of superequivalent adsorption where a reversal of surface charge takes place between the surface and Stern plane. A second plane defining the distance of closest approach of hydrated ions is also shown at a distance $x_2$. The smaller spheres are water molecules with oriented dipoles.

depicted in Figure 5.3, where we see that the potential actually changes sign before decaying slowly to zero in the bulk solution. This situation is often realized with polyelectrolytes such as poly(acrylic acid) or sodium hexametaphosphate, which can superadsorb on colloid surfaces. The ions or molecules in the Helmholtz layer are so strongly bound that an electric field applied to the colloid will cause motion of the particle, the adsorbed countercharge, and a monolayer or so of solvent molecules. Hence, the effective charge on the electrokinetic unit is not due solely to the surface charge but will be reduced (generally) by the presence of a plane of adsorbed counterions.

In the Gouy–Chapman–Stern–Grahame model, a second structural plane is also defined, which is illustrated in Figure 5.3. This is at a distance $x_2$, and is the distance of closest approach of solvated ions to the plane $x_1$, due to the finite size of the ions and their hydration shells. This second plane is usually termed the outer Helmholtz plane (OHP), with $x_1$ then being the inner Helmholtz plane (IHP). In this case, the electric potential decreases further between the inner plane of adsorbed anions and the OHP where counterions reach. It is the potential at the plane $x_2$ that then effectively orientates other ions in solution and induces the build-up of the space charge layer (or diffuse layer) of counterions around the particle.

### 5.2.2   The Diffuse Layer

Electroneutrality requires that, overall, the excess charge density around the charged colloid particle in the diffuse layer, $\sigma_{\mathrm{d}}$, must equal the charge density on the particle; that is,

$$\sigma_0 + \sigma_1 + \sigma_{\mathrm{d}} = 0 \tag{5.5}$$

The electric potential at any point in the difuse layer is calculated from Poisson's equation:

$$\nabla^2 \psi = \frac{-\rho}{\varepsilon_{\mathrm{r}} \varepsilon_0} \tag{5.6}$$

For a symmetrical $z:z$ electrolyte, the charge density at any point in the solution is

$$\rho = |z| e ([n_+] - [n_-]) \tag{5.7}$$

where $|z|$ is the absolute electrolyte valency, and $[n_+]$ and $[n_-]$ are the respective ion concentrations at that point in solution. Assuming that the ions are distributed in the electric field according to the Boltzmann equation, then at any point,

$$[n_\pm] = [n_\pm^\infty] \exp\left(\frac{-z_\pm e \psi}{kT}\right) \tag{5.8}$$

where $n^\infty$ is the bulk ion concentration in units of molecules per unit volume, and $\psi$ is the potential at that point relative to the bulk solution, where we define $\psi(\infty) = 0$. Combining Equations (5.6), (5.7), and (5.8), we obtain the Poisson–Boltzmann (PB) equation:

$$\nabla^2 \psi = 2 \frac{n^\infty z e}{\varepsilon_{\mathrm{r}} \varepsilon_0} \sinh\left(\frac{z e \psi}{kT}\right) \tag{5.9}$$

The boundary conditions for integration are that

$$\psi \to 0 \quad \text{as} \quad x \to \infty \tag{5.10}$$

$$\frac{d\psi}{dx} \to 0 \quad \text{as} \quad x \to \infty \tag{5.11}$$

while at the start of the diffuse layer, the potential must be $\psi_1$.

$$\psi_{(x=x_1)} = \psi_1 \tag{5.12}$$

The solution of the PB equation is not straightforward, and the method of solution can be simplified by considering four regimes in turn. These regimes consist of flat

**TABLE 5.1  Solutions to the Poisson–Boltzmann equation for microparticles and nanoparticles**

| | Small $\kappa a$ | Large $\kappa a$ |
|---|---|---|
| Low potentials | $\psi(r) = \psi_0 \dfrac{a}{r} \exp[-\kappa(r-a)]$ | $\psi(x) = \psi_0 \exp(-\kappa x)$ |
| High potentials | $\nabla^2 \psi = \dfrac{2zn^\infty e}{\varepsilon_r \varepsilon_0} \sinh\left(\dfrac{e\psi}{kT}\right)$ | $\tanh\left(\dfrac{ze\psi(x)}{4kT}\right) = \tanh\left(\dfrac{ze\psi_0}{4kT}\right)\exp(-\kappa x)$ |
| | where $\kappa^2 = \dfrac{2z^2 e^2 n^\infty}{\varepsilon_r \varepsilon_0 kT}$ | |

and curved surfaces with both high and low surface potentials. These different solutions are summarized in Table 5.1, and are considered in turn in the next sections.

### 5.2.3  The Diffuse Layer for Microparticles

If the particle radius $a$ is large compared to the double layer thickness, then the double layer can be treated as flat, and Cartesian coordinates can be used. Furthermore, if the diffuse layer potential at $x_1$ is small ($\psi \ll kT/ze$), then linearization of the exponential terms leads to

$$\nabla^2 \psi \equiv \frac{d^2\psi}{dx^2} = \kappa^2 \psi \tag{5.13}$$

where

$$\kappa^2 = \frac{2n^\infty e^2 z^2}{\varepsilon_r \varepsilon_0 kT} \tag{5.14}$$

$\kappa^{-1}$ is called the double layer thickness. Equation (5.13) can be integrated directly using the boundary conditions in Equations (5.10), (5.11), and (5.12) to yield

$$\psi(x) = \psi_1 \exp[-\kappa(x - x_1)] \quad x > x_1 \tag{5.15}$$

This shows that a charged particle has an apparent surface potential $\psi_1$, which falls off to $1/e$ of its surface value over a distance $\kappa^{-1}$ in an electrolyte solution. For high potentials such that $\psi_1 \gg 25$ mV/$z$ at 298 K, the linearization is no longer accurate, and Equation (5.9) must be integrated. The result is

$$\tanh\left(\frac{ze\psi(x)}{4kT}\right) = \tanh\left(\frac{ze\psi_1}{4kT}\right)\exp(-\kappa x) \tag{5.16}$$

Equation (5.16) reveals that even for high potentials the diffuse layer thickness is still $\kappa^{-1}$. The approximation of a flat double layer around a colloid particle will be

valid if $\kappa a \gg 1$. The curvature of the system obviously changes as a result of particle growth through coalescence or Ostwald ripening. To obtain the capacitance of the double layer we apply Gauss' law:

$$(\sigma_0 + \sigma_1) = -\varepsilon_r \varepsilon_0 \frac{d\psi}{dx}\bigg|_{x=x_1} \tag{5.17}$$

From Equation (5.15),

$$\frac{d\psi}{dx}\bigg|_{x=x_1} = -\kappa \psi_1 \tag{5.18}$$

and on substitution of Equation (5.18) into (5.17) we get

$$K_d = \frac{\sigma_0 + \sigma_1}{\psi_1} = -\frac{\sigma_d}{\psi_1} = \varepsilon_r \varepsilon_0 \kappa \tag{5.19}$$

Thus the diffuse layer around a particle with $\kappa a \gg 1$ and at low potentials behaves like a parallel plate capacitor, with thickness $\kappa^{-1}$, which is why $\kappa^{-1}$ is called "the diffuse layer thickness".

### 5.2.4  The Diffuse Layer for Nanoparticles

Nanosized particles are distinguished from their micrometer-sized counterparts by the fact that the double layer must be considered spherical because, for colloid particles with diameters of $< 100$ Å, the assumption of flat double layers is no longer accurate. For example, at 0.1 mM $NaNO_3$, the Debye length is 300 Å, so $\kappa a \sim 0.3$. Integration of Equation (5.9) must now be carried out in spherical coordinates. For small potentials, linearization of Equation (5.9) and integration yields

$$\psi(r) = \psi_1 \frac{a}{r} \exp[-\kappa(r - a)] \tag{5.20}$$

However, a surface potential $< 25$ mV is usually insufficient to prevent particle coalescence (see section 5.2.5). So although the simplification renders the solutions more tractable, it does not provide accurate results for stable colloids with higher surface potentials, and the use of the linearized forms is generally inadequate. For highly charged nanoparticles, which are colloidally stable, the potential distribution must be solved numerically through, for example, Runge–Kutta methods. This is described in detail in several books.[5]

The presence of the diffuse layer around an electrostatically stabilized colloid particle is essential. It is the repulsion experienced by two colloid particles as their double layers overlap that stabilizes them against coagulation. A high diffuse layer potential and a low electrolyte concentration, which increases the range of repulsion, are necessary for good colloid stability. It is usual to take the potential at $x_1$ to be

equal to the measured zeta potential from electrophoresis, which is the apparent potential on the particle when it is migrating in an electric field. In concentrating on electrostatic stabilization, we are ignoring the possibility that the particles may be stabilized by polymers or large surfactants, which may provide a steric barrier to coalescence. Steric stabilization is discussed in great detail by Vincent, and his review includes many examples.[6]

We can now write the total potential distribution between the metal or insulating particle surface and solution for a particle immersed in aqueous solution. For the model shown in Figure 5.2, we have

$$\psi(x_1) = \psi_0 - \sigma_0 \frac{x}{x_1} K_1 \quad 0 < x < x_1 \tag{5.21}$$

$$\psi(x > x_1) = f(\kappa, a, \psi_1) \tag{5.22a}$$

$$\psi_0 = E_{\text{redox}} - E_{\text{pzc}} \tag{5.22b}$$

Here, $f(\kappa, a, \psi_1)$ refers to one of the four solutions in Table 5.1. Clearly, even for a model with just a single inner region, there are a number of experimental variables that need to be measured in order to quantify the potential distribution. Given that $\varepsilon_1$ and $x_1$ are not really directly accessible to experimental verification, such simplifications are often advisable. For example, by assuming there is no specific adsorption from solution we can set $\sigma_1 = 0$, in which case $\sigma_0 = -\sigma_d$. However, this is clearly a poor approximation if a polyelectrolyte or surfactant has been used to stabilize the particles, or if a strongly chemisorbed ligand such as a thiol or amine derivative has been used to minimize particle growth during preparation. Little work has been done to characterize the electrical double layer of metal nanoparticles in the presence of specifically adsorbed redox couples. or to study the effect of simple carboxylic acids such as sodium citrate, which are extensively used to stabilize metal nanoparticles.

### 5.2.5  Nanoparticle Stability

We will see in the next sections that the electrical double layer controls the rate of electron transfer processes involving redox couples at metal or semiconductor surfaces. But for colloid redox chemistry, the electrical double layer plays an equally important role in determining the stability of the particles with respect to coagulation into larger aggregates. This is almost invariably an undesirable process, which will alter the optical, electrical, catalytic, and magnetic properties of nanoparticles. Hence we will now examine briefly the way the particle size, surface potential and diffuse layer all influence nanoparticle coalescence, then shift attention to chemical reactions taking place at the surface. What will become obvious is that we cannot tune the surface potential or zeta potential arbitrarily because low potentials affect colloid stability. In fact, a major difficulty in quantifying double layer kinetics in colloid systems is the problem of measuring redox reactions close to the pzc, since the colloids will coagulate rapidly. Yet such measurements provide the ideal reference point both for activation-controlled charge transfer, which depends strongly on

the value of the zeta potential, and for diffusion-limited reactions. This problem renders colloid redox chemistry much more difficult than conventional electro-chemistry with bulk electrodes, where the potentials can be reliably and reproducibly scanned over 2–3 V in electron potential.

For the case of low potentials, and small overlap between double layers, the electrostatic repulsive energy for two spheres of radius $a$ with zeta potential $\zeta$ approaching each other in a medium of Debye length $\kappa^{-1}$, with $r$ the center-to-center distance between the two particles, is given by

$$V_{\text{rep}}(kT) = 4\pi\varepsilon_r\varepsilon_0\zeta^2 \frac{a^2}{r} \exp\left[-\kappa a\left(\frac{r}{a} - 2\right)\right] \qquad (r > 2a) \qquad (5.23)$$

Particle coalescence is caused by van der Waals or dispersion forces acting between the surfaces. The nonretarded van der Waals interaction energy between particles of radius $a$ is given approximately by

$$V_{\text{att}}(kT) = -\frac{A}{6}\left[\frac{2a^2}{r^2 - 4a^2} + \frac{2a^2}{r^2} + \ln\left(1 - \frac{2a^2}{r^2}\right)\right] \qquad (5.24)$$

where $A$ is the so-called Hamaker constant for the metal–water–metal system under consideration. More exact forms are given by Hunter[5] and by Israelachvili,[7] as well as derivations for different particle geometries. Hamaker constants for a variety of materials are also given in Israelachvili's book. Notably, metals have much higher Hamaker constants than other materials, and hence metal colloids are much more prone to coagulation than other colloids. According to Derjaguin-Landau-Verwey-Overbeek (DLVO) theory it is the sum of these two energies that determines particle stability. The usual criterion is that a barrier of $15$–$20kT$ is sufficient to ensure colloid stability. The interaction energy is plotted as a function of the surface separation in Figures 5.4, 5.5, and 5.6 for various particle sizes, surface potentials, and Hamaker constants. It is clear from Equations (5.23) and (5.24) that both the attractive and repulsive interaction energies increase with particle radius. As a consequence, we can see in Figure 5.4 that the barrier height to colloid stability at fixed $\psi_0$ increases as the particle size increases. Consequently, there is an automatic tendency for coagulation of particles to slow down as coagulation proceeds. This factor may often determine the final particle size distribution following nucleation. But the secondary minimum also becomes deeper as the particle size increases. If two particles $> 10$ nm flocculate in solution, they will not be able to separate again easily, since their thermal energy will be insufficient to allow them to "diffuse" out of the secondary minimum. This can lead to slow flocculation or, in concentrated nanoparticles, to gelation. Conversely, nanoparticles should peptize relatively easily. It is important to recognize that rapid peptization is essential. A weak agglomerate of small particles, all held by a collective secondary minimum interaction energy, will behave in van der Waals terms like a larger particle and the van der Waals interaction energy with other freely diffusing particles will gradually increase if agglomeration is allowed to continue. Provided nanoparticles peptize quickly, the secondary
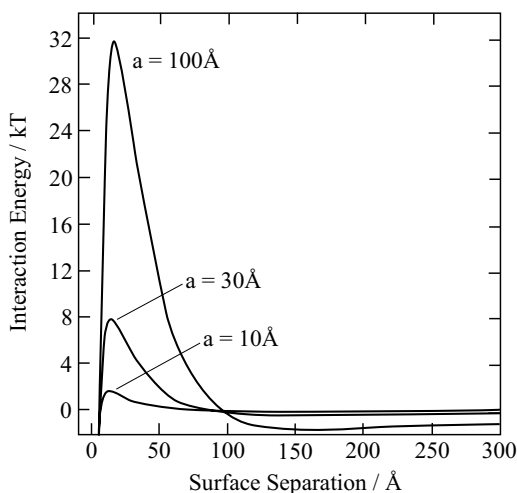
**FIGURE 5.4**   Plot of the interaction energy between two spherical gold particles in aqueous solution as a function of the particle separation, for several particle radii. Hamaker constant $= 25 \times 10^{-20}$ J, $I = 1$ mM, $\psi_0 = 0.10$ V, $a = 1.0$ nm, 3.0 nm, and 10.0 nm, Debye length $= 10$ nm. Note that the secondary minimum is negligible for nanoparticles, but becomes important above 10 nm.
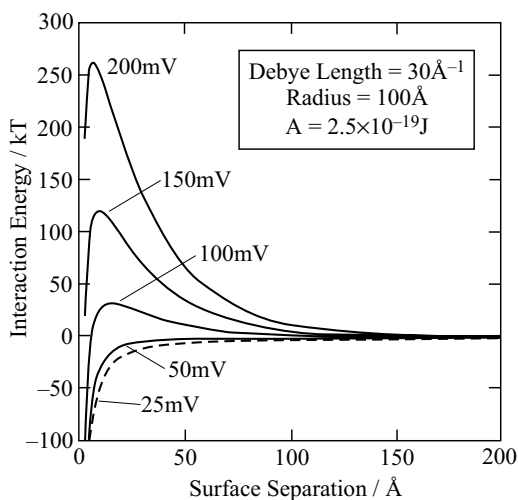


**FIGURE 5.5**   Plot of the interaction energy between two spherical gold particles in aqueous solution as a function of the particle separation for several surface potentials. Hamaker constant $= 25 \times 10^{-20}$ J, $I = 10$ mM, $a = 10$ nm, Debye length $= 3$ nm. Note that a zeta potential, $|\zeta| > 50$ mV, is necessary for colloid stability because of the high Hamaker constant.
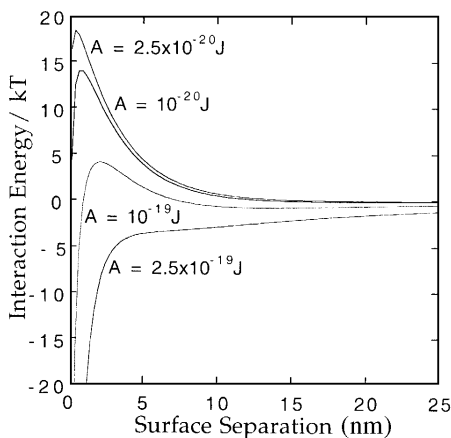
**FIGURE 5.6**   Plot of the interaction energy between two spherical particles in aqueous solution as a function of the particle separation, for different Hamaker constants. $\psi_0 = 0.050$ V, $a = 10$ nm, $I = 10$ mM. For the solution conditions shown, gold and most noble metal colloids would be very unstable, while latex colloids would be very stable in the same solution because of the smaller van der Waals interactions.

minimum around the temporary agglomerates will not have time to deepen further via aggregate–colloid encounters.

It is clear from these figures that only relatively small molecules should be necessary to prevent coalescence and particle coagulation of nanoparticles. Furthermore, the primary minimum is not as deep for nanoparticles as for larger particles. As a consequence even true coagulation into the primary minimum can be reversible for small nanoparticles if there is some form of steric stabilizer present on the particle surface. Chemisorbed molecules provide a steric barrier, and for particles $< 100$ Å in diameter, a steric layer of $> 2$ nm (equal to a little more than a $C_{18}$ chain) will generally be sufficient to offset the van der Waals interactions. However, $\psi_0$ should still be large to prevent the formation of loose agglomerates. Small stabilizers can be remarkably efficacious in stabilizing nanoparticle colloids. A simple demonstration of this is the stability of gold sols after addition of mercaptopropionic acid. The mercaptan group has a very strong affinity for gold surfaces, and this ensures a dense monolayer coverage on the surface. This is vividly demonstrated by high-resolution transmission electron microscopy (HRTEM). Ordered colloids can be observed with a spacing equal to about twice the stabilizer chain length.[8,9] These $HSC_2H_5COO^-Na^+$ capped gold particles coalesce reversibly on addition of ethanol or acid to the colloids to induce coalescence. If the colloid is centrifuged down and the supernatant fluid is removed, addition of a drop of base will restore the blood-red colloid at once. This shows that even a small chain length combined with a reasonable surface charge density is sufficient for the particles to escape the primary minimum.

The above sections highlight in a fairly generic way the importance of well-defined double layers in all colloid systems, whether we are interested in simply

stabilizing the particles or in studying chemical processes at the particle surface. We have concentrated on highlighting size effects since these are important for understanding the different behaviours of nanoparticle systems. As is fundamentally obvious, particle systems are intrinsically more complicated than electrodes because of the difficulty in measuring interfacial potentials and current flow when compared with bulk electrodes. Nevertheless, a number of groups have successfully monitored the electron transfer kinetics and established the discharge mechanisms in water for a number of metal colloids. Of most interest is hydrogen evolution from water, so we will now look at classical predictions about controlling and measuring rates of electron transfer between redox active molecules and metal colloids.

## 5.3   CHARGE TRANSFER

### 5.3.1   Mass Transfer-limited Reactions

In principle, the rates of both homogeneous and heterogeneous chemical reactions are determined by either mass transfer—that is, the macroscopic transport of materials to a common point where reaction is possible—or limited by the rate of actual reaction once the reactants are in the proximity of each other. In the following sections, we are concerned with redox couples undergoing electron transfer to or from metal nanoparticles. The reagents are usually produced by an extremely short excitation pulse, for example, by a laser or linear accelerator. The redox couples so formed will be homogeneously distributed within the solution within $\sim 10^{-7}$ s. We can then use steady-state diffusion equations, rather than the time-dependent equations, since colloid reactions usually take much longer than this. For example, for silver colloids with $a = 25$ Å, the half-life for reaction with the strong reductant $(CH_3)_2COH$ ($k = 5 \times 10^{10}$ M$^{-1}$ s$^{-1}$) is 10 ns only at 0.5 M Ag ions (corresponding to about 0.5 mM silver colloid *particles*). It is very unusual to work at metal ion concentrations around 0.5 M, because of both particle coalescence and the extremely high absorbance of such sols, which renders time-resolved work by spectroscopic means impossible. Hence in flash photolysis or pulse radiolysis or stop-flow systems, with which the kinetics of redox reactions with the colloids are likely to be investigated, steady-state conditions usually prevail. In fact, for silver sols, the observed rate of reaction is typically in the millisecond time range under pulse-radiolytic conditions. The rate constant for the steady-state, diffusion-controlled reaction in solution between a molecule and a colloid particle is given by the Smoluchowski expression,

$$k_{\text{diff}} = 4\pi R D \tag{5.25}$$

where $R = R_{\text{coll}} + R_{\text{rad}} \sim R_{\text{coll}}$ is the combined reaction radii of the electroactive species and the colloid particle, and $D = D_{\text{coll}} + D_{\text{rad}} \sim D_{\text{rad}}$, is the combined diffusion coefficient. However, charged species will also experience a force due to the electric field around the particle. In this case, the diffusive flux will "drive"

reactants toward the particle surface, which acts as a sink, while the electric field may augment or counteract the diffusive flux, further accelerating the reaction or retarding it. The flux of a hypothetical electron donor or reductant with concentration $c(r)$ and charge $z_R$ toward a spherical surface in the presence of a position dependent electric field $\psi(r)$ is

$$ J = -D\left[\frac{dc(r)}{dr} + c(r)\frac{z_R e}{kT}\frac{d\psi(r)}{dr}\right] \tag{5.26} $$

The boundary conditions are that $c = 0$ at $r = a$ (instantaneous reaction, so no molecules are at the surface) and $c = c^\infty$ (the bulk radical concentration) at $r = \infty$. Integration yields

$$ k_{\text{field}} = \frac{4\pi D}{\int_a^\infty \exp\left(\dfrac{z_R e\psi(r)}{kT}\right)r^{-2}\,dr} \tag{5.27} $$

Comparing Equations (5.25) and (5.27), we see that the integral in the denominator is the reciprocal of the "effective reaction radius." When $\psi(r) = 0$, Equation (5.27) reduces to the Smoluchowski equation (5.25); in the presence of a nonzero field, the denominator can be greater than or less than $a^{-1}$, depending on the signs of $z_R$ and $\psi(r)$. If they have the same sign, migration counteracts diffusion and the rate of particle–colloid encounters is lower than for neutral reactants. If $z_R$ and $\psi(r)$ have opposing signs, diffusion is aided by migration and the mass transfer-limited rate constant will exceed its usual "diffusion only" value. A similar situation exists in conventional ionic reactions in solution.

Solution phase reactants can only approach the surface to a distance $x_1$. Hence, the metal can be considered to have a radius $a$ and zeta potential $\zeta$, so that the boundary condition required for the integration of Equation (5.27) is $\psi(a) = \zeta$. Once at the shear plane or Helmholtz plane, transfer or deactivation is assumed to occur instantly. Thus for mass transfer-limited reactions, we need to know $D_{\text{rad}}$ and $a$, to calculate the Smoluchowski limit. In addition, when there is significant migration we need $n^\infty$ (the bulk electrolyte concentration), $z_R$ (the radical charge), and $\zeta$. To see how the field affects the mass transfer-limited rate constant, calculated values are shown in Figures 5.7 and 5.8 for conditions typical of nanosized metal colloids in aqueous solution. Figure 5.7 illustrates the dependence on the zeta potential (for $z_R = 1$) for three different electrolyte concentrations and Figure 5.8 the dependence of the mass transfer-limited rate constant on the radical charge (at $\zeta = -80$ mV). The flux of charged species due to migration rivals that due to the concentration gradient at high potentials and low ionic strength. When the two supplement each other, the rate may triple or quadruple, even at low radical charge. This should be readily discernible using flash photolysis or pulse radiolysis techniques. When the effects of the fluxes are opposing, the effect is far more dramatic, and the net flux to the colloid particle may be retarded by several orders of magnitude. Consequently,
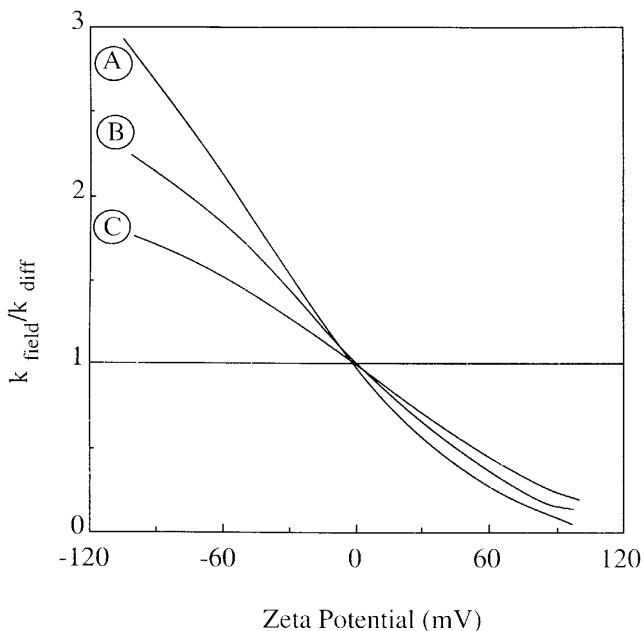
**FIGURE 5.7** Calculated effect of the diffuse double layer on the diffusion-limited rate constant for reaction between a molecule and a nanoparticle. Plot of the relative rate constant as a function of the zeta potential at three ionic strengths (A, 0.001 M; B, 0.01 M; C, 0.1 M) assuming $z_R = +1$, $a = 5$ nm, $D = 10^{-5}$ cm$^2$ s$^{-1}$.
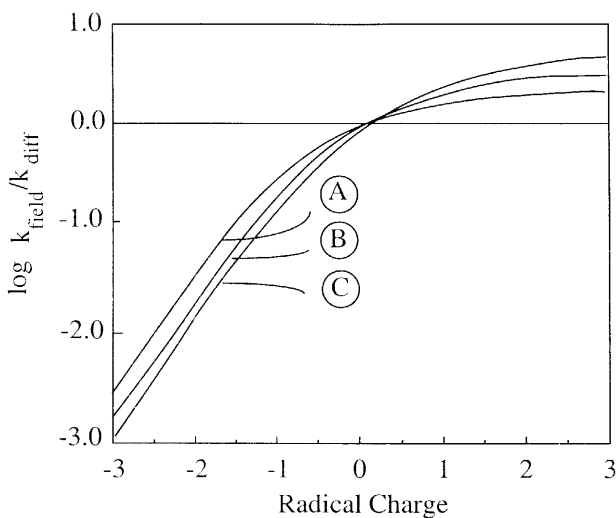


**FIGURE 5.8** Calculated effect of the diffuse double layer on the diffusion-limited rate constant for reaction between a molecule and a nanoparticle. Plot of the relative rate constant as a function of the radical charge at three ionic strengths (A, 0.1 M; B, 0.01 M; C, 0.001 M), assuming $a = 5$ nm, $D = 10^{-5}$ cm$^2$ s$^{-1}$, $\psi_0 = 0.08$ V.

the effect of the zeta potential on mass transfer will be most clearly seen when the double layer acts to retard diffusion. In some cases a second-order rate constant of just $10^7$ $M^{-1}$ $s^{-1}$ may correspond to the mass transfer-imposed limit on the rate of reaction. Given that low ionic strength and high zeta potentials are usually necessary for ionically stabilized sols, the usual criterion that the diffusion limit is reached at a value of $\sim 10^{10}$ $M^{-1}$ $s^{-1}$ will generally be invalid. Increases in salt concentration will decrease the importance of the migration term for mass transfer-limited reactions. The effects of added indifferent electrolyte will be to decrease $\zeta$, and to compress the double layer simultaneously. However, as can be seen from the figures, even in 0.1 M 1:1 electrolyte, pronounced deviations from the Smoluchowski value would be expected.

### 5.3.2   Activation-controlled Electron Transfer

For electron transfer into a colloid particle by a solution species (anodic reactions), the Tafel equation for the anodic electron transfer rate constant $k_{et}$ is given by

$$\log \frac{k_{et}}{k_{pzc}} = \frac{\beta F \, \Delta \psi}{2.303 RT} \tag{5.28}$$

where $\Delta \psi$ is the electric potential difference between the particle surface and the plane of electron transfer, and $k_{pzc}$ is the rate constant at $\Delta \psi = 0$. For simple cathodic electron transfer to an acceptor, the rate constant is given by

$$\log \frac{k_{et}}{k_{pzc}} = \frac{-(1 - \beta)F \, \Delta \psi}{2.303 RT} \tag{5.29}$$

The derivation of Equations (5.28) and (5.29) is given in standard electrochemistry texts, and a clear and detailed description is given in the text by Faulkner and Bard, and also in the classic text by Delahay.[10,11] In particular, these equations assume no chemical adsorption of the reactant. It is assumed the rate can be measured at an uncharged metal surface as a reference state, which is not generally practical unless the colloid is stabilized by polymers, which in turn may reduce the available, active surface of the metal.

If the ionic strength is high, the diffuse layer capacitance $K_d \to \infty$, and the total double layer field is confined to the Helmholtz layer. This is illustrated pictorially in Figure 5.9. At the same time, the zeta potential then approaches zero, and the potential difference acting on the transferring electron approaches $\Delta \psi \to \psi_0$. Under these conditions, the entire change in electrode potential can be considered to act on the electrons tunnelling from donor to surface (or surface to donor). However, in colloid systems, a high salt concentration will destabilize the sol, since if $\zeta \to 0$, there is no resistance to coagulation. Hence Equations (5.28) and (5.29) are extremely difficult to apply to colloid systems, since it is awkward to work either at the pzc or under conditions of high salt. To correct the equations for the situation of low ionic strength, a "double layer" correction is needed, which has been discussed in detail elsewhere. The exact distribution of the electric potential between the
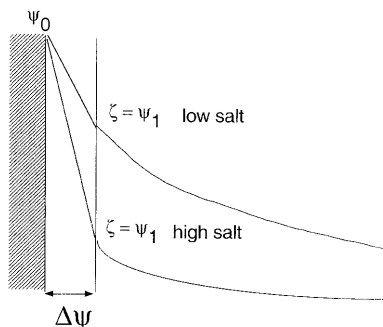
**FIGURE 5.9**    Model showing the effect of salt on a simple ZOS model double layer. If $\psi_0$ is fixed, then the potential difference across the Stern layer rises as salt is added, while the potential across the diffuse layer decreases concomitantly. Hence the zeta potential tends towards zero, and the potential across the Stern layer tends to $\psi_0$. The potential across the Stern or Helmholtz layer affects the rate constant for simple electron tunneling through Equations (5.28) and (5.29), while the zeta potential affects the concentration of species at the OHP where electron transfer takes place through Equation (5.8).

Helmholtz layer and the diffuse layer is sensitive to electrolyte concentration and particle size, as well as the capacitance of the Helmholtz layer, which is determined by its thickness and local dielectric constant, In Figure 5.10, we show some numerical results for the zeta or Helmholtz potential using the nonlinear PB equation and a Zero Order Stern (ZOS) model. As can be seen, the exact potential distribution, which determines the effective overpotential for electron transfer, depends sensitively on the chosen value for the Helmholtz capacitance.

### 5.3.3    Hydrogen Formation on Colloidal Metals

We conclude this outline of simple electron transfer reactions with metal colloid particles by looking at hydrogen evolution in terms of the equations we have just described. This reaction is fundamental to science and the human race, since renewable and clean energy sources are needed to replace rapidly depleting fossil fuels. It is well understood on metal electrodes, and the high surface area of nanoparticle systems makes metal nanoparticles attractive candidates for hydrogen catalysis.

Colloidal metals have long been known as potent catalysts of reactions in solution. Colloidal platinum, for example, is commonly used in hydrogenation reactions, and it also greatly accelerates the decomposition of hydrogen peroxide and hydrazine in aqueous solution. In these cases, the catalytic role of the metal may be investigated electrochemically, since the reactants are kinetically stable in aqueous solution. However, in the study of catalyzed redox reactions involving free radicals or photochemically generated species, the catalysts must be dispersed within the medium to compete successfully with recombination reactions and fast radiative (or
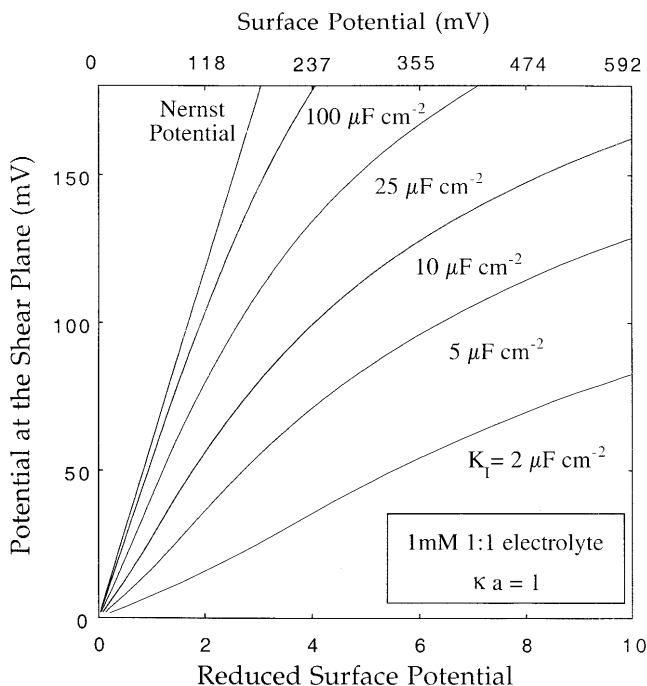
**FIGURE 5.10** The relative values of the diffuse layer potential and surface potential for a nanoparticle system where $I = 1$ mM and $a = 10$ nm as a function of the Helmholtz layer capacitance. Calculations for the diffuse layer capacitance from numerical solutions to the PB equation, combined with Equation (5.21) for the effect of the Helmholtz capacitance on the potential at $x_1$. For low values, the zeta potential rises almost as fast as the surface potential; but as the diffuse layer capacitance increases with surface potential, zeta eventually flattens off.

nonradiative) relaxation processes, which dissipate the chemical energy of the excited reactants. Radical deactivation reactions usually involve single electron or hydrogen atom transfers, and very often the role of the colloidal catalyst is to divert the reaction to a multielectron redox process rather than just accelerating the rate of the bulk solution reaction. Dispersed metal catalysts must therefore be capable of storing reducing equivalents as electrons or hydrogen atoms, thereby facilitating multielectron redox reactions in homogeneous solution.

Wagner and Traud were the first to formulate the concept of redox catalysis in order to explain open circuit (corrosion) potentials on zinc electrodes,[12] although the idea was already present in earlier papers by Frumkin.[13] It was suggested that the open circuit potential was determined by the kinetics of coupled electrode reactions. Their additivity principle stated that the measured $i-E$ curve was the algebraic sum of the individual $i-E$ curves for each electroactive redox couple. Furthermore, this idea implied that both oxidation and reduction reactions could take place simultaneously over the entire surface, and not just at distinct sites (the "local cell"

mechanism) as previously assumed. This concept was subsequently developed by Spiro and coworkers, who confirmed that the catalytic effect of a platinum electrode was directly related to the intrinsic electron exchange rates of the individual couples with platinum; that is, reactions involving reversible couples were more efficiently catalyzed than those with irreversible couples.[14] Their work also proved that catalysis by metals was truly electrochemical, and that the mechanism of catalysis did not simply involve adsorption of reactants onto the catalyst surface and thus faster rates of reaction by virtue of enhanced local concentrations, but proceeded by electron relay through the metal. Kiwi and Grätzel carried out the first systematic study of colloidal platinum as a photochemical hydrogen catalyst in a colloid system, and examined particle size, polymer stabilization, and interfacial electron transfer dynamics.[15] Henglein and Lilie demonstrated that an electrochemical mechanism was operative on colloidal silver-catalyzed free radical reactions[16] and Miller *et al.* used modified forms of Spiro's equations to treat hydrogen evolution by photo-generated and electrogenerated reductants on colloidal metals.[17,18]

The consensus that emerged throughout the 1980s is that the colloidal metal is considered to couple two (or more) electron transfer reactions; one is the oxidation of a reductant or donor species

$$D \leftrightarrow D^+ + e^- (\text{colloid}) \tag{5.30}$$

and the other is the reduction of an acceptor species by stored electrons on the catalyst

$$A + e^- (\text{colloid}) \rightleftharpoons A^- \quad E_{31}^0 > E_{30}^0 \tag{5.31}$$
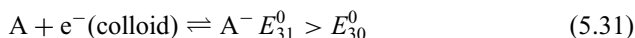
If we assume that electron transfer is activation controlled, the specific rate of reaction (mol cm$^{-2}$ s$^{-1}$) of the donor couple is given by

$$Rate1 = 4\pi a^2 k_1 [D^+] \exp[-(1-\beta_1)f(E - E_{\text{pzc}})] - 4\pi a^2 k_{-1}[D] \exp[\beta_1 f(E - E_{\text{pzc}})] \tag{5.32}$$

where we have included the back reaction of electrons with oxidized donors, and

$$Rate2 = 4\pi a^2 k_2 [A] \exp[-(1-\beta_2)f(E - E_{\text{pzc}})] - 4\pi a^2 k_{-2}[A^-] \exp[\beta_2 f(E - E_{\text{pzc}})] \tag{5.33}$$

for the acceptor couple, where $f = F/RT$, $A$ is the surface area of the particle, $\beta_1$ and $\beta_2$ are the anodic transfer coefficients for the respective reactions, and $k_1$ and $k_2$ are the rate constants for each half-reaction (cm s$^{-1}$) at $E_{\text{pzc}}$. The concentrations refer to the values at the plane of electron transfer, normally assumed to be the outer Helmholtz plane (OHP) as outlined in section 5.2.1. In deriving these equations, we have modified them slightly from the original by altering the reference point for the

potential from the equilibrium redox potential, where zero current flows, to $E_{pzc}$, where there is no overpotential driving the electron transfer.

Under steady-state conditions, the rates at which the colloid particle is charged and discharged are equal, and the mixed potential of the colloidal metal particles (versus NHE) is found from the condition

$$Rate1 = -Rate2 \qquad (5.34)$$

It is important to recognize that it is the transferred charge that couples the system. Donors transfer electrical charge to the metal particle. This makes the surface potential $E$ (and the zeta potential) more negative. The more negative the surface potential becomes, the faster the rate of electron transfer from the metal to the acceptor, as seen through Equation (5.33). The static charge that builds up creates a "mixed" surface potential that enables both oxidation and reduction to take place at the same speed. If both reactions are facile, and there is a reasonable difference in the redox potentials of the two couples, then the back reactions can be neglected, and the mixed potential occurs when

$$4\pi a^2 k_2[\text{A}] \exp[-(1 - \beta_2)f(E - E_{pzc})] = 4\pi a^2 k_{-1}[\text{D}] \exp[\beta_1 f(E - E_{pzc})] \quad (5.35)$$

If the rate of electron transfer becomes very high because the particle mixed potential is very positive or very negative, then the reaction may become diffusion-limited, in which case the rate will be given by Equation (5.25) or (5.27); for example, for diffusion-limited electron injection into metal colloid particles the mixed potential will occur when

$$4\pi a^2 k_2[\text{A}] \exp[-(1 - \beta_2)f(E - E_{pzc})] = 4\pi a D[\text{D}] \qquad (5.36)$$

This is the observed rate of reaction per particle of radius $a$. Multiplying through by the colloid particle concentration yields the observed rate of reaction in the solution. We have neglected diffuse layer effects. Under ideal conditions, both donor and acceptor reactions would occur under mass transfer control. Note that in writing the "overpotential" or potential driving the electron transfer as $E - E_{pzc}$, we can in principle convert this using Equation (5.2b) into the actual surface potential. This potential may be experimentally accessible to some degree through colloid electrophoresis.

In the case of hydrogen evolution, protons (or water in alkaline solution) are the electron acceptors. The hydrogen discharge reaction occurring on the metal colloid surface can be broken into two basic steps, a proton discharge step,

$$\text{H}^+ + \text{e}^- \rightarrow \text{H} \qquad (5.37)$$

followed by a discharge of hydrogen atoms either by surface recombination

$$H + H \rightarrow H_2(\text{ads}) \tag{5.38}$$

or by electrochemical discharge (Heyrovsky reaction)

$$H + e^- + H^+ \rightarrow H_2(\text{ads}). \tag{5.39}$$

In parallel with electrochemical studies, two types of behavior are observed in radical-catalyzed hydrogen production on colloidal metal.[19] When reaction (5.37) is the rate-determining step, proton uptake by the colloid occurs more slowly than electron transfer by radicals. It is necessary to accumulate significant electronic charge on the particles to drive the cathodic half-reaction, that is, proton reduction. The resulting excess negative charge alters the Helmholtz potential difference by decreasing $E$ in Equations (5.32) and (5.33), which slows down the rate of further electron transfer but accelerates the rate of proton transfer [by increasing the rate of the forward reaction in Equation (5.33)]. A stationary charge builds up on the metal until, under steady-state conditions, the rates of both proton and electron transfer to the colloid particles become equal. The stationary charge per particle increases with increasing rates of electron injection, and decreases as the pH is decreased. Some data for silver are shown in Figure 5.11, where the steady-state charge on a silver colloid is plotted against the solution pH (i.e., as a function of acceptor concentration) under conditions in which the electron injection rate has been held constant.[16] It is seen that the steady-state charge varies as the logarithm of the acceptor concentration. This fits in well with the predictions of Equations (5.35) and (5.36) if reaction (5.37) is the rate-determining step (rds). Reaction (5.37) seems to be the rds for gold, silver and cadmium sols, based on both pulse radiolysis and $\gamma$-radiolysis–conductivity results.[19] For more efficient catalysts like platinum and
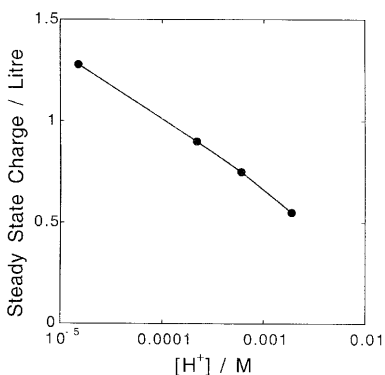


**FIGURE 5.11**   Steady-state, excess electron concentration on silver colloid particles as a function of pH under conditions where the cathodic charging rates are identical. Charging rate $\sim 5$ μM/min, $N_{\text{agg}} = 11,430$ Ag atoms per silver colloid, radius $= 3.6$ nm.

iridium, proton uptake is observed to occur at the same rate as radical consumption[20] Hence the platinum particles become covered with adsorbed hydrogen atoms, rather than free electrons. In this case, no transient charge builds up on the colloid during hydrogen evolution and, consequently, surface diffusion of hydrogen atoms or even molecular $H_2$ desorption may become rate-determining.

At the present time, it is difficult to determine whether reaction (5.38) or (5.39) is the rate-determining step for highly active platinum, iridium, or palladium sols, because of the difficulty in measuring the steady-state surface coverage by hydrogen atoms during catalysis. A complete solar energy conversion system capable of driving the photochemical oxidation and reduction of water has not been success-fully found to date. However, sacrificial photochemical systems in which hydrogen is formed from a "cheap" donor using semiconductor particles as photosensitizers have been examined with a view to applications in removal of water pollutants. The photoelectrons generated inside the semiconductor would form hydrogen or hydrogen peroxide (under anaerobic or aerobic conditions, respectively) on metal nanoparticles adsorbed to the semiconductor surface, while the photogenerated holes would oxidize pollutant molecules such as sulfides, PCBs, sewage or even harmful bacteria. The photoelectrochemistry of semiconductor and metal nanoparticlcs has been reviewed by one of the pioneers of this field.[21]

We have tried to outline what is generally accepted about the complex processes of electron transfer at colloid metal surfaces. A key issue is to what extent spec-troscopy might allow us to gain further insight into these surface processes. Hence, we now turn to one of the main features of metal nanoparticle systems, which is their optical properties. We will determine the basic equations for measuring the optical properties of small colloid particles, then focus on some of the peculiarities of metal particles in particular.

## 5.4   OPTICAL PROPERTIES

### 5.4.1   Light Absorption by Colloids

In the presence of a dilute colloidal solution containing *N particles* per unit volume, the measured attenuation of light of intensity $I_0$, over a pathlength $x$ cm in a spec-trophotometer is given in differential form as

$$\frac{dI(x)}{dx} = -NC_{\text{ext}}I(x) \tag{5.40}$$

which shows that the rate of loss of photons is proportional to the light intensity at distance $x$ into the medium, and also to the number density of light-extinguishing particles. Integration gives the solution absorbance,

$$A = \log_{10}\frac{I_0}{I(x)} = \frac{NC_{\text{ext}}x}{2.303} \tag{5.41}$$

where $C_{ext}$ is the extinction cross-section of a single particle. For spherical particles with a complex, frequency-dependent dielectric function $\varepsilon = \varepsilon' + i\varepsilon''$, embedded in a medium of dielectric function $\varepsilon_m$, $C_{ext}$ is given by[22]

$$C_{ext} = \frac{2\pi}{k^2} \sum_{n=1}^{n=\infty} (2n + 1)\, \mathrm{Re}(a_n + b_n) \tag{5.42}$$

where

$$k = \frac{2\pi\sqrt{\varepsilon_m}}{\lambda} \tag{5.43}$$

and $a_n$ and $b_n$ are the scattering coefficients, which are functions of $a$ and $\lambda$ in terms of Ricatti–Bessel functions. The extinction cross-section of a particle is often normalized to give the extinction cross-section per unit area:

$$Q_{ext} = \frac{C_{ext}}{\pi R^2} \tag{5.44}$$

Conventionally, chemists measure the extinction coefficient of a solution in units of $M^{-1}\,cm^{-1}$, where the colloid concentration is the *molar metal atom* concentration. For particles of radius $R$ (cm), this quantity is related to $Q_{ext}$ by

$$\varepsilon(M^{-1}\,cm^{-1}) = 3 \times 10^{-3} \frac{V_m Q_{ext}}{4(2.303R)} \tag{5.45}$$

where $V_m$ (cm$^3$ mol$^{-1}$) is the molar volume of the metal. Bohren and Huffman provide various approximations that may be used instead of the full series expansion. In particular, for very small particles where $kR \ll 1$, only the first, electric dipole term, is significant, and Equation (5.42) reduces to

$$C_{ext} = \frac{24\pi^2 R^3 \varepsilon_m^{3/2}}{\lambda} \frac{\varepsilon''}{(\varepsilon' + 2\varepsilon_m)^2 + \varepsilon''^2} \tag{5.46}$$

This equation can also be obtained by purely electrostatic arguments, and a succinct derivation is given elsewhere.[23] Note that $C_{ext}$ scales as $R^3$, while the number density decreases as $R^3$ for a given amount of colloidal material. Hence the absorption coefficient is independent of particle size. This is borne out for particles in the range up to about 30 nm, where scattering begins to be significant. At the other end of the scale, for very small particles $<5-10$ nm in diameter, the material properties themselves change, and this results in changes to the dielectric function, $\varepsilon(\omega)$, and hence to the colloid optical properties. A curious feature of Equation (5.46) is that there is no absorption if $\varepsilon'' = 0$, but there is also no absorption if $\varepsilon'' = \infty$.

### 5.4.2   Simple Dielectric Response of Free Electron Metals

The above equations link the amount of light scattered or absorbed by a spherical particle in a certain solution to the dielectric properties of the particle and of the solvent. The dielectric functions are difficult to calculate from first principles, and usually experimental data are used in calculations. However, in the case of many metals, the absorption in the visible region and up to the bulk plasma frequency (in the near-UV) is dominated by the free electron behavior, and the dielectric response is well described by the classical Drude model. According to this theory,[24] the electron within the metal is assigned its free mass $m_e$ and some velocity $v$. The electron is accelerated by the electric field vector of the incident radiation of frequency $\omega$,

$$E = E_0 \exp(-i\omega t) \tag{5.47}$$

The electron in the metal while being accelerated experiences collisions with the lattice, with other electrons, and with impurities at a rate proportional to its velocity. These collisions immediately reduce its velocity back to zero. Then the average velocity of the electron can be calculated to be roughly $eE\tau/m$, where $\tau$ is the time between collisions. The equation of motion is then

$$mx'' + \gamma x' = eE \tag{5.48}$$

The term $\gamma \ (= \tau^{-1})$ represents the viscous loss due to collisions. This is similar to the equation of motion for a simple harmonic oscillator, but with the restoring force set to zero. In a chemical bond, the displacement of the electron sets up a restoring force due to the positive nuclear charge on the ion, which "pulls" the electron back to the equilibrium bond length. In a metal, the nuclear charge is shielded by the other neighboring conduction electrons, so the electrons do not experience a restoring force. The only loss is the "viscous" drag on the electron, as it loses energy through lattice collisions, which results in energy being converted into phonons. Let us retain this restoring force in the equations, and see what effect it has on the overall conclusions we can draw. Then,

$$mx'' + \gamma x' + kx = eE_0 \exp(-\omega t) \tag{5.49}$$

The steady-state solution to this equation is

$$x = \frac{eE/m}{\omega_0^2 - \omega^2 - i\omega_d\omega} \tag{5.50}$$

Here we have used $\omega_0^2 = k/m$ and $\omega_d = \gamma/m$ and $\omega_0$ is the resonance frequency of the oscillator. We see that for a nonzero $\omega_0$, there will be a certain frequency for which $x$ will be a maximum, close to $\omega_0$. Also important is the fact that below $\omega_0$, the electrons have a displacement $x$ in the same direction as the applied field $E$. Above $\omega_0$, the displacement is in the opposite direction to the field. If we have $N$

such free electrons per unit volume, then this will create a dipole $P = Nex$ as the electrons oscillate at the driving frequency of the radiation. For a bulk material held between two parallel plates, the linear, dielectric function is defined via

$$P = \chi \varepsilon_0 E = \varepsilon_0 (\varepsilon - 1)E \tag{5.51}$$

Inserting Equation (5.51) into (5.50) yields

$$\varepsilon(\omega) = 1 + \frac{Ne^2/m\varepsilon_0}{\omega_0^2 - \omega^2 - i\omega_d\omega} \tag{5.52}$$

The real and imaginary parts of the dielectric function may be written

$$\varepsilon'(\omega) = 1 + \frac{(\omega_0^2 - \omega^2)\omega_p^2}{(\omega_0^2 - \omega^2)^2 + \omega_d^2\omega^2} \tag{5.53}$$

and

$$\varepsilon''(\omega) = \frac{\omega_d\omega_p^2\omega}{(\omega_0^2 - \omega^2)^2 + \omega_d^2\omega^2} \tag{5.54}$$

However, for the free electrons, $\omega_0$ is zero and for this special case we obtain

$$\varepsilon'(\omega) = \varepsilon^\infty - \frac{\omega_p^2}{\omega^2 + \omega_d^2} \tag{5.55}$$

$$\varepsilon''(\omega) = \frac{\omega_p^2\omega_d}{\omega(\omega^2 + \omega_d^2)} \tag{5.56}$$

$\varepsilon_\infty$ is the high-frequency dielectric constant due to interband and core transitions, and $\omega_p$ is the bulk plasma frequency,

$$\omega_p^2 = \frac{Ne^2}{m\varepsilon_0} \tag{5.57}$$

in terms of $N$, the concentration of free electrons in the metal, and $m$ the effective mass of the electron. Note the peculiar fact that a free electron metal can be considered as an oscillator where $\omega_0$ is zero. This means that for all frequencies, the oscillating electrons are out of phase with the applied field. This results in $\varepsilon'$ being negative over a very wide range, not just around a certain absorption frequency $\omega_0$.

In Figures 5.12 and 5.13, we have plotted out the dielectric functions for a simple oscillator and for the free electron case. In addition, we have fed those functions into Equation (5.46) to show how the "Mie" resonance bands appear. A high polarizability results when the oscillator has negative values of $\varepsilon'$. From Equation (5.55) it can be seen that over the whole frequency regime below the bulk plasma frequency
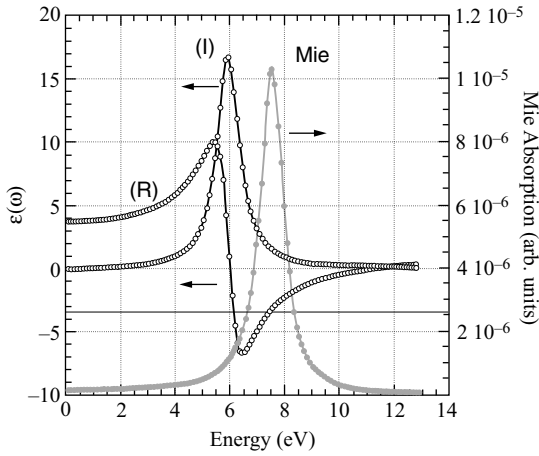
**FIGURE 5.12** Plot of the real (R) and imaginary (I) parts of the dielectric function of a simple harmonic oscillator as a function of frequency for values of $\omega_p = 10$ eV, $\omega_0 = 6$ eV, $\omega_d = 1$ eV, and also a plot of the scaled Mie absorption function: $\lambda^{-1} \, \mathrm{Im}((\varepsilon + 2\varepsilon_m)^{-1})$ (Equation 5.46), showing the Mie resonance. Note that the oscillator absorbs at a higher frequency than $\omega_0$ in the medium.
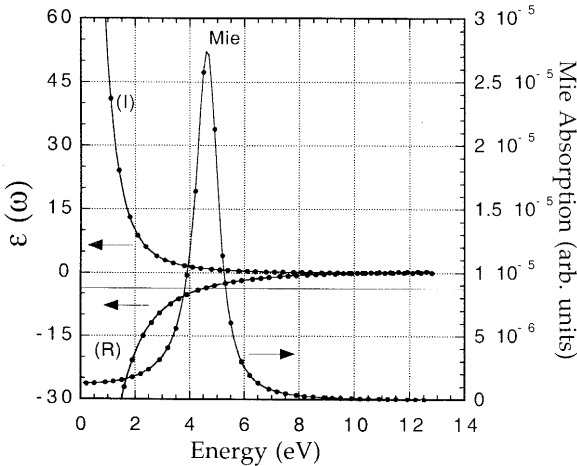


**FIGURE 5.13** Plot of the real (R) and imaginary (I) parts of the dielectric function of a simple free electron system as a function of frequency for values of $\omega_p = 10$ eV, $\omega_0 = 0$ eV, $\omega_d = 1$ eV, and also the scaled Mie absorption function, $\lambda^{-1} \, \mathrm{Im}((\varepsilon + 2\varepsilon_m)^{-1})$ showing the Mie resonance (Equation 5.46). Note that the free electrons absorb at a lower frequency than $\omega_0$ for the equivalent harmonic oscillator, because of the lack of restoring force, and the band is substantially more intense, due to the lower damping. For metals, the colloids have an intense band where the bulk metal does not appear to absorb strongly, and drastic color changes occur as the particles become smaller than the wavelength of light. For the harmonic oscillator, Mie absorption is close to the intrinsic band position, and color changes are not as pronounced.

of a metal, $\varepsilon'$ is negative, which is due to the fact that the polarization field is larger than, and opposite in sign to, the applied field. In a small metal particle the dipole created by the electric field of the light wave sets up a surface polarization charge, which effectively acts as a restoring force for the "free electrons." The net result is that the long-wavelength absorption by the bulk metal is condensed into a single, surface plasmon band. In the case of semiconductor crystallites, the free electron concentration is orders of magnitude smaller, even in degenerately doped materials (i.e, $\omega_p$ is smaller), and as a result surface plasmon absorption occurs in the infrared (IR) rather than in the visible part of the spectrum. Semiconductor crystallites therefore do not change color significantly when the particle size is decreased below the wavelength of visible light, although the IR spectrum may be affected. The strong color changes observed when semiconductor crystallites are in the quantum size regime ($R <\sim 50$ Å) are due to the changing electronic band structure of the crystal, which causes the dielectric function of the material itself to change.

### 5.4.3    Size Effects

It turns out that, for metals, the surface begins to affect the metal's properties when the particles are still 10–50 nm in size, and for accurate work on the nanoparticle optical properties a correction to the dielectric function for small metal particles needs to be introduced. For a bulk metal, $\omega_d$ is the relaxation or damping frequency, which is related to the mean free path of the conduction electrons, $R_{bulk}$, and the velocity of electrons at the Fermi energy, $v_F$, by

$$\omega_d = \frac{v_F}{R_{bulk}} \tag{5.58}$$

Fitting this value to the experimental data, values between $R = 10.8$ and 37 nm are obtained for gold, and values of about 52 nm for silver. In the Drude model, this length represents collisions of the electron with the lattice (phonon coupling) and defects. When the particle radius, $R$, is smaller than the mean free path in the bulk metal, conduction electrons are additionally scattered by the surface, and the mean free path, $R_{eff}$, becomes size-dependent with

$$\frac{1}{R_{eff}} = \frac{1}{R} + \frac{1}{R_{bulk}} \tag{5.59}$$

Equation (5.59) has been experimentally verified by the extensive work of Kreibig for both silver and gold particles right down to a size of 2 nm.[25] The advantage of the Drude model is that it allows changes in the absorption spectrum to be interpreted directly in terms of the material properties of the metal. In Figure 5.14, a "typical" surface plasmon band is shown, calculated using Equation (5.46) with parameters typical of silver for several values of the damping parameter $\omega_d$. The most important parameter affecting $\omega_d$ is the particle size. From Equations (5.55) and (5.58) it can be seen that decreases in the particle size lead to an increase in $\omega_d$, causing the band to broaden and the maximum intensity to decrease. The position of the peak is
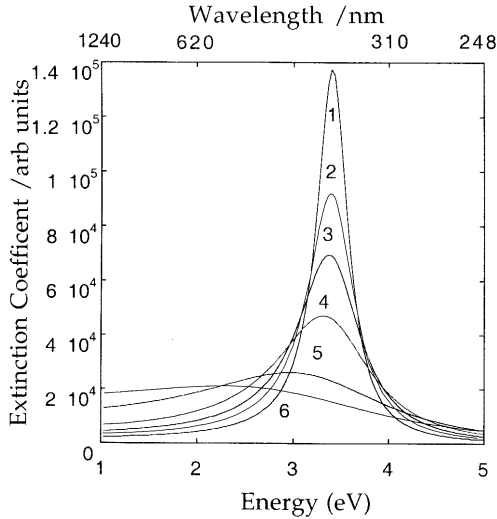
**FIGURE 5.14**   The mean free path effect on an SP band using Equation (5.46). If the damping frequency is increased, due to decreasing size or to impurities or grain boundaries or lattice defects, the surface plasmon band decreases in maximum intensity and broadens. Increasing $\omega_d$ increases $\varepsilon''$. Values used for the calculations are $\omega_p = 10$ eV, $\varepsilon_\infty = 5.0$, and damping values from 1 to 6 are $\omega_d = 0.4, 0.6, 0.8, 1.2, 2.4$ and $3.6$ eV. These values can be converted to mean free paths using Equation (5.58).

virtually unaffected by small changes to $\omega_d$, but for large damping a slow shift to lower energies occurs. For exceedingly small particles ($< 1-2$ nm), quantization of the energy levels within the conduction band takes place as the metal character of the particles begins to disappear, and the plasmon band characteristic of the delocalized electrons breaks up into discrete bands due to single electron optical transitions. In the case of silver particles, quantization results in a blue-shift of the plasmon band and a break-up into discrete excitation bands ranging from 260 to 395 nm.[26] In summary, the origin of the strong color changes displayed by small particles lies in the denominator of Equation (5.46), which predicts the existence of an absorption peak when

$$\varepsilon' = -2\varepsilon_m \qquad \text{(if } \varepsilon'' \text{ small)} \tag{5.60}$$

For metals, this results in a new absorption band shown in Figure 5.13. which alters the color of the metal dramatically as the size is decreased. For insulators and semiconductors, the Mie peak is close to the position of the bulk absorption bands, and the immediate effect of decreasing particle size is much smaller.

### 5.4.4   The Effect of the Solvent Refractive Index

One of the most obvious consequences of Equation (5.60) for the surface plasmon band is that the peak position will be affected by the dielectric properties of the
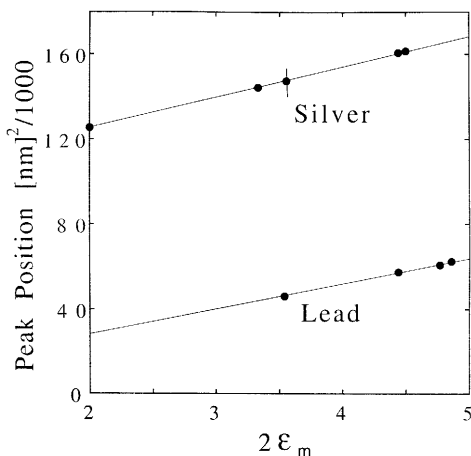
**FIGURE 5.15**    Plot of the surface plasmon peak as a function of the solvent refractive index ($\varepsilon_m = n^2$) for lead and silver colloids, showing experimental data in a range of matrices, and the fit to the experimental data using the approximation Equation (5.61).

solvent; $\varepsilon_m = n^2$, where $n$ is the refractive index of the (nonabsorbing) medium. Using Equations (5.55) and (5.57), we find, for small $\varepsilon''$, that the band position should obey

$$\lambda^2 = \lambda_p^2(\varepsilon_\infty + 2\varepsilon_m) \tag{5.61}$$

where $\lambda_p^2 = (2\pi c)^2/\omega_p^2$ is the metal's bulk plasma wavelength. From a plot of the observed band position in different solvents versus $2\varepsilon_m$, both the high-frequency dielectric constant and the bulk plasma frequency (or wavelength) can be extracted. A plot of $\lambda^2$ versus $2\varepsilon_m$ is shown for lead and silver colloids in Figure 5.15. From the data for lead we find that the bulk plasma energy is 11.3 eV and $\varepsilon_\infty = 1.1$,[27] not far from the values for the bulk metal. In the case of silver, the band position in water is variable, but interpolating the values from the salt matrices, we predict that the "true" position of the silver surface plasmon position band in water is $382 \pm 1$ nm. The high-frequency dielectric constant is estimated to be 5.9, not far from other estimates of 4.7–5.3. Adherence to Equation (5.61) demonstrates that the absorption of light by the particles over the spectral region is due to the absorption by conduction electrons, rather than interband transitions. Equation (5.61) is only an approximation but it works well for metals where the interband absorption is not too influential. For gold, the full Mie equations plus size effects need to be used to obtain good agreement with experiment. In addition, the dielectric data used should be for polycrystalline material. In Figure 5.16, we show the position of the surface plasmon band for gold as a function of the solvent refractive index. There is excellent agreement with theory if size effects are included.
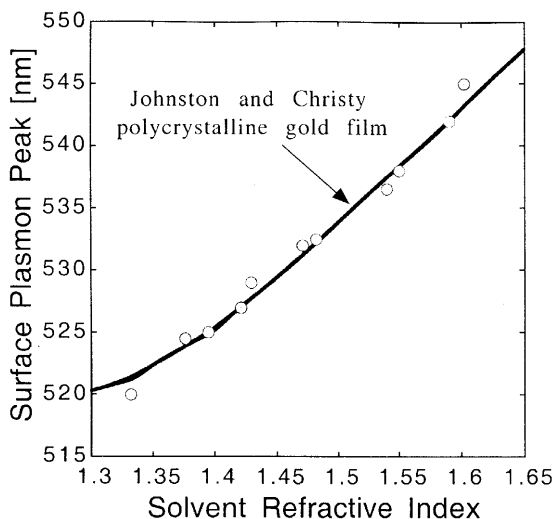
**FIGURE 5.16**    Plot of the surface plasmon peak as a function of the solvent refractive index for gold colloids, showing experimental data in a range of solvents, and the exact Mie theory predictions from Equation (5.42) using dielectric data for polycrystalline gold from Johnston and Christy.

Mie calculations by Creighton and Eadon[28] have indicated that, for the majority of metals, surface plasmon absorption contributes significantly to the UV–visible spectrum. Very little experimental work has been done on the more electropositive metal sols, because they are so readily oxidized by air, and the work is almost entirely confined to salt matrices.[29] However, more recently it has become possible to prepare well-characterized samples using radiolytically generated reductants to ensure rapid nucleation. A primary experimental difficulty is the determination of the particle size, since the sols dissolve instantaneously in air, and must be transferred into electron microscopes with the rigorous exclusion of oxygen. In Figure 5.17, the extinction spectra of cadmium sols are shown together with the calculated spectra using Equation (5.46). In this case the plasmon band is located at about 260 nm, and water absorption masks a small part of the high-energy flank of the plasmon band. The good agreement with the predictions of Mie theory supports the idea that the particles are small and reasonably round. In addition, since no size effect is included, but the width of the absorption band is pretty close to the experimental value, we can conclude that the mean free path for conduction electrons in cadmium is less than 10 nm. Cadmium sols are yellow, and in fact many metal sols appear yellow or brown in color. The reason for this is that the plasma frequencies for most metals lie in the UV, and the color of the nanoparticle colloid is due to the tail of the surface plasmon band: Being broad, it tends to produce a yellow color. Upon aggregation or growth, the band tends to broaden and deepen, so that the color changes slowly to a deeper brown.
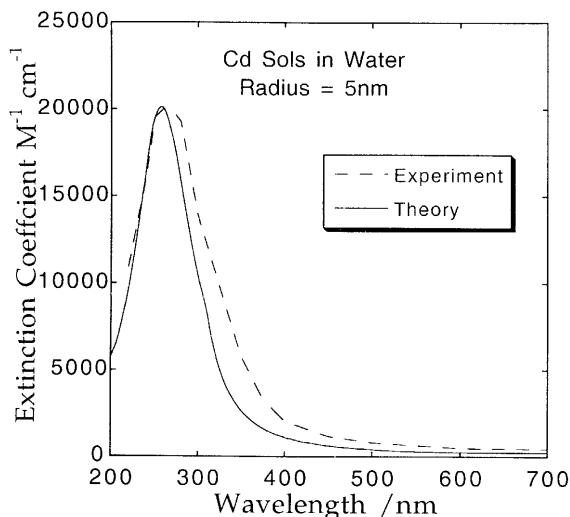
**FIGURE 5.17** Experimental and calculated spectra of colloidal cadmium. The surface plasmon band for cadmium is in the UV, as for most metal nanoparticles. The visible absorption of light is then just due to the tail of the SP band, and being broad tends to result in a yellow or pale brown color. The color depends only weakly on size. If the band red-shifts due to coalescence, the tail just becomes a little more intense and broader and the colloid becomes darker.

### 5.4.5  Electron Transfer and Plasmon Band Shifts

When electrons from a reductant transfer to a metal particle, the electrons are donated to the conduction band. The free electron density rises, and hence the plasma frequency of the metal must also rise. This implies a change in the dielectric function of the particles, and hence an optical shift. In fact it is clear that if $\omega_p$ rises, then a blue-shift in the spectrum should be observed. This has been demonstrated for silver colloids using pulse radiolysis. Irradiation of solutions containing 2-propanol and acetone produces the strong reducing radical $(CH_3)_2COH$. The radicals react with the sol particles according to

$$(CH_3)_2COH + Ag_n \rightarrow Ag_n^- + H^+ + (CH_3)_2CO \tag{5.62}$$
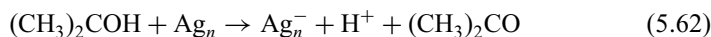
The transfer of electrons results in the release of protons into solution, and the resultant transient conductivity signal can be used to monitor the rate of electron transfer. This was discussed in section 5.3.3. Now we see that not only does electron transfer result in changes to the solution redox couple absorption, but that the colloid changes its absorption properties as well, when its charge state is altered. Absorption changes to the sol take place with bleaching at longer wavelengths and increased absorption at shorter wavelengths than the peak, as shown in Figure 5.18. Further
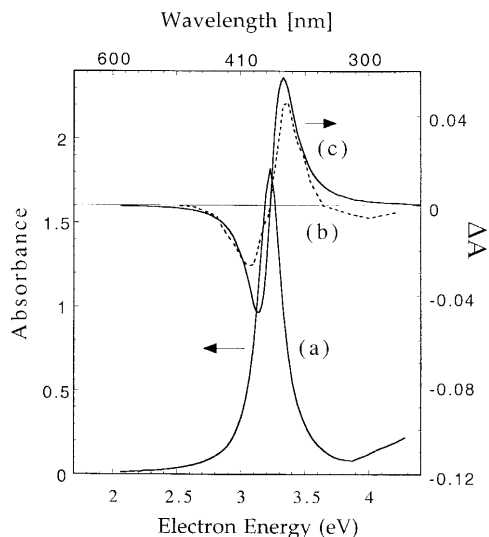
**FIGURE 5.18**    Curve a: Experimental spectrum of colloidal silver prepared by $\gamma$-radiolysis. Curve b: Observed change in the absorption spectrum of colloidal silver 10 m after electron injection by radiolytically produced donor radicals. Curve c: The calculated changes using Equation (5.42), after adjusting the electron density $N$.

bleaching occurs at 320 nm, close to the onset of $d$-band to Fermi level transitions. The discharge of the sols by solvent reduction or other oxidants limits the attainable negative charge on the particles:

$$e^-_{coll} + H^+ \rightarrow \tfrac{1}{2} H_2 \tag{5.63}$$

The transfer of electrons alters the free electron concentration and therefore the bulk plasma frequency, $\omega_p$. From Equations (5.46) and (5.57), it is clear that this will result in a blue-shift of the surface plasmon absorption band.

Nanosized metal particles have an enormous double layer capacitance ($K_{total} = 4\pi a^2 K_I$ from section 5.2.1) and in changing the environment in the solution from oxidizing to reducing a large double layer charge must build up on the particles. At fairly high salt concentrations the double layer capacitance is due to the Helmholtz layer, and inserting $\varepsilon_r = 6$, $x = 3$ Å, we get $K_I \sim 20\,\mu F\,cm^{-2}$. Then a crude estimate suggests that a 14% change in the electron density is needed if the redox potential in a 30 Å diameter particle is to be raised from the ambient level in air of about $+0.4$ V vs. NHE to around $-0.4$ V vs. NHE, where $H_2$ evolution begins. This corresponds to a plasmon band shift from 390 nm to 375 nm. This is consistent with the fact that citrate-stabilized silver sols typically have an absorption band around 385–390 nm, whereas extensively $\gamma$-irradiated silver sols (strong reducing conditions) possess absorption bands at $\lambda < 380$ nm and steadily evolve hydrogen.

Unless a reductant is used that has a redox potential identical to the potential of zero charge of polycrystalline silver ($-0.7$ V vs. NHE), chemically produced sols will always contain residual electric charge and will possess plasmon absorption bands shifted from the position expected for an electrically neutral particle. Based on the dielectric data for bulk silver, an uncharged silver colloid should have a maximum at $382 \pm 1$ nm; wavelengths shorter than this are due to cathodic polarization, and longer wavelengths to incomplete reduction of silver ions.

### 5.4.6  Temperature Effects

In previous sections we have examined the way that a variety of factors perturb the basic optical response of the colloid particles to radiation. We now are in a position to consider the general effects of heating.[30] Heat can affect solutions and particles in numerous ways. However, the most significant effect is a damping of the surface plasmon band. In order to account for the plasmon damping at elevated temperatures, we need to consider four possible contributions: metal expansion, solvent refractive index changes, solvent expansion, and resistivity changes in the metal as a function of temperature.

*Metal Expansion*  Expansion of the metal at higher temperatures will cause a decrease in electron concentration of approximately

$$\frac{N}{\Delta N} = \frac{\Delta V}{V} = \alpha \, \Delta T \tag{5.64}$$

Using the bulk expansion coefficient for silver of $\alpha = 1.9 \times 10^{-5} \, °\mathrm{C}^{-1}$, we get a fractional decrease in $N$ of about 0.1% over a 50 degree range. This decrease in $N$ will decrease $\omega_{\mathrm{p}}$, and since the peak occurs when

$$\varepsilon_\infty + 2\varepsilon_{\mathrm{m}} = \frac{\omega_{\mathrm{p}}^2}{\omega_{\mathrm{peak}}^2} \tag{5.65}$$

it is clear that volume expansion of the metal will shift the band to longer wavelengths, away from interband transitions. Since these transitions act as a source of damping, this red-shift actually leads to a slight increase in the intensity of the surface plasmon band, as well as a perceptible red shift.

*Solvent Refractive Index Changes*  The refractive index of the solvent decreases with increasing temperature. Assuming that it is dispersionless—independent of wavelength—then we see from Equation (5.61) that a decrease in $\varepsilon_{\mathrm{m}}$ will shift the peak to higher frequencies. Due to interband transitions, the blue-shift will also cause some damping. The variation in $n_0$ with increasing temperature for water is

$-1.58 \times 10^{-4}\ °C^{-1}$ and reasonably linear from 20 to 70°C. This leads to a predicted damping of the absorption amounting to

$$\frac{dA}{A\ dT} = -0.00007°C^{-1} \tag{5.66}$$

in water. Over about 10 degrees, we expect about a 0.1–0.2% decrease in absorption.

*Solvent Volume Expansion*   At constant pressure, the heating of colloid solutions will also cause the solvent to expand. The change in volume is simply

$$V_s(T) = V_s(20°C)(1 + \alpha_s\ \Delta T) \tag{5.67}$$

where $\alpha_s$ is the expansion coefficient. Then it is apparent that

$$\frac{dA}{A\ dT} = -\alpha_s \tag{5.68}$$

The value of $\alpha_s$ is not quite linear over the range 20–70°C; taking $\alpha_s = 4.14 \times 10^{-4}\ °C^{-1}$ for water we see that there is a significant effect.

*Resistivity Changes*   The absorption of colloidal metals in solution is affected by both solvent refractive index and solvent volume changes as the temperature is increased. In addition, heating of the metal increases the metal resistivity, because the electrons are more readily scattered by lattice vibrations. Within the Drude model this implies a decrease in mean free path or alternatively a higher scattering rate, $\omega_d$. This increases $\varepsilon''$ through Equation (5.56) and ultimately results in surface plasmon broadening. The peak intensity decrease is directly proportional to the increase in resistivity or $\varepsilon''_{peak}$:

$$A_{max} = \frac{18\pi N V \varepsilon_m^{3/2}}{\lambda \varepsilon''_{peak}} \tag{5.69}$$

Scattering reduces $R_{bulk}$, so that the effective mean free path in small particles as a function of temperature will be given by

$$\frac{1}{R(T)} = \frac{1}{R_{part}} + \frac{1}{R_{bulk}(T)} \tag{5.70}$$

For example, the temperature coefficient of the electrical resistance of gold is linear over the range 0–80°C, and has the value $\beta = 0.0034°C^{-1}$. The bulk resistivity is 2.44 $\mu\Omega$ cm, which corresponds to a mean free path of $R_{bulk} = 370$ Å if $v_F = 1.4 \times 10^6\ m\,s^{-1}$ using $\sigma = Ne^2 R/m v_F$ for the bulk DC conductivity. The actual change in band intensity depends on the particle size through Equation (5.70).

Larger particles show a substantially stronger effect than smaller particles. Substituting into Equation (5.69), we find that

$$\frac{dA}{A\,dT} = \frac{-\beta}{1 + R_{\text{bulk}}/R_{\text{part}}} = -6.04 \times 10^{-4}\,^\circ\text{C}^{-1} \tag{5.71}$$

This amounts to a 0.6% decrease over 10 degrees. In summary, we see that the temperature dependence is contributed to substantially by three different processes. Both resistance changes and solvent expansion appear to be the most important factors in aqueous solution. Solvent refractive index effects are perceptible but a factor of 5–6 smaller. The measurement of the temperature dependence of the metal spectra is probably not a good way to examine the behavior of the conduction electron population, unless care is taken to subtract these other factors.

### 5.4.7   Core–Shell Particles

In the previous sections we have examined the effects of electron transfer, particle size, and solvent properties on the optical spectra of nanosized particles. Dramatic optical shifts are also associated with the electrodeposition of metal atoms onto metal particles to form bilayer colloids. When electric charge is accumulated on metal particles, they are cathodically polarized, and the surface plasmon band is blue-shifted. In the presence of metal ions, electrodeposition of metal atoms can compete with proton reduction for the stored electrons.[27] A number of papers have demonstrated that the formation of well-defined bilayer or multilayer metal particles is possible by this technique, the first case being Zsigmondy's classic work on the use of gold nuclei to form monodisperse silver particles.[31] When electrons are transferred to a metal nanoparticle, the particles are cathodically polarized like a bulk metal electrode. The electrochemical potential becomes more negative, until hydrogen evolution begins to compete with electron accumulation, as discussed in section 5.3.3. However, in the presence of other metal ions, metal ion reduction to form a shell can compete. Metal deposition causes dramatic blue-shifts and strong damping. One monolayer (ML) of lead atoms can shift the plasmon band by 40 nm. Lead on a silver sol is discernible to the eye at 0.1 ML. The reasons for these strong shifts can be understood by considering the extinction cross-section of a small core–shell particle:

$$C_{\text{ext}} = 4\pi R^2 k$$
$$\times \text{Im}\left[\frac{(\varepsilon_{\text{shell}} - \varepsilon_{\text{m}})(\varepsilon_{\text{core}} + 2\varepsilon_{\text{shell}}) + (1 - g)(\varepsilon_{\text{core}} - \varepsilon_{\text{m}})(\varepsilon_{\text{core}} + 2\varepsilon_{\text{shell}})(\varepsilon_{\text{m}} + 2\varepsilon_{\text{shell}})}{(\varepsilon_{\text{shell}} + 2\varepsilon_{\text{m}})(\varepsilon_{\text{core}} + 2\varepsilon_{\text{shell}}) + (1 - g)(2\varepsilon_{\text{shell}} - 2\varepsilon_{\text{m}})(\varepsilon_{\text{core}} - \varepsilon_{\text{shell}})}\right]$$
$$\tag{5.72}$$

where $\varepsilon_{\text{m}}$ is the real dielectric function of the surrounding medium, $g$ is the volume fraction of the shell layer, and $R$ is the radius of the *coated* particle. When $g = 0$, Equation (5.72) reduces to Equation (5.46) for an uncoated sphere, and for $g = 1$,

Equation (5.72) yields the extinction cross-section for a sphere of the shell material. The condition for excitation of the surface mode is that the denominator equal zero, or

$$\varepsilon_{\text{core}} = -2\varepsilon_{\text{shell}} \frac{\varepsilon_{\text{shell}}g + \varepsilon_{\text{m}}(3 - g)}{\varepsilon_{\text{shell}}(3 - 2g) + 2\varepsilon_{\text{m}}g} \tag{5.73}$$

Around monolayer coverage, $g \ll 1$ and we can simplify this to

$$\varepsilon_{\text{core}} \sim -2\varepsilon_{\text{m}} - 2g(\varepsilon_{\text{shell}} - \varepsilon_{\text{m}})/3 \tag{5.74}$$

Assuming the real part of the dielectric functions for both metals are given by Equation (5.55), we find on substitution into Equation (5.74) that

$$\frac{\lambda_0^2}{\lambda^2} = 1 + \frac{2g \, \Delta\omega_{\text{psc}}^2}{3\omega_{\text{pc}}^2} \tag{5.75}$$

where $\lambda_0$ is the position of the surface plasmon band prior to deposition, $\omega_{\text{pc}}$ is the core metal's bulk plasma frequency, and $\Delta\omega_{\text{psc}}$ is the difference in the bulk plasma frequencies of the shell and core metals. The origin of the shift is the difference in plasma frequencies of the two metals in the core and shell. The electrons in the shell oscillate at a higher frequency than those in the core, and this causes the absorption band to shift slowly to higher frequencies. For cadmium and lead, which have similar bulk plasma energies of about 12 eV, the slope of a plot of $\lambda^2$ versus $g$ is predicted to be around 0.8, which is fairly close to the experimental value.[27] In Figure 5.19 the calculated spectra of lead-coated silver sols is shown. The spectra are remarkably similar to those obtained experimentally, even though bulk dielectric data are used for core and shell to model the deposition of atoms of metal on the silver surface. The use of the bulk dielectric constants to model the shift due to deposition of less than a monolayer of metal atoms is clearly questionable, although it yields almost the correct optical behavior. An even simpler "chemical" explanation of the surface plasmon shifts during the deposition of the first monolayer is as follows. Both lead and cadmium are divalent, and each adatom occupies a single lattice site but contributes two electrons to the particle conduction band. The overall electron density increases (though the electrical double layer is not being charged significantly because the extra charge is neutralized by the divalent lattice cation). The rate of plasmon band shift is then predicted to be just

$$\frac{\lambda_0^2}{\lambda^2} = 1 + \frac{zV_{\text{m}}(\text{Pb})[\text{Pb}]}{V_{\text{m}}(\text{Pb})[\text{Pb}] + V_{\text{m}}(\text{Ag})[\text{Ag}]} \tag{5.76}$$

where $z$ is the *difference* in valency of the lead and silver lattice ions, and the $V_{\text{m}}$ are the molar volumes. This model predicts that all divalent metals will cause a blue-shift of the surface plasmon band, but monovalent adatoms a much weaker shift.
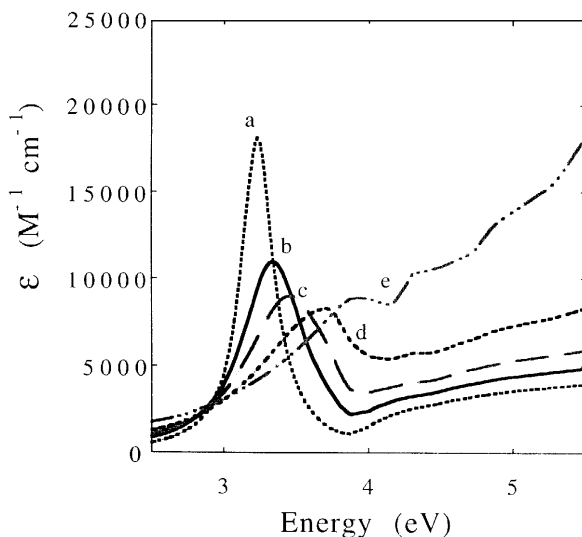
**FIGURE 5.19**  Extinction coefficient of lead-coated silver particles (6 nm diameter with mean free path correction) in water as a function of the shell thickness: a, no shell; b, 0.1 nm; c, 0.2 nm; d, 0.3 nm; e, 0.7 nm lead shell.

This simple model is only valid for submonolayer coverage, because it treats the adatoms as dopants. not as a discrete layer.

Any shell with a different refractive index from the solvent will cause a perceptible shift in the plasmon band position, even if the shell material is colorless! For silica, with a refractive index higher than water, Equation (5.74) predicts a red-shift in the surface plasmon band when it deposits from solution. In fact, the nucleation and growth of a shell may be monitored quite readily in a spectrophotometer cell. In Figure 5.20, we show the spectra of 15 nm gold particles around the plasmon peak as the first 4 nm of silica are deposited from a saturated sodium silicate solution. The chemistry of the system is given in the review by Liz-Marzán *et al.*[32] If the shell is grown substantially, the solution eventually becomes milky as light scattering from the shell becomes noticeable. Since Rayleigh scattering varies as $R^6/\lambda^4$, it quickly dominates the "absorption" spectrum, and causes a blue-shift in the peak position due to the scattering increasing rapidly at shorter wavelengths. This is shown in Figure 5.21 for both the experimental data for Au @ SiO$_2$ colloids and according to Equation (5.72). The initial red-shift is the effect of the increased dielectric constant of the shell compared to the solvent. The blue-shift then takes over as scattering increases. If the shell has a lower refractive index than the solvent, the band will initially blue-shift. Figure 5.22 shows an image of some of the core–shell particles created to examine the optical effects of the dielectric shell on the surface plasmon absorption of gold nanoparticles.
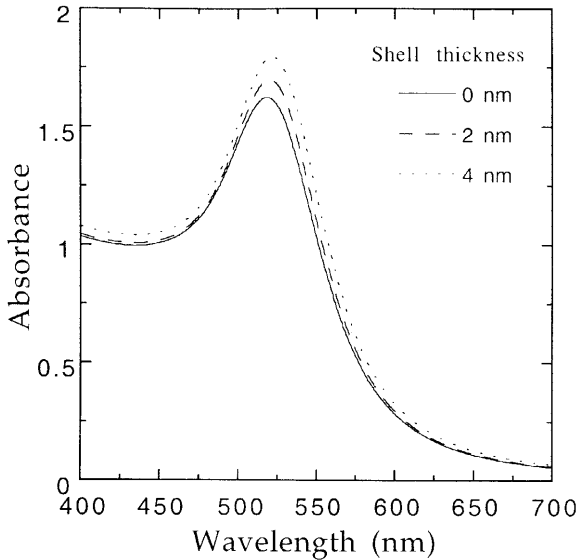
**FIGURE 5.20**   Spectrum of 15 nm colloidal gold in water following the deposition of 0, 2, and 4 nm of silica. Note that the band becomes red-shifted and more intense following coating. Coalescence leads to band broadening. Reprinted with permission from L. M. Liz-Marzán, M. Giersig, P. Mulvaney, *Langmuir*, *12*, 4329, © 1996 American Chemical Society.
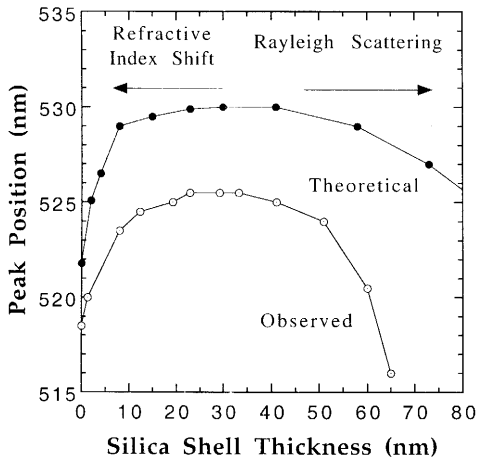


**FIGURE 5.21**   Position of the SP band as a function of the silica shell thickness in water. At low thicknesses, the primary effect is a red-shift due to the increasing refractive index around the particles. For larger particles Rayleigh scattering from the shell causes a blue-shift. The theoretical curves are a little red-shifted due to errors in the dielectric data for bulk gold of just 1–2%.
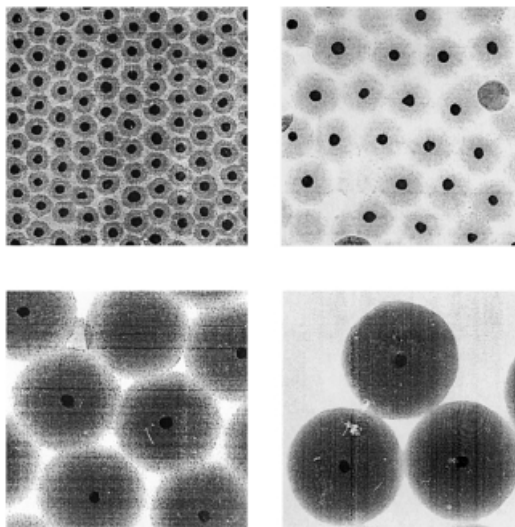
**FIGURE 5.22**   TEM images of gold colloids with various thicknesses of silica. The first two samples are relatively transparent to the eye, the last two are turbid. The gold core is 15 nm diameter in all images.

## 5.5   COLLOID ELECTROCHEMISTRY

### 5.5.1   Electrode–Colloid Equilibrium

We have been correlating electron transfer processes with optical changes in the colloid spectrum. It transpires that electrical processes are coupled to optical ones, allowing new spectroscopic methods to be used to monitor electron transfer, adsorption, and surface nucleation processes *in situ* at particle surfaces. These measurements work best for nanoparticles, where light scattering is minimal, and the dipole model for the absorption spectrum can be used with confidence. One continual problem has been establishing the redox potential of colloids on an electrochemical scale, which would allow the application of conventional electro-chemical models to colloid electrochemistry with more confidence. If it could be demonstrated that colloid particles equilibrated themselves with macroscopic elec-trodes immersed into the colloid solution, then one could read off the colloid redox potential directly using the electrode as a conventional $E_h$ indicator. This is frequently done in soil chemistry, but with little direct justification. A platinum electrode is embedded into aquifers, soils, rivers, or streams, and its steady-state potential is used to determine whether oxidizing or reducing conditions prevail in the soil. Combined with pH and oxygen concentrations, it is sometimes used to deter-mine the active half-cell reaction dominating the prevailing redox chemistry within the sample. Yet in fact, little has been done to prove that colloid particles can equilibrate with an electrode, nor has the timescale needed for such equilibrium to be attained been considered. In the previous sections, we have seen that the color of a

silver colloid changes with electronic charge stored on it. Hence it can act as an indicator for electron transfer processes. In particular, we can ask whether charge can transfer between a metal colloid particle and a macroscopic electrode.[33] Given that both have significant double layers, we may well expect that the particles will never contact the electrode and hence that transfer will be negligible.

The final part of this chapter involves correlating the absorption spectrum of silver particles with electrode potential. An optically transparent thin layer electrode (OTTLE) cell will be used. This electrode is a gold mesh that is transparent enough for optical measurements to be made through it. It was originally designed to examine the spectra of electrochemical intermediates. A full discussion of the technique is presented by Heinemann.[34]

When a gold mesh is immersed into a thin colloidal silver solution at +0.15 V versus a reference Ag/AgCl microelectrode in the same medium, no optical changes are observed over time. At this potential a silver electrode is at equilibrium with the silver colloid particles. The solutions are bubbled with nitrogen and usually contain both an electrolyte to reduce the cell resistance and a polymer to reduce colloid aggregation at the high ionic strengths of the solutions. In Figure 5.23, UV-visible spectra of the colloid are shown before and after a potential step to −0.6 V from the starting potential of +0.15 V. Initially, the absorption band maximum of the sol is located at 400 nm. After application of the potential step, the absorption spectrum changes, and the band blue-shifts to a new position with a maximum at 392 nm. This spectrum is quite reproducible for minutes at a time. As can also be seen from Figure 5.23, when the potential is stepped back to +0.15 V the absorption band red-shifts and broadens until it resembles that of the silver sol before the initial potential step is imposed. These simple effects are a clear indication that electron transfer between an electrode and a metal nanoparticle can occur, and that charge transfer can occur in both directions.
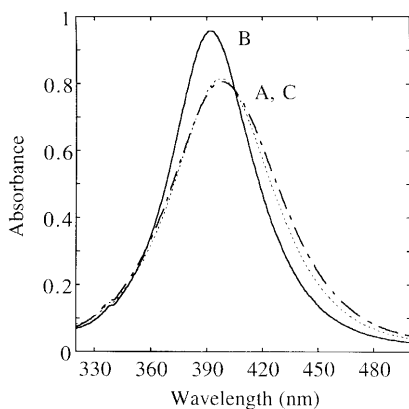


**FIGURE 5.23** Spectrum of colloidal silver at +0.15 V vs. Ag/AgCl (curve A), after application of a potential step to −0.60 V and after a second potential step back to +0.15 V (curve C). Reprinted with permission from T. Ung, D. Dunstan, M. Giersig, P. Mulvaney, *Langmuir*, *13*, 1773, © 1997 The American Chemical Society.

To demonstrate that the optical shifts are caused entirely by electron transfer between the working electrode and the colloid particles, and to determine the kinetics of electron transfer, the absorbance can be monitored as a function of time at 393 nm after the potential step is applied. The results are shown in Figure 5.24. The potential of the mesh is held at the open circuit value of $+0.15$ V, and after steady absorbance readings are obtained from the silver sol, a potential step to $-0.6$ V is applied. The absorbance of the sol changes immediately, with rapid increases in absorption being seen that level off after some 150 s in the experiment shown. When this new, steady absorbance value is achieved, the potential is stepped back to the original value. Immediately, the absorbance decreases again at almost the same rate, until the original value is attained about 200 s later. Since the measured absorbance is due to all the particles in the OTTLE cell between the cell walls and the electrode, *all* the silver particles in the OTTLE cell must have equilibrated with the mesh on the timescale of the absorbance changes seen in Figure 5.24. The silver particles in the 50 μm wide cell not only diffuse to the gold mesh on this timescale, they also collect the necessary charge for electrochemical equilibrium to be attained. Using the value of $D = 5 \times 10^{-7}$ cm$^2$ s$^{-1}$, obtained directly by Dynamic Light Scattering (DLS), a silver particle will diffuse a distance of $x^2 \sim Dt \sim 80$ μm in 150 s, which corresponds well to the thickness of the OTTLE cell, which is 75 μm. Thus the observed absorption transients are exactly those required to deplete the cell of "unreacted" particles. This suggests that not only does electron transfer occur, but that it may be taking place close to the diffusion-limited rate of encounters of the particle with the cathodically polarized electrode.

In Figure 5.25, the equilibrium position of the silver colloid surface plasmon absorption band is shown after application of different potential steps to the sol. The peak positions are accurate to within 0.4 nm. All potentials are measured relative to
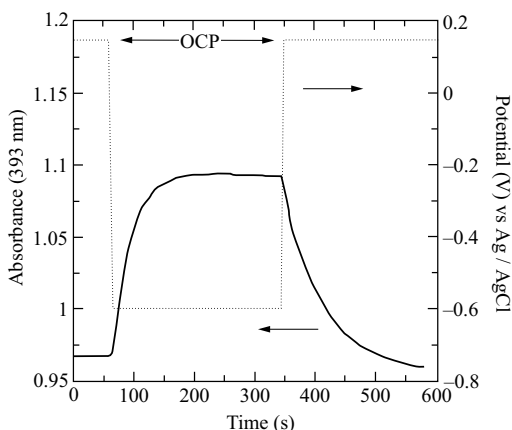


**FIGURE 5.24** Change in absorbance of a silver colloid when a potential step is applied to the colloid from 0.15 V to $-0.6$ V vs. Ag/AgCl. The open circuit potential (OCP) is about $+0.15$ V, and no significant absorbance change to the colloid was observed when this potential was applied. Reprinted with permission from T. Ung, D. Dunstan, M. Giersig, P. Mulvaney, *Langmuir*, *13*, 1773, © 1997 The American Chemical Society.

Ag/AgCl. As can be seen, starting from an open circuit potential of +0.15 V vs. Ag/AgCl, and a surface plasmon band position at 400 nm, it is possible to blue-shift the band to about 392 nm by application of potentials of up to −0.8 V to the gold mesh. At more negative potentials, hydrogen evolution from both mesh and the particles prevents further shifts from occurring, or at least from being measured accurately, due to bubble accumulation in parts of the OTTLE cell. Application of a more positive potential to the gold mesh results in a red-shift of the colloid absorption band, and this attains a value of 404 nm at potentials greater than +0.4 V vs. Ag/AgCl. The limiting factor in this case is particle oxidation. From the Nernst potential for bulk silver,

$$E(\text{vs. Ag/AgCl}) = +0.577 + 0.059 \ \log_{10}[\text{Ag}^+] \tag{5.77}$$

we see that a silver sol will show noticeable dissolution (1–10% absorbance decrease) when the electrode potential is maintained in the region +0.34 to 0.40 V. When the potential of the working electrode is maintained at values any more positive than this, total dissolution of the colloid is observed.

From the resonance condition, $\varepsilon' = -2\varepsilon_m$, it follows that the peak positions are related directly to the relative electron concentration through

$$\lambda_f^2 = \lambda_i^2 \ \frac{N_i}{N_f} \tag{5.78}$$

where $N$ is the conduction electron concentration, and subscripts i and f refer to initial and final states, respectively. It is then readily shown that for nanosized
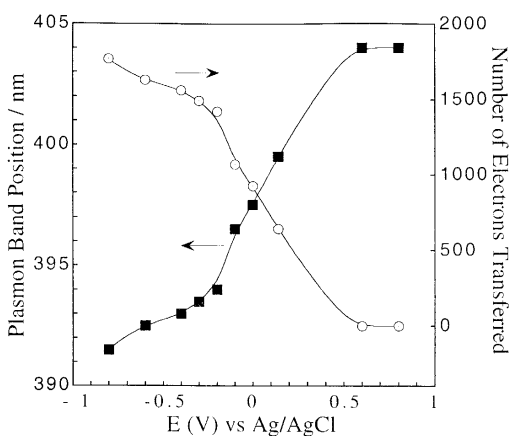


**FIGURE 5.25**   Position of the surface plasmon band of colloidal silver as a function of the electrode potential. Also shown is the number of electrons needed to be transferred to move the band from 392 nm to longer wavelengths. Reprinted with permission from T. Ung, D. Dunstan, M. Giersig, P. Mulvaney, *Langmuir*, *13*, 1773, © 1997 The American Chemical Society.

particles the capacitance of the electrical double layer, $K$, is related to the electro-optical shift by

$$K = \frac{\Delta\sigma}{\Delta E} = \frac{(\lambda_f^2/\lambda_i^2 - 1)aF}{3V_m\,\Delta E} \tag{5.79}$$

Inserting $\lambda_i = 404$ nm and $\lambda_f = 392$ nm, $a = 5.65$ nm, $F = 96487$ C mol$^{-1}$, and $V_m = 10.26$ cm$^3$ mol$^{-1}$, for which $E$ varies from $+0.4$ V to $-0.7$ V, we obtain $K = 80$ µF cm$^{-2}$, a result in reasonable agreement with direct capacitance measurements for polycrystalline silver. From the spectral shift, 1790 electrons are needed to alter the position of the surface plasmon band from 404 to 392 nm, or to raise the electrochemical potential from $+0.4$ V to $-0.7$ V, which corresponds to a surface charge density increase of 6.2%. If the double layer capacitance remained independent of size for particles down to 1 nm in diameter, we can see from Equation (5.79) that a similar potential jump would entail charge density changes of around 50%!

These final results draw together our use of optical methods to investigate electron transfer processes and other surface effects on small particles. We have combined ideas from electrochemistry, homogeneous kinetics, and Mie theory to allow us to probe and examine surface chemical events at metal nanoparticle surfaces.

## 5.6   CONCLUSIONS

There are currently intensive efforts on several fronts to pursue the ideas presented in this chapter further, and there are a number of outstanding problems that need to be solved. Some of these puzzles are as follows.

- *Adsorbate damping:* Numerous ligands cause damping of the surface plasmon band, particularly mercaptans, and it is most pronounced for silver.[35] These interactions are important because adsorbed ligands or capping agents are almost mandatory for controlled nucleation and growth of monodisperse metal nanoparticles.
- *Nucleation:* This is one of the most important problems in science. What determines the nucleation pathways of metal atoms or clusters, how does it depend on ligands, and how does the cluster redox potential change with size and time during nucleation? How important is the double layer, not only in controlling particle growth but in facilitating nucleation?
- *Nanoparticle redox potentials:* We have stressed in this chapter the importance of defining the double layer around metal nanoparticles; it controls particle size during growth, the stability with respect to coalescence, and the kinetics of chemical processes at the metal surface. There is no simple way to measure the redox potential at present in a reliable and simple way, nor can we measure the

potential of zero charge on an electrochemical scale in a reproducible and reliable way.

However, despite the plethora of issues that need to be addressed there have been numerous new discoveries involving the basic science of metal nanoparticles. These build upon the basic foundations discussed here and demonstrate the continuing fascination of nanomaterials. The following are some of these novel discoveries:

- *Single-electron processes:* Gold colloids less than about 3 nm in size show well-defined cyclic voltammograms with single-electron redox potentials, analogous to molecular redox couples. It is possible now to take a metal colloid and transfer a single electron to each colloid particle. In some cases these colloids can be dried and stored as reagents, redissolved in solution and used in redox reactions again. The distinct redox chemistry occurs as the capacitance of the particles becomes so small that the double layer charging induced by a single electron alters the redox potential or Fermi level in the metal by more than 25 mV, which makes it measurable above thermal noise. These quantized chemical approaches to metal redox chemistry are reviewed by Templeton *et al.*[36]

- *Energy dissipation in hot metals:* When irradiated by subpicosecond laser pulses, the photon energy absorbed by nanoparticles is first dissipated by electron–electron coupling (hot-to-cold electron cooling), then by electron–lattice interactions (phonon production), and finally by transfer of lattice energy to the solvent bath. Numerous optical applications depend upon a knowledge of the kinetics of these processes, and how they depend upon particle size. Hartland *et al.* have shown that a further process is involved, whereby the heating of the lattice causes the metal nanoparticles to undergo acoustic breathing, that is, expansion and contraction cycles on a picosecond timescale. This metal expansion causes the plasma frequency to decrease and increase (section 5.4.6). and leads to oscillations in the plasmon band absorption. Thus there is a coupling of the optical energy into mechanical modes.[37]

- *Bioassays:* Mirkin and colleagues have demonstrated that by conjugating the gold nanoparticles to DNA strands, the color changes associated with gold colloid aggregation can also be used in bioassays to monitor single nucleotide polymorphisms in DNA complementary strands. The complex optical effects leading to this unusual bioapplication of metal nanoparticles has been discussed by Storhoff *et al.*[38] Natan and coworkers have pushed the sensor applications of gold nanoparticles through film-based technologies. Gold colloid film electrodes can be used for bioassays and via their enormous Surface Enhanced Raman Spectroscopy (SERS) sensitivity for a variety of detection and monitoring applications.[39]

- *Novel synthetic routes:* Finally, great progress has also been made in scaling up metal nanoparticle synthesis, particularly through the use of nonaqueous solvents. The extensive work by Klabunde[40–42] and coworkers on inverse micelle approaches to particle size control, and more recently the high-

temperature synthetic routes described by Murray,[43] have greatly facilitated the application of nanoparticles in a wide range of fields.

In this chapter we have examined some of the basic redox chemistry and optical properties of small nanosized metal particles. We have derived or presented the basic equations necessary to model electron transfer kinetics and for diffusion processes for molecule–particle interactions; some fundamental optical effects have been determined in terms of Mie theory; and finally interactions between metal nano-particles and an electrode have been considered. Nevertheless, many basic problems have not yet been resolved.

## ACKNOWLEDGMENTS

## REFERENCES

1. W. A. Weyl, *Coloured Glasses*, Society of Glass Technology, Sheffield, UK, **1951**.
2. M. Faraday, *Phil. Trans. Roy. Soc. London*, **1857**, *147*, 145.
3. G. Mie, *Ann. Phys.*, **1908**, *25*, 377.
4. P. Debye, *Ann. Phys.*, **1909**, *30*, 57.
5. R. J. Hunter, *Foundations of Colloid Science*, Vol. 1, Oxford University Press, New York, **1989**.
6. B. Vincent, *Adv. Colloid Interface Sci.*, **1974**, *4*, 193.
7. J. Israelachvili, *Intermolecular and Surface Forces*, 2nd edition, Academic Press, San Diego, CA, **1992**.
8. M. Giersig, P. Mulvaney, *Langmuir*, **1993**, *9*, 3408.
9. M. Giersig, P. Mulvaney, *J. Phys. Chem.*, **1993**, *97*, 6334.
10. A. J. Bard, L. R. Faulkner, *Electrochemical Methods*, Wiley, New York, **1980**.
11. P. Delahay, *Double Layer and Electrode Kinetics*, Wiley, New York **1965**.
12. C. Wagner and W. Traud, *Z. Elektrochem.*, **1938**, *44*, 391.
13. A. N. Frumkin, *Z. Phys. Chem.*, **1932**, *160*, 116.
14. M. Spiro, *J. Chem. Soc., Faraday Trans. 1*, **1979**, *75*, 1507.
15. J. Kiwi and M. Grätzel, *J. Am. Chem. Soc.*, **1979**, *101*, 7214.
16. A. Henglein and J. Lilie, *J. Am. Chem. Soc.*, **1981**, *103*, 1059.
17. D. Miller and G. McLendon, *Inorg. Chem.*, **1981**, *20*, 950.
18. D. S. Miller, A. J. Bard, G. McLendon, J. Ferguson, *J. Am. Chem. Soc.*, **1981**, *103*, 5336.

19. A. Henglein, *Top. Curr. Chem.*, **1988**, *143*, 113.

20. M. S. Matheson, P. C. Lee, D. Meisel, E. Pelizzetti, *J. Phys. Chem.*, **1983**, *87*, 394.

21. G. McLendon, in *Energy Resources through Photochemistry and Catalysis*, M. Grätzel (editor), Academic Press, New York, **1983**, ch. 4, pp 99–122.

22. C. F. Bohren, D. R. Huffman *Absorption and Scattering of Light by Small Particles*, Wiley, New York, **1983**.

23. L. Genzel, T. P. Martin, *Phys. Stat. Sol. (b)*, **1972**, *51*, 91.

24. C. Kittel, *Introduction to Solid State Physics*, 2d edition, Wiley, New York, **1956**.

25. U. Kreibig, M. Vollmer, *Optical Properties of Metal Clusters*, Vol. 25, Springer, Berlin, **1995**.

26. A. Henglein, P. Mulvaney, T. Linnert, *Faraday Discuss.*, **1991**, *92*, 31.

27. P. Mulvaney, *Langmuir*, **1996**, *12*, 788.

28. J. A. Creighton, D. G. Eadon, *J. Chem. Soc., Faraday Trans.*, **1991**, *87*, 3881.

29. A. E. Hughes, S. C. Jain, *Adv. Phys.*, *28*, 717.

30. L. M. Liz-Marzán, P. Mulvaney, *New J. Chem.*, **1998**, *22*, 1285.

31. R. Zsigmondy, P. A. Thiessen, *Das Kolloidale Gold*, Akadem. Verlag, Leipzig, **1925**.

32. L. M. Liz-Marzán, M. Giersig, P. Mulvaney, *Langmuir*, **1996**, *12*, 4329.

33. T. Ung, D. Dunstan, M. Giersig, P. Mulvaney, *Langmuir*, **1997**, *13*, 1773.

34. R. W. Murray, W. R. Heineman, G. W. O'Dom, *Anal. Chem.*, 1967, *39*, 1666.

35. T. Linnert, P. Mulvaney, A. Henglein, *J. Phys. Chem.*, **1993**, *97*, 679.

36. A. C. Templeton, M. P. Wuelfing, R. W. Murray, *Acc. Chem. Res.*, **2000**, *33*, 27.

37. J. H. Hodak, I. Martini, G. V. Hartland, *J. Chem. Phys.*, **1998**, *108*, 9210.

38. J. J. Storhoff, A. A. Lazarides, R. C. Mucic, C. A. Mirkin, R. L. Letsinger, G. C. Schatz, *J. Am. Chem. Soc.*, **2000**, *122*, 4640.

39. L. A. Lyon, M. D. Musick, P. C. Smith, B. D. Reiss, D. J. Pena, M. J. Natan, *Sensors and Actuators B—Chemical*, **1999**, *54*, 118.

40. X. M. Lin, G. M. Wang, C. M. Sorensen, K. J. Klabunde, *J. Phys. Chem.*, **1999**, *103*, 5488.

41. X. M. Lin, C. M. Sorensen, K. J. Klabunde, *Chem. Mater.*, **1999**, *11*, 198.

42. X. M. Lin, C. M. Sorensen, K. J. Klabunde, G. C. Hadjipanayis, *Langmuir*, **1998**, *14*, 7410.

43. S. Sun, C.B. Murray, *J. Appl. Phys.*, **1999**, *85*, 4325.

# 6  Magnetism

C. M. SORENSEN

Department of Physics, Kansas State University, Manhattan, Kansas

## 6.1  INTRODUCTION

Magnetism and magnetic phenomena are well known to all of us, scientist and layperson alike. If we are technically inclined, we come to realize that magnets are important for motors, actuators, information storage media, electrical power transformation, electronic circuits, ferrofluids, and medical applications. A deeper look into the science of magnetism shows us that it is a remarkably rich and multifaceted area of study. Thus it is a daunting task to summarize and explain this vast and detailed field in one chapter.

The intent here is to review aspects of magnetism that the author has personally found useful and necessary in research involving nanoparticle magnetism. Thus this is not so much a chapter on nanoscale magnetism, but rather a chapter describing what you need to know to do nanoscale magnetism. Throughout this chapter three excellent references have been drawn upon extensively: the book by Cullity,[1] now a classic in its field; Kittel's[2] chapters on magnetism in his solid state physics book; and the very accessible book by Jiles.[3] Any of these can be consulted for more detailed description of the phenomena described below.

## 6.2  FUNDAMENTAL CONCEPTS

### 6.2.1  Atomic Origins of Magnetism

It is well known that matter is electronic in nature; that is, all atoms are made of positive and negative charges (protons and electrons) that are strongly bound together via the electrostatic (Coulomb) force. This force is a consequence of the electric field, which reaches out from a charge across space to cause a force on a

second charge. It is also well known that electricity and magnetism are integrally tied together as different aspects of the same thing—the electromagnetic interaction. Interestingly, there is a break in this symmetry in that, whereas electric fields occur spontaneously from electronic charges (indeed, they are each other) there are no magnetic "charges,"—in other words, magnetic monopoles do not exist. Because of this, the sole source of the magnetic field is relative motion of an electric charge and the observer. Thus magnetism is a result of moving charges. From an atomic view of matter, there are two electronic motions: the orbital motion of the electron, and the spin motion of the electron. Except for some nuclear magnetic effects, which are much smaller and which we will not discuss, these two electron motions are the source of macroscopic magnetic phenomena in materials.

## 6.2.2  Magnetic Variables and Units

The magnetic field strength (or intensity) is usually represented by $H$. $H$ will be reserved for fields that result solely from free currents, such as an electric current flowing in a wire. The magnetic moment per unit volume of a magnetic material is measured by $M$, the magnetization (or polarization). $M$ results from the two atomic motions: the orbital and spin motion of the electron, mentioned above. These are often viewed macroscopically as equivalent or effective currents. Finally, the general case of a field due to both free and equivalent currents is described by the magnetic induction, $B$. These three quantities are tied together in the field equation

$$B = H + 4\pi M \quad \text{[cgs]} \tag{6.1}$$

Thus $B$ can result from a combination of $H$ and $M$. For example, an electromagnet made by winding coils of copper wire around an iron rod and then passing a current through the wire has an $H$ from this current, an $M$ from atomic motion of the electrons in the iron, and a total $B$ that is the sum of these two as described by Equation (6.1).

The units of $H$, $M$, and $B$ are fundamentally all the same, as implied by Equation (6.1), and depend on the system of units being used. There are a number of unit conventions, each with advantages and disadvantages. There are currently three systems of units that see widespread use. Historically, workers in magnetic materials have used the cgs (centimeter, gram, second) or Gaussian system. More recently attempts have been made to change over to the SI system (in mechanics SI implies mks—meter, kilogram, second). There are two SI systems, the Kennelly and the Sommerfeld conventions, the latter slowly gaining acceptance in the magnetism community. Table 6.1 gives the units for the important magnetic quantities.

Conversion factors are:

1 oersted (Oe) $= (1000/4\pi)\,\text{A}\,\text{m}^{-1}$

1 gauss (G) $= 10^{-4}$ tesla (T)

1 emu $\text{cm}^{-3} = 1000\,\text{A}\,\text{m}^{-1}$

**TABLE 6.1    Magnetic units.** A is ampere, cm is centimeter, m is meter, emu is electromagnetic unit, $B$ is magnetic induction, $H$ is magnetic field strength, $M$ is magnetization of a substance per unit volume, $\mu_0 = 4\pi \times 10^{-7}$ newton/ampere$^2$ is the permeability of free space. In the SI-Kennelly convention the magnetization is $I$, the intensity of the magnetization

| Quantity | cgs (emu) | SI (Sommerfeld) | SI (Kennelly) |
|---|---|---|---|
| $B$ | gauss | tesla | tesla |
| $H$ | oersted | $A\,m^{-1}$ | $A\,m^{-1}$ |
| $M$ | $emu\,cm^{-3}$ | $A\,m^{-1}$ | – |
| $I$ | – | – | tesla |
| Field equation | $B = H + 4\pi M$ | $B = \mu_0(H + M)$ | $B = \mu_0 H + I$ |
| Energy | $E = -\mu \cdot H$ | $E = -\mu_0 \mu \cdot H$ | $E = -\mu \cdot H$ |

With the information in Table 6.1, one can show:

$$1\ \text{emu} = 1\ \text{erg Oe}^{-1}$$
$$= 1\ (\text{erg cm}^3)^{1/2}$$
$$1\ \text{Oe} = 1\ (\text{erg cm}^{-3})^{1/2}$$

Also note that in the cgs system the magnetization $M$ can also be written per gram of substance. Then one often finds the symbol $\sigma$ used, viz.

$$\sigma = M/\rho \quad (\text{emu g}^{-1}) \tag{6.2}$$

where $\rho$ is the mass density.

Examples of magnetic fields are those of the earth, for which $B \simeq 0.8\ \text{G} = 8 \times 10^{-5}\ \text{T}$, or near a pole of a common permanent magnet where $B \sim 1000\ \text{G}$, etc. Beware, however, because usage of magnetic units is often not careful and units get mixed.

### 6.2.3    Magnetic Susceptibility and Permeability

Perhaps the most common magnetic experiment is to apply a magnetic field to a material and measure the magnetization induced by the field. The measure of how effective an applied field is for inducing a magnetic dipole is the susceptibility of the material, defined as

$$\kappa = M/H \tag{6.3}$$

This susceptibility is unitless, as seen by Equation (6.1). However, it can be expressed in terms of units if $M$ is taken as $emu\,cm^{-3}$ for then $\kappa$ has units of

**TABLE 6.2   Permeabilities of some common ferromag-
netic substances.[4] Permeability is a function of applied
field and temperature. The values quoted here are
maximum values**

| Substance | Permeability, $\mu$ |
|---|---|
| Transformer steel | $5 \times 10^3$ |
| Cold-rolled steel | $2 \times 10^3$ |
| High-purity iron | 920 |
| 4% Si in Fe | $7 \times 10^3$ |
| 78 Permalloy | $10^5$ |
| Supermalloy | $10^6$ |

emu cm$^{-3}$ Oe$^{-1}$. For this reason, it may be thought of as the susceptibility per unit
volume. Dividing by the density of the material yields the mass susceptibility,

$$\chi = \kappa/\rho \quad (\text{emu g}^{-1} \text{ Oe}^{-1}) \tag{6.4}$$

or dividing by the mole weight yields the molar susceptibility,

$$\chi_M = \chi/\text{mole wt} \quad (\text{emu mol}^{-1} \text{ Oe}^{-1}) \tag{6.5}$$

A quantity closely related to the susceptibility is the permeability $\mu$ defined by

$$\mu = B/H \tag{6.6}$$

The physical content of Equation (6.6), especially if it is rewritten as $B = \mu H$, is that
a field $H$, generated by a current, when applied to a material of large permeability
(e.g., $\mu$ of iron can range to thousands, see Table 6.2), is enhanced by the factor of $\mu$
to create a large field $B$.

From Equations (6.1), (6.3), and (6.6) it is easy to show that

$$\mu = 1 + 4\pi\kappa \tag{6.7}$$

Remember that this expression holds for the cgs system of units; similar expressions
hold for other units systems.

## 6.3   MAGNETIC MATERIALS

For most of us the term "magnetism" conjures up visions of pieces of iron being
attracted across a distance by magnets. The layman sees only iron as magnetic; other
materials are not affected by magnets. Nothing could be further from the truth,
however, because all materials are affected by a magnetic field, although most only

weakly so. The nature of the interaction with a magnetic field allows us to classify (roughly) magnetic phenomena into three major categories:

1. *Ferromagnetism*: Here the interaction is strongly attractive toward a magnetic pole. Iron, cobalt, and nickel are the classic examples of ferromagnets. A list of some ferromagnetic (and ferrimagnetic) materials is given in Table 6.3.
2. *Paramagnetism*: Here the interaction is weakly attractive toward a magnetic pole. A list of some paramagnetic materials is given in Table 6.4.
3. *Diamagnetic*: Here the interaction is weakly repulsive from a magnetic pole. The vast majority of substances are diamagnetic, including water, $SiO_2$, wood, plastics, NaCl, $CaCO_3$, and most organic and biological materials. Some diamagnetic materials are listed in Table 6.5.

These classifications are rough. Below we will refine the meaning of ferromagnetic in terms of the coupling between adjacent atoms. Strictly speaking, ferrimagnets, such as magnetite ($Fe_3O_4$), are not ferromagnets but are included in the "ferromagnetic" classification above. Another category of weakly attractive materials are antiferromagnets, which are definitely not paramagnets. Extensive tables of magnetic properties are given in reference 4.

If the material is not itself a magnet—if it has no permanent magnetic polarization—then the interaction occurs because the applied field induces the material to become a magnet, that is, it induces a magnetization $M$ into the material. Then the two magnets, one given, one induced, interact.

For a paramagnetic substance, $\kappa$ is small and positive. Typical values fall in the range $10^{-3}$ to $10^{-5}$ at room temperature. Because the value is positive, the induced moment has the same direction as the applied field. Figure 6.1a depicts a permanent magnet creating a field near a paramagnetic material. The field lines for $B$ are away from the north pole of the magnet; hence, with $\kappa > 0$, the induced dipole points away from the north pole of the magnet as well. The paramagnetic material has been polarized, so it is now a magnet as well. The south pole of the induced dipole is at the tail of the dipole vector, the north pole is at the head, as drawn. From elementary magnetostatics we know that a dipole tends to align with the applied field, so a nonsymmetric piece of paramagnetic material would align with its long axis parallel to the field. We also know that the total force on a dipole in a uniform field is zero, but the field near a pole piece is far from uniform, growing weaker with distance. Thus, the attractive force between the permanent magnet's north pole and the induced magnet's south pole will dominate the repulsive interaction of the permanent and induced north poles for an overall attraction. This scheme holds true for a ferromagnetic material since $\kappa > 0$ again. The difference, and it is major, is that ferromagnetic susceptibilities are typically orders of magnitude greater than paramagnetic ones, so that the force is much greater as well.

A diamagnetic material has $\kappa < 0$, with typical values on the order of $10^{-5}$ to $10^{-6}$. Thus, when such a material experiences an applied field, the induced moment is small and opposite to the field, as depicted in Figure 6.1b. The induced dipole

**TABLE 6.3    Ferromagnetic and ferrimagnetic materials**

| Substance | Saturation Magnetization $M_s$, in emu cm$^{-3}$ (or emu g$^{-1}$) | | Bohr Magnetons per Formula Unit | Curie Temperature | |
|---|---|---|---|---|---|
| | Room Temperature | 0 K | | (°C) | (K) |
| Fe | 1714(218) | 1745(222) | 2.22 | 770 | 1043 |
| Co | 1422(159) | 1435(161) | 1.72 | 1131 | 1404 |
| Ni | 484(54.4) | 512(57.5) | 0.604 | 358 | 631 |
| Gd | – | 2003 | 7.12 | 16 | 289 |
| Dy | – | 2920 | 10.0 | −188 | 85 |
| $Cu_2MnAl$ | 500 | 550 | (4.0) | 437 | 710 |
| MnAs | 670 | 870 | 3.4 | 45 | 318 |
| MnBi | 620 | 680 | 3.52 | 357 | 630 |
| $CrO_2$ | 515 | – | 2.03 | 113 | 386 |
| $MnO{\cdot}Fe_2O_3$ | 410 | 560 | 5.0 | 300 | 573 |
| $FeO{\cdot}Fe_2O_3$ | 480 | 510 | 4.1 | 585 | 858 |
| $CoO{\cdot}Fe_2O_3$ | 400 | 475 | 3.7 | 520 | 793 |
| $NiO{\cdot}Fe_2O_3$ | 270 | 300 | 2.4 | 585 | 858 |
| $CuO{\cdot}Fe_2O_3$ | 135 | 160 | 1.3 | 455 | 728 |
| $MgO{\cdot}Fe_2O_3$ | 110 | 140 | 1.1 | 440 | 713 |
| $BaO{\cdot}Fe_2O_3$ | 380 | 530 | – | 450 | 723 |
| Alnico | – | – | – | 850 | 1123 |
| $SmCo_5$ | – | – | – | 720 | 993 |
| $Nd_2Fe_{14}B$ | – | – | – | 312 | 585 |
| EuO | – | 1920 | 6.8 | −204 | 69 |
| EuS | – | – | – | −256.5 | 16.5 |
| $GdMn_2$ | – | 215 | 2.8 | 30 | 303 |
| $Gd_3Fe_5O_{12}$ | 0 | 605 | 16.0 | 291 | 564 |
| $Y_3Fe_5O_{12}$ (YIG) | 130 | 200 | 5.0 | 287 | 560 |

Compiled from references 2, 3, and 4.

would try to rotate from this anti-aligned state to an aligned state, but the dipole is not connected to the material, rather its direction is determined by the applied field. If the object is not symmetric, e.g., a long cylinder, the cylinder will align perpendicular to the field so that the total induced moment, which would lie across the axis of the cylinder still antiparallel to $H$, will be minimized. In this anti-aligned state with the gradient in the applied field, we see that the repulsion of the nearby north poles dominates the attraction of the permanent magnet's north pole with the distant induced south pole, to yield an overall repulsion.

Figure 6.2 shows the magnetic state of the elements at room temperature. We see that most metals are paramagnetic. Iron, cobalt, and nickel, and below 16°C gadolinium, are ferromagnetic. Most nonmetals are diamagnetic.

**TABLE 6.4   Magnetic molar susceptibility of some paramagnetic substances at room temperature**

| Substance | Susceptibility, $\chi_M$ ($10^{-6}$ emu $mol^{-1}$ $Oe^{-1}$) |
|---|---|
| Aluminum | 16.5 |
| Chromium | 180 |
| Chromium sulfate ($Cr_2(SO_4)_3$) | 11,800 |
| Cobalt chloride ($CoCl_2$) | 12,660 |
| Copper sulfate ($CuSO_4 \cdot 5H_2O$) | 1460 |
| Gadolinium sulfate ($Gd(SO_4)_3$) | 511,200 |
| Iron chloride ($FeCl_3 \cdot 6H_2O$) | 15,250 |
| Iron sulfate ($FeSO_4 \cdot 7H_2O$) | 11,200 |
| Potassium | 20.8 |
| Oxygen ($O_2$) | 3450 |
| Oxygen (liquid) | 7700 |
| Sodium | 16 |
| Sodium dichromate ($Na_2Cr_2O_7$) | 55.6 |
| Titanium | 153 |
| Vanadium | 255 |

Compiled from reference 4.

### 6.3.1   Diamagnetism

Diamagnetism results from a fundamental principle of electromagnetism, known as Lenz's law, which states that when a conducting loop is acted upon by an applied magnetic field a current is induced in the loop that counteracts the change in the field.

From a semiclassical, atomic point of view, the electron orbits are resistanceless, so the induced current remains after the field has been applied and is constant. The conduction electrons of a metal, the Fermi sea, also respond in a resistanceless manner. This is also true for superconductors, which are perfectly diamagnetic (i.e., $\kappa = -1$) and hence show total exclusion of the applied field.

The diamagnetism of atoms, ions, and molecules can be modeled as if the orbits of the electrons were current loops. The induced moment is proportional to the current times the area of the loop. Current will depend on the passage of charge, which is the number of electrons times the charge on the electron, $e$, and on the frequency of the orbital motion, which also depends on the charge $e$. Thus one might expect a susceptibility with functionality going as $Ze^2 \langle r^2 \rangle$, where $r$ is the orbital radius. Indeed, the simple Langevin theory of diamagnetism predicts

$$\kappa = -\frac{NZe^2}{mc^2} \langle r^2 \rangle \tag{6.8}$$

In Equation (6.8), $N$ is the number of atoms per unit volume, $m$ is the electron mass, and $c$ is the speed of light.

**TABLE 6.5** **Magnetic molar susceptibility of some diamagnetic substances**

| Substance | Susceptibility, $\chi_M$ ($10^{-6}$ emu mol$^{-1}$ Oe$^{-1}$) |
|---|---|
| Argon | $-19.6$ |
| Bismuth | $-280$ |
| Calcium carbonate | $-38.2$ |
| Carbon (diamond) | $-5.9$ |
| Carbon (graphite) | $-6.0$ |
| Copper | $-5.46$ |
| Gold | $-28$ |
| Helium | $-1.88$ |
| Lead | $-23$ |
| Mercury | $-24.1$ |
| Neon | $-6.74$ |
| Nitrogen ($N_2$) | $-12$ |
| Silicon dioxide | $-29.6$ |
| Silver | $-19.5$ |
| Sodium chloride | $-30.3$ |
| Sulfur | $-15.5$ |
| Water | $-12.97$ |
| Water (ice 0°C) | $-12.65$ |
| Xenon | $-43.9$ |
| Acetone | $-33.7$ |
| Benzene | $-54.8$ |
| Carbon tetrachloride | $-66.6$ |
| Carbon tetrabromide | $-93.7$ |
| Ethanol | $-33.6$ |
| Methanol | $-21.4$ |
| n-Octane | $-96.6$ |
| n-Pentane | $-63.1$ |
| Toluene | $-66.1$ |

Compiled from reference 4.

Equation (6.8) tells us that large atoms (high $Z$ and large $\langle r^2 \rangle$) have large diamagnetic susceptibilities. It also shows no temperature dependence, a key parameter for other types of magnetism. Table 6.5 gives the diamagnetic susceptibility for a few selected materials.

## 6.3.2 Paramagnetism

Paramagnetism occurs when the atomic, ionic, or molecular constituents have a nonzero magnetic moment. Then an applied field can align these moments to create a positive susceptibility. The diamagnetic response is still present, but the atomic moments have a much greater magnitude than the induced diamagnetic moments. The source of atomic scale magnetic moments is unbalanced angular momentum of

(a)



(b)
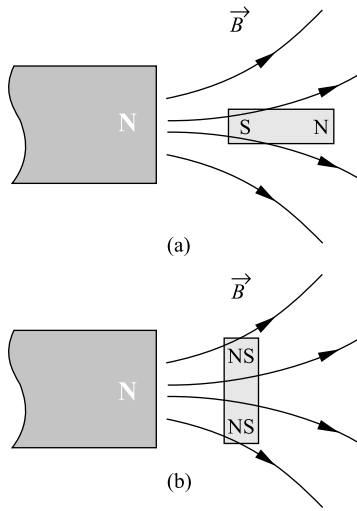
**FIGURE 6.1**  A magnetic field applied to an elongated material. (a) When $\kappa > 0$, the induced dipole is in the same direction as the applied field and the net force is attractive. (b) When $\kappa < 0$ (diamagnetic) the induced dipole is opposite to the applied field and to minimize this unfavorable antiparallel alignment the material rotates its axis perpendicular to the field. The net force is repulsive.

the electrons, either orbital or spin. Both angular momenta yield a magnetic moment given by

$$\mu = g\mu_B J \tag{6.9}$$

In Equation (6.9), $g$ is the so-called $g$ factor. For a free electron, $g \simeq 2.00$. The Bohr magneton $\mu_B$ is given by

$$\mu_B = \frac{e\hbar}{2mc} = 0.927 \times 10^{-20} \quad \text{emu} \tag{6.10}$$



**FIGURE 6.2**  Magnetic state of the elements at room temperature ($T = 20°C$). *Gadolinium becomes ferromagnetic at 16°C.

where $\hbar = h/2\pi$ and $h$ is the Planck constant. This is the fundamental unit of magnetism. Note its magnitude: a macroscopic quantity of Bohr magnetons, say $\sim 10^{23}$, would yield a healthy magnet; a fact which fortunately does transpire. Finally, Equation (6.9) contains the angular momentum quantum number $J$, which is of order unity. For a free electron the angular momentum is purely spin and so $J = S = \frac{1}{2}$, hence

$$\mu = g\mu_B S = \mu_B \qquad (6.11)$$

Nonzero magnetic moments leading to paramagnets can occur in many materials. Spin moments can result in atoms or molecules with an odd number of electrons, in transition metals with partially filled $d$-shells, and in rare earths with partially filled $f$-shells. Orbital moments also contribute in the rare earths (hence their large moments), but are quenched to zero in the transition metals. Many other metals are paramagnetic due to the electrons within $kT$ (the thermal energy) of the top of the conduction band (Pauli paramagnetism). There are a few cases of compounds with an even number of electrons that are paramagnetic, such as molecular oxygen.

Even a very small applied field would readily align all the atomic moments and create a significant polarization if it were not for the randomizing effect of thermal motion. Indeed, the energy of magnetic moment alignment in an applied field and the thermal energy, which causes randomization, are the primary actors in the phenomena of paramagnetism and ferromagnetism. The simplest model that uses this competition is the Langevin model of paramagnetism, which gives us our first intuition into the importance of temperature for magnetic properties.

**6.3.2.1   The Langevin Model of Paramagnetism**   We consider $N$ atoms each with a magnetic moment of $\mu$. In an applied field the moment tends to align with the field and the energy of interaction is

$$\begin{aligned} U &= -\vec{\mu} \cdot \vec{H} \\ &= -\mu H \cos\theta \end{aligned} \qquad (6.12)$$

where $\theta$ is the angle between $\vec{\mu}$ and $\vec{H}$. Note that Equation (6.12) assumes that the moment can point in any direction relative to $\vec{H}$. This is only true for non-quantum-mechanical moments. While such moments do exist (for example, see the description of superparamagnetism below), this is definitely not true for atomic moments, so we proceed with caution.

The total moment of the macroscopic body will be proportional to $\mu$, the number of atoms (per unit volume) $N$, and the degree of alignment. The alignment is measured by $\cos\theta$, and since there are many moments, we need the average of $\cos\theta$. Thus

$$M = N\mu\langle\cos\theta\rangle \qquad (6.13)$$

The average alignment $\langle\cos\theta\rangle$ can be obtained from the probability of having a given $\cos\theta$. In a system in thermal equilibrium at temperature $T$, the probability is given by the Boltzmann distribution

$$p(U) = e^{-U/kT} \tag{6.14}$$

In Equation (6.14) $k$ is Boltzmann's constant, $k = 1.38 \times 10^{-16}$ erg K$^{-1}$. Then

$$\langle\cos\theta\rangle = \frac{\int\cos\theta\, e^{-U/kT}\, d\Omega}{\int e^{-U/kT}\, d\Omega} \tag{6.15}$$

The integration is over all solid angles, $d\Omega$. The integration is straightforward and one obtains

$$M = N\mu L(x) \tag{6.16a}$$
$$L(x) = \coth x - x^{-1} \tag{6.16b}$$
$$x = \mu H/kT \tag{6.16c}$$

Equation (6.16b) is the Langevin function. In Equation (6.16c) the parameter $x$ is the ratio of magnetic alignment energy to thermal randomizing energy, and hence gives emphasis to the competition between these two.

   To gain a feel for the Langevin result we look at its properties at small and large $x$. At small $x$,

$$L(x) \simeq x/3 \tag{6.17}$$

Hence the magnetization is

$$M \simeq \frac{N\mu^2 H}{3kT} = \frac{C}{T}\, H \tag{6.18}$$

This result with its inverse temperature dependence is known as the Curie law, and $C$ is the Curie constant given by

$$C = \frac{N\mu^2}{3k} \tag{6.19}$$

Equation (6.18) applies when $kT \gg \mu H$. For example, if $\mu = \mu_B = 0.927 \times 10^{-20}$ erg Oe$^{-1}$, and if $T \simeq 300$ K (roughly room temperature), $x = 1$ when $H = 1.2 \times 10^5$ Oe $= 12$ T. Thus, it takes huge fields to align paramagnets significantly at normal temperatures. On the other hand, if $T = 4$ K, then a relatively modest field of $H = 1.6 \times 10^3$ Oe $= 0.16$ T will give $x = 1$ and some alignment.

At large $x$, $L(x) \to 1$, and all the moments are aligned. This is called the saturation magnetization,

$$M_s = N\mu \tag{6.20}$$

In Figure 6.3 $L(x)$ is plotted against $x$.

**6.3.2.2  *Quantum Effects***   An atomic scale angular momentum will be controlled by quantum mechanics and hence only selected, discrete values of moment orientation relative to the applied field will be allowed. For an angular momentum $J$ there will be $2J + 1$ possible orientations of the moment as described by the azimuthal quantum number $m_J = J, J - 1, \ldots, -J$. After this modification, the physics of alignment in an applied field at finite temperature is the same, viz., the competition between field alignment and thermal randomization. The Boltzmann distribution is still used to calculate the average orientation. The general result is

$$M = NgJ\mu_B B_J(x) \tag{6.21a}$$

where

$$B_J(x) = \frac{2J+1}{2J}\coth\left(\frac{(2J+1)x}{2J}\right) - \frac{1}{2J}\coth\left(\frac{x}{2J}\right) \tag{6.21b}$$



$$x = \mu H / kT$$
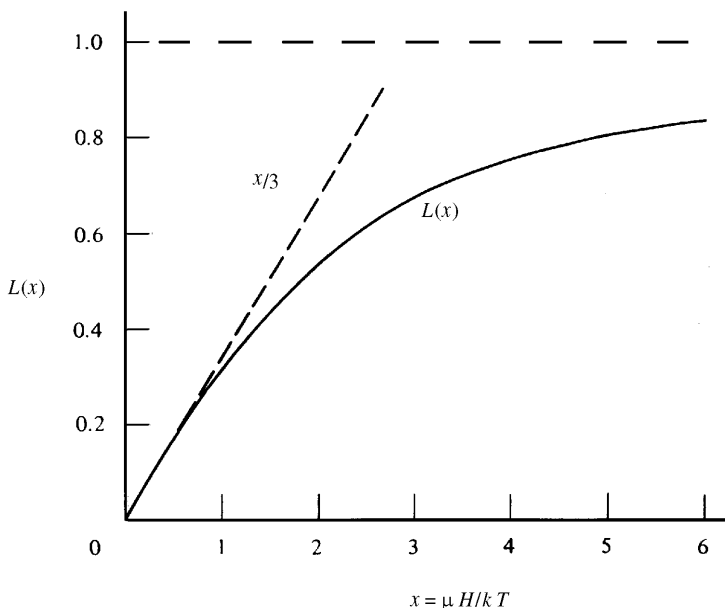
**FIGURE 6.3**   The Langevin function for classical paramagnetism.[1]

and

$$x = gJ\mu_B H/kT \tag{6.21c}$$

The function $B_J(x)$ is called the Brillouin function.

For $x \ll 1$, a typical situation near room temperature, one can show that Equations (6.21) yield

$$M \simeq \frac{NJ(J+1)g^2\mu_B^2}{3kT} H \tag{6.22}$$

The Curie law, $M = C/T$, is regained. The effective magnetic moment resides in the Curie constant $C$ and is equal to $\mu_{\text{eff}} = g\sqrt{J(J+1)}\mu_B$ by comparison with Equations (6.18) and (6.22).

The Brillouin function has two significant limits with $J$. When $J = \frac{1}{2}$, there are only two states and it is easy to show that

$$M = N\mu \tanh x \tag{6.23}$$

results. When $J \to \infty$, the Brillouin function becomes the Langevin function (Equation 6.16b).

Figure 6.4 shows a plot of $M$ versus $x = gJ\mu_B H/kT$ for the Brillouin result (Equations 6.21), for various $J$, and we see that the shape evolves somewhat as we go from the simplest quantum mechanical limit of two states ($J = \frac{1}{2}$) to the classical, Langevin limit ($J \to \infty$).
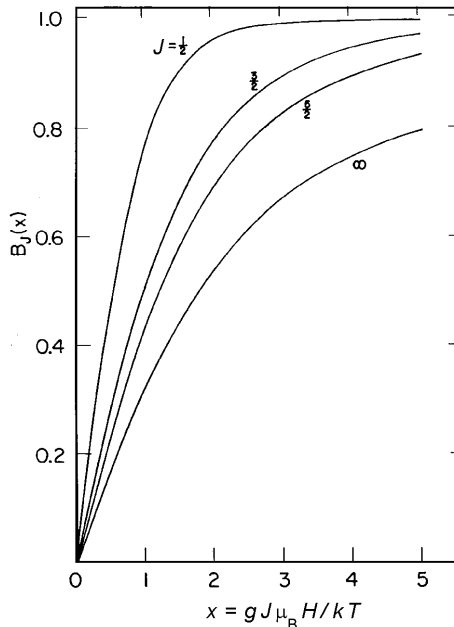


**FIGURE 6.4** The Brillouin function for quantum paramagnetism for various values of $J$.

***6.3.2.3 Experimental Implications*** From an experimentalist's point of view, the theory above implies that magnetization data for a paramagnet fall on a universal curve if plotted as a function of $H/T$. Conversely, any data that show universality with plotting $M$ versus $H/T$ imply the system could be paramagnetic.

A very useful technique is the Curie plot, in which inverse susceptibility is plotted versus $T$. By the Curie law (Equation 6.18), $\kappa = C/T$. Thus, a straight line is obtained if the system is paramagnetic. Furthermore, the inverse of the slope of $\kappa^{-1}$ versus $T$ yields $C$, the Curie constant, from which the magnetic moment of the atomic entity can be determined from Equations (6.19) or (6.22). Figure 6.5 shows a schematic of the behavior of both $\kappa$ and $\kappa^{-1}$ versus $T$ for a paramagnet.

### 6.3.3 Ferromagnetism

***6.3.3.1 The Curie–Weiss Law*** The Curie law for paramagnetism (Equation 6.15) has been found to hold for many materials. However, many other materials display a somewhat modified behavior described by

$$\kappa = \frac{C}{T - \theta} \tag{6.24}$$
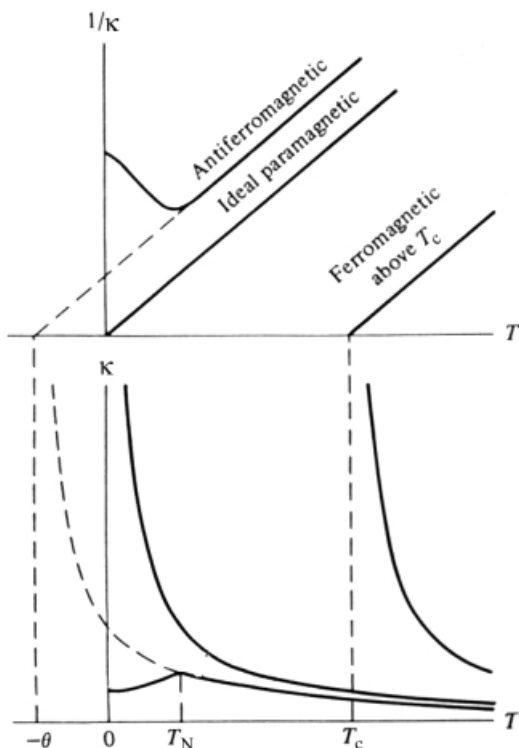


**FIGURE 6.5** The behavior of the susceptibility $\kappa$ and its inverse as a function of temperature for para-, ferro-, and antiferromagnetic materials.[1]

where $\theta$ is a critical temperature that can be either positive or negative. This modification is called the Curie–Weiss law. Equation (6.24) is a remarkable result because it diverges at $\theta$, which is a finite temperature when $\theta$ is positive. Since $\kappa = M/H$, this means that a net magnetization ($M \neq 0$) can be achieved even if the applied magnetic field is zero. We would say the system has a spontaneous magnetization.

To explain this empirical result, Weiss proposed that the atomic moments were interacting with each other magnetically. To model this interaction he assumed that the net interaction on a given moment is an effective magnetic field, a mean field, due to all the other moments. It is reasonable to propose that this effective field is proportional to the magnetization of the material, hence

$$H_{\mathrm{E}} = \alpha M \tag{6.25}$$

Then the total field experienced by any given moment is

$$H_{\mathrm{tot}} = H + \alpha M \tag{6.26}$$

It is with this total field that the thermal energy "fights." Thus, the Curie law still holds but with the modification

$$\kappa' = \frac{M}{H_{\mathrm{tot}}} = \frac{C}{T} \tag{6.27}$$

Substitution of Equation (6.26) into (6.27) yields

$$\kappa = \frac{M}{H} = \frac{C}{T - \alpha C} \tag{6.28}$$

With this, we regain the Curie–Weiss law of Equation (6.24) with $\theta = \alpha C$.

A more careful look at the data near the divergence or critical temperature $T_{\mathrm{c}} = \theta$ for materials following the Curie–Weiss law (e.g., ferromagnets) reveals that the susceptibility is better described by

$$\kappa \propto (T - T_{\mathrm{c}})^{-\gamma} \tag{6.29}$$

where $\gamma \sim 1.3$, inconsistent with the mean field prediction. Furthermore, using $T_{\mathrm{c}} = \alpha C$ leads to unrealistically large values of $H_{\mathrm{E}}$; for example, for iron $T_{\mathrm{c}} \simeq 1000\,\mathrm{K}$ and then $H_{\mathrm{E}} \sim 10^7\,\mathrm{Oe}$! Thus, the mean field theory has serious problems. More accurate theories consider only nearest-neighbor interactions for the atomic moments and the interactions are not magnetic, but rather due to what is called an exchange interaction, which is quantum mechanical in origin. The Weiss theory works semiquantitatively because the basic concept of an interaction between atomic moments is correct.

Weiss, in 1906, realized that the spontaneous magnetization that occurs below $T_{\mathrm{c}}$ could be used to explain ferromagnetism. Then we view a ferromagnet as a material

that is self-starting. However, there must be more because if there is only a molecular field, every piece of iron would have a significant dipole moment, and this is obviously not the case. To contend with this, Weiss proposed that ferromagnetic materials can partition themselves into domains. Each domain is saturated by its molecular field, but the domains align in a manner that leaves a net zero magnetization. We will discuss domains below.

A theory for the temperature dependence of the spontaneous magnetization can be developed by simply substituting $H = H_e = \alpha M$ into the equations for the paramagnetic magnetization. The most general approach would use the Brillouin function. We write

$$M = M_0 B_J \left( \frac{gJ\mu_B \alpha M}{kT} \right) \tag{6.30}$$

Such an equation must be solved numerically. One finds for $T > \theta = \alpha C$, $M = 0$, but for $T < \theta$ a temperature dependent spontaneous magnetization occurs, $M_s(T)$, which is the solution to Equation (6.30). Recall from Equation (6.28) that $\theta = \alpha C$. Then if we define the reduced variables $m = M_s(t)/M_0$ and $t = T/\theta$, we can write

$$m = B_J(m/t) \tag{6.31}$$

Equation (6.31) shows that for a given $J$ all data for a variety of ferromagnetic materials would lie together if plotted with reduced variables. This is a "law of corresponding states," very similar to the same law found for fluids near critical points. Figure 6.6 shows the numerical solutions to (6.30) and some data for iron, cobalt, and nickel.

Expansion of (6.30) at small $m$ shows that $m \sim (t-1)^{1/2}$. In fact experiment gives $m \sim (t-1)^\beta$ with the critical exponential $\beta \simeq 0.35$. As with the susceptibility exponent above, this discrepancy is due to the mean field nature of the Curie–Weiss theory. Theories involving only local, nearest-neighbor interactions are successful in predicting the correct exponents.

When $M_s(T) \to M_0$ at low temperature, Equation (6.30) again fails to predict the proper temperature dependence. In this regime, when all the spins are nearly aligned, the thermal energy can excite spin waves, quantized excitations of the atomic spins tipped slightly away from the perfectly aligned state, as drawn in Figure 6.7. Then the magnetization follows Bloch's law:

$$M(T) = M_0(1 - BT^b) \tag{6.32}$$

$B$ is called the Bloch constant and the Bloch exponent is $b = d/2$, where $d$ is the spatial dimension, typically $d = 3$. Figure 6.8 shows an example of Bloch's law for both bulk and nanoscale materials.[5]

### 6.3.3.2 Origins of Ferromagnetism
Weiss molecular field theory is very successful in semiquantitatively describing the onset and behavior of ferromagnet-
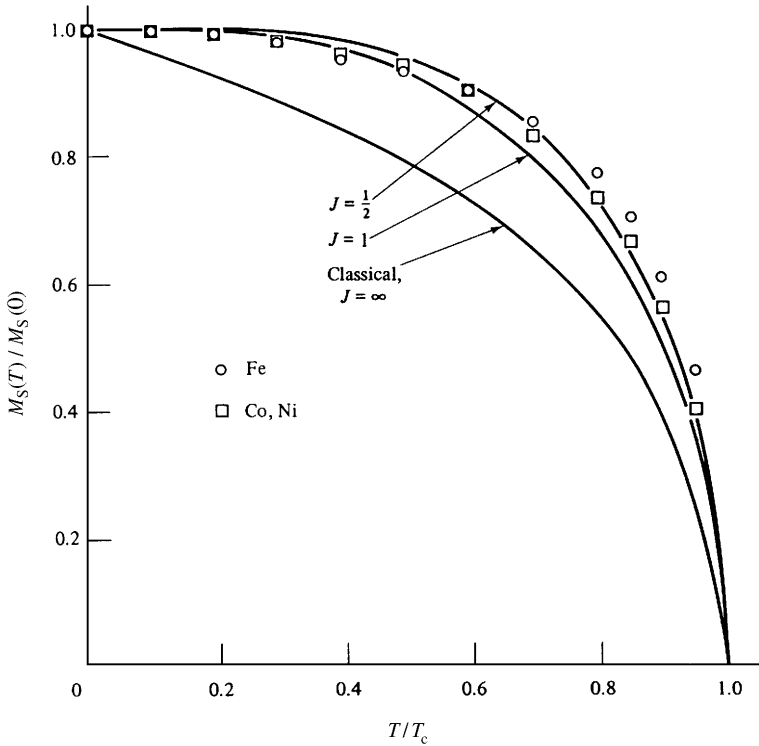
**FIGURE 6.6**  Saturation magnetization versus temperature, both as scaled variables. Lines are predictions of the mean field theory for ferromagnetism using the quantum Brillouin function with three different $J$-values. Points are data for iron, cobalt, and nickel.[1]

ism. It predicts spontaneous magnetization (i.e., does not need an applied field) below a critical temperature, called the Curie temperature, and paramagnetic behavior (Curie–Weiss) above. We have seen, however, that it misses in the details of the temperature dependence, and the magnitude of the molecular field seems unreasonably high. This latter aspect implies that the origin of the interatomic coupling is unknown. The true physical origin of the coupling was elucidated by Heisenberg in 1928, following the Heitler–London treatment of the hydrogen molecule. Quantum mechanics provides for an exchange interaction, as it is now called, between two atoms based on symmetry, the Pauli exclusion principle, and the coulombic interaction. A two-electron system, one from each atom, can have one of either two spin configurations: parallel or antiparallel signs. If the atoms are brought near to each other, the electron wavefunctions will overlap, and if they are from the same atomic quantum state, the Pauli exclusion principle will enhance the probability for the electron wavefunction to overlap if the spins are antiparallel and tend to keep them apart when the spins are parallel, for then all four quantum numbers (three atomic, one spin) would be the same. This, combined with the coulombic interaction, means that parallel and antiparallel spin configurations will have different energies.
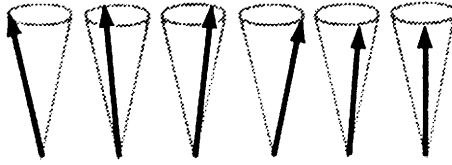
**FIGURE 6.7** Schematic drawing of spin wave. Kittel, *Introduction to Solid State Physics*, 7E, Copyright© **1995** John Wiley & Sons, Inc. Reprinted by permission of John Wiley & Sons, Inc.

Heisenberg showed that these effects lead to an exchange energy given by

$$E_{\text{ex}} = -2J_{\text{ex}}\vec{S}_i \cdot \vec{S}_j \tag{6.33}$$

between neighboring spins, $\vec{S}_i$ and $\vec{S}_j$. $J_{\text{ex}}$ is called the exchange integral. If $J_{\text{ex}}$ is positive, the lower energy configuration is that of parallel spins, and hence parallel magnetic moments as required for ferromagnetism. If $J_{\text{ex}}$ is negative, the antiparallel configuration results, a situation that leads to antiferromagnetism.
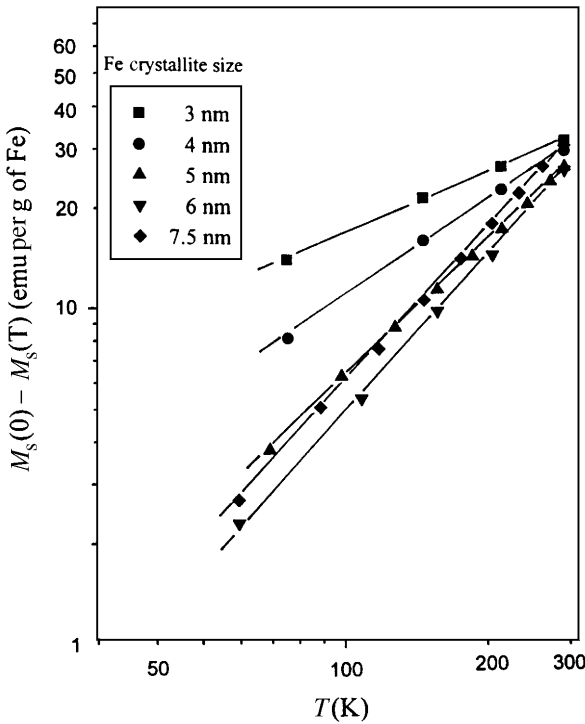


**FIGURE 6.8** Saturation magnetization depression relative to its value at 0 K versus temperature for different size iron crystallites in a matrix of $MgF_2$. By Bloch's law (Equation 6.32), this log–log plot should have a slope of $b$. Reprinted with permission from D. Zhang et al, *Phys. Rev. B*, **1998**, *58*, 1467, American Physical Society.

Interestingly, the most common situation is $J_{ex} < 0$, antiparallel coupling (this happens in the covalent bond of the hydrogen molecule). However, fortunately (for much of our technology!) $J_{ex} > 0$ also occurs in rare cases and ferromagnets can result. Slater found empirically that a correlation exists between the ratio of the interatomic distance $2r_a$ to the radius of the incompletely filled $d$ shell $r_d$ of some transition metal elements and the sign of the exchange integral. Subsequently, Bethe was able to use quantum mechanics to explain this observation. The result is called the Bethe–Slater curve and is shown in Figure 6.9. Unbalanced spins in the $d$ subshell of iron, cobalt, and nickel are the source of their magnetism. The Bethe–Slater curve correctly differentiates iron, cobalt, and nickel as having positive $J_{ex}$ and hence being ferromagnetic. Moreover, the magnitude of $J_{ex}$ is in the order of Ni–Fe–Co, which is also the order of their Curie temperatures. It also correctly predicts the antiferromagnetism of chromium and manganese, and correctly correlates their antiferromagnetic ordering temperatures. It also implies that if one could somehow change the atomic spacings, magnetic properties would change. Thus, alloys such as MnBi are ferromagnetic because the manganese atoms are farther apart in the alloy than in the pure metal and hence $2r_a/r_d$ has increased, taking manganese into the $J_{ex} > 0$ regime of the Bethe–Slater curve. These successes have occurred despite criticism of the Bethe calculation.

### 6.3.3.3   *Band Theory*

We next contend with the problem of identifying the source of magnetic moments in the first row of transition metals, most notably iron, cobalt, and nickel. A first guess would be to look at the unbalanced spins in the $3d$ shell that is being filled as one progresses across the row from scandium to zinc. At scandium the first electron is added to the $3d$ shell "below" the $4s$ shell that was filled beyond argon with potassium and calcium. After scandium, as electrons are added, they all go in (by Hund's rule) with the same spin, say spin-up, until at chromium and manganese five spin-up electrons reside in the $3d$ shell (chromium has a $3d^5 4s^1$ configuration, manganese has $3d^5 4s^2$). This excess spin yields a spin magnetic moment of $5\mu_B$ for these atoms. Progressing now to higher atomic number, the spin-down half of the $3d$ shell fills, compensating the already filled spin-up shell; thus iron has a $4s^2 3d^6$ configuration and a net spin of 4. And, indeed, these magnetic
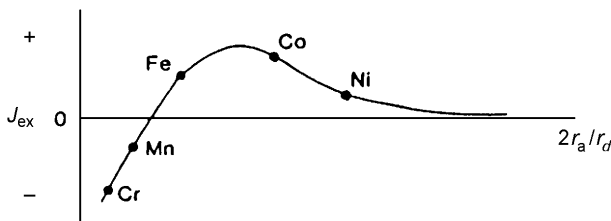


**FIGURE 6.9**   The Bethe–Slater curve. $2r_a/r_d$ is the atomic separation divided by the radius of the atomic $d$-shell; $J_{ex}$ is the exchange integral and positive values yield ferromagnetic coupling, negative values yield antiferromagnetic coupling.

moments are observed, with various perturbations, in insulating compounds of the transition metals.

Much of this changes when the atoms are brought together to form a solid metal. Most notably, the discrete atomic energy levels broaden greatly to form electronic bands. In the 3d transition metals, the outermost 4s state broadens the most, followed by the 3d level, which also broadens significantly. The shells closer to the nucleus do not overlap significantly, hence neither do they broaden. Figure 6.10 gives a schematic picture of the 4s and 3d bands and significant overlap in energy (plotted on the vertical axis) is seen. The density of states per energy interval is plotted horizontally, to the right for the 4s bands and to the left for the 3d band. The total area of each band in this diagram is the total number of possible states per atom: two for the 4s and 10 for the 3d, a remnant of the atomic configuration. The extent to which these bands are filled by electrons depends on the number of 3d plus 4s electrons in the atom. The level to which the bands are filled is the Fermi level, and such levels are shown for the atoms manganese through zinc.

Consider nickel, which has eight 3d electrons and two 4s electrons in the atomic state. In the metal these ten electrons fill up and mix in both the 3d and 4s bands to the same Fermi level. It is known from the magnetic properties of nickel that the 3d is filled to the 9.4 electron level and the 4s band is filled to the 0.6 level.

It is at this point that the exchange energy comes into play. We have discussed how exchange creates the coupling of magnetic moments necessary for spontaneous magnetization. But it has another related, and very important, role which is to create a spin imbalance in the band. Since parallel spins interact with a different energy
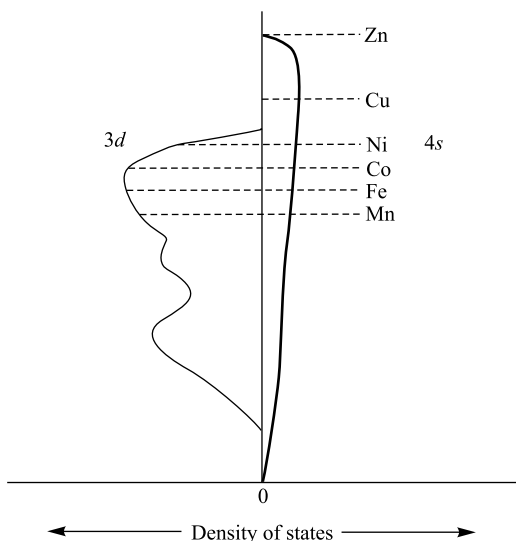


**FIGURE 6.10**   Schematic of the 3d and 4s electron bands of the first-row transition elements. Fermi levels are marked for various elements.

from antiparallel spins, the $3d$ band splits into spin-up and spin-down with different energies. Thus the nearly filled (9.4) $3d$ band of nickel is in fact a completely filled spin-up band of five electrons and a partially filled spin-down band of 4.4 electrons. The net result is 0.6 unbalanced spin, from which a net magnetic moment of $0.6\mu_B$ results.

We can now extend this picture to other elements in the $3d$ row of the periodic table. Moving left to cobalt removes one $3d$ electron per atom, so if nickel is short 0.6 electrons, cobalt should be short 1.6. Likewise, iron and manganese should be short 2.6 and 3.6, respectively, and in all cases their spins are unbalanced. Moving to the right to copper adds an electron and overfills the $3d$ band by 0.4 electrons. Thus, copper is not ferromagnetic because the $3d$ band is full, hence there is no spin imbalance. The magnetic moments thus should be short by values times $\mu_B$, the Bohr magneton. This linear prediction is plotted in Figure 6.11 along with the measured moments; reasonable agreement is seen, thus substantiating the band theory.

Slater used these ideas to explain the ferromagnetism of simple alloys. For example, what is the magnetic moment of an equimolar mixture of nickel and copper? Since nickel has a $3d$ band underfilled by 0.6 electrons and copper has a $3d$ band overfilled by 0.4 electrons, this equimolar mixture should have a $3d$ band filling of $(0.5)(+0.6) + (0.5)(-0.4) = +0.1$ and hence be ferromagnetic with a moment of $0.1\mu_B$ per atom. Similar arguments can be made with success for other combinations of $3d$ elements. This theory is useful not only for alloys but for the general concept that if one can manipulate the $d$-band of a transition metal, one can manipulate its magnetism.
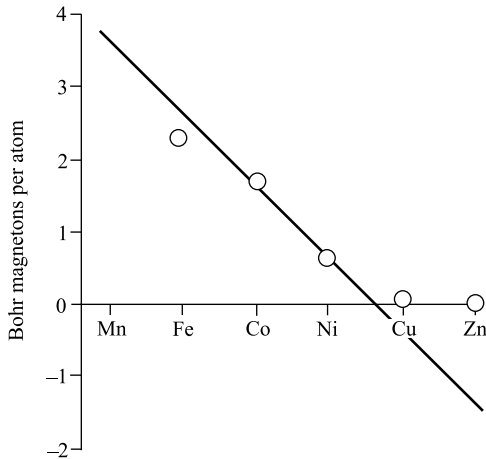


**FIGURE 6.11**   Band theory prediction (line) for the number of Bohr magnetons per atom for a number of the $3d$ transition metals. A value less than or equal to zero implies the metal is not ferromagnetic. Circles are data.

**6.3.3.4** *Antiferromagnetism*    In an antiferromagnet, exchange coupling exists between neighboring moments that causes the moments to align in an antiparallel fashion: the exact opposite of a ferromagnet. Thus, in terms of the Heisenburg hamiltonian of Equation (6.33), the exchange integral $J_{ex}$ is negative. This antiparallel alignment causes the system to have a small, positive susceptibility, because an applied field tends to align the spins and this induced alignment is larger than the diamagnetism of the electron orbitals. Similar to ferromagnets, the exchange energy can be defeated at high temperature and then the system becomes paramagnetic.

The behavior of the antiferromagnetic susceptibility is depicted in Figure 6.5 and in more detail in Figure 6.12. For temperatures greater than a critical temperature, the susceptibility follows a paramagnetic Curie–Weiss law with a negative $\theta$. Thus, ferromagnets and antiferromagnets are akin at high $T$ following Curie–Weiss, differing only in the sign of $\theta$. This kinship and difference are a direct consequence of the same Heisenburg hamiltonian but differing signs in the exchange integral. Below the critical temperature $T_N$, the Néel temperature, the system orders. Thereafter, the susceptibility decreases with decreasing temperature because the tendency for antiparallel alignment increases. Many antiferromagnetic systems are known, usually ionic compounds such as metallic oxides, sulfides, chlorides, and so on. Both chromium and manganese are antiferromagnetic, although their susceptibilities do not obey the Curie–Weiss law. See Table 6.6 for other examples.

A microscopic view of an antiferromagnet is depicted in Figure 6.13. There we see two sublattices, usually called A and B. A molecular field theory for antiferromagnetism incorporating only the antiparallel interaction of the A and B
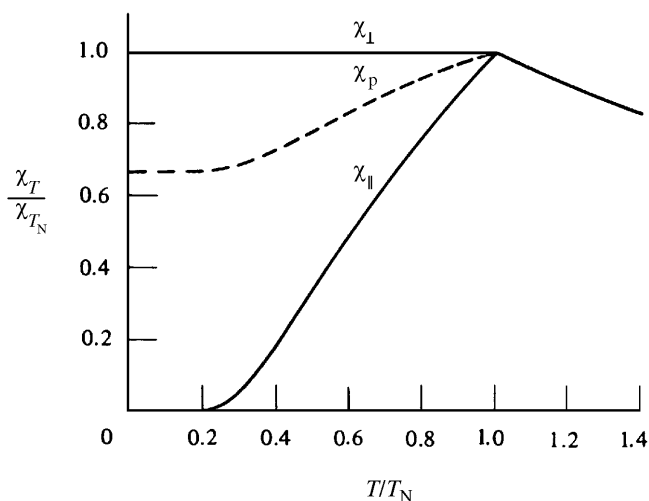


**FIGURE 6.12**    Antiferromagnetic susceptibility (mass) as a function of temperature. $\chi_{\parallel}$ is for the applied field parallel to the spin axis, $\chi_{\perp}$ is for the applied field perpendicular to the spin axis, and $\chi_p$ is for a powder sample with random spin axes.[1]

**TABLE 6.6  Antiferromagnetic substances**

| Substance | Paramagnetic Ion Lattice[a] | Transition Temperature $T_N$ (K) | Curie–Weiss $\theta$ (K) | $\dfrac{\theta}{T_N}$ | $\dfrac{\chi(0)}{\chi(T_N)}$ |
|---|---|---|---|---|---|
| MnO | fcc | 122 | 610 | 5.0 | 0.69 |
| MnO$_2$ | bct | 84 | – | – | 0.93 |
| $\alpha$-MnS | fcc | 154 | 465 | 3.0 | 0.82 |
| $\beta$-MnS | fcc | 155 | 982 | 6.3 | – |
| MnTe | hex. layer | 307 | 690 | 2.25 | – |
| MnFe$_2$ | bc tetr. | 67 | 82 | 1.24 | 0.76 |
| FeF$_2$ | bc tetr. | 79 | 117 | 1.48 | 0.72 |
| FeCl$_2$ | hex. layer | 24 | 48 | 2.0 | < 0.2 |
| FeO | fcc | 198 | 570 | 2.9 | 0.8 |
| $\alpha$-Fe$_2$O$_3$ | rhomb. | 950 | 2000 | 2.1 | – |
| FeS | hex. layer | 613 | 857 | 1.4 | – |
| CoCl$_2$ | hex. layer | 25 | 38.1 | 1.53 | – |
| CoF$_2$ | bct | 40 | 53 | 1.3 | – |
| CoO | fcc | 291 | 330 | 1.14 | – |
| NiCl$_2$ | hex. layer | 50 | 68.2 | 1.37 | – |
| NiO | fcc | 525 | ~2000 | ~4 | – |
| $\alpha$-Mn | complex cubic | ~100 | – | – | – |
| Cr | bcc | 308 | – | – | – |
| CrSb | hex. layer | 723 | 550 | 0.76 | ~$\frac{1}{4}$ |
| Cr$_2$O$_3$ | rhomb. | 307 | 485 | 1.58 | – |
| FeCO$_3$ | complex | 35 | 14 | 0.4 | ~$\frac{1}{4}$ |
| CuCl$_2$·2H$_2$O | rhomb. | 4.3 | 5 | 1.2 | – |

Compiled from references 1 and 2.

[a] hex., hexagonal; tetr., tetragonal; rhomb., rhombic.
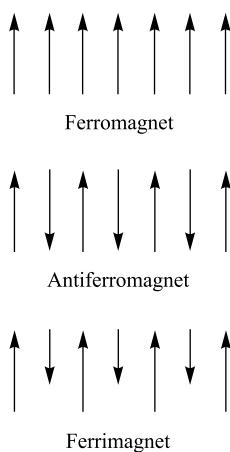


FIGURE 6.13  Schematic depiction of spin arrangements in a ferromagnet, an antiferromagnet, and a ferrimagnet.

sublattices predicts that $\theta/T_N = 1$. Table 6.6 shows that this is rarely the case and the reason is due to interactions within each sublattice.

The exchange interaction in antiferromagnetic ionic solids occurs indirectly via a mechanism called superexchange. The nearest neighbors to the metallic ions, which carry the magnetic moment, are anions such as $O^{2-}$, $S^{2-}$ and $Cl^-$. Thus, for two metallic ions to communicate their spin states to each other they must work through an anion. This occurs by spin polarizing the outer electron orbitals of the anion so the spin information can be conveyed.

Antiferromagnets can be quite complex and do not always display the canonical behavior of Figure 6.12. This is especially true for nonionic systems such as metallic chromium and manganese and alloy systems. In such cases neutron diffraction, which can sense spin alignments at the atomic level, is necessary to positively identify an antiferromagnet.

### 6.3.3.5  *Ferrimagnetism*    Ferrimagnets are similar to antiferromagnets in that two sublattices exist that couple through a superexchange mechanism to create an antiparallel alignment. However, unlike an antiferromagnet, the magnetic moments on the ions of the sublattices are not equal and hence they do not cancel; rather, a finite difference remains to leave a net magnetization. This spontaneous magnetization is defeated by the thermal energy above a critical temperature called the Curie temperature, and then the system is paramagnetic. The behavior of the susceptibility of a ferrimagnetic is depicted in Figure 6.14. At high temperatures Curie–Weiss behavior is seen with $\kappa^{-1}$ linear with $T$. As for an antiferromagnet, this linear behavior extrapolates to a negative $\theta$. Near the Curie temperature, $\kappa^{-1}$ versus $T$ is curved.

A microscopic view of a ferrimagnet is depicted in Figure 6.13.

A large number of ferrimagnets are known; a major class of which are the ferrites. There are two types of ferrites: cubic and hexagonal. Cubic ferrites have the general
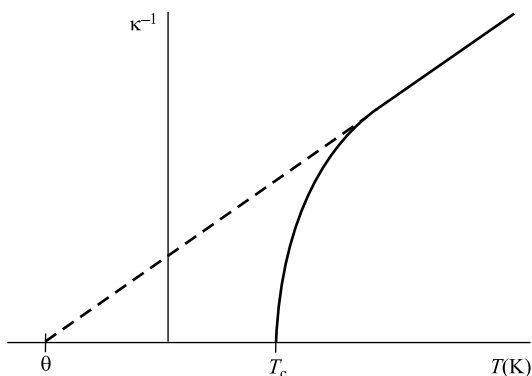


**FIGURE 6.14**    Curie plot, inverse susceptibility versus temperature, for a ferrimagnet (solid line). $T_c$ is the Curie temperature below which the system has a spontaneous magnetization. Dashed line is the Curie–Weiss law.

formula $MO \cdot Fe_2O_3$, where M is a divalent metal cation such as Mn, Ni, Fe, Co, and Mg. One of these is the oldest known magnetic material, magnetite or loadstone which is $FeO \cdot Fe_2O_3$ or equivalently $Fe_3O_4$. Hexagonal ferrites have the general formula $MO \cdot 6Fe_2O_3$. Perhaps the best-known example is barium ferrite, $BaO \cdot 6Fe_2O_3$.

As the general formulas imply, the ferrites have two sublattices. In the cubic ferrites the metallic ions in the A sublattice are tetrahedrally coordinated by oxygen atoms, whereas the ions in the B sublattice are octahedrally coordinated. Such a structure is called a spinel, and they are quite complex because there are 56 atoms in the unit cell. Moreover, the ions in the two sublattices can interchange depending on synthesis conditions or thermal treatment.

Ferrimagnets are technologically useful because they have a spontaneous magnetization and they are insulators as well.

Other classes of ferrimagnetic materials include the garnets and some alloys.

## 6.4   MAGNETIC PHENOMENA IN FERROMAGNETIC MATERIALS

### 6.4.1   Magnetic Anisotropy

In many situations the susceptibility of a material will depend on the direction in which it is measured. Such a situation is called magnetic anisotropy. When magnetic anisotropy exists, the total magnetization of a ferromagnet $M_s$ will prefer to lie along a special direction called the easy axis. The energy associated with this alignment is called the anisotropy energy and in its lowest order form is given by

$$E_a = K \sin^2 \theta \qquad (6.34)$$

where $\theta$ is the angle between $M_s$ and the easy axis. $K$ is the anisotropy constant.

There are several causes from which anisotropy may occur, including those induced by stress and prior mechanical handling of the material. Here we will discuss two important and common sources of anisotropy, which are magneto-crystalline anisotropy and shape anisotropy.

**6.4.1.1  *Magnetocrystalline Anisotropy***   Only magnetocrystalline anisotropy, or simply crystal anisotropy, is intrinsic to the material; all other anisotropies are induced. In crystal anisotropy, the ease of obtaining saturation magnetization is different for different crystallographic directions. An example is a single crystal of iron for which $M_s$ is most easily obtained in the [100] direction, then less easy for the [110] direction, and most difficult for the [111] directions. These directions and magnetization curves for iron are given in Figure 6.15. The [100] direction is called the easy direction, or easy axis, and because the other two directions have an overall smaller susceptibility, the easy axis is the direction of spontaneous magnetization when below $T_c$. Both iron and nickel are cubic and have three different axes, whereas
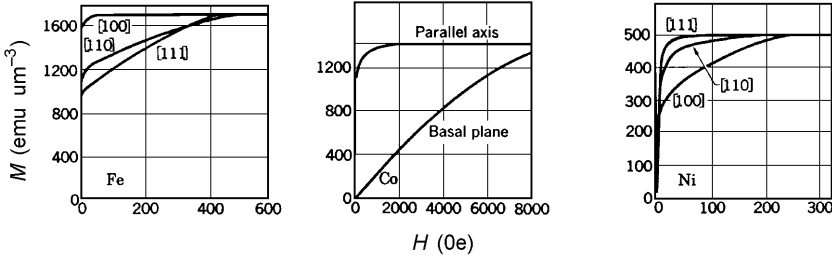
**FIGURE 6.15** Magnetization curves for single crystals of iron, cobalt, and nickel along different directions. Kittel, *Introduction to Solid State Physics*, 7E. Copyright© **1995**, John Wiley & Sons, Inc. Reprinted by permission of John Wiley & Sons, Inc.

cobalt is hexagonal with a single easy axis perpendicular to the hexagonal symmetry (the *c*-axis). Figure 6.15 also gives magnetization curves for cobalt and nickel.

One may now imagine a situation in which the system has spontaneous magnetization along the easy axis but a field is applied in another direction. Redirection of the magnetization to be aligned with the applied field requires energy (through the change in $\vec{M} \cdot \vec{H}$), hence the crystal anisotropy must imply a crystal anisotropy energy given by Equation (6.34) for a uniaxial material. This energy is an intrinsic property of the material and is parametrized, to lowest order, by the anisotropy constant $K = K_1$ which has units of erg per $cm^3$ or gram of material. Roughly speaking $K_1$ is the energy necessary to redirect the magnetization. Table 6.7 gives values for a number of materials. For a uniaxial material with only $K_1$, one can show (see below) that the field necessary to rotate the magnetization 90° away from the easy axis is

$$H = 2K_1/M_s \qquad (6.35)$$

Similar expressions with $H \sim K_1/M_s$ apply to cubic systems. As an example, consider uniaxial cobalt with $M_s$ from Table 6.3 and $K_1$ from Table 6.7, one

**TABLE 6.7  Anisotropy constants**, $K_1$

| Material | Structure | $K_1$ ($10^5$ erg cm$^{-3}$) |
|---|---|---|
| Fe | cubic | 4.8 |
| Ni | cubic | −0.45 |
| FeO·Fe$_2$O$_3$ | cubic | −1.1 |
| CoO·Fe$_2$O$_3$ | cubic | 20 |
| Co | hexagonal | 45 |
| Gd | hexagonal | 20 |
| Dy | hexagonal | 5000 |
| SmCo$_5$ | hexagonal | $1.1 \times 10^4$ |
| YCo$_5$ | hexagonal | 550 |
| BaO·Fe$_2$O$_3$ | hexagonal | 33 |

Compiled from references 1 and 3.

calculates $H = 6300$ Oe to saturate $90°$ from the easy axis. In fact, the experimental value is $\sim 12{,}000$ Oe because in cobalt a higher order anisotropy constant, $K_2$, makes a contribution to this recalcitrance.

The physical origin of the magnetocrystalline anisotropy is the coupling of the electron spins, which carry the magnetic moment, to the electronic orbit, which in turn is coupled to the lattice. Recall it was the strong coupling of the orbit to the lattice via the crystal field that quenched the orbital angular momentum.

***6.4.1.2 Shape Anisotropy***   It is easier to induce a magnetization along a long direction of a nonspherical piece of material than along a short direction. This is so because the demagnetizing field is less in the long direction, because the induced poles at the surface are farther apart. Thus, a smaller applied field will negate the internal, demagnetizing field. For a prolate spheroid with major axis $c$ greater than the other two and equal axes of length $a$, the shape anisotropy constant is

$$K_s = \frac{1}{2}(N_a - N_c)M^2 \tag{6.36}$$

where $N_a$ and $N_c$ are demagnetization factors. For spheres, $N_a = N_c$ because $a = c$. It can be shown that $N_c + 2N_a = 4\pi$; then in the limit $c \gg a$, that is, a long rod, $K_s = 2\pi M^2$. Thus a long rod of iron with $M_s = 1714$ emu cm$^{-3}$ would have a shape anisotropy constant of $K_s = 1.85 \times 10^7$ erg cm$^{-3}$. This is significantly greater than the crystal anisotropy, see Table 6.7, so we see that shape anisotropy can be very important for nonspherical materials.

## 6.4.2   Magnetic Domains

An ordinary piece of iron at room temperature is well below its Curie temperature, thus the exchange energy can align neighboring atomic moments so that they may act cooperatively to yield a macroscopic total moment. How is it then that this piece of iron in the absence of an applied field has no magnetic moment? The resolution to this paradox was given by Weiss in 1906, who proposed that a macroscopic magnetic material will break up into domains that align themselves in such a manner as to minimize the total effective moment of the material.

A magnetic field contains energy proportional to the field squared and its volume extent. Thus the magnetostatic energy of a single domain of parallel spins can be decreased by breaking it into smaller, oppositely aligned domains. This beneficial decrease in energy would continue with further breaking into more and yet smaller domains were it not for another energy that increases with declining size. This energy is the exchange energy at the boundary between oppositely aligned domains which, by the ferromagnetic nature of the coupling, fights against the antialignment.

This competition between the magnetostatic energy and what we will call the domain wall limits the break-up of the material to domains of a finite size. This process is represented in Figure 6.16.
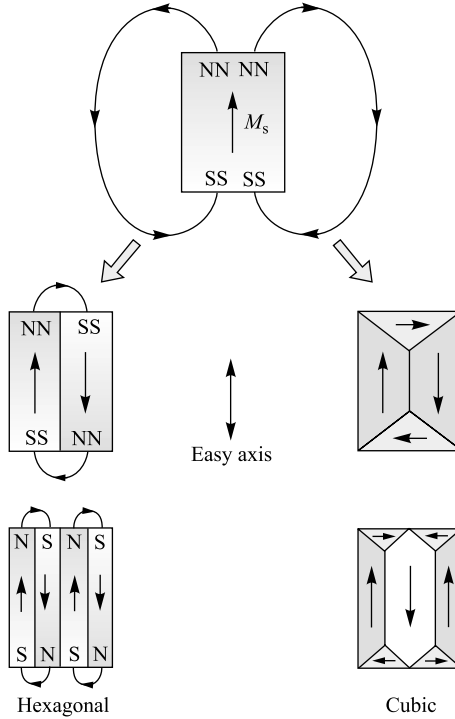
**FIGURE 6.16**   Domain creation and the associated magnetostatic field for both hexagonal and cubic crystals. Note how the external field decreases, and hence the magnetostatic energy decreases, as the system breaks into domains.

The boundary between domains, the domain wall, is a result of another competition of energies. The exchange interaction between two antiparallel spins in a ferromagnet is so unfavorable that the material tends to develop a wall of finite thickness, so that the 180° difference in spin alignments between domains can be shared by many spins as depicted in Figure 6.17, and hence a thick wall is favored. However, only the two antiparallel spins are along the material's easy axis, so that those in the finite thickness wall are tipped away from the easy axis. This gives rise to the magnetocrystalline anisotropy energy, which is not favorable and hence tends to minimize the thickness of the wall. This competition leads to an optimal wall thickness given approximately by

$$l \simeq \sqrt{kT_c/Ka} \qquad (6.37)$$

with a surface energy of

$$\gamma \simeq \sqrt{kT_c K/a} \qquad (6.38)$$
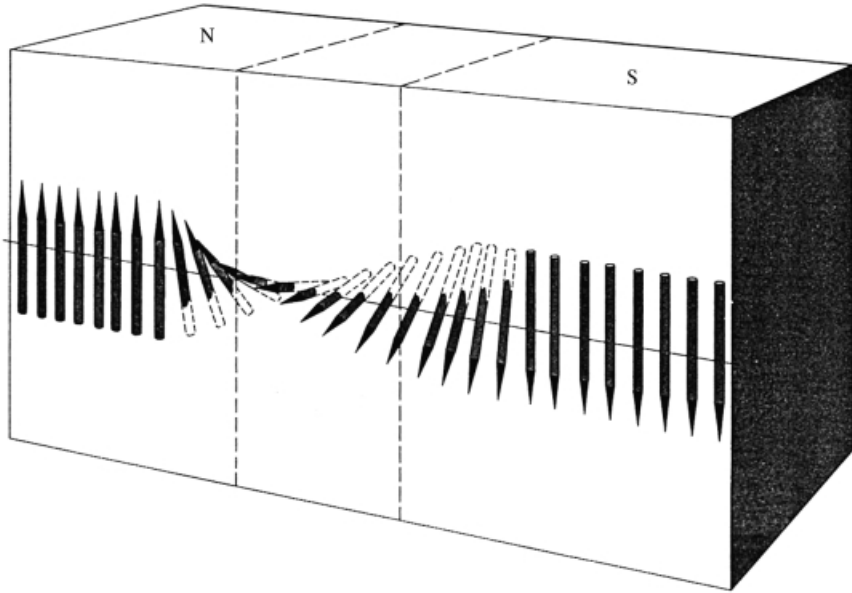
**FIGURE 6.17** Depiction of the spin orientation rotation through the domain (Bloch) wall. Kittel, *Introduction to Solid State Physics* 7E. Copyright© **1995** John Wiley & Sons, Inc. Reprinted by permission of John Wiley & Sons, Inc.

where $a$ is the lattice spacing. Typical values are domain walls of a few hundred angstroms thick with energy on the order of $1\,erg\,cm^{-2}$.

Domains can be observed via a number of techniques including the Bitter method, which involves treating the surface of the magnetic material with colloidal $Fe_3O_4$, Lorentz microscopy with a transmission electron microscope, and optical polarization methods using either the Kerr or Faraday effects.[1]

### 6.4.3 Hysteresis

When a ferromagnetic material is magnetized by an increasing applied field and then the field is decreased, the magnetization does not follow the initial magnetization curve obtained during the increase. This irreversibility is called hysteresis. An example of a full or major (i.e., $M$ is taken to near $M_s$) hysteresis curve (or loop) is given in Figure 6.18. At extremely high applied fields, the magnetization approaches the saturation magnetization, $M_s$. Then if the field is decreased to zero, the $M$ versus $H$ curve does not follow the initial curve but instead lags behind until, when $H = 0$ again, a remanant magnetization remains, the remanence $M_r$. If the field is now applied in the reverse direction (a negative field), $M$ is forced to zero at a field magnitude called the coercivity, $H_c$. Increasing this negative field still further forces the magnetization to saturation in the negative direction. Symmetric behavior of this hysteresis curve is obtained as $H$ is varied widely between large positive and negative values. One could say that hysteresis is due to internal friction. Hence the area inside the loop is the magnetic energy that is dissipated while circling the loop.
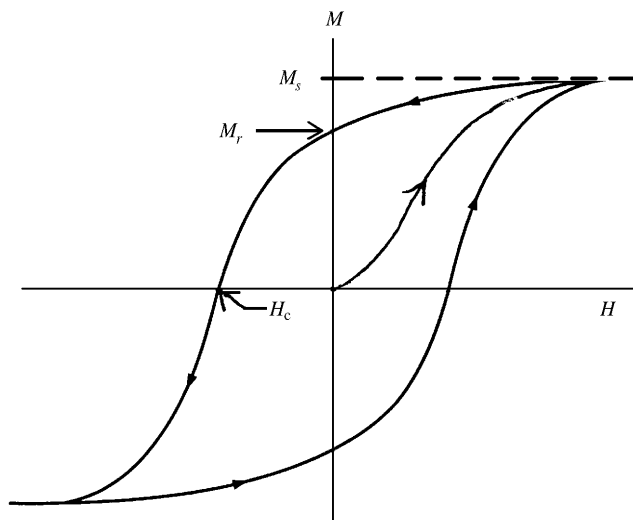
**FIGURE 6.18**    A full-loop hysteresis curve. $M_s$ is the saturation magnetization, $M_r$ is the magnetization remanence (at $H = 0$), and $H_c$ is the coercivity.

Cardinal points along the hysteresis curve are $M_s$, $M_r$, and $H_c$. Permanent magnets used in motors, generators, loudspeakers, and "refrigerator magnets" require large $M_s$ and $M_r$. It is also desirable that permanent magnets not be easily demagnetized by unexpected fields, hence a large coercivity is good as well. Materials with $H_c \gtrsim 100$ Oe are called hard magnets. The combination of large $M_r$ and $H_c$ can be parametrized by the energy product, which is the maximum value of $M \cdot H$ in the second (demagnetizing) quadrant of the hysteresis curve.

Soft magnetic materials are those with small $H_c$, typically $H_c < 10$ Oe. (The boundary between hard and soft is somewhat arbitrary and indefinite). Soft materials are needed for transformer cores because in AC applications the hysteresis loop is circled 60 times a second and, since the area of the loop represents dissipated energy, this energy is lost with every cycle. Other applications for soft materials are in electronic circuits.

The initial magnetization curve starting from the origin at $(H, M) = (0, 0)$ has a number of interesting features shown in Figure 6.19. Overall, the curve may be divided into two regimes. A schematic representation of the magnetization process is shown in Figure 6.20. Initially, when $H = 0$, Figure 6.20 shows a ferromagnetic sample with two domains each with the saturation magnetization along the easy axes but in opposite direction so that in total $M = 0$. As a finite field is applied, at some small angle relative to the easy axis, the domain less aligned with the field diminishes in favor of the one more aligned via domain wall motion to the right. This process causes the magnetization to increase in a parabolic manner concave upward, as shown in Figure 6.19. This continues until the sample is one domain. Further increase of the component of $M_s$ along the direction of the applied field $H$ requires
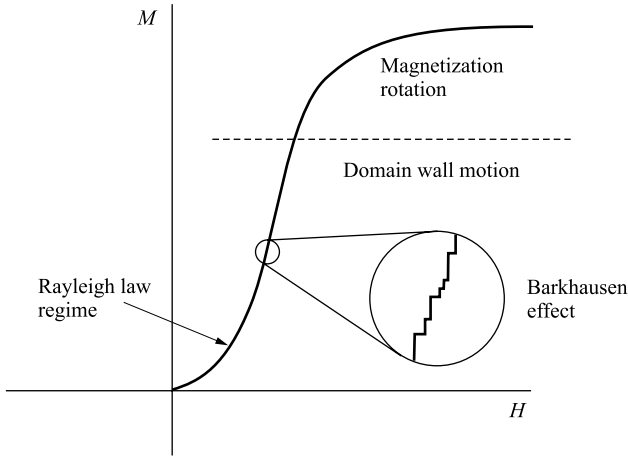
**FIGURE 6.19** Initial magnetization curve showing regions of domain wall motion and the Barkhausen effect and magnetization rotation.

rotation of the $M_s$ vector away from the easy axis. Thus at high fields, this curve bends over to yield a knee in the curve also shown in Figure 6.19.

Detailed description of the low-field behavior of the initial magnetization is given by the Rayleigh law, which describes the permeability $\mu$ as

$$\mu = \mu_0 + vH \tag{6.39}$$

In Equation (6.39), $\mu_0$ and $v$ are the Rayleigh constants of the material. These constants range widely, from 30 to $10^5$ for $\mu_0$ and from 0.5 to $1.2 \times 10^7$ for $v$, and depend on the material, temperature, and degree of cold work. Since $B = \mu H$,

$$B = \mu_0 H + vH^2 \tag{6.40}$$

hence the parabolic nature of $M$ versus $H$ at low $H$.
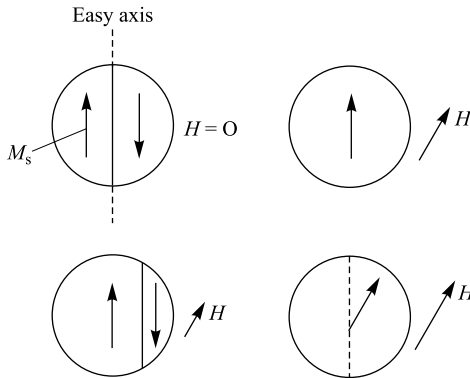


**FIGURE 6.20** Schematic of how a sample becomes magnetized along the direction of an applied field $H$ as the field increases, initially by domain wall motion and then, at high fields, by magnetization rotation.

In the regime of domain wall motion due to changing $H$, the magnetization is found to change not continuously but rather in a series of very small jumps. This is called the Barkhausen effect. A magnified view of the $M$ versus $H$ curve shows $M$ varying like a random staircase (Figure 6.19). This Barkhausen effect is due to the domain walls sticking at inclusions as they attempt to move with changing $H$.

At large fields, past the knee in the $M$ versus $H$ curve when $M$ is rotating against the anisotropy, the behavior of $M$ can be well described by the law of approach to saturation:

$$M(H) = M_s(1 - a/H) \tag{6.41}$$

This can be useful for experimental determination of $M_s$ in materials that are hard to saturate since extrapolation of $M$ versus $H^{-1}$ is linear and at $H^{-1} \to 0$ the extrapolation is $M_s$.

## 6.5   SMALL-PARTICLE MAGNETISM

The magnetism of small ferromagnetic particles (e.g., 1 μm or less) is dominated by two key features:

- There is a size limit below which the specimen can no longer gain a favorable energy configuration by breaking up into domains, hence it remains with one domain.
- The thermal energy can, with small enough size, decouple the magnetization from the particle itself to give rise to the phenomenon of superparamagnetism.

These two key features are represented by two key sizes (or length scales), the single domain size and the superparamagnetic size, each of which is described below.

### 6.5.1   Single-domain Particles

We saw above how the magnetostatic energy of a ferromagnet could be decreased by restructuring the material into domains. There is a limit to this because formation of domains costs energy due to domain wall formation. Thus in a large body there could be a minimum domain size below which the energy cost of domain formation exceeds the benefits from decreasing the magnetostatic energy. This further implies that a single particle of size comparable to the minimum domain size would not break up into domains.

This scenario does indeed occur because of the different functionalities with size of the two competing energies. For a particle of size $D$ (diameter) the magnetostatic energy is proportional to $M_s^2 D^3$ because (1) the energy density in the field goes as $B^2$ hence $M_s^2$, and (2) the total energy is the energy density times a volume, hence the $D^3$ proportionality. Domain formation requires creation of walls, which are an area. Hence if $\gamma$ is the domain wall energy per unit area, we expect a $\gamma D^2$ functionality for

the total domain wall energy. Now consider large $D$, then the $D^3$ term of the magnetostatic energy dominates, so to alleviate this the smaller $D^2$ term of wall formation concedes and domains form. However, at small $D$, the $D^2$ term will dominate and wall formation will be too costly and the particle will not break into domains. The critical size, or single domain size $D_s$, below which a particle will not form domains, is where these two energies are equal. If we ignore proportionality constants, this implies $\gamma D_s^2 \sim M_s^2 D_s^3$ to yield

$$D_s \sim \gamma/M_s^2 \tag{6.42}$$

This result (essentially a dimensional analysis) is surprisingly accurate (good to an order of magnitude). Typical values for $D_s$ range from 10 to 100 nm, as shown in Table 6.8,[6] with elongated particles tending to have large $D_s$.

### 6.5.2 Coercivity of Single-domain Particles

Magnetization reversal in single-domain particles must occur via spin rotation since there are no domain walls to move. Because of this, single-domain particles have a larger coercivity compared to multidomain systems because, generally speaking, it is harder to rotate the magnetization than to move a domain wall.

Most simply, magnetization can rotate by coherent motion of the atomic spins, but other motions—fanning and curling—can occur. We consider each below.

***6.5.2.1 Coherent Rotation of the Magnetization*** If the spins move coherently together, then they can be represented collectively by $M_s$. The response of $M_s$ to an applied field is hindered by the anisotropy (crystalline, shape, stress, or whatever) and for coherent rotation was first considered by Stoner and Wolfarth. The lowest-order and simplest term in the anisotropy energy is given by Equation (6.34),

$$E_a = K \sin^2 \theta \tag{6.34}$$

**TABLE 6.8  Estimated single-domain size for spherical particles**

| Material | $D_s$ (nm) |
|---|---|
| Fe | 14 |
| Co | 70 |
| Ni | 55 |
| $Fe_3O_4$ | 128 |
| $\gamma$-$Fe_2O_3$ | 166 |

From reference 6.

The applied field supplies a potential energy of

$$E_f = -\vec{M}_s \cdot \vec{H} \tag{6.43}$$

The equilibrium direction of $\vec{M}_s$ is where the total energy, $E_{tot} = E_a + E_f$ has a minimum. To find this, one differentiates and sets $dE_{tot}/d\theta = 0$.

Consider the situation in which the applied field is perpendicular to the easy axis. Then the field alignment energy is $-M_s H \sin\theta$ and a minimum in $E_{tot}$ is found at $\sin\theta = M_s H/2K$. Thus the component of $M_s$ parallel to the applied field, $M_s \sin\theta$, is proportional to $H$. Since $\sin\theta \le 1$, this component saturates to $M_s$ when

$$H = 2K/M_s \tag{6.44}$$

$M$ versus $H$ for this case is shown in Figure 6.21.

Now consider when $H$ is applied antiparallel to $M_s$, which is along the easy axis, in an attempt to reverse the direction of $M_s$. In this case $H$ applies no torque and so $M_s$ is not even slightly rotated, so $M = M_s$ remains. However, with increasing $H$, the magnetic energy for reversal, $M_s H$, eventually becomes great enough that the minimum in the total energy shifts from the original $M_s$ antiparallel to $H$ to $M_s$ parallel to $H$ at $H = 2K/M_s$. The system makes this jump and this leads to a square hysteresis curve, also shown in Figure 6.21, with coercivity given by Equation (6.44).

So far we have only considered the situations where the applied field is perpendicular or antiparallel to $M_s$ along the easy axis. Other initial orientations can be attacked in the same manner, viz., minimization of the total energy. One finds that the two cases we have considered represent extremes of the possible hysteresis curves, totally closed (no hysteresis) and totally open (square). Other orientations
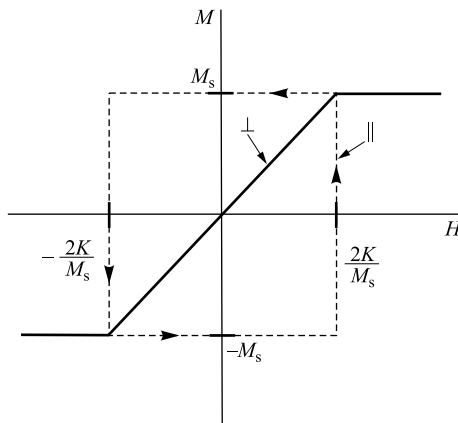


**FIGURE 6.21** Hysteresis loops for applied fields perpendicular ⊥ and parallel ∥ to the easy axis.
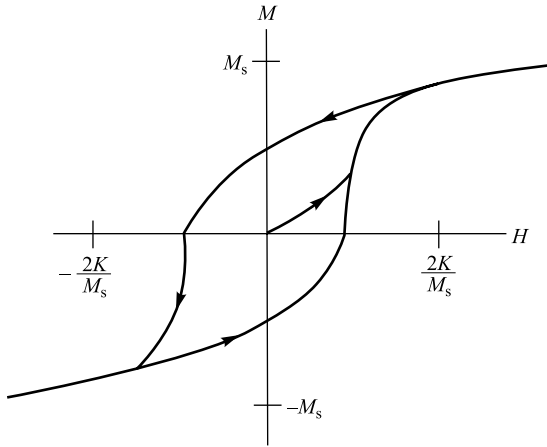
**FIGURE 6.22** Hysteresis loops for field applied to an ensemble of uniaxial, single-domain particles with random easy axes.

yield hysteresis curves between these limits. Very often when dealing with particles, the easy axes are randomly oriented. Then a hysteresis curve results that is an average over all orientation. This average is shown in Figure 6.22.

We have not yet considered the source of the anisotropy $K$. It could occur due to crystalline anisotropy, shape, stress, or, in small particles, to surface anisotropy. Table 6.9 contains calculated coercivities $H_c = 2K/M_s$ for iron due to the shape anisotropy. There we see a typical result that for even modest shape ratios, $c/a$, the shape anisotropy can be very large. This can be shown to be true for stress anisotropy as well. Thus for particles, shape can dominate the coercivity.

**TABLE 6.9 Calculated shape anisotropies (Equation 6.36) and coercivities (Equation 6.44) (easy axis aligned with field) for single-domain iron particles ($M_s = 1714\,\text{emu cm}^{-3}$)**

| Shape | | | |
|---|---|---|---|
| $c/a$ | $N_a - N_c$ | $K_s$ ($10^5\,\text{erg cm}^{-3}$) | $H_c$ (Oe) |
| 1.0 | 0 | 0 | 0 |
| 1.1 | 0.47 | 7 | 820 |
| 1.5 | 1.89 | 28 | 3300 |
| 2.0 | 3.01 | 44 | 5200 |
| 5.0 | 5.2 | 77 | 9000 |
| 10 | 5.9 | 87 | 10,100 |
| $\infty$ | $2\pi$ | 92 | 10,800 |

**6.5.2.2   *Fanning***   Magnetization reversal by the fanning mechanism is relevant in chains of particles or highly elongated particles. In a chain the $M_s$ vector of each particle interacts with its neighbors via the magnetic dipolar interaction. Thus the dipoles line up, north to south, and like to remain in alignment, hence causing an anisotropy even if no others exist. This has been called an interaction anisotropy. An applied field in the opposite direction tends to reorient these dipoles, but the reorientation may occur either coherently as depicted in Figure 6.23 or incoherently also depicted in Figure 6.23. The incoherent realignment is called fanning.

Fanning reversal leads to a square hysteresis loop. The $H_c$ is one-third as large as for a coherent reversal and can be calculated to be

$$H_c(\text{fanning}) = \pi M_s/6 \tag{6.45}$$

Equation (6.45) works fairly well for some real systems, even in situations where the approximation of a chain of pointlike particles used to derive (6.45) is poor, for example, in highly elongated particles.

**6.5.2.3   *Curling***   To visualize magnetization reversal by curling, place the initial magnetization along positive $z$-axis and imagine each atomic spin rather than the total $M_s$. Next apply a field $H$ along the negative $z$-axis in an attempt to reverse the total $M_s$. Now consider an $xy$ plane slice of this, depicted in Figure 6.24. As the total $M_s$ turns to reverse, the atomic spins could either stay parallel so that their $xy$ components are equal—this would be coherent rotation as in Figure 6.24a—or they could rotate away from the $z$-axis with different $xy$ components. If these $xy$ components are always perpendicular to a radius vector in the $xy$ plane as in Figure 6.23b, this is called curling.

For an infinitely long particle, the energy barrier to reversal via curling is entirely exchange. The logic to this can be seen in Figure 6.24b, which shows how the atomic spins are not parallel, so that exchange energy is involved, and are parallel to the surface, so that there are no poles on the surface, hence there is no magnetostatic



$H_{\text{applied}}$
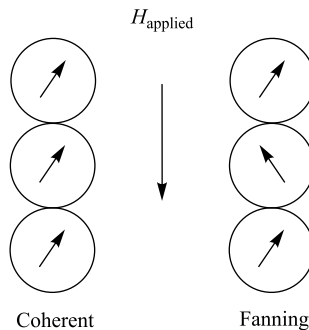
Coherent                    Fanning

**FIGURE 6.23**   Schematics of coherent and fanning rotation of magnetization in particles, initially upward, with an applied field downward.
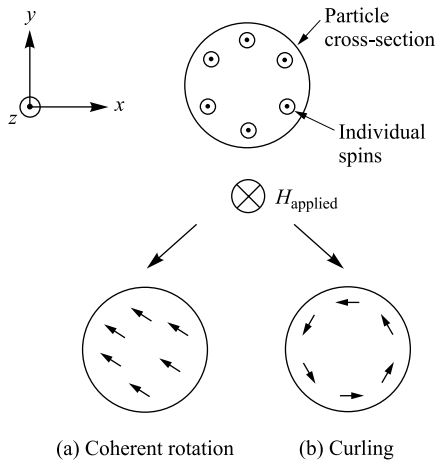
**FIGURE 6.24**   Diagram to illustrate and compare coherent and curling rotation of particle magnetization due to an applied field. Particle cross-sections are shown. Initially the magnetization is out of and normal to the page; then a field is applied into and normal to the page. The coherent (a) and curling (b) responses are illustrated.

energy. For finite lengths, the magnetostatic energy becomes important as well. Curling has a size dependency because smaller particles force the average angle between adjacent atomic spins to be greater, hence the exchange is more effective in resisting the reversal. It is for this reason that small particles reverse coherently, whereas large particles use curling. For iron this crossover occurs at roughly 15 nm.

### 6.5.3   Superparamagnetism

Below the Curie temperature of a ferromagnet or ferrimagnet, all the spins are coupled together and so cooperate to yield a large total moment. This moment is bound rigidly to the particle by one or more of the variety of anisotropies that we have discussed, and the energy of this bond is $KV$, where $V$ is the volume of the particle. With decreasing particle size, $KV$ decreases until the thermal energy $kT$ can disrupt the bonding of the total moment to the particle. Then this moment is free to move and respond to an applied field independent of the particle. This moment is the moment of the particle and is equal to $\mu_p = M_s V$. It can be quite large, thousands of Bohr magnetons. An applied field would tend to align this giant (or super) moment, but $kT$ would fight the alignment just as it does in a paramagnet. Thus, this phenomenon is called superparamagnetism.

   If the anisotropy is zero or very weak, one would expect that the total moment $\mu_p = M_s V$ could point in any direction, hence the Langevin function of Equation (6.16) would apply. If $K$ is significantly greater than zero, $\mu$ could appoint in either of the two directions along the easy axis and then the two-state Brillouin function would apply (Equation 6.23). Both of these, however, are an approximation to $M$

versus $H$ for a real superparamagnet because the system of particles is no doubt polydisperse, so that there is a distribution of $\mu_p$ values, and the particles would most likely have random orientation, hence random easy axes. Despite this lack of a precise qualitative description of $M$ versus $H$, two key qualities remain for a superparamagnetic system: (1) lack of hysteresis, and (2) data of different temperatures superimpose onto a universal curve of $M$ versus $H/T$. Both these features are illustrated in Figure 6.25.

The phenomenon of superparamagnetism is, in fact, timescale-dependent due to the stochastic nature of the thermal energy. The anisotropy energy $KV$ represents an energy barrier to the total spin reorientation; hence the probability for jumping this barrier is proportional to the Boltzmann factor $\exp(-KV/kT)$. This can be made quantitative by introducing an attempt timescale $\tau_0$, which describes the timescale over which $\mu_p$ attempts to jump the $KV$ barrier. Then the timescale for a successful jump is

$$\tau = \tau_0 \, e^{-KV/kT} \tag{6.46}$$

The attempt timescale is about $10^{-9}$ s. The typical experiment with a magnetometer takes 10 to 100 s; and if $M_s$ reverses at times shorter than the experimental timescales, the system appears superparamagnetic. Using $\tau \simeq 100$ s and $\tau_0 = 10^{-9}$ s, one obtains from (6.46), for the critical volume,

$$V_{sp} = 25kT/K \tag{6.47}$$

A particle with volume smaller than this acts superparamagnetically on the 100 s experimental timescale. Typical superparamagnetic sizes for spherical (magnetocrystalline anisotropy only) iron and cobalt particles are 16 and 7.6 nm, respectively, for $T = 300$ K.
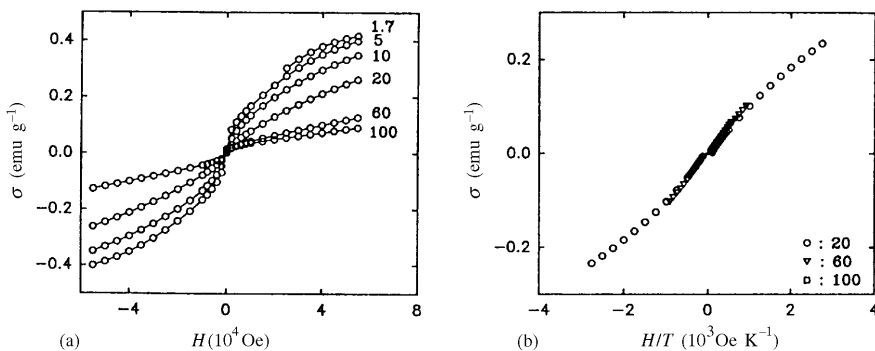


**FIGURE 6.25** Magnetization for very small, $\sim 0.6$ nm, cobalt particles. (a) Data are plotted versus applied field $H$; (b) the same data plotted versus $H/T$. The collapse of the data to a single curve in (b) indicates superparamagnetism. J P Chen, C M Sorenson, K J Klabunde and G C Hadjipanayis. In: *Nanophase Materials*, edited by G C Hadjipanayis and R W Siegel, Kluwer Dordrecht, 1994, with kind permission from Kluwer Academic Publishers.

Equation (6.47) can be rearranged to yield

$$T_{\mathrm{B}} = KV/25k \qquad (6.48)$$

$T_{\mathrm{B}}$ is called the blocking temperature; below $T_{\mathrm{B}}$ the free movement of $\mu_{\mathrm{p}} = M_{\mathrm{s}}V$ is blocked by the anisotropy; above $T_{\mathrm{B}}$, $kT$ kicks the moment loose so that the system appears superparamagnetic.

We have seen above, when discussing single-domain particle hysteresis, that an applied field can modify the anisotropy energy barrier. One then finds that for the experimental timescale of $100\,\mathrm{s}$ superparamagnetism begins when

$$25kT = KV\left(1 - \frac{HM_{\mathrm{s}}}{2K}\right)^2 \qquad (6.49)$$

Solving this for $T$, a new, and lower at finite $H$, blocking temperature $T_{\mathrm{B}}$ can be calculated. Essentially the applied field is lowering the $KV$ barrier so that superparamagnetism begins at a lower $T$. If one solves for $H$, one obtains the coercivity for small single-domain particles in the size regime immediately above the superparamagnetic size:

$$H_{\mathrm{c}} = \frac{2K}{M_{\mathrm{s}}}\left[1 - \left(\frac{25kT}{KV}\right)^{1/2}\right] \qquad (6.50)$$

Recall that $2K/M_{\mathrm{s}}$ is the coercivity without the help of thermal activation. Since $V_{\mathrm{p}} = 25kT/K$, and $V \sim D^3$, one finds

$$H_{\mathrm{c}} = \frac{2K}{M_{\mathrm{s}}}\left[1 - \left(\frac{D_{\mathrm{p}}}{D}\right)^{3/2}\right] \qquad (6.51)$$

On the other hand, if Equation (6.48) is used with (6.50), one finds

$$H_{\mathrm{c}} = \frac{2K}{M_{\mathrm{s}}}\left[1 - \left(\frac{T}{T_{\mathrm{B}}}\right)^{1/2}\right] \qquad (6.52)$$

This temperature functionality is illustrated in Figure 6.26.

The importance of the timescale dependency of superparamagnetism is well illustrated by Mössbauer experiments on magnetic particles. If the system of particles is ferromagnetic, a sextet of Mössbauer lines is observed, whereas if the system is superparamagnetic, a doublet is observed. The gamma-ray interaction of the
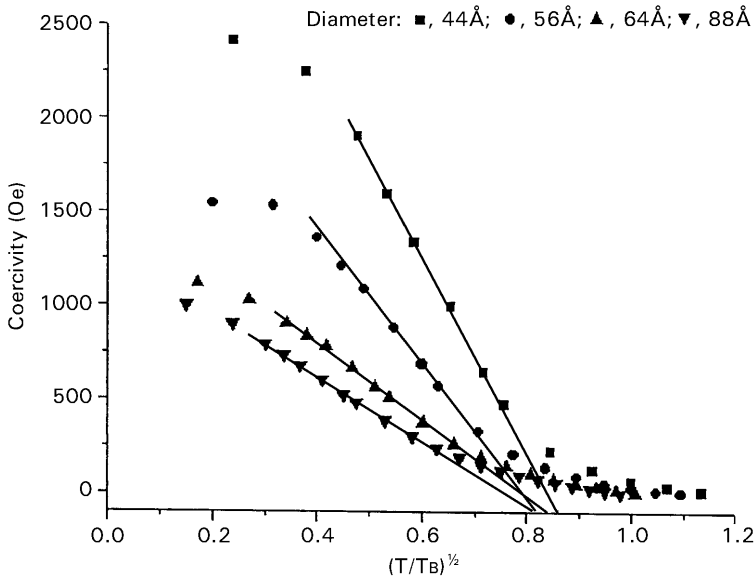
**FIGURE 6.26** Temperature dependence of the coercivity of single-domain cobalt particles below the blocking temperature $T_B$, illustrating the functionality of Equation (6.52). Rounding of this functionality between $(T/T_B)^{1/2} \simeq 0.8$ to 1.0 is due to the polydispersity of particle sizes. Used with permission from *J. Mater. Res.*, *14*, 1542, **1999**, Materials Research Society.

Mössbauer experiment works on a very quick timescale, on the order of $10^{-7}$ s. Thus by Equation (6.46) one expects

$$\frac{T_B(\text{Mössbauer})}{T_B(\text{Magnetometer})} \simeq 5.5 \qquad (6.53)$$

or

$$\frac{D_P(\text{Mössbauer})}{D_P(\text{Magnetometer})} \simeq 0.6 \qquad (6.54)$$

The blocking temperature can be easily measured in the laboratory with a magnetometer. With $T_B$, one can then infer values for the particle size, anisotropy, or saturation magnetization through Equation (6.48). The procedure is to cool the sample under zero applied field, so-called zero-field cooling (ZFC), to a temperature well below the suspected $T_B$. Then apply a small field of $\sim 100$ Oe. If $T < T_B$, the individual particle's moments are bound to the particles, point in random directions, and will not be very susceptible, so the induced magnetization will be small. The system is then warmed at a uniform $dT/dt$. As $T$ approaches $T_B$ from below, $kT$ will begin to loosen up the moments from the particles and the induced $M$ will rise. At

$T_B$, the moments are unblocked and hence are free to align with the applied field to yield a large total $M$. As $T$ increases above $T_B$, $M$ falls via the Curie law, $M \sim T^{-1}$ because the system is a (super)paramagnet. Thus a peak occurs at $T_B$. An example of this is given in Figure 6.27. Another example is given in Figure 6.28, which shows that $T_B$ is modified when the particles interact via the magnetic dipole interaction.

The data in Figure 6.27 are for cobalt particles synthesized in our laboratory. Their diameters were measured with a transmission electron microscope. The total moment $\mu_p$ was determined by fits to the Langevin function for $T > T_B$, and the effective anisotropy and saturation magnetization were determined from all these with Equation (6.48). The results are shown in Table 6.10.

### 6.5.4 The Coercivity of Small Particles

We can pull together much of the discussion above into Figure 6.29 which gives a schematic of the coercivity as a function of particle size. At large size the particles have many domains; thus, magnetization reversal is dominated by domain wall motion, which is relatively easy, hence the coercivity is low. However, as particle size decreases, the coercivity is found empirically to follow

$$H_c = a + \frac{b}{D} \tag{6.55}$$
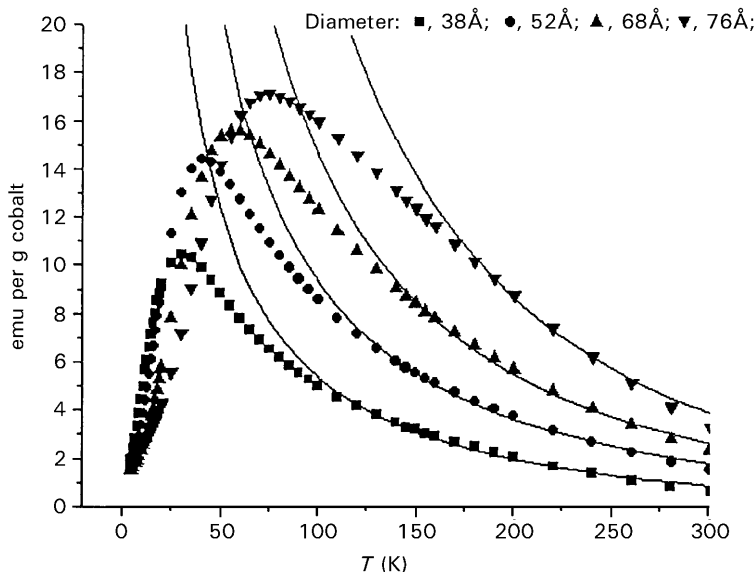


**FIGURE 6.27** Magnetization versus temperature for small cobalt particles. The particles were zero-field cooled and then warmed under an applied field of 100 Oe. Peaks in the data curves indicate the blocking temperatures. Lines are high-$T$ fits to the Langevin function. Used with permission from *J. Mater. Res.*, *14*, 1542, **1999**, Materials Research Society.
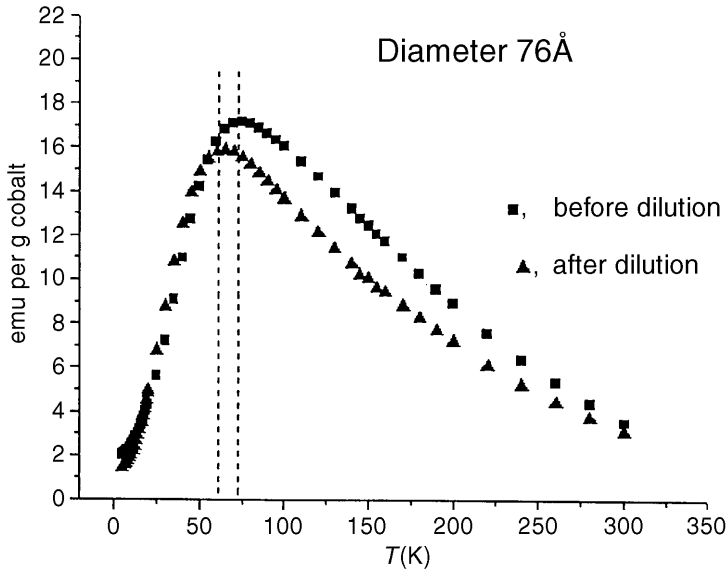
**FIGURE 6.28**  As in Figure 6.26, but when the particles are not diluted, the blocking temperature appears higher due to interparticle magnetic dipole interaction. Used with permission from *J. Mater. Res.*, *14*, 1542, **1999**, Materials Research Society.

until the single-domain size is reached. Equation (6.55) is not well understood theoretically. The largest coercivities occur at the single-domain size. Below this, $H_c$ falls off due to thermal activation over the anisotropy barriers, leading to Equation (6.52) and superparamagnetism at the superparamagnetic size for which $H_c = 0$.

The behavior represented in Figure 6.29 is shown for a real system in Figure 6.30. The system is iron encapsulated in magnesium prepared in our laboratory.[5] For $T \geq 77$ K the coercivity rises from zero at $D \leq 4$ nm, the superparamagnetic regime, and peaks near $D = 20$ nm. This peak size is in reasonable accord with the theo-

**TABLE 6.10  Size-dependent magnetic properties of cobalt nanoparticles**

| TEM Diameter (nm) | $T_B$ (K) | $K_{eff}$ ($10^6 \, erg \, cm^{-3}$) | $\mu_p$ ($\mu_B$) |
|---|---|---|---|
| 3.8 | 29 | 3.5 | 1700 |
| 5.2 | 40 | 1.9 | 2900 |
| 6.8 | 58 | 1.2 | 5400 |
| 7.6 | 76 | 1.1 | 11,000 |
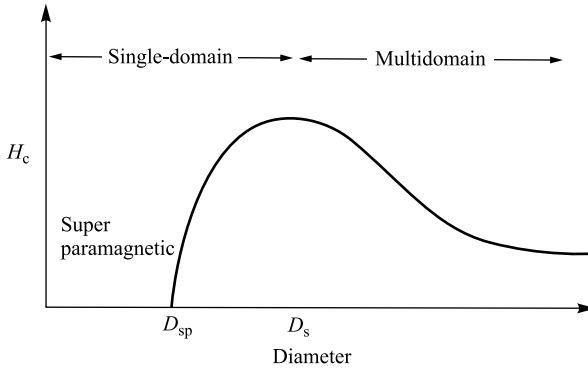
**FIGURE 6.29**   Particle coercivity versus size ($\sim$ diameter). $D_{sp}$ is the superparamagnetic size; $D_s$ is the single-domain size.

retical prediction for the single domain size, $D_s \simeq 14$ nm, given in Table 6.8. For yet larger sizes, $H_c$ falls and the overall shape of $H_c$ versus $D$ is the same as expected from Figure 6.29. Note that for $T = 10$ K the particles with $D \simeq 3$ to 5 nm that were superparamagnetic at 77 K no longer are, indicating a blocking temperature for these sizes between 10 and 77 K.
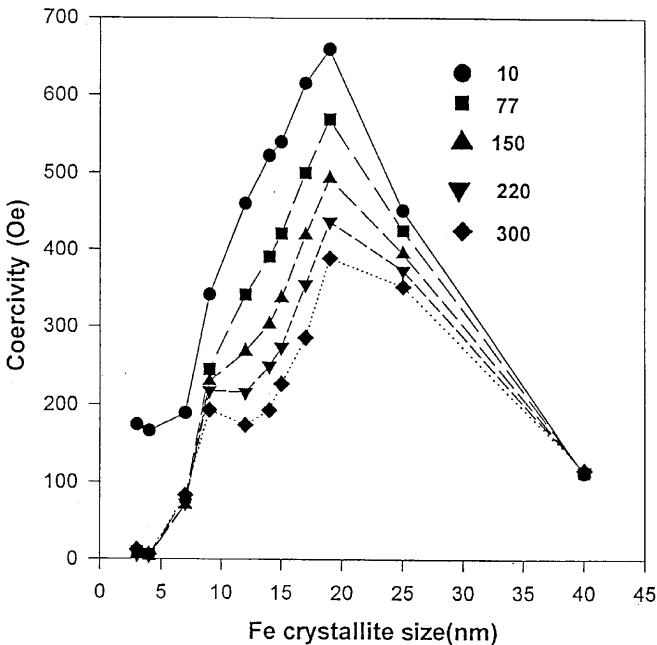


**FIGURE 6.30**   Coercivities versus size for iron particles encapsulated in magnesium.

## 6.6    REVIEW OF SOME ISSUES IN NANOSCALE MAGNETISM

The properties of ultrafine or nanoscale particles has stimulated considerable interest in the recent past due to inherent scientific interest as well as great potential for development of novel and useful materials. Nanoscale particles display a wide variety of unusual behavior when compared to the bulk for two major reasons: finite size effects in which electronic bands give way to molecular orbitals as the size decreases; and surface/interface effects.

For magnetic properties it is largely the latter, surface/interface effects, which cause significant differences compared to the bulk. In a nanoscale particle the surface atoms/bulk atoms ratio is sufficiently large ($\sim$50% for diameter $\simeq$ 3 nm) that surface/interface effects can dominate the magnetic properties. One useful point of view is that small particles represent surface matter in macroscopic quantities. For instance, 10 mg of 3 nm cobalt particles would contain 5 mg of surface cobalt.

Surface/interfacial effects may be classified along the following lines:

(1) Symmetry breaking at surface or interface causing changes of (a) band structure, (b) atom coordination, and (c) lattice constant.
(2) Electronic environment/charge transfer at the interface with, for example, (a) ligands, (b) other metals, (c) insulators, and (d) semiconductors.

A considerable amount of new knowledge of size effects on intrinsic magnetic properties has come from work on gas phase clusters of atoms whose magnetic moments have been measured with Stern–Gerlach apparatus.[7,8] Systems studied have included 3$d$ transition metals iron, cobalt, and nickel; a 4$d$ transition metal, rhodium; and rare earths gadolinium and terbium. Sizes ranged from several atoms per cluster up to a few hundred, the latter corresponding to particle diameters of $\sim$2 nm. The 3$d$ transition metals showed superparamagnetic behavior (as expected) with enhanced ($\sim$30–40%) magnetic moments per atom as shown in Figure 6.31. Theory ascribes enhancement to changes in atomic coordination, symmetries, and/or lattice constants.[9] Reduction may be a surface effect resulting in weaker exchange. An exciting discovery, stimulated by theory,[10] is that rhodium (a 4$d$ transition metal) clusters, $Rh_n$, $n = 9$–31, are ferromagnetic.[11] This is thought to arise because of reduced coordination and icosohedral symmetry. Of course, all these changes are ultimately due to the very small size of the particle.

Small metallic clusters have also been incorporated into cluster compounds. For example, palladium clusters up to $Pd_{561}$ with ligated phenyl and oxygen, $Pd_{561}Phen_{36}O_{200}$, have been made.[12] These compounds have never shown ferromagnetism but have shown interesting quantum size effects in their paramagnetic properties. Calculations indicate for palladium that a 5.5% lattice expansion would make it ferromagnetic.[13] Why are rhodium gas phase clusters ferromagnetic yet palladium cluster compounds are not? The answer could have a lot to do with electron-donating ligands on the palladium cluster compound. For instance, Rosch et al.[14] studied nickel clusters and saw the ferromagnetism quenched as CO ligands
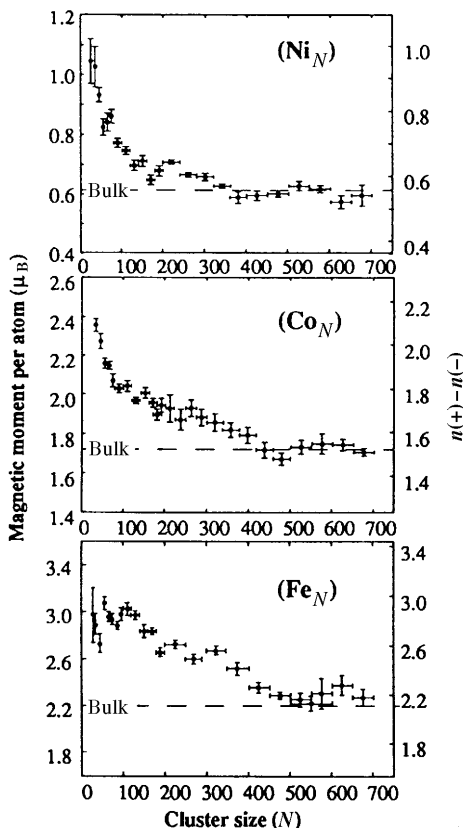
**FIGURE 6.31**   Low-temperature average magnetic moment per atom for nickel clusters at 78 K, cobalt clusters at 78 K, and iron clusters at 120 K as a function of the number $N$ of atoms in the cluster. The right-hand scale gives the spin imbalance per atom. Reprinted with permission from "Magnetic and Thermal Properties", In *Proceedings of the Scientific and Technology of Atomically Engineered Materials*, **1996**, World Scientific Publishing Co Pte Ltd.

were attached. An example from our work is given in Figure 6.32 where it is shown that 4.4 nm cobalt particles ligated with dioctyl sulfide show a large reduction in the saturation magnetization. Thus, surface interactions are very important, and the Stern–Gerlach clusters are unique because they are not interacting with other substances.

At the surface, the coordination number of each surface atom is smaller than within the bulk, hence the $d$-band of a collection of transition metal atoms at the surface is narrower than in the bulk, leading to a high density of states and hence enhanced magnetism.[15–17] The surface magnetic moments are enhanced by 10–30% over their bulk values in ferromagnetic iron, nickel, and body-centered cubic cobalt (100) and (110) surfaces.[16] A dramatic case is the chromium (001) surface, which undergoes a ferromagnetic phase transition, with an enhancement of about $3\mu_B$ in its magnetic moment as compared to its bulk value (which is antiferromagnetic in
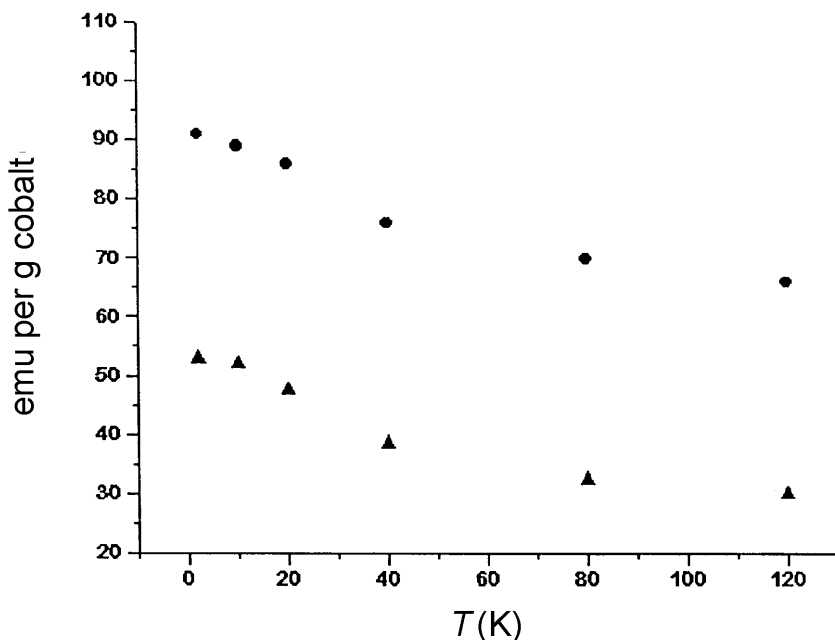
**FIGURE 6.32**     Saturation magnetization of 4.4 nm cobalt particles with (▲) and without (●) dioctyl sulfide ligation.

nature).[17,18] By contrast, the results of experiments with vanadium (100) surfaces show a stable paramagnetic state for the surface and yield a 9% contraction of the topmost interlayer spacing.[17] Experimental findings[19] on thin films of iron, nickel and cobalt show enhancements of surface moment by 30%, 20%, and 150%, respectively, as compared to their bulk.

Interfaces or small particles may have significant changes in the lattice constant relative to bulk. For example, a study of nanophase ($d \sim 6$ nm) compressed iron showed two Mössbauer sextets that indicated the presence of both a bulk and an interfacial iron phase.[20] The overall density of the composite was $\sim 75\%$ of the bulk, indicating that the interfacial phase was less dense than the bulk. The interfacial iron had larger hyperfine fields and isomer shifts than bulk iron. The greater isomer shift was due to a smaller electron density. The enhanced hyperfine field was due to greater exchange, a result of moving to the right on the Bethe–Slater curve due to the greater lattice spacing in the expanded interfacial phase. Rayl et al.[21] cosputtered nickel and $SiO_2$ to create small nickel particles with a lattice constant increased by 9%. This caused a lowering of $T_c$, which correlated well with changes caused by high-pressure studies, which decrease the lattice spacing. Again this decrease in $T_c$, and hence exchange constant $J_{ex}$, correlates with the inference from the Bethe–Slater curve. Would an expanded interfacial phase of palladium show ferromagnetism? Analogously, an expanded lattice for chromium could yield ferromagnetism. Could manganese be altered from antiferromagnetic to ferromagnetic in such an interfacial phase?

At an interface an adjacent metal may perturb the $d$-band. For example, copper on nickel decreases the moment per atom of nickel[22] because copper donates electrons to the nickel $d$-band, thus partially filling the unpaired hole. On the other hand, iron next to silver sees an enhancement in $\mu$ per atom.[23] Similar opposing examples exist so the situation, while robust with phenomena, is very complex.[24,25] One can glean from the literature that an important interfacial effect is the electronic interaction between adjacent materials. As discussed above, electron donation by ligands to palladium and cobalt and by both copper and nickel suppressed the magnetic moment in a straightforward manner. Other examples include cobalt particles precipitated in copper;[26,27] iron particles in mercury;[28] and our own work involving iron in $MgF_2$[5] shown in Figure 6.33. This is very similar to the dioctyl sulfide ligand quenching for cobalt particles described above with, most likely, the same physics. Here we see that the smaller iron particles have smaller $M_s$. The quenching of $M_s$ occurs due to donation of electrons from the $MgF_2$, which surrounds the iron particle. The donated electrons partially fill the spin-unbalanced $d$-band of the iron, decreasing the magnetic moment per atom. The larger quench for smaller particles is



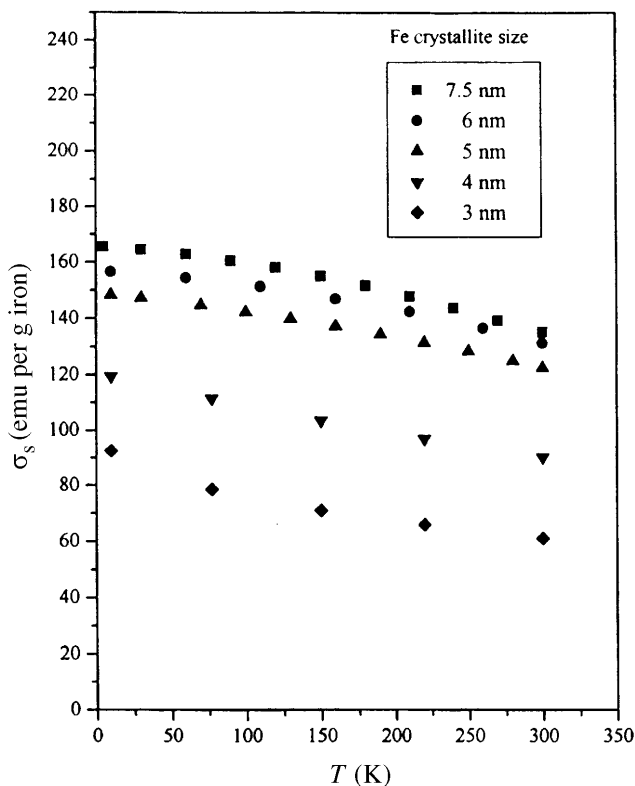**FIGURE 6.33**   Saturation magnetization versus temperature for different-sized iron crystallites in the $[MgFe_2]Fe$ system. For bulk ion, $\sigma_s = 220$ emu g$^{-1}$. Reprinted with permission from D. Zhang et al, *Phys. Rev. B*, **1998**, *58*, 14167, American Physical Society.

due to the greater fraction of surface/interfacial iron. The relevant parameter is the electronegativity of the two substances. If the transition metal is more electronegative, it takes electrons and partially fills its $d$-band holes to become less magnetic, whereas if it is less electronegative, the reverse occurs. Such a proximity correlation does not appear to be discussed in the literature, but it is consistent with available data and the Slater picture of transition metal alloys[29] discussed briefly above. Electronegativity is not important in Slater's picture because the metals are atomically mixed, but the simple concept of $d$-band hole filling with concomitant change in $\mu$ per atom is the same as that used above.

In many situations particles display a dead layer on their surface in which the magnetization is either reduced or zero. This causes the total saturation magetization of the sample to be less than in the bulk, more so for smaller particles. If the layer is of constant thickness, independent of the diameter of the particle, it is easy to show that then the magnetization is inversely proportional to the diameter. An example[30] of this behavior is shown in Figure 6.34.

The thermal behavior of the magnetization is also affected by the large fraction of surface material in nanoparticle systems. The data in Figure 6.8 for iron particles encapsulated in $MgF_2$ show that the magnetization is decreased more by temperature for smaller particles. Analysis of these data, as well as data for iron encapsulated in magnesium, with Bloch's law showed that Bloch's law was still valid, but both the Bloch constant Bloch exponent were size-dependent, as shown in Figures 6.35 and 6.36. The large increase in $B$ indicates that small-particle magnetization is very susceptible to temperature, most likely due to the reduced coordination of the iron atoms at the surface.[5]

Another common effect seen for nanoscale particles is surface anisotropy, that is, an (additional) energy binding the magnetization to the particle analogous to the crystal anisotropy. This occurs because the spins at the surface see the broken symmetry at the surface and this affects the spin alignment relative to the surface.

The hard magnetic properties of particles are also very important because of their potential applications in magnetic recording media. Coercivities in the range of a few
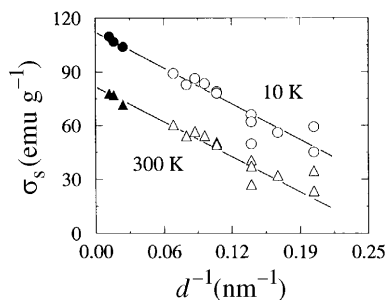


**FIGURE 6.34** Saturation magnetization versus inverse mean particle diameter for $MnO \cdot Fe_2O_3$ particles prepared by aerosol spray pyrolysis (solid symbols) and aqueous phase precipitation (open symbols). The lines are guides for the eye. From *Aerosol Science & Technology*: "Aerosol Spray Pyrolysis Synthesis of Magnetic Manganese Ferrite Particles". *19*, 453–467. Copyright **1993**. Cincinnati, OH. Reprinted with permission.
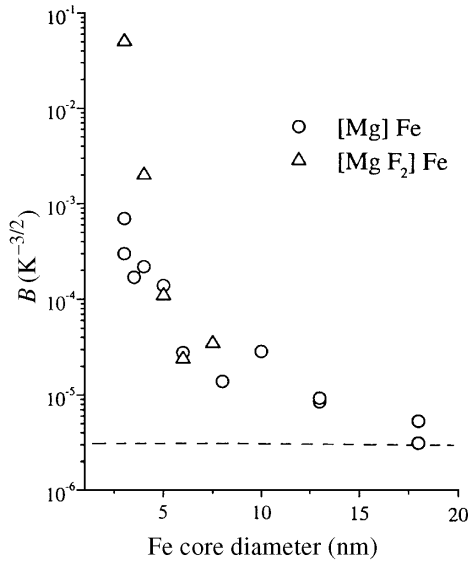
**FIGURE 6.35**   Bloch constant as a function of iron particle size. Iron particles are encapsulated in either magnesium or $MgF_2$. Dashed line is bulk value. Reprinted with permission from D. Zhang et al, *Phys. Rev. B*, **1998**, *58*, 14167, American Physical Society.
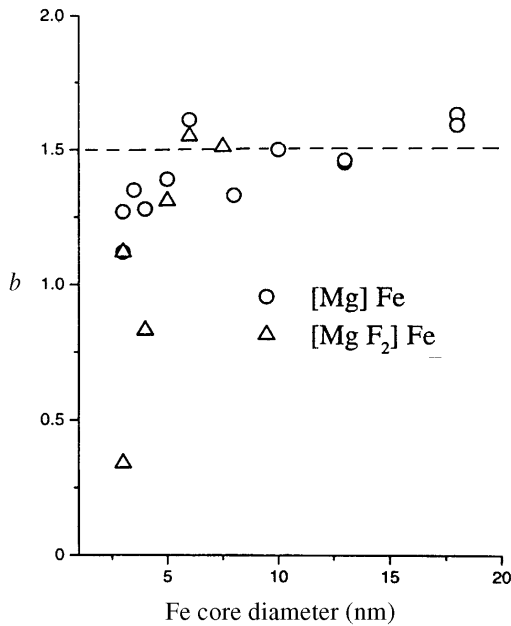


**FIGURE 6.36**   Bloch exponent as a function of iron particle size. Iron particles are encapsulated in either magnesium or $MgF_2$. Dashed line is bulk value. Reprinted with permission from D. Zhang et al, *Phys. Rev. B*, **1998**, *58*, 14167, American Physical Society.

kOe, which are much higher than the values of their bulk counterpart, have repeatedly been reported for the last 3–4 decades.

A magnetic coating material on a nanoparticle can have a dramatic effect on coercivity (often discussed in terms of exchange anisotropy[1]). Meikeljohn and Bean[31] studied fine particles of cobalt metal with an outer layer of CoO. An usually large $H_c$ was explained in terms of exchange coupling between the spins of the ferromagnetic cobalt and antiferromagnetic CoO; thus the reversal of the spins of cobalt atoms in the cobalt core material was resisted by the strong crystal anisotropy of the CoO.

Analogous results were obtained in our laboratory[32] for iron particles. $H_c$ was found to increase with a decrease in particle size from 12 nm to 3 nm, while $\sigma_s$ increased with increasing size. These results were explained by proposing that $H_c$ is strongly affected by the interaction between the iron oxide shell and the iron core. The highest $H_c$ obtained at room temperature was 1050 Oe for a particle with a 14.0 nm core, and its value at 10 K was 1425 Oe. However, smaller particles with 2.5 nm core size went from a negligible $H_c$ at 150 K to 3400 Oe at 10 K, showing the much stronger influence of temperature on the smaller nanoparticles. It was proposed that the smaller iron core "feels" much more the effect of the iron oxide shell, due to the higher iron oxide/iron ratio. The strong decrease in $H_c$ with temperature increase was explained as due to the onset of superparamagnetic behavior of the iron oxide shell.

An important conclusion is that surface coatings in such small particles can dominate $H_c$ and can also control the temperature dependence. The coating spins couple to the core via exchange, resulting in an exchange anisotropy.

## GLOSSARY OF SYMBOLS

| | |
|---|---|
| $a$ | Lattice spacing |
| $a$ | Minor axis of spheroid |
| $b$ | Bloch exponent |
| $B$ | Bloch constant |
| $B$ | Magnetic induction (gauss) |
| $B_J$ | Brillouin function |
| $c$ | Major axis of spheroid |
| $c$ | Speed of light |
| $C$ | Curie constant |
| $D$ | Diameter |
| $e$ | Electron charge |
| $E_a$ | Anisotropy energy |
| $g$ | Landé $g$-factor |
| $H$ | Magnetic field strength (Oe) |

| | |
|---|---|
| $H_c$ | Coercivity |
| $J$ | Orbital angular momentum quantum number |
| $J_{ex}$ | Exchange integral |
| $k$ | Boltzmann's constant |
| $K$ | Anisotropy constant |
| $K_1$ | Magnetocrystalline anisotropy constant |
| $K_s$ | Shape anisotropy constant |
| $L$ | Langevin function |
| $m$ | Electron mass |
| $M$ | Magnetization (emu cm$^{-3}$) |
| $M_J$ | Azimuthal quantum number |
| $M_0$ | Saturation magnetization at 0 K |
| $M_r$ | Remanence |
| $M_s$ | Saturation magnetization |
| $N$ | Atoms per unit volume |
| $N_a, N_c$ | Demagnetization factors |
| $p$ | Probability |
| $r$ | Atomic orbital radius |
| $r_a$ | One half the interatomic distance |
| $r_d$ | Radius of the $d$-shell |
| $S$ | Spin angular momentum quantum number |
| $T$ | Absolute temperature |
| $T_B$ | Blocking temperature |
| $T_c$ | Curie temperature |
| $T_N$ | Néel temperature |
| $V_{sp}$ | Superparamagnetic particle volume |
| $U$ | Potential energy |
| $x$ | $= \mu H / kT$ |
| $Z$ | Atomic number |
| $\alpha$ | Proportionality factor |
| $\beta$ | Critical exponent |
| $\chi$ | Mass susceptibility (emu g$^{-1}$ Oe$^{-1}$) |
| $\chi_M$ | Molar susceptibility (emu mole$^{-1}$ Oe$^{-1}$) |
| $l$ | Domain wall thickness |
| $\gamma$ | Critical exponent |
| $\gamma$ | Domain wall energy |
| $\hbar$ | Planck's constant $h$ divided by $2\pi$ |
| $\kappa$ | Susceptibility (emu cm$^{-3}$ Oe$^{-1}$) |

| | |
|---|---|
| $\mu$ | Magnetic moment |
| $\mu$ | Permeability |
| $\mu_{\mathrm{o}}$ | Permeability of free space |
| $\mu_0$ | Rayleigh constant |
| $\mu_{\mathrm{B}}$ | Bohr magneton |
| $\mu_{\mathrm{p}}$ | Moment of a superparamagnetic particle |
| $v$ | Rayleigh constant |
| $\Omega$ | Solid angle |
| $\rho$ | Mass density ($\mathrm{g\,cm^{-3}}$) |
| $\sigma$ | Magnetization ($\mathrm{emu\,g^{-1}}$) |
| $\theta$ | Angle |
| $\theta$ | Curie–Weiss critical temperature |
| $\tau$ | Timescale to jump anisotropy energy barrier |
| $\tau_0$ | Timescale for attempt to jump anisotropy energy barrier |

## REFERENCES

1. B. D. Cullity, *Introduction to Magnetic Materials*, Addison-Wesley, Reading, MA, **1972**.

2. C. Kittel, *Introduction to Solid State Physics*, Wiley, New York, 1971.

3. D. Jiles, *Introduction to Magnetism and Magnetic Materials*, Chapman and Hall, London, **1991**.

4. R. C. Weast (editor), *Handbook of Chemistry and Physics*, Vol. 57, CRC Press, Cleveland, OH, **1976–1977**.

5. (a) D. Zhang, K. J. Klabunde, C. M. Sorensen, G. C. Hadjipanayis, *Phys. Rev. B*, **1998**, *58*, 14167.
   (b) D. J. Zhang, Ph.D. thesis, Department of Chemistry, Kansas State University, **1996**.

6. D. L. Leslie-Pelecky and R. D. Rieke, *Chem. Mater.*, **1996**, *8*, 1770.

7. S. E. Apsel, J. W. Emmert, J. Deng, J. G. Louderback, L. A. Bloomfield, in *Proceedings of the Science and Technology of Atomically Engineered Materials*, P. Jena, S. N. Khanna, B. K. Rao (editors), World Scientific, Singapore, **1996**, pp. 325–332.

8. J. M. L. Billas, D. Gerion, A. Hirt, A. Chatelain, W. A. de Heer, in *Proceedings of the Science and Technology of Atomically Engineered Materials*, P. Jena, S. N. Khanna, B. K. Rao (editors), World Scientific, Singapore, **1996**, pp. 341–350.

9. S. N. Khanna, S. Linderoth, *Phys. Rev. Lett.*, **1991**, *67*, 742.

10. B. V. Reddy, S. N. Khanna, B. I. Dunlap, *Phys. Rev. Lett.*, **1993**, *70*, 3323.

11. A. J. Cox, J. G. Lauderback, L. A. Bloomfield, *Phys. Rev. Lett.*, **1993**, *71*, 923.

12. J. M. van Ruitenbeek, M. Jurgene, G. Schmid, D. A. van Leeuwen, H. W. Zandbergen, L. J. de Jongh, *Z. Phys. D*, **1991**, *19*, 267.

13. H. Chen, N. E. Brener, J. Callaway, *Phys. Rev.*, **1989**, *40*, 1443.

14. N. Rosch, L. Ackerman, G. Pucchioni, and B. I. Dunlop, *J. Chem. Phys.*, **1991**, *95*, 7004–7007.

15. S. Blugel, *Phys. Rev. Lett.*, **1992**, *68*, 851.

16. A. J. Freeman, C. L. Fu, J. I. Lee, T. Ogushi, in *Physics in Magnetic Materials*, M. Takashi *et al.* (editors), World Scientific, Singapore, **1987**, p. 221.

17. R. H. Victora, L. M. Falicov, *Phys. Rev. B*, **1985**, *31*, 7335.

18. L. E. Klebanoff, S. W. Roby, G. Liu, D. A. Shirley, in *Magnetic Properties of Low Dimensional Systems*, L. M. Falicov, J. L. Moran-Lopez (editors), Springer, Berlin, **1986**, p. 55.

19. H. Hasegawa, F. Herman, *J. Phys. C*, **1988**, *8*, 1667.

20. U. Herr, J. Jing, R. Birringer, U. Gonser, H. Gleiter, *Appl. Phys. Lett.*, **1987**, *50*, 471.

21. M. Rayl, P. J. Wojtowicz, M. S. Abrahams, R. L. Harvey, C. J. Buiorchi, *Phys. Lett.*, **1971**, *36A*, 477.

22. U. Gradmann, *J. Mag. Magn. Mater.*, **1986**, *54–57*, 733.

23. U. Gradmann, H. J. Elmers, M. Przybylski, *J. Phys. Paris*, **1989**, *49*, C8-1665.

24. C. L. Flu, A. J. Freeman, T. Oguchi, *Phys. Rev. Lett.*, **1985**, *54*, 2700.

25. C. Rau, G. Xing, M. Robret, *J. Vac. Sci. Technol.*, **1988**, *A6*, 759.

26. J. J. Becker, *J. Appl. Phys.*, **1958**, *29*, 317.

27. G. Abersfelder, *et al.*, *Phil. Mag.*, **1980**, *B41*, 519.

28. C. P. Bean, I. S. Jacobs, *J. Appl. Phys.*, **1956**, *27*, 1448.

29. J. C. Slater, *J. Appl. Phys.*, **1937**, *8*, 385.

30. Q. Li, C. M. Sorensen, K. J. Klabunde, G. C. Hadjipanayis, *Aerosol Sci. Technol.*, **1993**, *19*, 453.

31. W. H. Meikeljohn, C. P. Bean, *Phys. Rev.*, **1957**, *105*, 904.

32. S. Gangopadhyay, G. C. Hadjipanayis, B. Dale, C. M. Sorensen, K. J. Klabunde, V. Papaefthymiou, A. Kostikas, *Phys. Rev.*, **1992**, *45*, 9778.

# 7 Chemical and Catalytic Aspects of Nanocrystals

KENNETH J. KLABUNDE and RAVICHANDRA S. MULUKUTLA

Department of Chemistry, Kansas State University, Manhattan, Kansas

## 7.1 INTRODUCTION

In this chapter a variety of important aspects that center around unusual chemical properties of nanocrystals will be considered. This chemistry in large part concerns surface features, but unusual structures of aggregates will also be considered, including nanocrystal superlattices, diblock copolymers, and others. First, surface chemistry and catalysis will be considered.

Surface chemistry is of vital importance in numerous processes, including corrosion, adsorption, oxidation, reduction, and catalysis. Particles in the 1–10 nm range open a new vista in surface chemistry because surface–reactant interactions can become stoichiometric. This is for two reasons. First, the huge surface areas of the nanostructured material dictate that many of the atoms are or the surface, thus allowing good "atom economy" in surface–gas, surface–liquid, or even surface–solid reactions. Figure 7.1 illustrates the calculated numbers of iron atoms on spherical iron metal nanoparticles that are surface or bulk (interior) atoms. Note that quite small sizes are necessary; indeed, a 3 nm particle has 50% of the atoms on the surface, while a 20 nm particle has fewer than 10%. Thus demonstrates that it is necessary to "get small" in order to benefit from the atom economy desired.[1] A second aspect of surface chemistry that nanoparticles feature is enhanced intrinsic chemical reactivity as size gets smaller. This feature will be made clear as this chapter unfolds. The reasons for this enhanced reactivity are most likely due to changes in crystal shape: for example, changes from cubic to polyhedral shapes, when the surface concentration of edges and corner sites goes up considerably, as demonstrated in Figures 7.2 and 7.3 for MgO crystals. However, there are other features that can affect "surface energy." As crystal size becomes smaller,
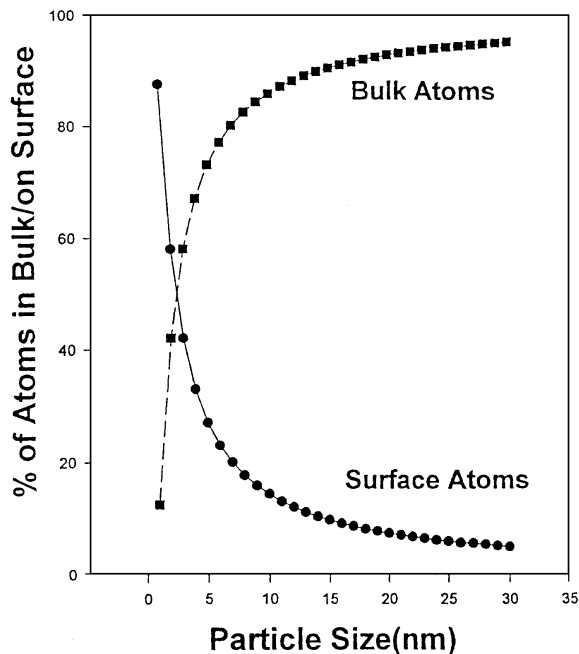
**FIGURE 7.1** Calculated surface to bulk atom ratios for spherical iron nanocrystals. Reprinted with permission from *J. Phys. Chem.*, **1996**, *100*, 12142–12153. Copyright 1996 American Chemical Society.[1a]
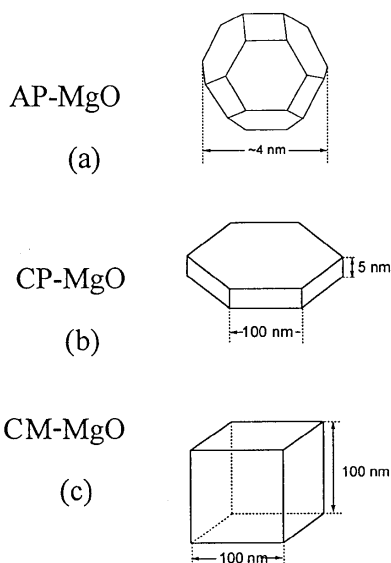


**FIGURE 7.2** Models of (a) nanocrystalline (AP-MgO); (b) microcrystalline (CP-MgO); (c) normal commercially available (CM-MgO) magnesium oxide crystals. Reprinted with permission from *Clusters & Nanostructure Interfaces*, **1999**, p. 578, World Scientific Publishing Co Pte Ltd.[1b]
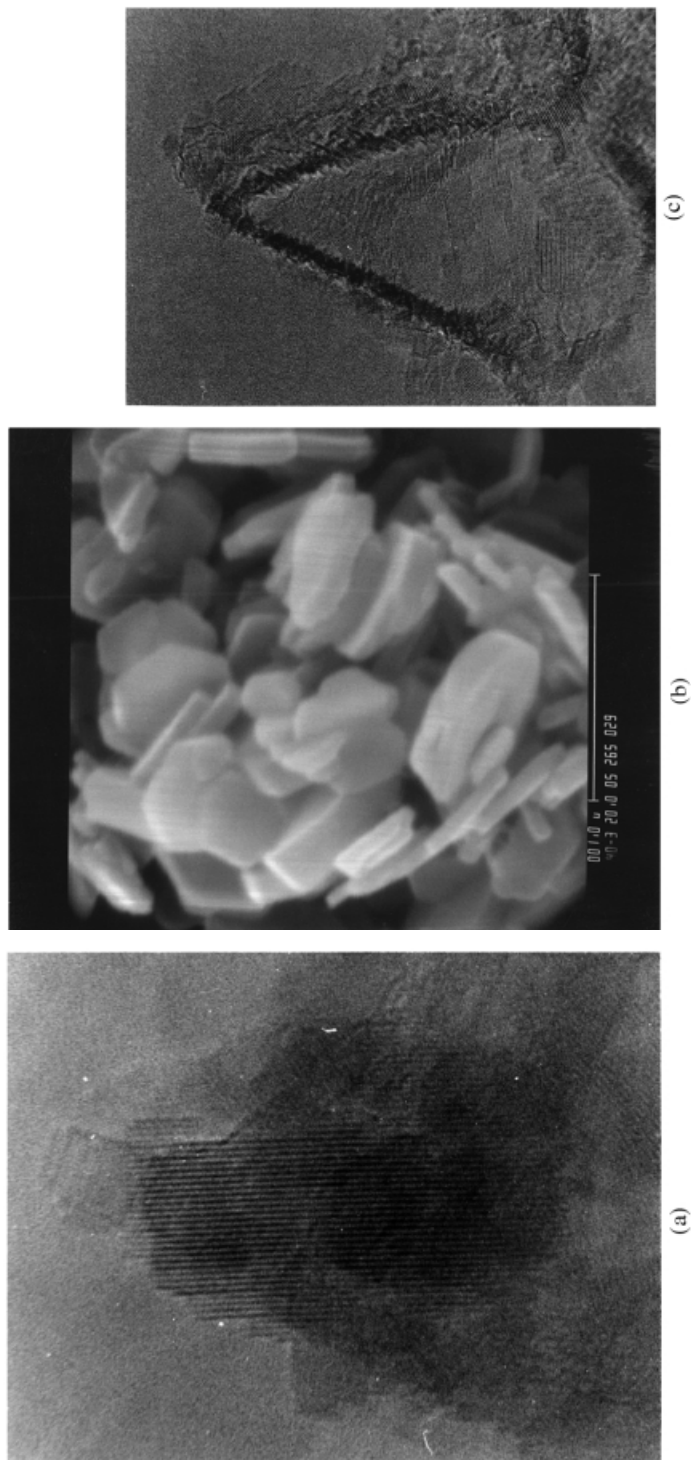
**FIGURE 7.3** Electron micrographs of (a) one 4 nm nanocrystal (AP-MgO) and (b) microcrystalline (CP-MgO); and (c) high-resolution TEM of small aggregate of nanocrystalline (AP-MgO) magnesium oxide.

anion/cation vacancies of the Frenkel or Schottky type become prevalent. Also, atoms on the surface can be distorted in their bonding patterns.[2]

Since surface chemistry is of such overwhelming importance in our technological world, it is difficult to overemphasize the importance of these new features brought in by the nanoparticle regime.[3–5] Now atom economy[6,7] and surface chemical reactions, be they stoichiometric or catalytic, can be joined. This will undoubtedly lead to a wealth of new techniques and applications. Adsorption, catalysis, medication utilization, acid–base reactions and neutralizations, and desirable reactions in which solids are consumed will all be significantly affected. These and related topics will be discussed in this chapter. The emphasis will be on how nanocrystals differ from normal microcrystals in their surface chemistry and catalytic properties. Due to the historical significance of the nanostructured regime in heterogeneous catalysis, this topic will be considered first.

## 7.2 NANOMATERIALS IN CATALYSIS

### 7.2.1 Metals

The literature is rich with examples where metallic nanoparticles exhibit different catalytic activities or selectivities due to nanocrystal size.[4,5] There have been extensive discussions of why these differences exist and certain aspects are briefly discussed below.

***7.2.1.1 Electronic Effects*** Electron density changes at catalytic sites can vary due to particle size. However, this concept is rather ill-defined and difficult to separate from electronic effects of the catalyst supports present. Nevertheless, there is certainly convincing evidence that ionization energies do change with metal particle size; for example, gas phase nickel clusters for $Ni_3$ to $Ni_{90}$ exhibit ionization energies that do not smoothly approach the work function as the number of atoms increases, but show an oscillation as a function of cluster size.[8,9]

***7.2.1.2 Support Effects (Electronic and Decoration Effects)*** Small metal particles bound to a metal oxide surface (the catalyst support) can most assuredly be affected electronically by the nature of the metal oxide. Generally the metal particle is believed to be chemically bound through $M_{(n)}$–$O_{(surf)}$ linkages, and this can occur by interaction of metal clusters with surface OH groups followed by proton reduction and metal oxidation. The catalyst supports employed vary in Lewis acid/base character, and it might be expected that MgO would be more electron-donating than neutral $SiO_2$ or Lewis-acidic $ZrO_2$ or $Al_2O_3$. Furthermore, smaller metal clusters on such supports would be more significantly altered in electron density than would larger clusters. Therefore, the size of the catalytically active metal particles does make a difference.

Another interesting phenomenon is the tendency of some supports to form deposits on the catalytic metal particles, thereby forming catalytically active inter-
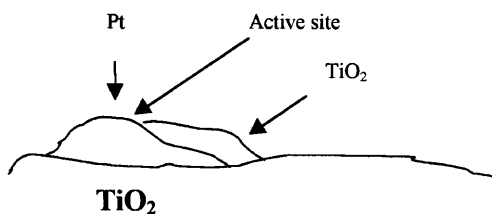
**FIGURE 7.4**   Model of Pt/TiO$_2$ catalyst where a TiO$_2$ patch "decorates" the platinum nanoparticle.

face sites, such as with M$_{(n)}$–TiO$_2$ composites (Figure 7.4). This interface site could also be sensitive to metal particle size through electronic or geometric features.[10]

*7.2.1.3  Shape Effects*   Shape effects have several manifestations. First of all, certain chemical reactions are "structure-sensitive" (hydrogenolysis of cyclopropane, dehydrocyclization, etc.).[11–13] This means, that as the reactant approaches, several adjacent surface metal atoms are required for the adsorption and catalytic transformation to proceed. Naturally, if the catalyst metal particle is so small that it either does not possess the necessary number of atoms (say 2–10 atoms), or the shape is such that these atoms do not exist as a flat plane, then the reaction cannot proceed. In another manifestation of shape effects, it is often assumed that the active sites are at low coordination (edges, corners), and the smallness of the catalytic particle can affect crystal shape and therefore surface concentration of edge/corner sites. For example, a polyhedral shape possesses a much larger number of edge/corner sites compared with a cubic shape (this is illustrated in Figure 7.2 for a metal oxide, but the same can apply for metals). Indeed, there are numerous convincing studies of the effects of edge/corner sites on adsorption and catalytic rates.[14,15]

   With this background, it is now appropriate to more thoroughly analyze important historical studies of the effect of metal particle size on catalytic behavior. A significant number of such studies have appeared and an extensive review appeared in 1982.[13] In the context at hand, effects of particle size will be the main concern. Studies of nickel supported on SiO$_2$ or Al$_2$O$_3$ in ethane hydrogenolysis (7.1) suggested that catalytic activity per unit surface area of nickel decreased as the nickel crystallite size increased.[12]

$$CH_3CH_3 + H_2 \xrightarrow{\text{metal catalyst}} 2CH_4 \qquad (7.1)$$
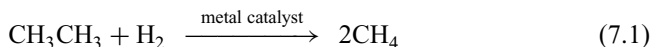
For rhodium it was found that an optimum crystallite size existed. These results demonstrated that ethane hydrogenolysis was structure-sensitive, and implied that crystal structure/shape was important. Boudart[11] and coworkers did not find particle size effects in cyclopropane hydrogenolysis over platinum nanocrystals (7.2), and suggested that on platinum this reaction was "facile," meaning that the majority of

sites on the catalyst surface possess ample activity such that surface heterogeneity is not important.

$$\Delta + H_2 \xrightarrow{\text{Pt catalyst}} CH_4 + CH_3CH_3 \qquad (7.2)$$
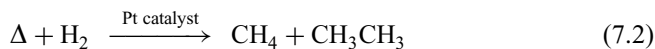
In a series of elegant studies Corrolleur, Gault, and their coworkers demonstrated the importance of particle size effects on mechanisms and product distributions of hydrogenolysis reactions over Pt catalyts.[16–19] Carbon-13-labeled hexane and methylcyclopentane were converted under hydrogen pressure and platinum catalysts by two distinct processes, and different-sized crystallites governed which process was favored. Methylcylopentane (MCP) was examined in some detail. The selectivities for cleavage at the $a$, $b$, and $c$ bonds of MCP were affected by platinum crystallite size (Figure 7.5). For example, on 4.5 nm (supported on SiO$_2$), the ratio of $c/a$ was 1.5, while on 1.5 nm platinum this ratio was 0.55. However, the $b/c$ ratio did not change much with platinum crystallite size change.[16] By comparing SiO$_2$ and Al$_2$O$_3$ supports, it was shown that support effects were not important. Since these studies were carried out 30 years ago, little information on platinum crystallite shape was available at the time, but the authors attributed their results to the presence of different types of special surface defects. In hindsight it is tempting to say that bond $a$ is susceptible on small crystallites simply because it is accessible to the "protruding" edges or corners on a small polyhedral shape, whereas on larger crystals far fewer such sites would be available; indeed, more flat planes would be present that might not be able to accept the $a$-bond site due simply to steric effects.

## 7.2.2 Recent Progress

### 7.2.2.1 *Metals*    It is obvious from historical aspects that catalysis by metal particles has always dealt with nanosized structures. However, with the recent
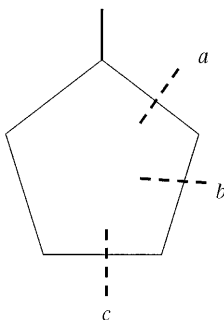


**FIGURE 7.5** Positions of cleavage of methylcyclopentane during hydrogenolysis over platinum nanocrystals.

development of new techniques, methods, and instrumentation, a "nanomaterials revolution" has been born. This has affected many areas of science, including metal catalysis. That is, in recent years a more focused study of size and shape effects has been undertaken.

One aspect of this new approach has been the development of unique methods for synthesizing small metal particles with the intention of producing ultrasmall sizes (even as small as an atom). One series of studies dealt with the solvated metal atom dispersion (SMAD) method in which vaporized metal atoms were trapped in frozen organic matrices. Upon warming, attempts were made to trap the solvated metal atoms on catalyst supports. In fact very small metal atom aggregates were trapped on $SiO_2$, MgO, $Al_2O_3$ and C, and these materials did exhibit rather unusual catalytic properties.[20] The main conclusions drawn were that the SMAD method did allow the synthesis of very highly dispersed heterogeneous catalysts directly with no metal salt reduction step involved, and that catalytic properties could be tailored by choice of solvent (pentane, toluene, THF, xenon). This remarkable finding implies that metal cluster growth[21] by atom aggregation in different low-temperature solvents leads to different morphologies/shapes, and this in turn affects catalytic properties (Figure 7.6). Further experimentation indicated that, when metal atoms aggregated in this way, the small incipient metal clusters were capable of C–H and C–C cleavage of alkanes at relatively low temperatures (below $-100°C$). Thus, the clusters were surprisingly reactive. Note from Figure 7.6 how nickel particle shapes are different when the clusters are grown in pentane versus toluene, and also that these same materials exhibited quite different catalytic behavior in a simple probe reaction, that of 1,3-butadiene hydrogenation.[21]

In related work, Akhmedov[22] and Vitulli and coworkers[23] have shown that the SMAD synthesis of noble metal catalysts yields metal particles of very unusual properties, assumed to be due to their very small size. For example, Pt-SMAD catalysts were quite effective for hydrogenation of *p*-chloronitrobenzene to dicyclo-hexylamine, a reaction that was found to be strongly correlated with particle size.

In a study of Pt-Re-SMAD catalysts prepared on various supports, extremely high activities for alkane hydrogenolysis were observed, and turnover frequencies (number of molecules converted per surface metal atom per second) as high as 84 were found. For toluene, $H_2$ treatment with a Pt-Re/zeolite system led to complete conversion to methane, ethane, propane, and butane at $350°C$, a reaction not observed with conventional catalysts. In this work it was found that rhenium deposited on top of the platinum yielded the most active catalyst, indicating that platinum partly covered with rhenium was the most effective.

In another recently established nanotechnology area, nanometer-sized (1–10 nm) metal particles have been protected by polymer wrappings. For instance, Toshima[24,25] and coworkers have trapped mono- and bimetallic particles of copper and palladium by chemical reduction of metal ions in the presence of poly(*n*-vinyl-2-pyrolidone). A remarkable feature of these solution dispersed colloids is that catalytic reactions on the metal particle surfaces proceed with ease, showing that the polymer chains surrounding the particles are porous and mobile. In this way Cu–Pd nanoparticles wrapped in the pyrolidone polymer were stable and soluble in organic
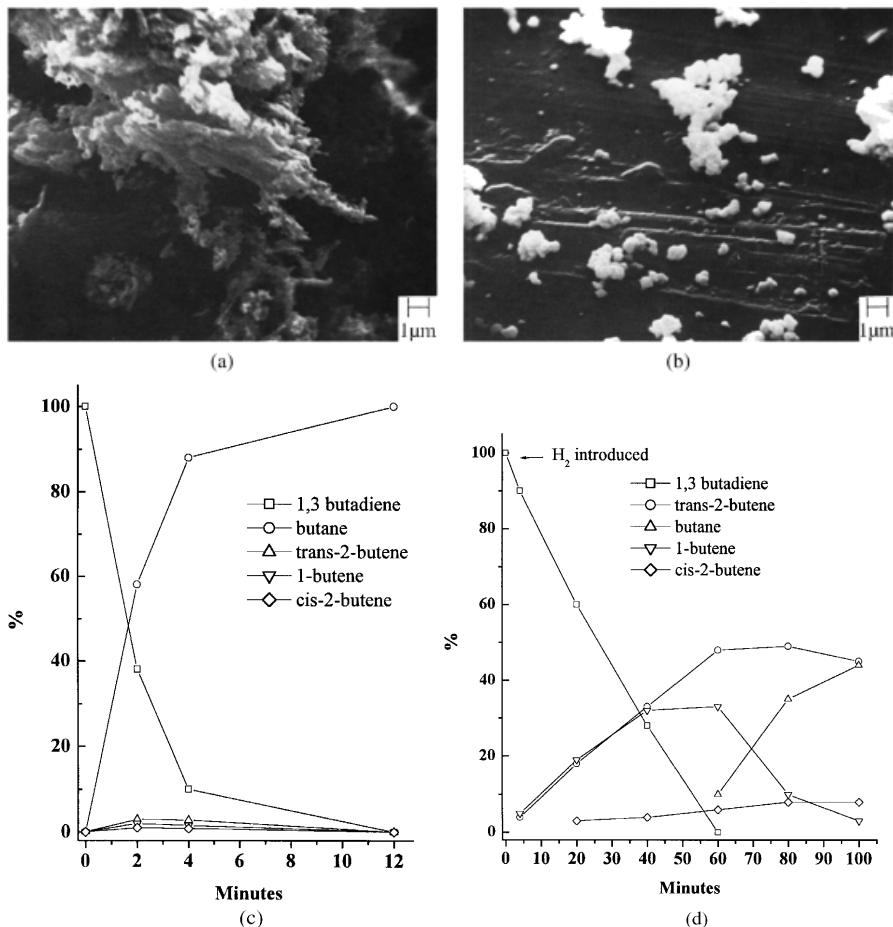
**FIGURE 7.6** Scanning electron micrographs of nickel nanoparticles formed from nickel atoms (a) in cold pentane and (b) cold toluene; (c) hydrogenation of 1,3-butadiene over Ni-pentane nanoparticles; (d) hydrogenation of 1,3-butadiene over Ni-toluene nanoparticles. Figures a & b reprinted in part with permission from *J. Am. Chem. Soc.*, **1976**, *98*, 1021–1023. Copyright 1976 American Chemical Society. Figures c & d reprinted with permission from *J. Catalysis*, **1978**, *54*, 254–268. Copyright 1978 Academic Press.[21a,b]

solvents, and served as a selective hydration catalyst for converting acrylonitrile to acrylamide. Indeed, several selective homogeneous nanoparticle catalysts have been reported and the unique feature is the ability of the polymer chain to protect and stabilize the metal particle from oxidation while allowing penetration of reactants for the desired catalytic reactions.[26,27]

Bonnemann and coworkers[28,29] and Bradley and coworkers[30] have also produced interesting catalysts by metal ion reduction/particle stabilization procedures. For example, platinum nanoparticles were stabilized by enantiomeric ligands, and these materials served as homogeneous catalysts for asymmetric reactions.

In another excellent example of a nano-effect in heterogeneous catalysis, Haruta[31] and coworkers have reported the synthesis of ultrafine gold nanoparticles smaller than 10 nm that were uniformly dispersed on transition metal oxides. The method involves co-precipitation from an aqueous solution of $HAuCl_4$ and the nitrates of various transition metals. The catalysts $Au/\alpha$-$Fe_2O_3$, $Au/Co_3O_4$, and $Au/NiO$ were highly active for CO oxidation even at a temperature of $-70°C$, showing enhanced catalytic activities due to the combined effect of gold crystallite size and the selection of appropriate transition metal oxide support.

Kung[32] and coworkers have prepared gold particles of about 5–10 nm on $\gamma$-$Al_2O_3$ and these were found to be highly active and selective for CO oxidation in a hydrogen-rich stream. Catalysts prepared with larger gold particles were less active and selective for CO oxidation.

This work clearly illustrates a nano-effect, but what is the underlying explanation for it? Is it because the $\gamma$-$Al_2O_3$, $TiO_2$, $\alpha$-$Fe_2O_3$, NiO, or $Co_3O_4$ supports affect the small gold particle? Is it because the small gold particles have a different shape, such as polyhedral with numerous edge/corner sites? Even if one of these questions is answered in the affirmative, further probing is necessary; that is, how is the catalytic mechanism affected?
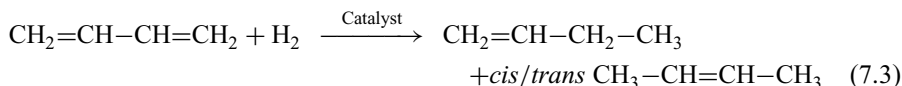
Goodman and coworkers have shed some light on these questions by using model single-crystal surfaces of $TiO_2$ as catalyst support for small gold clusters.[33] Their experimental technique employed ultrahigh vacuum (UHV). A $TiO_2$ thin film was deposited on an underlayer of Mo(100), which forced the formation of a $TiO_2$(001) crystal face. Then gold vapor was deposited, and it is assumed that gold islands form. Therefore, 0.25–5 monolayers of gold corresponded to average gold nanoparticle (island) diameters of 2.5–6.0 nm, and the presence of these clusters was confirmed by scanning tunneling microscopy (STM). Then $CO/O_2$ gas mixtures were admitted and the $CO \rightarrow CO_2$ reaction was studied at different temperatures and pressures. The apparent activation energy $E_a$ for the oxidation reaction from 350 to 450 K varied from 1.7 to 5 kcal mol$^{-1}$ as the gold nanoparticle sizes increased. A maximum rate was found for particles of 3.2 nm. This work clearly confirmed that the CO oxidation is a structure-sensitive reaction, and that gold cluster size is important. Goodman and coworkers propose a reasonable explanation: Suppose that $O_2$ dissociative chemisorption takes place along with CO adsorption. If oxygen atoms and/or CO molecules are held too strongly on the smallest gold clusters, then their movement on the surface to form $CO_2$ will be slowed down. On the other hand, on the largest gold clusters the adsorption energy may be too low, so that formation of the CO–O pairs is not favorable, and so product formation will be slower (Figure 7.7). Kung[32] and coworkers have also examined the Haruta catalysts in some detail. Their approach has been to examine a series of reactions over $Au/TiO_2$ catalysts with different gold nanoparticle sizes. One reaction studied was hydrogenation of 1,3-butadiene (Equation 7.3).

$$CH_2{=}CH{-}CH{=}CH_2 + H_2 \xrightarrow{\text{Catalyst}} CH_2{=}CH{-}CH_2{-}CH_3$$
$$+cis/trans\ CH_3{-}CH{=}CH{-}CH_3 \quad (7.3)$$
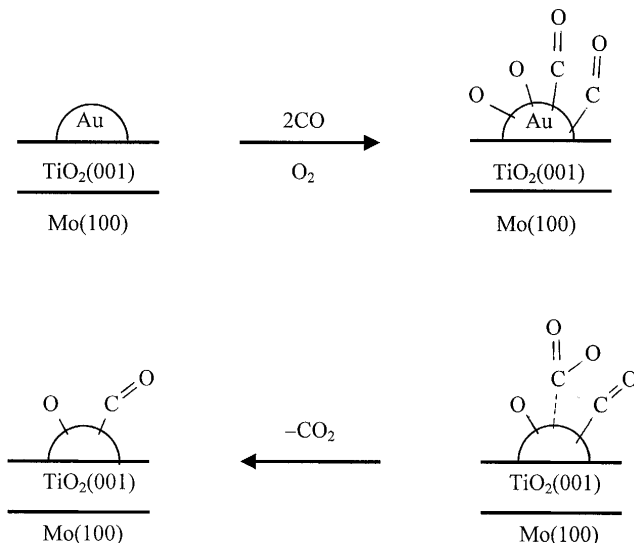
**FIGURE 7.7**   Representation of CO oxidation on gold nanoparticles of 2.5 to 6.0 nm. Adsorption, surface migration, and product formation are most rapid on a 3.2 nm gold particle.

No size effect was found in this chemistry. Indeed, for the Au/TiO$_2$ system it appears that oxidation reactions are the most sensitive to nanoparticle size effects, and this may be due to smaller particles being more reactive with O$_2$. However, a balance is necessary between the ability to rapidly dissociate O$_2$, coupled with the ease with which the absorbed oxygen atoms can migrate on the gold surface.

Considerable progress is being made on the synthetic front such that many types of new nanostructured catalysts are becoming available. For example, Watkins and coworkers[34] have dissolved organometallic precursors in supercritical CO$_2$, and cyclooctadiene (COD) PtMe$_2$ in CO$_2$ upon treatment with hydrogen causes platinum atoms to be released that aggregate to nanoparticles. In this way platinum or other metals can be deposited on high-surface-area supports or into the more polar regimes of block copolymers. Thus, treatment of polystyrene-B–polyvinylpyridine block copolymer with a palladium organometallic precursor allowed the metal compound to be imbibed into the more polar regions of the polymer, namely, the poly-vinylpyridine regions. Upon hydrogen treatment, the palladium clusters deposited on the vinylpyridine moieties.

Hahn[35] and Ying[36] and their coworkers have reported chemical vapor synthesis of nanostructured catalysts. For example, Pd/TiO$_2$, Pd/Mn$_3$O$_4$, Pd/CeO$_2$, and Pd/ZrO$_2$ have been reported where the oxide support is nanocrystalline.

Similarly, vapors of palladium orgonometallics have been allowed to contact nanocrystalline supports such as zeolites or MCM-41, where very small palladium clusters were deposited (Equation 7.4).

$$\text{(Cp)—Pd} + \text{MCM-41} \xrightarrow[\text{vacuum}]{80°C} \xrightarrow{\substack{300°C \\ H_2}} \text{Pd/MCM-41} \qquad (7.4)$$
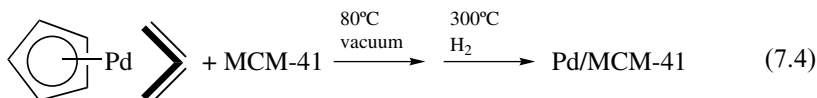
This catalyst was quite effective for the Heck arylation of alkenes, as shown in Equation (7.5).

$$R\text{—}C_6H_4\text{—}X + \overset{O}{\underset{O-Bu^n}{\|}} \xrightarrow[-HX]{\text{Pd/MCM-41}} R\text{—}C_6H_4\text{—}CH{=}CH\text{—}C(O)\text{—}O\text{—}Bu^n$$

$$(7.5)$$
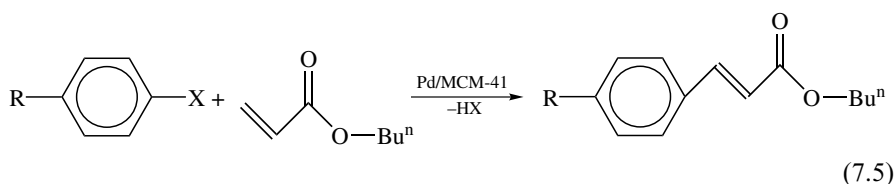
A very high turnover number (TON) of about 1000 was observed, and this was superior to more classical homogeneous catalysts for this process. In addition, the Pd/MCM-41 catalyst was air stable and easy to recover.[37]

Several research groups have employed ultrasound to decompose organometallic precursors to yield metallic nanoparticles.[38] For example, Suslick[39,40] and coworkers sonicated ironpentacarbonyl, tricarbonylnitrosylcobalt, or appropriate mixtures of these two precursors in polyvinylpyrrolidone solution in *n*-hexanol to generate black colloidal solutions. The particle size ranged from 3 to 7 nm as detected by transmission electron microscopy (TEM). These Fe–Co nanometer-scale metal colloids are homogeneous and magnetic studies showed that they are superparamagnetic and function as useful ferrofluids.

As a final example, Gates and coworkers[41,42] have made a concerted effort to produce clean, structurally characterized supported metal clusters by decarbonylations of metal carbonyls. In this way, $Ir_4(CO)_{12}$ was adsorbed on MgO support and the CO ligands were removed by heat treatment in helium at 300°C and then treated in hydrogen at 300°C. Careful analysis using extended X-ray absorption fine structure (EXAFS) strongly suggests that the $Ir_4$ cluster was produced intact. Interestingly, this catalyst showed low activity in a chosen model reaction; however, upon heating and of movement of iridium clusters, sintering, and growth, the catalytic activity increased, indicating that larger iridium particles are the most important catalytic species.

### 7.2.2.2  *Metal Oxides and Sulfides*    There have been several interesting examples of nanostructured metal oxides and sulfides exhibiting unusual catalytic properties.

For instance, methanol synthesis over a ZnO catalyst is well known (7.6), but the use of nanocrystalline ZnO enhances conversion considerably (Table 7.1).[43]

$$CO_2 + 3H_2 \xrightarrow{\text{ZnO}} CH_3OH + H_2O \tag{7.6}$$
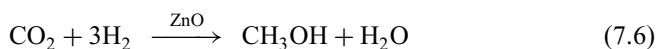
The data in Table 7.1 illustrate a comparision of 3 nm versus 35 or 44 nm ZnO cystallites used for this reaction. This catalytic reaction appears to be related linearly with surface area, and enhanced surface reactivity per $nm^2$ was not evident, which suggests that the reactive sites on a molecular scale are very similar for both the larger and smaller crystallites.

Superbase sites on nanocrystalline MgO have been prepared by potassium metal doping.[44] Crystallites of MgO of 4 nm size were treated with varying amounts of potassium vapor and on the surface $K^+$ and $e^-$ sites were formed, where the free electrons associate with surface sites to yield superbase reactive zones. Upon exposure to alkenes, allyl anions are formed by proton abstraction and these anions can alkylate ethylene (7.7).

$$H_3CCH=CH_2 + CH_2=CH_2 \xrightarrow{\text{K/MgO}} CH_3CH_2CH_2CH=CH_2 + \text{heptenes} \tag{7.7}$$
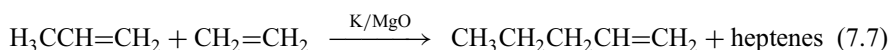
Figure 7.8 shows the percent conversion for nano versus microcrystals of MgO. Here again, the catalytic behavior was dependent on surface area, and presumably is related to the number of active sites formed by the potassium doping. It was shown that on nanocrystalline MgO a much higher surface concentration of superbase sites formed; therefore, this example shows that special catalytic sites were attainable on nanocrystals, and not on the microcrystals.

**TABLE 7.1  Methanol synthesis using microcrystalline versus nanocrystalline metal oxides as catalysts**

| Sample | Crystallite Size (nm) | Surface Area ($m^2 g^{-1}$) | Appearance | Conversion of $CO_2$ to $CH_3OH$ (%) |
|---|---|---|---|---|
| NC-NiO | 3 | 320 | Dark green | 64.2 |
| CM-NiO | 59 | 1.2 | Dark green | 0 |
| NC-ZnO | 4 | 130 | White | 37.1 |
| CM-1-ZnO | 44 | 3.9 | White | 0 |
| CM-2-ZnO | 33 | 20 | White | 29.5 |
| NC-ZnO/CuO | 4–7 4(ZnO) 7(CuO) | 138 | Dark gray | 58.6 |

CM-1-ZnO, commercial sample 1.
CM-2-ZnO, commercial sample 2.
NC-ZnO/CuO, 1:1 molar ratio nanocrystalline composite.
CM-NiO, commercially available sample.
NC-NiO, nanocrystalline sample.
NC-ZnO, nanocrystalline sample.
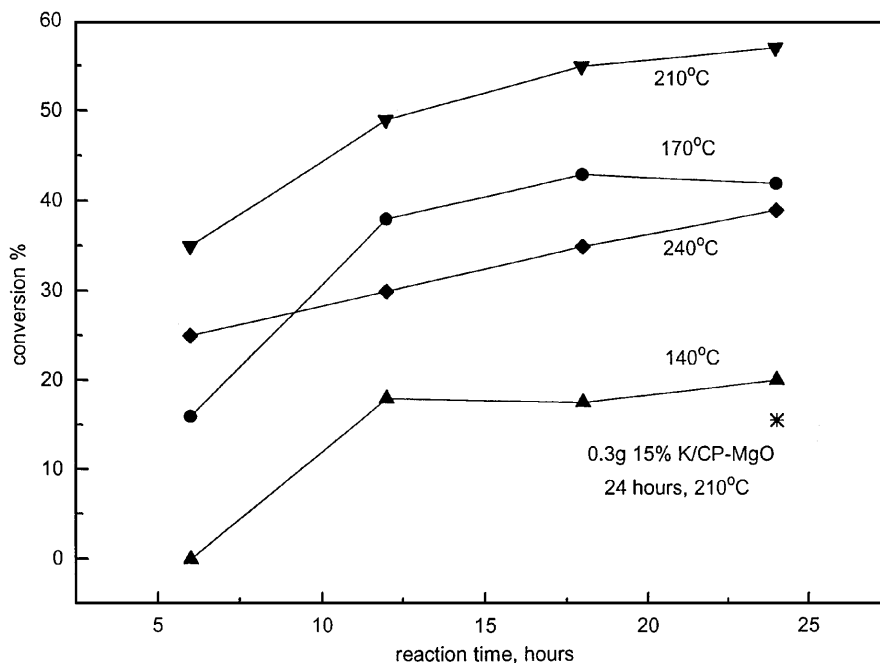
**FIGURE 7.8**   Conversion of ethylene/propylene mixtures to pentenes and heptenes for nanocrystalline (AP-MgO) potassium metal-doped MgO. The asterisked point refers to potassium metal-doped microcrystalline MgO (CP-MgO). Reprinted with permission from *J. Catalysis*, **1999**, *185*, 506–512. Copyright 1999 Academic Press.[44]

Catalytic chlorination of alkanes has also been achievable using nanocrystalline MgO.[45] Remarkably, $Cl_2$ gas is adsorbed in large amounts by the MgO, and the chemical reactivity of the $Cl_2$–MgO adduct is more similar to Cl atoms than $Cl_2$ molecules; that is, in the dark $Cl_2$ does not chlorinate alkanes, whereas the adduct does. However, the selectivity of $Cl_2$–MgO adduct is somewhat higher than that of Cl atoms. These observations lead to the tentative conclusion that on the MgO nanocrystals dissociative chemisorption takes place, and Cl atomlike species are trapped, probably by sharing of electron density with surface $O^{2-}$ anions. Somewhat surprisingly, the chlorination of methane and other alkanes proceeds in a catalytic fashion, showing that the secondary MgO/HCl reaction to form $MgCl_2/H_2O$ is slow compared with the chlorination and regeneration as illustrated in Figure 7.9. However, many questions remain to be answered concerning this chemistry; does the alkyl radical R˙ capture Cl˙ on the surface or in the gas phase? If R˙ is momentarily surface bound, does it bind to $Mg^{2+}$ or $O^{2-}$? Are surface defect sites involved? Further work is needed to further clarify this unusual chemistry.

There are several other examples in recent literature that demonstrate the unique properties of inorganic nanocrystals in catalysis. Wilcoxon and coworkers,[46] for example, have explored the use of $MoS_2$ semiconductor nanoparticles for the
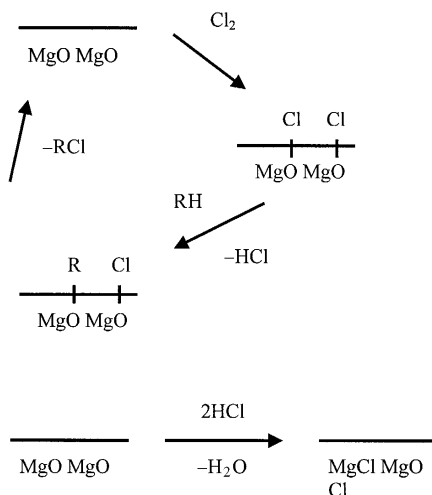
**FIGURE 7.9**   Proposed sequence of catalytic chlorination of alkanes by nanocrystalline MgO.

photooxidation of phenol. The bandgap of small $MoS_2$ crystals can be tuned across the visible spectrum. When the particle diameter is about 4.5 nm there is an absorbance edge at about 550 nm wavelength, and so visible light ($>450$ nm) can photoexcite the $MoS_2$, and the hole generated can take part in the photooxidation of phenol. Interestingly, larger $MoS_2$ particles (diameter 8–10 nm), which possess a lower energy bandgap, could not take part in this photoxidation. Furthermore, combination of small amounts of $MoS_2$ nanocrystals with $TiO_2$ as a catalyst support ($TiO_2$ possesses a bandgap in the UV region) allowed even more efficient phenol photoxidation. Presumably, multiphoton (visible light) excitation of $MoS_2$ led to some $TiO_2$ excitation also, and thereby more oxidizing potential.

Ying and coworkers[47] have utilized $CeO_{2-x}$ nanoparticles in the selective reduction of $SO_2$ by CO, and the catalysts exhibit excellent poisoning resistance to $H_2O$ and $CO_2$. The $CeO_{2-x}$ materials were found to possess a significant concentration of $Ce^{3+}$ and oxygen vacancies, even after 500°C calcination, and these defect sites, along with high surface areas, may be responsible for the enhanced catalytic performance.

An additional example of the novelty of nanocrystallinc oxides in catalysis has been given by Moser and coworkers,[48] who have developed a very clever sequence in which metal salt solutions are allowed to mix with precipitation agents just prior to entering a high-shear zone where mechanical cavitation, high-velocity mixing, and high pressure cause shear stress on the incoming sol. In this way a wide variety 1–10 nm metal oxide particles can be produced. For example mixed oxides such as $PbZr_{0.5}Ti_{0.5}O_3$ and $Cu_{0.22}Zn_{0.68}Al_{0.10}O_x$ have been prepared. Catalytic activities of these small particles are quite high compared with those of microcrystals.

**7.2.2.3   *Lewis Acid Catalysts***   Solid superacid catalysts[49–51] usually consist of metal oxides with high-metal cations (such as $Zr^{4+}$ in $ZrO_2$) further promoted by

coordinating $SO_4{}^{2-}$ anions.[49,51] The effect of the promoter is to further intensify the Lewis acid character of the metal ion sites. Although the exact structure of the catalytic sites is still not clear, solid superacids such as $ZrO_2$–$SO_4$ possess acid strengths much greater than that of concentrated sulfuric acid. These materials are capable of hydride abstraction from alkanes, with the concomitant formation of carbocation intermediates that then rearrange to more stable cations, followed by recapture of hydride. In this way, isomerization of *n*-alkanes to branched alkanes is possible under quite mild conditions (7.8).

$$CH_3CH_2CH_2CH_3 \xrightarrow{ZrO_2-SO_4} \overset{\overset{\textstyle CH_3}{\textstyle |}}{CH_3CHCH_3} \tag{7.8}$$
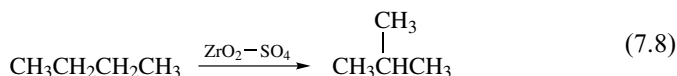
The application of nanocrystalline $ZrO_2$ in this chemistry has met with some success.[52,53] An interesting aspect is that the tetragonal crystal structure was preferentially obtained and was stable to 700°C, whereas conventional micro-crystalline samples converted to monoclinic. A systematic study of different aerogel synthesis parameters delineated how surface areas and pore structure could be controlled by varying precursor $Zr(OR)_4$ concentration and acid (hydrolysis catalyst) concentration (Equation 7.9). Control of the gelation step was important, as was a high-temperature supercritical drying step. Doping of this nanocrystalline $ZrO_2$ with sulfuric acid yielded a high-surface-area superacid. The presence of the $H_2SO_4$ did not change textural properties, but surface areas and pore volumes were actually increased by the surface doping.

$$Zr(O-Pr^n)_4 + H_2O \xrightarrow[\substack{H^+ \text{ catalyst} \\ 45 \text{ seconds}}]{CH_3CH_2OH \text{ solvent}} \{Zr(O)(O-H)_x\} \text{ gel} \tag{7.9}$$

255°C
autoclave
removal of
solvent

$ZrO_2$
105 m² g⁻¹
7 nm crystallites

$\xleftarrow[\text{air}]{500°C}$

$ZrO_2$
tetragonal
phase
390 m² g⁻¹
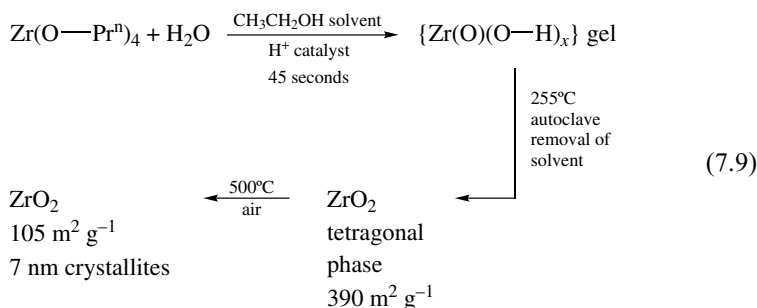
The aerogel prepared nanocrystalline $ZrO_2$–$SO_4$ was capable of butane isomer-ization, and relative activity was dependent on $SO_4$ loading. In fact nanocrystalline $ZrO_2$ required about a 25–30% loading of sulfur to attain maximum activity, whereas microcrystalline $ZrO_2$ required only about 10%. It seems that the nanocrystalline sample was capable of taking on large sulfate loadings, even more than monolayers, and still retain good catalytic activities. Conventional microcrystalline samples were more sensitive to sulfate loading, and when monolayer coverage was exceeded, a precipitous drop in activity resulted.

Selectivity in Lewis acid processes can also be affected by nanostructured catalysts. This has been found to be the case in the dehydrohalogenation of 1-chlorobutane.[54] Passing 1-chlorobutane over nanocrystalline MgO first causes a partial conversion of surface MgO to $MgCl_2$, and the resulting MgO–$MgCl_2$ composite is a highly active catalyst for the formation of butenes[54] (Equation 7.10).

$$ClCH_2CH_2CH_2CH_3 + MgO \xrightarrow{\text{350°C}} [MgCl_2]MgO + H_2O + \text{butenes}$$

$$\quad (7.10)$$

$$ClCH_2CH_2CH_2CH_3 \xrightarrow{[MgCl_2]MgO} \text{butenes} + HCl$$
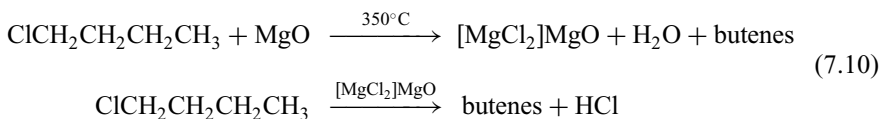
In a flow reactor system this catalyst is very long-lived, and the 1-butene and HCl are readily carried out of the reactor zone. Interestingly, this reaction does not proceed nearly as efficiently over microcrystalline MgO. It is clear that the catalytic sites produced from nanocrystalline MgO are numerous and of a special shape/orientation, but unfortunately little is yet known about these sites.

### 7.2.2.4 *Metal/Metal Halide Catalytic Processes: Photography* Wöste and coworkers,[55] through deposition of gas phase silver metal clusters of specific size ($Ag_2$, $Ag_3$, $Ag_4$), have elucidated how the classic silver–silver bromide photographic process may work. Only when $Ag_4$ (not $Ag_2$ or $Ag_3$) was deposited on AgBr did the catalytically enhanced photographic development take place. This result suggests that $Ag_4$ is a key species that is formed when silver bromide photographic film is exposed to light. Wöste estimated that about 10 photons are necessary to produce one $Ag_4$ species (stoichiometrically, at least four photons would be necessary). It was proposed that at defect sites on the AgBr surface photons cause free electrons to be formed, which migrate to the surface and reduce silver ion to silver atoms. These atoms then aggregate to form $Ag_4$, which appears to be a thermodynamically favored species. The $Ag_4$ clusters must later serve as catalysts for further silver ion reduction to silver nanoparticles in the photographic developer solution (Equation (7.11).

$$AgBr \xrightarrow{h\nu} Ag^0 \longrightarrow \longrightarrow Ag_4$$

$$\frac{Ag_4}{AgBr} \xrightarrow[\substack{\text{reducing} \\ \text{agent}}]{\text{developer}} \frac{Ag_x \text{ nanoparticles}}{AgBr} \qquad (7.11)$$
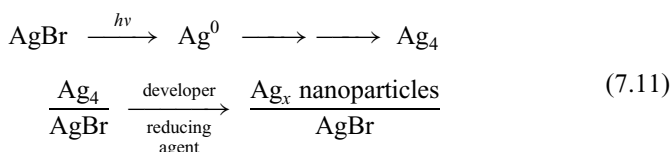
## 7.3    NANOSTRUCTURED ADSORBENTS

It is helpful to reiterate the underlying tenets of why nanostructured materials are so useful in chemistry. First, they possess very large surface areas and, second, nanocrystal shapes usually afford large surface concentrations of edge/corner and various defect sites, or other unusual structural features, such as channels or well-defined

cavities. For these reasons, when a potential adsorbate approaches the surface it has an abundance of acceptor sites available to it. In addition to these aspects nano-structured materials, when consolidated, can exhibit unusual pore structure, and in this way exhibit steric effects on adsorption processes. Nanostructural sorbents are proving to be wonderfully versatile, and represent one of the most important areas for rapid development.

## 7.3.1 Metals

In the area of nanotechnology, "gold has become the standard," even as it has served for centuries as the standard in monetary policy. Gold easily forms nanoparticles, is not readily oxidized, and exhibits different colors dependent on particle size. Therefore, it is not surprising that there are some excellent examples where gold particles and films show selective adsorbent properties. For example Hwang and Bartelt,[56] using STM, observed that ridges on a gold film act as nucleation sites for nickel atom clustering and island growth. Similar behavior was observed by Ikemiya and Gewirth[57] where dimethy sulfoxide (DMSO) was found to adsorb preferentially to step edges on Au(111). Likewise, on Au(100) the DMSO molecules showed an affinity for the terraces. The authors state that "the origin of this enhanced trapping probability is likely electronic in origin." Their results were explained as due to electron transfer from lone pairs on S and O to the gold surface, and this charge transfer would be enhanced at electropositive sites on the surface. The elevated ridge sites would be more electropositive than their neighbors not elevated above the plane, and this explains the electronic effect that attracts the DMSO nonbonding electron pairs. This preferential adsorption on edges/corner/ridges has also been observed with benzene on Cu(111),[58,59] and $C_{60}$ on Au(111) and Cu(111).[60,61]

Nanostructured features of several metals have aided hydrogen adsorption. Such materials with high hydrogen storage per unit volume and mass are becoming more important with the onset of vehicular fuel-cell applications. Magnesium metal, being very light, can store up to 7.7 wt% hydrogen. However, the adsorp-tion/desorption kinetics are slow. Thus, nanostructured materials were employed, as follows. In the first report, the SMAD (solvated metal atom dispersion, see section 7.2.2) method was employed to prepare, in THF solvent, Mg-SMAD nanoparticles[62] in the form of thin flakes that were extremely reactive toward hydrogen, exhibiting an activation energy for adsorption of 9.9 kcal mol$^{-1}$. This was compared with normal magnes-ium (block appearance with smooth surfaces) of 25 kcal mol$^{-1}$. Furthermore, these unique flakes caused $H_2/D_2$ scrambling to form HD with a rate of $1.35 \times 10^{19}$ molecules s$^{-1}$ g$^{-1}$ at 0°C. Normal "activated" magnesium did not cause this reaction even at higher temperatures. This is another clear example showing that small crystallite size and shape can have profound effects on reactivity.

High-surface-area magnesium and $Mg_2Ni$ have been prepared by ballmilling of bulk materials. In fact, the presence of $Mg_2Ni$ catalyzes the dissociation of $H_2$ so that

the ratio of hydrogen adsorption is increased considerably (Equation 7.12). Other catalysts such as FeTi and LaNi$_5$ are also effective.[63]

$$Mg + H_2 \xrightarrow{\text{Mg}_2\text{Ni}} MgH_2 \qquad (7.12)$$
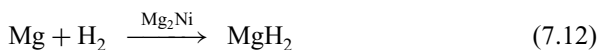
Dragieva and coworkers have used a borohydride reduction scheme to prepare a wide variety of transition metal nanoparticles containing boron and hydrogen[64–66] (Equation 7.13).

$$Co^{2+} + BH_4{}^- \xrightarrow{\text{H}_2\text{O}} Co_xB_yH_z \qquad (7.13)$$
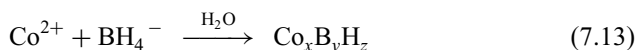
Similar materials have been prepared in the presence of rare earth metal ions, and a series of NiM nanoparticle composites have been prepared. In addition to exhibiting interesting magnetic properties, these metal nanoparticles adsorb hydrogen from the borohydride process to form particles useful in metal hydride batteries. For example, $Co_xB_yH_z$ nanoparticles were pressed and partially sintered and tested in 20% KOH solutions as electrodes for metal hydride rechargeable batteries. Electrodes prepared under low pressures (20–30 MPa) and sintering temperatures of 200–300°C showed the best characteristics with respect to hydrogen electrochemical adsorption–desorption. At higher sintering temperatures a considerable loss in the number of sites available for hydrogen storage was seen. Under the best conditions a discharge capacity of 250 mA h g$^{-1}$ was attained. The best performance was found for electrodes that were made of consolidated, amorphous particles, and TEM investigation revealed a very porous network in which the entire mass would be available for hydrogen adsorption at active sites. These results again reinforce the idea that nanoparticles possess many reactive sites that are readily available to reactants.

### 7.3.2  Controlled Pore Size Materials

*7.3.2.1  Zeolites*  Aluminosilicates make up a huge family of self-assembled inorganic materials with reasonably well-defined pore sizes and large pore volumes. Several formulations have become vitally important in catalytic cracking and other chemical and fuel processing steps, for example, ZSM-5 (Figure 7.10). When Mobil researchers learned how to synthesize these materials in commercial quantities, industrial catalysis was fundamentally changed. Zeolite catalysts are now used to process several billion barrels of petroleum each year.

Numerous commercial processes have been developed based both on size exclusion due to the zeolite pores and on selective molecular diffusion into the pores. These size effects, coupled with the ability to tailor Lewis acid sites within the pores,
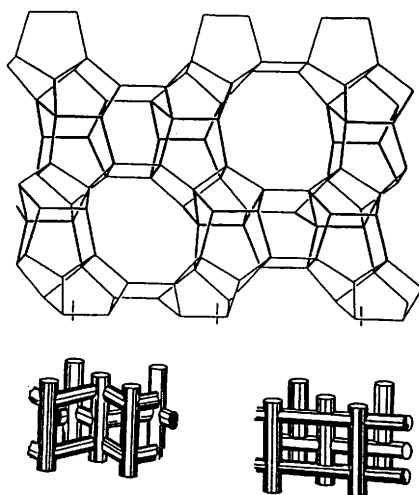
**FIGURE 7.10** The three-dimensional channel structure of ZSM-5 zeolite. Reprinted with permission from Cox, D. IWGN Workshop Report, **1999**.[67]

has opened up many avenues for new catalytic processes. An illustrative example is the isomerization of isomers of xylene and ethylbenzene.[67]



| *o*-Xylene | *m*-Xylene | *p*-Xylene | Ethylbenzene |
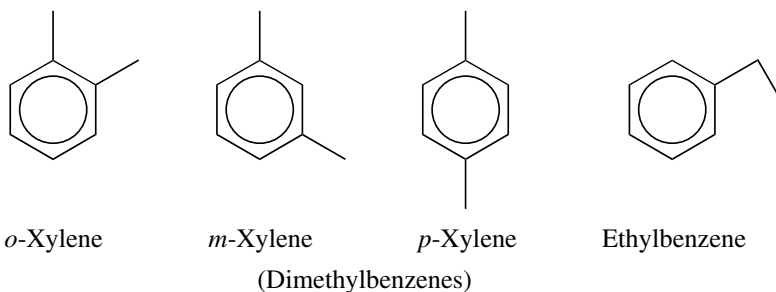
(Dimethylbenzenes)

These are all $C_8H_{10}$ isomers, but the chemical industry has a great demand for *p*-xylene, and so a process that converts the *o*- and *m*-isomers and ethylbenzene to *p*-xylene would be quite valuable. H-ZSM-5 has a 0.6 nm pore size that allows *p*-xylene to diffuse rapidly through, whereas the other isomers get "hung up" in the pores and at high temperature isomerize to different isomers until the *p*-xylene isomer is formed, which then escapes. In this way a mixture of these isomers can be rapidly enriched in the valuable *para* product.

Actually, a large family of crystalline nanostructured aluminosilicates are possible, and the zeolite's channel dimensions depend on the number of oxygens in the ring, and this, in turn depends on the $Al_2O_3$ to $SiO_2$ ratio. As the nanostructure is varied, the number of oxygens in the ring can vary from 4 to 12 while ring diameter ranges from 0.12 to 0.80 nm. Even channel diameters up to 1.5 nm are possible

depending on whether the zeolite exhibits a three-dimensional structure consisting of intersecting straight and zigzag channels or two-dimensional configurations.

Another example of how these channels can affect chemical sorption and passage is that of *n*-hexane versus cyclohexane. *n*-Hexane has a kinetic molecular diameter of about 0.5 nm and so can easily pass through a 10-oxygen ring size, whereas cyclohexane with kinetic molecular diameter of 0.7 nm cannot, at least not easily. Therefore, a zeolite with a 10-oxygen ring size channel of 0.63 nm could be used to separate a mixture of *n*-hexane and cyclohexane.

These size exclusion properties, coupled with the fact that inner channels can be chemically modified by ion exchange to render the zeolite more or less acidic, make zeolites extremely valuable as selective catalysts, sorbent, and membranes.[68]

### 7.3.2.2   *MCM-41 and Other Controlled Pore Silicates*

A new dimension was opened up by Kresge and coworkers[69] when they devised an organic templating method for the assembly of molecular silicate building blocks. In this process advantage is taken of the tendency of surfactant molecules to form vesicles with the outer surfaces of the resulting cylinders consisting of ionic hydrophilic groups. The addition of ionic silicates/aluminates causes the cylindrical shapes to be coated with these $SiO_2$ or $SiO_2$–$Al_2O_3$ precursors, and under the proper conditions of concentration, pH, and temperature, sheaths of zeolitic material are formed in cylindrical shapes (Figure 7.11).[70] Upon oxidative removal of the organic surfactant, a collection of hollow zeolite cylinders are formed with pore sizes ranging from 2 to 10 nm, a much broader range than was possible with normal zeolitic materials.

This templating approach can also be used to form pure $SiO_2$ materials, or nonsiliceous materials of the general MCM-41 shapes. Indeed, the ability to synthesize zeolite materials with controlled pore sizes in the 0.4 to 1.0 nm range continues to expand the possibilities for innovation in catalytic, sorption, and separation science.[71–73]

### 7.3.2.3   *Pillared Clays*

Related to the zeolites are natural and synthetic clays that are made of three-dimensional structures from two-dimensional clay minerals. Pillared clays[74,75] were formed by introducing highly positive charged inorganic polymeric cations into a smectite clay with low layer charge; the resulting structure
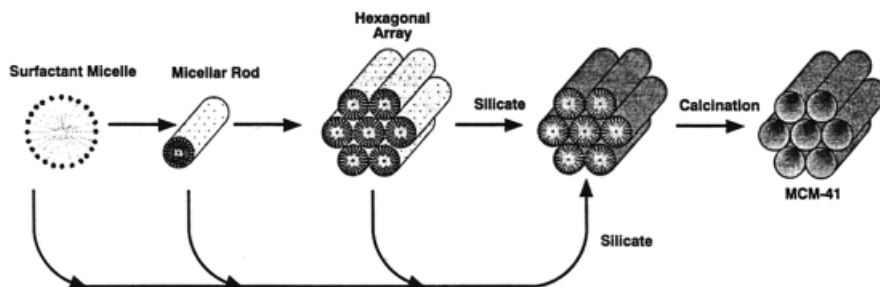


**FIGURE 7.11**   Synthesis sequence of MCM-41. Reprinted with permission from *J. Am. Chem. Soc.*, **1992**, *114*, 10834. Copyright 1992 American Chemical Society.[70]

has well-defined pores larger than those available in zeolites. A typical example is aluminum keggin ion $[Al_{13}O_4(OH)_{24}(H_2O)_{12}]^{7+}$, which can create a free distance of 10–22 Å between the pillars. Several pillaring agents can be used to prepare pillars of chromium, zirconium, titanium, etc. and the pore size depends on the choice of pillaring agent and several other factors. The pillared clays can provide a wide range of pore sizes that were applied in catalytic cracking reactions. Shape-selective reactions were also studied with different pore sizes of $Al_{13}$ pillared clays.

**7.3.2.4  Carbon Nanotubes**   After the discovery of the soccer ball structure $C_{60}$,[76,77] representing a new form of elemental carbon, further varieties of unusual forms of carbon have been elucidated. A particularly fascinating and potentially useful form is the "nanotube".[78] Nanotube structures are made up of graphitelike carbon (mainly $C_6$ ring fusions) possessing enough $C_5$-ring fusions to allow curvature into cylinders. These cylinders, or tubes, can be single-walled (SWNT) or multiwalled nanotubes, and can be closed at one end or both ends. They are really nanofibers.

The ends of nanotubes are somewhat more chemically reactive due to the strain involved, and oxidative chemical methods have been reported for opening the ends of the tubes. Once the tubes open, large surface areas become available, and they possess excellent adsorbent properties. This might be expected to be the case since high-surface-area graphite (carbon black) has long been used as an effective adsorbent for organic impurities and is used commercially in large amounts for air, water, and other purification purposes. The nanotubes adsorb hydrogen gas and methane in large amounts[79,80] and microporous hollow carbon fibers have also exhibited high permeability and selectivity as hydrogen-selective membranes.

Carbon nanotubes and relatives, such as the fullerenes, endohedral fullerenes, metal-coated fullerenes, carbon nanoparticles, porous carbons, carbon fibers, and carbon aerogels have all "burst on the scene" in a spectacular way during the last few years. Many interesting properties have been discovered. An example is that carbon nanotubes could be semiconducting or conducting depending on the diameter of the nanotube. Nanotubes can also be used as templates for building tubular structures of metal oxides; for example, nanotubes of $ZrO_2$ have been prepared by coating treated carbon nanotubes with a zirconium compound and then oxidizing (burning) the carbon away.[81] Of course, carbon nanotubes can also be used as normal carbon fibers are used, for reinforcing polymers or concrete.[82] The literature is rich in recent reports of improved syntheses, properties, and potential uses of carbon nanotubes and related materials. The future looks bright if the cost of large-scale manufacture can be brought down.

### 7.3.3  Pelletized Nanocrystals

An unexpected finding has been that some nanocrystalline oxides and hydroxides retain their high surface area and large pore volumes upon pressure-induced pelletization of the free flowing powders.[54] Table 7.2 illustrates some data collected on nanocrystalline $Mg(OH)_2$. Note from Table 7.2 that little change in surface areas/

TABLE 7.2    Surface area and pore size distribution of magnesium hydroxide in powder and pellet forms

| Sample Loads (lb) | Surface Area ($m^2 g^{-1}$) | Total Pore Volume ($cm^3 g^{-1}$) | Crystallite Size (nm) | Average Pore Diameter (nm) |
|---|---|---|---|---|
| powder | 364 | 0.898 | 4.7 | 9.87 |
| 1000 | 371 | 0.833 | 4.5 | 8.97 |
| 2000 | 359 | 0.660 | 4.7 | 7.34 |
| 3000 | 370 | 0.670 | 4.2 | 7.26 |
| 5000 | 366 | 0.586 | 4.3 | 6.41 |
| 10,000 | 383 | 0.436 | 4.3 | 4.55 |
| 20,000 | 342 | 0.290 | 4.3 | 3.39 |

Reprinted with permission from *J. Am. Chem. Soc.*, **2000**, *122*, 12142. Copyright 2000 American Chemical Society.[54]

pore volumes occur upon pressing even to pressure as high as 5000 pounds. However, at still higher pressing loads changes do occur and, in fact, some control of areas, pore sizes, and pore volumes can be achieved by choice of pressing load.

This unexpected behavior is apparently due to the rigid nanostructure that forms upon rapid solvent removal from an aerogel precursor. Figure 7.3 illustrates this for MgO, where the small crystals and an embryonic pore structure can be seen (also see Figure 4.10).

This pressure-induced pore structure change can be used to advantage, and it has been shown that, when the pores are large, the alcohols $CH_3OH$, $CH_3CH_2OH$, and $CH_3CH_2CH_2CH_2OH$ were all adsorbed well, but upon closing down the pore size, selective adsorption based on molecular size was possible.[54]

## 7.4    NANOPARTICLES AS NEW CHEMICAL REAGENTS

High surface areas and intrinsically high surface reactivities allow surface reactions to approach stoichiometric conversion with nanoparticles. Gas–solid reactions and liquid–solid reactions take on a new dimension, and solids in nanoparticle form now enter the chemist's arsenal as chemical reagents in a much more meaningful way.

### 7.4.1    Metals

There are historically numerous reactions of metals in which the metal is consumed. With the entry of nanoparticles, these reactions can be carried out much faster at lower temperatures. One example is the Grignard reagent preparation. Many years ago Rieke and coworkers[83–86] showed that small magnesium particles, formed by reduction of magnesium salts with potassium metal in ether solvents, were extremely reactive with organohalides. For example, chlorobenzene and even fluorooctane smoothly formed Grignard reagents under mild conditions (Equations 7.14). Numerous metals in nanoparticle form exhibit such enhanced reactivities and this

has been useful in organic synthesis in a variety of ways. One example is that copper in an activated form allows the coupling of epoxyalkyl halides[83]

$$C_6H_5Cl + Mg^* \xrightarrow{25°C} C_6H_5MgCl$$

$$C_6H_5F + Mg^* \xrightarrow{25°C} C_6H_5MgF$$

$$C_8H_{17}F + Mg^* \xrightarrow{25°C} C_8H_{17}MgF$$

(7.14)
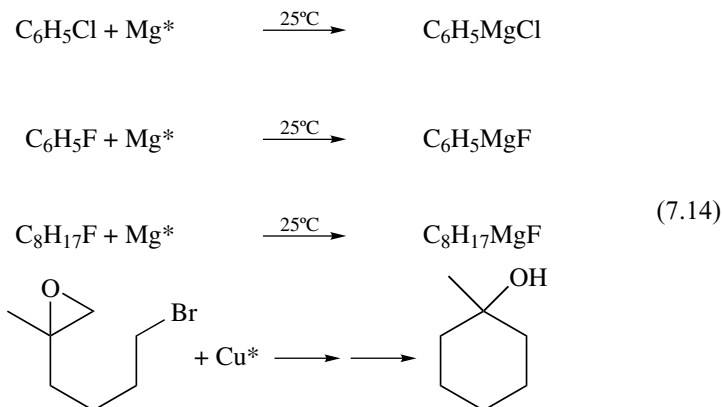


Another method of preparation of nanoparticulate metals is the SMAD method, described in section 7.2.2. Metal atoms are allowed to cluster to nanoparticles in low-temperature solvents, which leads to highly reactive fine powders.[84] Indeed, small metal clusters are often observed to be more reactive than single atoms, under similar low-temperature conditions.[87,88] For example, nickel atoms do not react with alkanes at 77 K, but clusters that form from the atoms on slight warming do react. Also, small $Mg_n$ clusters react with alkyl halides in frozen argon matrices, whereas magnesium atoms do not (Equation 7.15).

$$\underset{\text{(isolated in argon at 9 K)}}{Mg/Mg_2/Mg_3} + CH_3Br \longrightarrow Mg \text{ atoms} + \underset{\text{(Mg}_2/\text{Mg}_3 \text{ consumed)}}{CH_3Mg_2Br + CH_3Mg_3Br}$$

(7.15)
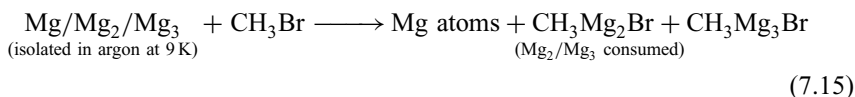
These observations have been rationalized as due to (1) clusters having lower ionization energies, and if electron transfer is necessary to initiate a reaction this can facilitate the process; (2) favorable thermodynamics of forming several bonds and being able to form cluster type molecules; and (3) clusters being more polarizable.

These considerations help explain why the SMAD metal nanoparticles are so reactive. Magnesium-SMAD particles reacted readily at low temperature with various aryl halides; 2-chloroallyl benzene gave a 85% yield of the Grignard; bromopentachlorobenzene at −30°C gave a 77% yield of $C_6F_5MgBr$ in 45 minutes.

The importance of being able to initiate and carry out Grignard preparation at low temperatures was further demonstrated by studies of strained ring systems, where the low temperature discouraged rearrangements (Equations 7.16).[89–91]



$$\tag{7.16}$$
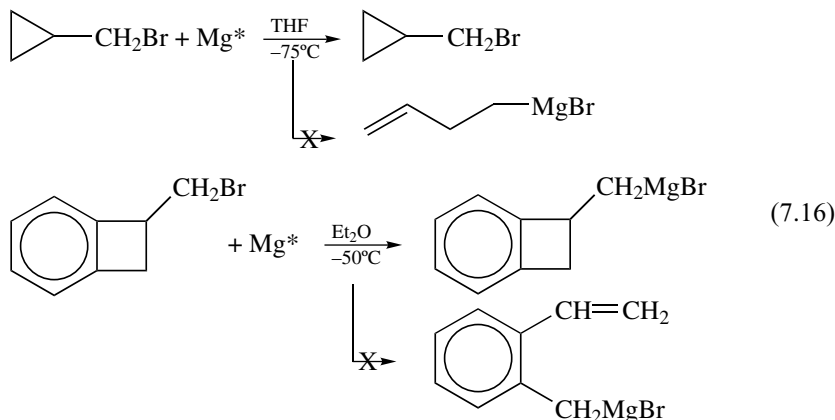
Numerous other examples of the high reactivity of SMAD metals have been reported. Thus Cd-hexane slurries react with R-I to give RCdI + R$_2$Cd. Also, Zn-hexane slurries react with CH$_3$I to yield (CH$_3$)$_2$Zn + ZnI$_2$. Zn-solvent slurries could be used for the Simmons–Smith cyclopropanation with CH$_2$Br$_2$ (7.17).



$$\tag{7.17}$$
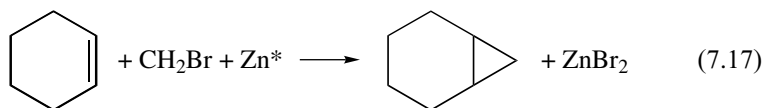
Other interesting reactions under mild conditions are summarized in Scheme (7.18).

$$Al^* + C_6H_5Br \longrightarrow (C_6H_5)_3Al_2Br_3$$
$$Al^* + (C_6H_5)_2Hg \longrightarrow (C_6H_5)_3Al + Hg$$
$$In^* + EtI \longrightarrow Et_2InI + EtInI_2$$
$$Sn^* + MeI \longrightarrow MeSnI_3 + Me_2SnI_2 + Me_3SnI$$
$$Pb^* + MeI \longrightarrow Me_3PbI + Me_3PbI + PbI_2$$
$$Ni^* + C_6H_5CH_2Cl \longrightarrow C_6H_5CH_2CH_2C_6H_5$$

$$\tag{7.18}$$
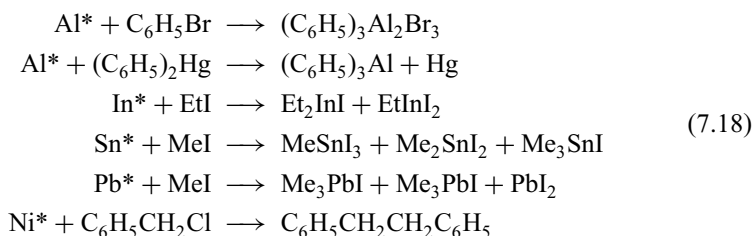
These and other extensive studies show that metal nanoparticles are reactive enough that they can be considered as new reagents for organic and organometallic synthesis directly from the metal. These active metal powders are stable in storage, and so represent a broad new class of reagents for the chemist.

These examples from the 1970s and 1980s predate the more recent interest in "nanomaterials" and in fact, the term "nano" had not at that time been brought into

common use. During the 1980s, the decade when the "nanotechnology era" started, new instrumentation allowed more quantitative assessment of metal cluster reactivities, where "metal cluster" refers to metal atom aggregates of 2–300 atoms, quite small compared with the many thousands of atoms in a metal nanoparticle. It became possible to prepare gas phase neutral metal clusters and to begin to assess chemical and physical properties.

Several examples are discussed below and have been chosen to illustrate that for bare metal clusters (which are very small nanoparticles) cluster size and structure affects chemical reactivity.

Cox, Kaldor, Trevor, and their coworkers[92,93] have studied gas phase platinum clusters and their reactivity with alkanes and aromatics. Their work demonstrated the first reaction of methane with an unsupported metal cluster, and a distinct cluster size dependance was observed, where $Pt_2$–$Pt_5$ were most reactive and $Pt_6$–$Pt_{24}$ less so. The $CH_4$ reactions yielded $Pt_nC_{1,2}H_y$ species and larger clusters retained high ratios of hydrogen. Platinum clusters reacted with larger alkanes, causing extensive dehydrogenation. Indeed, some alkanes were dehydrogenated to aromatics, and these reactions were very cluster size dependent. Cyclohexane, for example, yielded benzene–Pt complexes:

$$\left(\text{\raisebox{-1ex}{\Large\textbigcircle}}\right)_2 \!\!-\!\!(Pt)_n + 6H_2$$
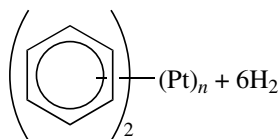
These studies indicated that low-coordination platinum atoms (edges/corners) were more reactive than closely packed surface metal atoms. Another interesting phenomenon was reported by El-Sayed and coworkers.[94,95] Gas phase niobium metal clusters were allowed to react with ethyl bromide and 2-bromopropane. The reaction of small niobium clusters ($n \leqslant 4$) with either compound yielded the same amount of bromide abstraction product $Nb_2Br$ (detected by ionization to $Nb_nBr^+$ and mass spectrometry). However, when $n$ was 5 or greater, the yield went down considerably for the 2-bromopropane. These results were attributed to steric crowding such that on the larger clusters the approach of the bound bromine was not as facile with the 2-bromopropane as with the ethyl bromide which indicates that small clusters are better able to obtain close approach to the bromoalkane, because the metal atoms are more "protruding." However, as the clusters get bigger, the surface atoms are no longer as accessible. Numerous other cluster size–cluster structure sensitive reactions have been reported and have been discussed in an earlier review.[9]

## 7.4.2 Metal Oxide Reactions

### 7.4.2.1 *Near Stoichiometric Adsorption; $SO_2$, $CO_2$, HCl, HBr, $SO_3$* There are numerous demonstrated instances where nanocrystalline metal oxides exhibit

enhanced surface reactivities (over and above that predicted by surface area alone). One such example is the surface adsorption of sulfur dioxide on MgO.[96] At room temperature and 20 torr pressure, MgO nanocrystals tightly chemisorbed 6 molecules of $SO_2$ per $nm^2$ of surface, whereas larger microsize crystals adsorbed only 1.8 molecules per $nm^2$. Furthermore, the smaller crystals favored a monodentate type adsorption mode, whereas the larger ones favored a bidendate mode. These differences were attributed to morphological features of the two types of crystals (see Figures 7.2 and 7.3).



Nanocrystals adsorb            Microcrystals adsorb 1/3
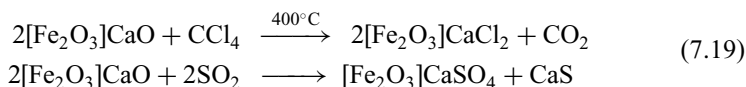a monolayer at 20 torr         of a monolayer at 20 torr
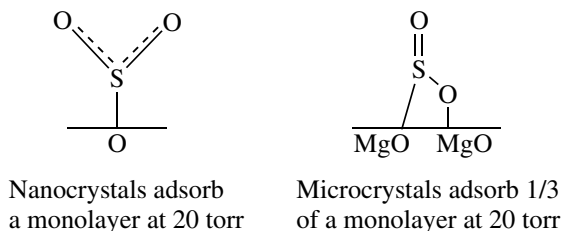
Interestingly at higher pressure, multilayers were weakly adsorbed on microcrystals, and this was attributed to the formation of more ordered, denser multilayers, apparently possible because of the preponderance of flat (100) planes. So again, crystal shape plays a role in adsorption properties. Similar results were observed with other acid gases, such as $CO_2$, HCl, HBr, and $SO_3$.[97] In these cases very large amounts of these gases adsorbed on nanocrystalline MgO on a mole per mole basis. However, at pressures of 100 torr or higher the microcrystalline samples adsorbed more on a molecules per $nm^2$ basis, apparently because of the formation of more ordered multilayers.

In general it was concluded that nanocrystalline MgO possesses an enhanced surface reactivity toward acid gases. However, when multilayer adsorption occurred, the more ordered surfaces on larger crystallites became more important. This multilayer adsorption was encouraged by higher gas pressure, although weak physisorption rather than chemisorption was involved. It is possible that both polarization (electronic) effects and morphological effects are involved in these adsorption processes.

An important point is that these types of ambient temperature adsorptions take place in such large amounts that the metal oxides can be considered as almost stoichiometric reagents. Consider that 4 nm MgO crystallites have 30% of the total metal ions on the surface. When a monolayer of $SO_2$ is adsorbed, this means that 30% of the available MgO is useful. This is indeed very different from normal solid–gas reactions, where generally less than 5% of the surface is available.

### 7.4.2.2 Destructive Adsorptions at Elevated Temperature: Stoichiometric Mineralization of Chlorocarbons, Hydrogen Sulfide, and Sulfur Dioxide   Nanocrystals are often quite capable of solid–gas stoichiometric reactions, and these reactions can be catalyzed by transition metal ions. For example, a monolayer of

$Fe_2O_3$ on nanocrystals MgO (or CaO) led to greatly enhanced efficiencies for chlorocarbon destruction and sulfur dioxide adsorption[98-100] (Equations 7.19).

$$2[Fe_2O_3]CaO + CCl_4 \xrightarrow{400°C} 2[Fe_2O_3]CaCl_2 + CO_2$$
$$2[Fe_2O_3]CaO + 2SO_2 \longrightarrow [Fe_2O_3]CaSO_4 + CaS$$

$$(7.19)$$

In the chlorocarbon case the presence of the iron oxide catalytically enhanced solid state ion–ion exchange deep into the CaO particle, and the formation of $CaCl_2$ on the surface did not serve to protect the inner core. These results have been interpreted in terms of reaction steps that are all thermodynamically favored, as shown in Figure 7.12. Upon reaction of $CCl_4$ with $[Fe_2O_3]CaO$ nanoparticles, $FeCl_3$ forms first, followed by $[FeCl_3]CaO$ undergoing $O^{2-}–Cl^-$ solid state exchange to give $[Fe_2O_3]CaCl_2$. A second approach of $CCl_4$ causes $FeCl_3$ to form again, and this mobile (fairly low-melting) $FeCl_3$ seeks out more CaO, perhaps at fissures or edges/corners of the CaO nanocrystal. Repetition of these steps leads to complete consumption of the CaO to form $CaCl_2$, such that this solid gas reaction becomes stoichiometric. This is a true catalytic effect of $Fe_2O_3$ since it has been shown that
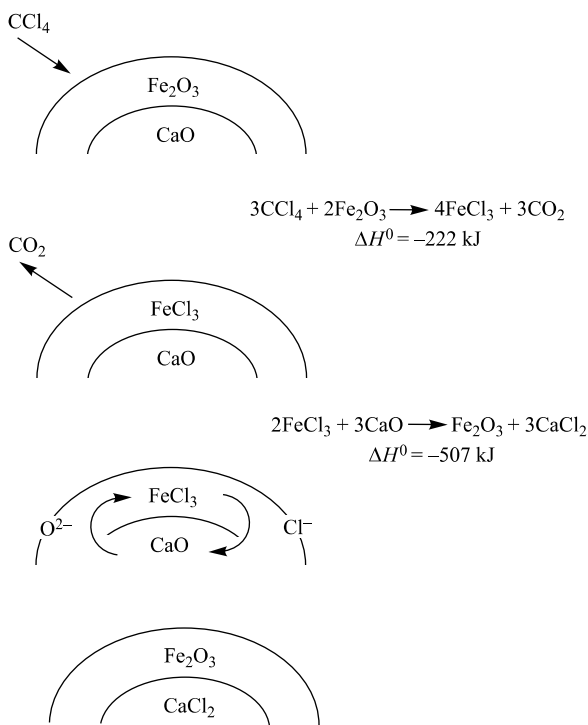


**FIGURE 7.12** Reaction steps of core–shell $Fe_2O_3$-coated nanoparticles of CaO with gaseous $CCl_4$. Reprinted with permission from *J. Catalysis*, **1998**, *180*, 24–35. Copyright 1998 Academic Press.[100]

even after extensive $CCl_4$ reaction (but less than stoichiometric), $Fe_2O_3$ was present, having been efficiently regenerated by the remaining CaO core.[101]

The catalytic behavior of transition metal oxides in this chemistry is quite common, as is the effectiveness for promoting the destructive adsorption of $CCl_4$. The order of catalytic reactivity was found to be V > Mn > Co > Fe > Zn > Ti > Cu > Ni > Cr oxides. $V_2O_5$ was found to be the very best catalyst and the results were highly reproducible.

Other destructive adsorption reactions in the 400–500°C range have also been reported, such as 1,3-dichlorobenzene and dimethyl methyl phosphonate (DMMP). However, some molecules were not susceptible to the catalytic action, such as trichloroethylene. Evidently, the catalytic effect of transition metal oxides depends a great deal on the intimate mechanistic details that are, of course, different for each adsorbate, and there is still little understanding of these reaction details. Even in the simplest case of $CCl_4$, the $Cl^-/O^{2-}$ solid state exchange step is poorly understood. It seems likely that the availability of multiple oxidation states for the catalyst material is beneficial, judging from the metal ions that are most effective (V, Mn, Co, Fe). Figure 7.13 illustrates a possible reaction sequence for vanadium catalysis.

It is interesting that this type of catalysis was found to function in several cases, namely, chlorocarbon dehalogenation/oxidation, organophosphorus compound adsorption/decomposition, and sulfur dioxide adsorption/immobilization. It appears that this phenomenon may be fairly widespread. It should be emphasized that both the nanocrystalline nature of the core oxide and the catalytic effect of the shell material are necessary. These two functions allow solid–gas reactions to be stoichiometric at moderate temperatures, and this opens up new opportunities in materials synthesis, chemistry, and catalysis.

Another interesting example of this stoichiometric chemistry (noncatalyzed) has been reported by Ying and coworkers.[102] Nanocrystalline ZnO was allowed to interact with hydrogen sulfide; a series of oxide particles were compared, and the order of efficiencies was ZnO > $ZnFe_2O_4$ > CaO > CdO > $PbO_2$ > $In_2O_3$ > $Cr_2O_3$ > CuO. The solid state chemistry that takes place is controlled by the rate with which



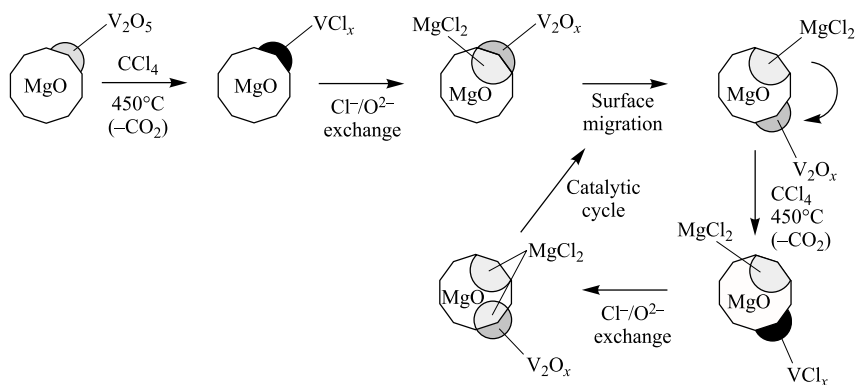**FIGURE 7.13**    Illustration of how $V_2O_5$ may catalyze $Cl^-/O^{2-}$ exchange in $CCl_4$ destructive adsorption. Reprinted with permission from *J. Catalysis*, **1998**, *180*, 24–35. Copyright 1998 Academic Press.[100]

$S^{2-}$ can penetrate into the ZnO crystal while $O^{2-}$ migrates to the surface, forming water. This reaction is thermodynamically favored, which helps to drive the ion–ion exchange (7.20).

$$ZnO + H_2S \longrightarrow ZnS + H_2O \qquad \Delta H_{rxn} = -77 \text{ kJ} \qquad (7.20)$$

Oxide–oxide exchange in nanocrystalline MgO has also been observed when a series of experiments with MgO–$H_2\,^{18}O$ were carried out.[103] Pulses of $H_2\,^{18}O$ were passed over the MgO particles at 300°C and surface hydroxyl groups exchanged; at 500°C surface lattice $O^{2-}$ exchanged, and at 700°C the inner lattice layer of $O^{2-}$ exchanged (7.21).



$$(7.21)$$
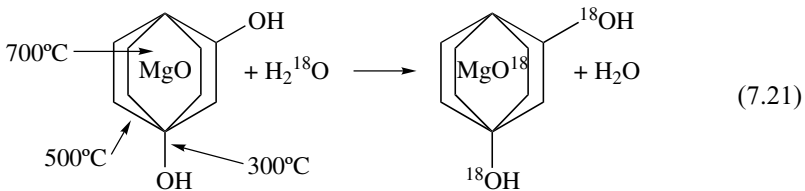
Since the nanocrystals were constructed of about 20 layers, and at 700°C about eight layers on average were exchanged, a large portion of all the ions were accessible to the $H_2\,^{18}O$ exchange.

### 7.4.2.3 Destructive Adsorption at Ambient Temperature

Another interesting feature of nanocrystalline metal oxides is that their surfaces interact very strongly with polar organic molecules, usually by dissociative chemisorption processes, and these are also examples of "destructive adsorption." This behavior has been observed with aldehydes, ketones, and alcohols on MgO or $Al_2O_3$ nanocrystals. Strongly exothermic interaction takes place. In the case of acetaldehyde on MgO, heat was given off and an orange color developed, and almost one mole of the aldehyde was destructively adsorbed for every mole of MgO employed. The surface chemistry that takes place involves the loss of the aldehydic proton, probably by initial coordination of the carbonyl oxygen to $Mg^{2+}$ followed by proton transfer to surface $O^{2-}$ [104] (7.22).



$$(7.22)$$
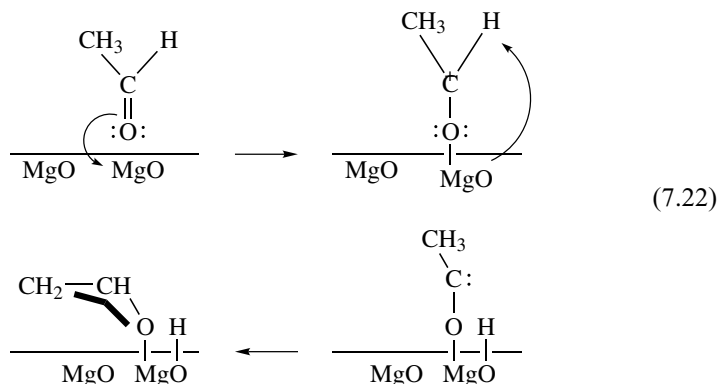
Studies by IR showed that the aldehyde C−H was diminished in intensity very quickly, and that lower energy $v$C=O and $v$C=C slowly appeared. It is likely that polymeric materials formed when the next molecule approached, since this amount of acetaldehyde destructively adsorbed is much larger than a monolayer (at least six layers in fact).

Destructive adsorption does not occur on high-surface-area carbon adsorbents. Therefore, nanocrystalline metal oxides, with their polar nature and high surface reactivities, bring a new useful dimension, and this has proven valuable in the quest to find protective measures against chemical and biological warfare.[105]

Chemical warfare agents are either organophosphonates or sulfur halides, and these classes of organic compounds strongly interact with nanocrystalline oxides such as MgO or CaO.[106,107]

$$CH_3—P(=O)—F$$
$$OCH(CH_3)C(CH_3)_3$$

$$ClCH_2CH_2SCH_2CH_2S$$
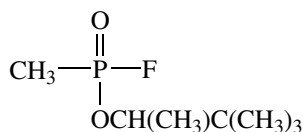
Soman (nerve agent)
**GD**
(3,3-dimethyl-2-butyl methylphosphonofluoridate)

Mustard Gas
**HD**
(2,2-dichloroethyl sulfide)

$$CH_3CH_2O—P(=O)(CH_3)—SCH_2CH_2N[CH(CH_3)_2]_2$$
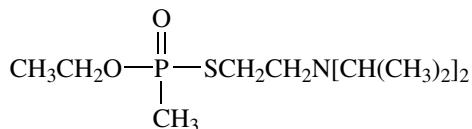
**VX**
(*O*-ethyl-*S*-[2-(diisopropylamino)]ethyl methylphosphonothiolate

Thus, Soman reacts with MgO nanoparticles by elimination of HF by the utilization of residual surface −OH groups, and complete degradation to nontoxic fragments occurred (7.23).
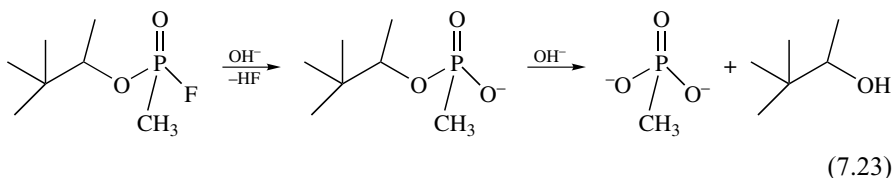


$$(7.23)$$

The HF formed would react with the basic MgO surface to produce $MgF_2$ and $H_2O$. In the case of VX, the thiolate group was displaced followed by the alkoxy group, again yielding an adsorbed $P(O)(O^-)_2CH_3$ methylphosphonic acid dianion. With

HD, a competition between dehydrohalogenation to yield a divinyl compound and chloride substitution by surface −OH was observed (7.24).



$$(7.24)$$
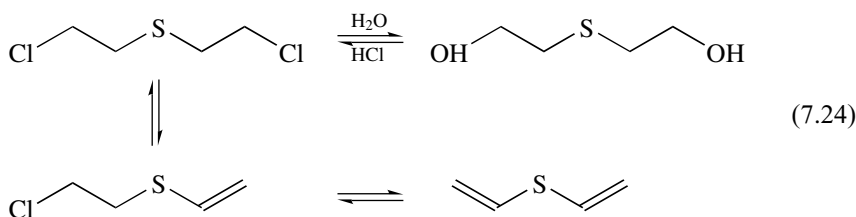
In all cases nontoxic residues were produced at room temperature, and the reaction rate was material-transfer limited. Thus, the thick oil VX was the slowest to react completely. Working with the less toxic substance paraoxon, as a mimic, more detailed surface chemistry analysis has been carried out on MgO and ZnO samples (7.25).



$$(7.25)$$
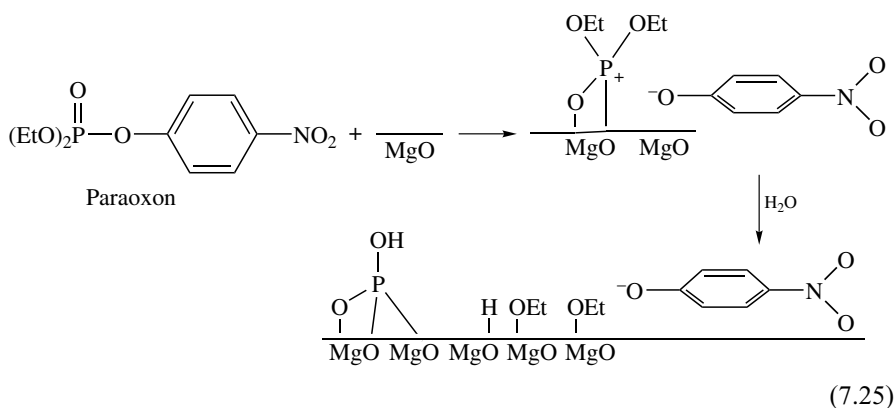
An immediate cleavage of the P−OAr bond to yield surface bound p-nitrophenoxy anion (yellow) takes place, and over time the ethoxy groups are also lost. The paraoxon is dismantled and immobilized in large amounts, and about one paraoxon molecule per $nm^2$ of MgO surface is destructively adsorbed (a monolayer). The presence of small amounts of water facilitates the detoxification of these warfare agents and their mimics. This suggests that surface hydroxide is important in promoting the desired chemistry. Indeed, in the case of CaO nanocrystals–water combinations, a catalytic dehydrohalogenation can take place.[107]

Bacteria (including spores and vegetative cells), viruses, and toxins are also destroyed by MgO nanocrystals when chlorine adducts are employed.[45] Figure 7.14 shows TEM photos of *Bacillus cereus* spores before treatment with MgO-Cl$_2$, and after. Note the accumulation of MgO nanocrystals on the interior of the spore. Clearly the outer membrane has been ruptured and the polar organic material (DNA, proteins) inside has been strongly adsorbed by the MgO. Although the mechanism

(a)                                      (b)
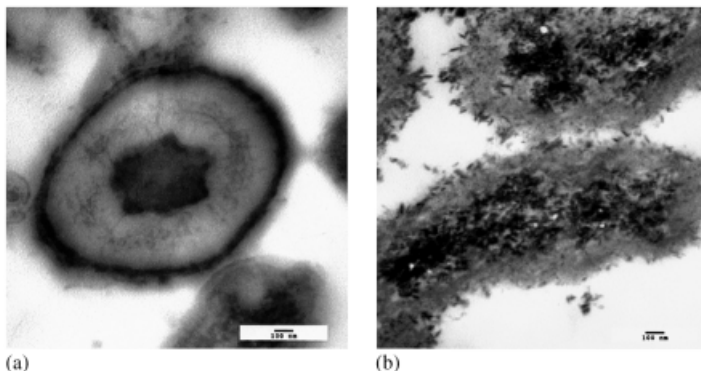
**FIGURE 7.14**   Transmission electron micrographs of *Bacillus cereus* spores (a) before, and (b) after exposure to dry nanoparticulate MgO–Cl$_2$ solid adduct.

by which bacterial spores are killed is unclear, it appears that the oxidizing power of the chlorine and the abrasive nature of the nanoparticles are both necessary features.

These and similar studies of *Bacillus globiggi*, *Bacillus subtilis*, and M$_2$ virus simulant are of significance for antibiological warfare measures (*B. cereus* and *B. globiggi* are mimics of anthrax spores), and may be of importance in insect control and other biological control measures.

### 7.4.3   Nanocomposite Polymers

It has been found that nanoparticulate solids and nanofibers added to polymers as "fillers" cause remarkable changes in properties; 200 nm clay platelets blended into a variety of polymers allows better mechanical properties (stiffer, higher modulus, dent resistant) in strength and hardness. Although there are many reports[108] of such changes, and nanoplatelets, particles, or fibers all produce noticeable effects, understanding of this phenomenon is lacking. It is known that the properties of the resultant composite depend on filler concentration and the particle size and shape of the filler, as well as the type of interaction with the polymer matrix. Thus, the theory of filler reinforcement of polymers predicts the formation of a boundary layer of a matrix material on the surface of the filler.[109] A stronger interaction should produce a boundary layer of greater thickness, and the polymer molecules in the boundary layer differ from the bulk due to decreased mobility, resulting in a higher glass transition. If the filler particles are closely spaced, all of the polymer molecules may be located in the boundary layers. Filler particles in the nanometer range have a large surface-to-volume ratio and may have stronger interactions with the polymer matrix. Once again the enhanced chemical reactivity of nanoparticles versus microparticles has importance. Additionally, the changed physical properties of the nanoparticles can be significant. Thus, Petrovic and coworkers[109] have produced transparent

polyurethane $SiO_2$ nanoparticle composites, since the nanoparticles are much smaller than the wavelength of light.

In addition, the interparticle distance in filled materials is naturally a function of particle diameter and concentration. Simple calculations show that at 10% volume concentration, interparticle distance will be about one particle diameter; that is, if filled with 1 mm particles each will be separated from the next by 1 mm, whereas if filled with 1 nm particles, each particle will be separated from the next by 1 nm. Certainly in the 1 nm case the particles will have an effect on each other, and will create boundary layers that engulf nearly the entire polymer.[110]

Many property changes caused by nanofillers have been reported (hardness, scratch resistance, toughness, etc.), and this is an important emerging area in the field of organic–inorganic composites.[15,111,112]

### 7.4.4 Fluids, Inks, and Dyes

Organic dye molecules in nanoparticle form allow for higher performance at lower concentrations. They give less light scatter and sharper absorption in dye and ink applications.[113]

Ferrofluids consist of magnetic particles suspended (usually by ligated surfactant molecules) in oil or water. The particles are individual permanent magnets, and when an external magnetic field is applied the fluid becomes magnetized; it then exhibits unusual fluid mechanical phenomena. Such fluids can suspend larger particles. Also, they can serve as contaminant exclusion seals, vacuum seals, and dampers in stepper motors. With improvements and lower price, nanoferrofluids might find applications as cooling fluids and nanoscale bearings, and in magnetically controlled heat conductivity.[114]

### 7.4.5 Block Copolymers and Dendrimers

Another truly fascinating area in nanostructured materials in chemistry is the manipulation of three-dimensional structures of immiscible components of block copolymers. These materials have similarities to micelle and vesicle structures; however, the two copolymers are covalently bound to one another as A-(A)$_n$-A-B-(B)$_n$-B where A and B are polymer chains that are either immiscible or have quite different chemical/physical properties from each other. Rodcoil molecules are made up of a polymer chain (A) that is fairly rigid or rodlike, which is connected to a polymer that readily forms coils. These diblock polymers can form a wide array of structures on the nanometer scale, due to intermolecular (noncovalent, supramolecular) interactions.[115] The possibilities for useful functional materials seems almost endless.

A specific example has been given by Wooley[116] and coworkers when an amphiphilic diblock polymer of poly($\varepsilon$-caprolactone)-b-poly(acrylic acid) (PCL-b-PAA) was manipulated to form core-shell nanoparticulate domains (which can serve as mimics of globular proteins). The diblock polymers self-assembled into polymer micelles, and after cross-linking of the outer shell portion, the PCL core was

removed by hydrolysis, leaving a "nanocage." These hollow nanoparticles are expected to allow for high guest loading or to exhibit other unusual properties.

Dendrimers are more well defined than polymers, and are three-dimensional highly branched macromolecular structures whose physical and chemical properties can be controlled over a wide temperature range. Indeed, dendrimers are molecules that are nanoscale in size, generally with spheroidal dimensions. A two-dimensional representation of a fifth-generation dendrimer[117] is shown in Figure 7.15. The
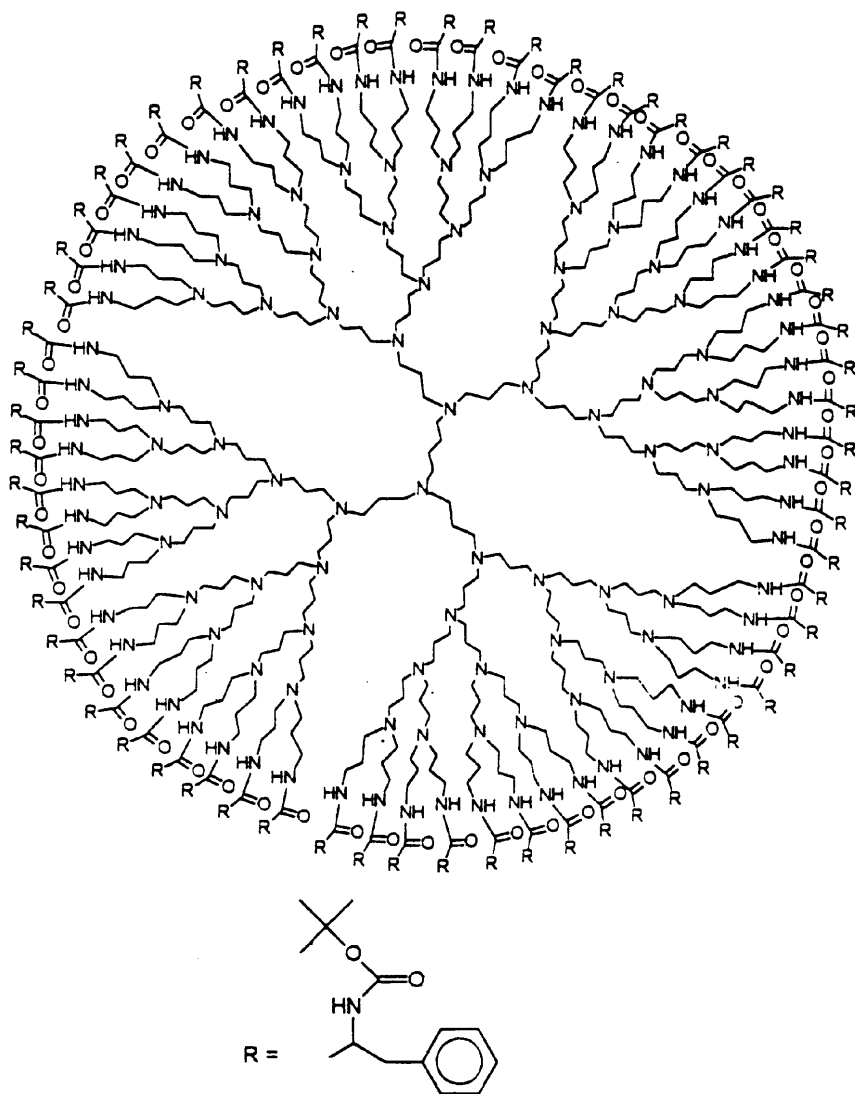


**FIGURE 7.15**   Two-dimensional representation of modified fifth-generation dendrimer. Reprinted with permission from *Langmuir*, **2000**, *16*, 3884–3892. Copyright 2000 American Chemical Society.[117]

properties of these nanostructures can be controlled and future applications look bright.

### 7.4.6    Nanocrystal Superlattices

This tour of nanoparticle structures and chemistry is nearly at an end. It is appropriate now to consider one further aspect where chemical manipulation of nanoparticle surfaces can lead to controlled aggregation into "supercrystals," also termed nanocrystal superlattices. Just as atoms or molecules can come together to form crystals, certain nanocrystals can come together to form crystals. As is often the case, gold has led the way, and two- and three-dimensional superlattices have been reported by several groups.[118–123]

In one study, gold particles were prepared by an inverse micelle of didodecyldimethylammonium bromide (DBAB) in toluene when gold ions were reduced by sodium borohydride.[122] By addition of dodecane thiol the DDAB was replaced and then removed by ethanol wash. In this way the gold particles were ligated by $CH_3(CH_2)_{11}SH$, resulting in a dark blue toluene-soluble material that readily crystallized into two- and three-dimensional superlattices. These crystals could be heated up and redissolved to form single particles (red), and slowly cooled to reform the aggregates (blue). This process can be followed by UV–visible spectroscopy.

The properties of these superlattice crystals are yet to be thoroughly investigated. Their collective properties could be important in optical switching, information storage, and other areas. However, at this time perhaps the most important task is the investigation of their physical and chemical nature, for example, lattice energies, specific heats, melting points, and exact structures.

### 7.5    CONCLUSIONS

The realization that nanoscale materials possess unique chemical properties allows an even greater appreciation of the future importance of the nanotechnology field.

### REFERENCES

1a. K. J. Klabunde, J. Stark, O. Koper, C. Mohs, D. Park, S. Decker, Y. Jiang, I. Lagadic, D. Zhang, *J. Phys. Chem.*, **1996**, *100*, 12142.

1b. K. J. Klabunde, S. Decker, E. Lucas, O. Koper, in *International Symposium on Cluster and Nanostructure Interfaces*, World Scientific Pub., New Jersey, Richmond, VA, P. Jena, S. N. Khanna, B. K. Rao (editors) Oct. **1999**.

 2. D. F. Shriver, P. W. Atkins, C. H. Langford, *Inorganic Chemistry*, 2nd edition, W. H. Freeman, New York, **1994**.

 3. W. M. H. Sachtler, *Ber. Bunsenges.*, **1995**, *99*, 1295.

 4. C. R. Henry, *Appl. Surf Sci.*, **2000**, *164*, 252.

 5. R. J. Puddephatt, *Met. Clusters. Chem.*, **1999**, *2*, 605.

6. B. M. Trost, *Angew. Chem.*, *Int. Ed. Eng.*, **1995**, *34*, 259.

7. B. M. Choudary, M. L. Kantam, L. P. Santhi, *Catal. Today*, **2000**, *57*, 17.

8. M. Knickebein, S. Wang, S. J. Riley, *J. Chem. Phys.*, **1990**, *93*, 94.

9. K. J. Klabunde, *Free Atoms*, *Clusters*, *and Nanoscale Particles*, Academic Press, San Diego, CA, **1994**, *126*, 127.

10. L. Bonneviot, G. L. Haller, *J. Catal.*, **1991**, *130*, 359.

11. M. Boudart, A. W. Aldag, J. E. Benson, N. A. Dougharty, G. G. Harkins, *J. Catal.*, **1966**, *6*, 92.

12. D. J. C. Yates, J. H. Sinfelt, *J. Catal.*, **1967**, *8*, 348.

13. S. C. Davis, K. J. Klabunde, *Chem. Rev.*, **1982**, *82*, 153.

14. D. I. Hagen, G. A. Somorjai, *J. Catal.*, **1976**, *41*, 466.

15. J. E. Mark, *Heterogen. Chem. Rev.*, **1996**, *3*, 307.

16. F. G. Gault, *Adv. Catal.*, **1981**, *30*, 1.

17. C. Corrolleur, F. G. Gault, D. Juttard, G. Maire, J. M. Muller, *J. Catal.*, **1972**, *27*, 466.

18. C. Corrolleur, S. Corrolleur, F. G. Gault, *J. Catal.*, **1972**, *24*, 385.

19. C. Corrolleur, D. Tomanova, F. G. Gault, *J. Catal.*, **1972**, *24*, 201.

20. K. J. Klabunde, Y. X. Li, B. J. Tan, *Chem. Mater.*, **1991**, *3*, 30.

21a. K. J. Klabunde, H. F. Efner, T. O. Murdock, R. Ropple, *J. Am. Chem. Soc.*, **1976**, *98*, 1021.

21b. K. J. Klabunde, S. C. Davis, H. Hattori, Y. Tanaka, *J. Catal.*, **1978**, *54*, 254.

22. V. Akhmedov, K. J. Klabunde, *J. Mol. Catal.*, **1988**, *45*, 193.

23. G. Vitulli, E. Pitzalis, A. Verazzani, P. Alessandra, P. Pertici, P. Slavador, G. Martra, *Mater. Sci.*, *Forum*, **1997**, part 2, "Synthesis and Properties of Mechanically Alloyed and Nanocrystalline Materials", p. 235.

24. Y. Wang, H. Liu, N. Toshima, *J. Phys. Chem.*, **1996**, *100*, 19533.

25. P. Lu, J. Dong, N. Toshima, *Langmuir*, **1999**, *15*, 7980.

26. Y. Wang, N. Toshima, *J. Phys. Chem.*, **1997**, *101*, 5301.

27. W. Yu, Y. Wang, H. Liu, W. Zhang, *J. Mol. Catal.*, **1996**, *112*, 105.

28. H. Bonnemann, G. Braun, W. Brijoux, R. Brinkman, A. Schulz, K. Seevogel, K. Siepen, *J. Organomet. Chem.*, **1996**, *520*, 143.

29. H. Bonnemann, G. A. Braun, *Angew. Chem.*, *Int. Ed. Eng.*, **1996**, *35*, 1992.

30. D. De. Caro, J. S. Bradley, *Langmuir*, **1997**, *13*, 3067.

31. M. Haruta, N. Yamada, T. Kobayashi, S. Iijima, *J. Catal.*, **1989**, *115*, 301.

32. G. K. Bethke, H. H. Kung, *Appl. Catal. A General*, **2000**, *194–195*, 43.

33. M. Valden, S. Pak, X. Lai, D. W. Goodman, *Catal. Lett.*, **1998**, *56*, 7.

34. J. J. Watkins, T. J. McCarthy, *Chem. Mater.*, **1995**, *7*, 1991.

35. H. Hahn, in *Processing and Catalytic/Chemical Properties of Nano Structural Materials*, Lahaina, Hawaii, January 2000, United Engineering Foundation, New York, **2000**; web site: www.engfnd.org; conf. chairs M. L. Trudeau, J. Ying, V. Provenzano.

36. J. J. McCue, J. Y. Ying, in *Proccssing and Catalytic/Chemical Properties of Nano Structural Materials*, Lahaina, Hawaii, January 2000, United Engineering Foundation, New York, **2000**; web site: www.engfnd.org; conf. chairs M. L. Trudeau, J. Ying, V. Provenzano.

37. C. P. Mehnert, J. Y. Ying, *J. Chem. Soc., Chem. Commun.*, **1997**, 2215.

38. R. V. Kumar, Y. Diamant, A. Gedanken, *Chem. Mater.*, **2000**, *12*, 2301.

39. K. S. Suslick, M. Fang, M. Mdleleni, T. Hyeon, J. Ries, *Book of Abstracts*, *213th ACS National Meeting*, San Francisco, **1997**, INOR-629.

40. K. S. Suslick, M. M. Fang, T. Hyeon, J. Ries, *Book of Abstracts*, *213th ACS National Meeting*, San Francisco, **1997**, INOR-267.

41. S. E. Deutsch, G. Mestl, H. Knozinger, B. C. Gates, *J. Phys. Chem.*, **1997**, *101*, 1374.

42. A. M. Ferrari, K. M. Neyman, M. Mayer, M. Staufer, B. C. Gates, N. Rosch, *J. Phys. Chem. B*, **1999**, *103*, 5311.

43. C. Carnes, K. J. Klabunde, Unpublished work.

44. N. Sun, K. J. Klabunde, *J. Catal.*, **1999**, *185*, 506.

45. N. Sun, K. J. Klabunde, *J. Am. Chem. Soc.*, **1999**, *121*, 5587.

46. T. R. Thurston, J. P. Wilcoxon, *J. Phys. Chem.*, **1999**, *103*, 11.

47. A. Tschope, J. Y. Ying, *Nanostruct. Mater.*, **1994**, *4*, 617.

48. S. C. Emerson, C. F. Coote, H. III. Boote, J. C. Tufts, R. LaRocque, W. R. Moser, *Surf. Sci. Catal.*, **1998**, *118*, 773.

49. M. Hino, K. Arata, *Chem. Lett.*, **1979**, 1359.

50. K. Arata, *Adv. Catal.*, **1990**, *37*, 165.

51. K. Tanabe, H. Hattori, T. Yamaguchi, *Crit. Rev. Surf. Chem.*, **1990**, *1*, 1.

52. A. F. Bedilo, K. J. Klabunde, *Nanostruct. Mater.*, **1997**, *8*, 119.

53. A. F. Bedilo, K. J. Klabunde, *J. Catal.*, **1998**, *176*, 448.

54. R. Richards, W. Li, S. Decker, C. Davidson, O. Koper, V. Zaikovski, A. Volodin, T. Rieker, K. J. Klabunde, *J. Am. Chem. Soc.*, **2000**, *122*, 4921.

55. L. Wöste, in *International Symposium on Cluster and Nanostructure Interfaces*, World Scientific Pub., New Jersey, Richmond, VA, P. Jena, S. N. Khanna, B. K. Rao (editors) Oct. **1999**.

56. R. Q. Hwang, M. C. Bartelt, *Chem. Rev.*, **1997**, *97*, 1063.

57. N. Ikemiya, A. A. Gewirth, *J. Phys. Chem B.*, **2000**, *104*, 873.

58. S. J. Stranick, M. M. Kamna, P. S. Weiss, *Surf. Sci.*, **1995**, *338*, 41.

59. S. J. Stranick, M. M. Kamna, P. S. Weiss, *Science*, **1994**, *266*, 99.

60. E. I. Altman, R. J. Colton, *Phys. Rev. B*, **1993**, *48*, 18244.

61. T. Hashizume, T. Sakurai, *Vac. Sci. Technol. B*, **1994**, *12*, 1992.

62. H. Imamura, T. Nobunaga, M. Kawahigashi, S. Tsuchiya, *Inorg. Chem.*, **1984**, *23*, 2509.

63. D. M. Cox, in *Interagency Working Group in Nanoscience Engineering and Technology (IWGN) Workshop Report: Nanotechnology Research Directions*; *Vision for Nanotechnology R and D in the Next Decade*, M. C. Roco, R. S. Williams, P. Alivisatos (editors), Published by Int. Tech. Research Institutes, WTEC Division, Loyola College, **1999**, p. 138.

64. M. Mitov, A. Popov, J. Dragieva, *Colloids Surf. A. Physicochem. Eng. Aspects*, **1999**, *149*, 413.

65. M. Mitov, A. Popov, I. Dragieva, *J. Appl. Electrochem.*, **1999**, *29*, 59.

66. I. Dragieva, in *Nano-Crystalline and Thin Film Magnetic Oxides*, I. Nedkov, M. Ausloos (editors), Kluwer Academic Publishers, Dordrecht, **1999**, pp. 165–176.

67. D. M. Cox, in *Interagency Working Group in Nanoscience Engineering and Technology (IWGN) Workshop Report: Nanotechnology Research Directions*; *Vision for Nanotechnology R and D in the Next Decade*, M. C. Roco, R. S. Williams, P. Alivisatos (editors), Published by Int. Tech. Research Institutes, WTEC Division, Loyola College, **1999**, p. 137, 138.

68. A. Kuperman, S. Nadimi, S. Oliver, G. A. Ozin, J. M. Garces, M. M. Olken, *Nature*, **1993**, *365*, 239.

69. C. T. Kresge, M. E. Leonowicz, W. J. Roth, J. C. Vartuli, J. S. Beck, *Nature*, **1992**, *359*, 710.

70. J. S. Beck, J. C. Vartuli, W. J. Roth, M. E. Leonowicz, K. D. Schmitt, C. T. W. Chu, D. H. Olsen, E. W. Shepard, S. B. McCullen, J. B. Higgins, J. L. Schlender, *J. Am. Chem. Soc.*, **1992**, *114*, 10834.

71. H.-P. Lin, C.-Y. Mon, *Science*, **1996**, *273*, 765.

72. Q. Huo, D. I. Margolese, U. Ciesla, P. Feng, T. E. Gier, P. Siegar, R. Leon, P. M. Petroff, F. Schuth, G. D. Stucky, *Nature*, **1994**, *368*, 317.

73. J. Sun, J. Y. Yin, *Nature*, **1997**, *389*, 704.

74. T. J. Pinnavaia, H. Kim, *NATO ASI Ser. C*, **1992**, *352*, 79.

75. A. Clearfield, *Adv. Catal. Nanostruct. Mater.*, Moser, William R., (editor), Academic Press, San Diego, CA, **1996**, p. 345.

76. R. F. Curl, R. E. Smalley, *Science*, **1988**, *242*, 1017.

77. R. F. Kroto, *Angew. Chem.*, *Int. Ed. Eng.*, **1992**, *31*, 111.

78. M. S. Dresselhaus, G. Dresselhaus, *Annu. Rev. Mater. Sci.*, **1995**, *25*, 487.

79. C. W. Jones, W. J. Koros, *Carbon*, **1994**, *32*, 1419.

80. M. B. Rao, S. Sircar, *Gas Separation and Purification*, **1993**, *7*, 279.

81. C. N. R. Rao, B. C. S. Kumar, A. Govindaraj, *Chem. Commun.*, **1997**, 1581.

82. O. Lourie, O. M. Cox, H. D. Wanger, *Phys. Rev. Lett.*, **1998**, *81*, 1638.

83. R. D. Rieke, R. M. Wehmeyer, T. C. Wu, G. W. Ebert, *Tetrahedron*, **1989**, *45*, 443.

84. P. Cintas, *Activated Metals in Organic Synthesis*, CRC Press, Boca Raton, FL, **1993**, p. 212.

85. R. D. Rieke, *Science*, **1989**, *246*, 1260.

86. Ch. Elschenbroich, A. Salzer, *Organometallics*, *A Concise Introduction*, VCH, Weinheim, **1992**, *2*, 41.

87. Y. Imizu, K. J. Klabunde, *Inorg. Chem.*, **1984**, *23*, 3602.

88. K. J. Klabunde, A. J. Whetten, *J. Am. Chem. Soc.*, **1986**, *108*, 6529.

89. E. P. Kundig, C. Perret, *Helv. Chim. Acta*, **1981**, *64*, 2606.

90. W. Oppolzer, E. P. Kundig, P. M. Bishop, C. Perret, *Tetrahedron Lett.*, **1982**, *23*, 3901.

91. K. J. Klabunde, G. Cardenas-Trivino, in *Active Metals Preparation*, *Characterization*, *Applications*, Chap. 6, A. Fürstner (editor), VCH, Weinheim, **1996**, p. 237.

92. D. J. Trevor, D. M. Cox, A. J. Kaldor, *J. Am. Chem. Soc.*, **1990**, *112*, 3742.

93. R. L. Whetten, D. M. Cox, D. J. Trevor, A. Kaldor, *J. Phys. Chem.*, **1985**, *89*, 566.

94. M. A. El-Sayed, *J. Phys. Chem.*, **1991**, *95*, 3898.

95. L. Song, M. A. El-Sayed, *Chem. Phys. Lett.*, **1988**, 281.

96.  J. V. Stark, K. J. Klabunde, *Chem. Mater.*, **1996**, *8*, 1904.

97.  J. V. Stark, K. J. Klabunde, *Chem. Mater.*, **1996**, *8*, 1913.

98.  K. J. Klabunde, A. Khalee, D. Park, *High Temp. Mater. Sci.*, **1995**, *33*, 99.

99.  S. Decker, K. J. Klabunde, *J. Am. Chem. Soc.*, **1996**, *118*, 12465.

100. Y. Jiang, S. Decker, C. Mohs, K. J. Klabunde, *J. Catal.*, **1998**, *180*, 24, 35.

101. S. Decker, I. Lagadic, K. J. Klabunde, A. Michalowicz, J. Mosocovici, *Chem. Mater.*, **1998**, *10*, 674.

102. J. T. Sweeney, J. Y. Ying, in *Processing and Catalytic/Chemical Properties of Nano Structural Materials*, Lahaina, Hawaii, January 2000, United Engineering Foundation, New York, **2000**; web site: www.engfnd.org; conf. chairs M. L. Trudeau, J. Ying, V. Provenzano.

103. Y. X. Li, K. J. Klabunde, *Chem. Mater.*, **1992**, *4*, 611.

104. A. Khaleel, P. N. Kapoor, K. J. Klabunde, *Nanostruct. Mater.*, **1999**, *11*, 459.

105. E. M. Lucas, K. J. Klabunde, *Nanostruct. Mater.*, **1999**, *12*, 179.

106. G. W. Wagner, P. W. Bartram, O. Koper, K. J. Klabunde, *J. Phys. Chem. B*, **1999**, *103*, 3225.

107. G. W. Wagner, O. B. Koper, E. Lucas, S. Decker, K. J. Klabunde, *J. Phys. Chem. B*, **2000**, *104*, 5118.

108. E. C. Lee, in *Commercialization of Nanostructured Materials*, Wyndam Miami Beach, Miami, FL, Knowledge Foundation, Boston, **2000**.

109. Z. S. Petrovic, I. Javnis, A. Waddon, G. J. Banhegyi, *Appl. Polymer. Sci.*, **2000**, *76*, 133.

110. J. T. Koberstein, *J. Polym, Sci. Polym. Phys. Ed.*, **1983**, *21*, 1439.

111. R. W. Siegel, *ACS Polym. Mater. Sci. Eng.*, **1995**, *73*, 26.

112. G. A. Ozin, A. Stein, G. D. Stucky, J. P. Goder, in *Inclusion Phenomena and Molecular Recognition*, *Proceedings*, *5th International Symposium*, *1988*, J. L. Atwood (editor), Plenum, New York, **1990**, p. 379.

113. J. E. Mendell, *Interagency Working Group in Nanoscience Engineering and Technology (IWGN) Workshop Report: Nanotechnology Research Directions*; *Vision for Nanotechnology R and D in the Next Decade*, M. C. Roco, R. S. Williams, P. Alivisatos (editors), Published by Int. Tech. Research Institutes, WTEC Division, Loyola College, **1999**, p. 71.

114. R. E. Rosenweig, *Ferrohydrodynamics*, Cambridge University Press, New York, **1995**.

115. S. I. Stupp, M. U. Pralle, G. N. Tew, L. Li, M. Sayor, E. R. Zubarev, *MRS Bull.*, **2000**, *25*, 42.

116. Qi. Zhang, E. E. Remsen, K. L. Wooley, *J. Am. Chem. Soc.*, **2000**, 3642.

117. X. Zhang, M. Wilhelm, J. Klein, M. Pfaadt, E. W. Meijer, *Langmuir*, **2000**, *16*, 3884.

118. H. Weller, *Angew. Chem.*, *Int. Ed. Eng.*, **1996**, *35*, 1079.

119. R. P. Andres, J. D. Bielefeld, J. I. Henderson, D. B. James, V. R. Lolagunta, W. J. Kubiak, W. J. Mahoney, R. G. Osifchin, *Science*, **1996**, *273*, 1690.

120. C. B. Murray, C. R. Kagan, M. G. Bawendi, *Science*, **1995**, *270*, 1335.

121. R. L. Whetten, J. Bentley, N. D. Evans, K. B. Alexander, *Adv. Mater.*, **1998**, *10*, 808.

122. X. M. Lin, C. M. Sorenson, K. J. Klabunde, *Chem. Mater.*, **1999**, *11*, 198.

123. J. P. Wilcoxon, R. L. Willamson, R. J. Banghman, *Chem. Phys.*, **1993**, *98*, 9933.

# 8 Specific Heats and Melting Points of Nanocrystalline Materials

OLGA KOPER AND SLAWOMIR WINECKI

Nanoscale Materials, Inc., Manhattan, Kansas

## 8.1 INTRODUCTION

Specific heat and melting temperature are considered as the most fundamental thermal properties of any solid material. Historically the successful explanation of specific heats of solids, accomplished during the first decades of the twentieth century, was a foundation of modern solid state physics. Today specific heats of solids are considered to be quite well understood for bulk materials. As we will learn, this is not the case for nanocrystalline materials.

Specific heat and melting temperature were extensively studied for most known solids and the results of these measurements are tabulated in various publications. In the case of nanoparticles, specific heats and melting points are still a subject of ongoing research due to interesting effects observed for these novel materials. This chapter is intended to give a brief introduction to these subjects.

## 8.2 SPECIFIC HEAT

Specific heat is the characteristic quantity of a material that describes the amount of heat necessary to increase the temperature of a solid. It is defined as

$$C = \frac{\Delta Q}{\Delta T \times m} \tag{8.1}$$

where $\Delta Q$ is an amount of heat required to increase the temperature by $\Delta T$, and $m$ is the mass of the sample. Depending on the field of application, different units are

used to express specific heat, with the most common $J\,kg^{-1}\,K^{-1}$ or $cal\,g^{-1}\,K^{-1}$. In fact, the specific heat of water was used to define the calorie as a unit of energy; the specific heat of water at ambient conditions is $1\,cal\,g^{-1}\,K^{-1}$. Frequently, the specific heat is not given per unit mass, but rather per mole of the material. This convention changes units of specific heat to $J\,mol^{-1}\,K^{-1}$ or equivalent.

The specific heat of solids is usually measured at a constant pressure $p$, such as atmospheric pressure, and is represented by the symbol $C_p$. The theoretical specific heat of solids is most often calculated for constant volume $v$, and is denoted by $C_v$. The difference between $C_p$ and $C_v$ for solids and liquids (but not for gases) is very small and often both quantities are used in the literature interchangeably.

To introduce the features of specific heats of nanocrystalline materials, a brief introduction to specific heats of polycrystalline materials is given. Then selected experimental results for specific heats of nanocrystalline materials are presented.

### 8.2.1  Specific Heats of Polycrystalline Materials

#### 8.2.1.1  *Specific Heats of Polycrystalline Materials at Intermediate and High Temperatures*

*Dulong–Petit Law*   P. Dulong and A. Petit observed in 1819 that specific heats of solids at room temperature (expressed in $J\,g^{-1}\,K^{-1}$) differ widely from one solid to another, but the molar specific heats (expressed in $J\,mol^{-1}\,K^{-1}$) are nearly the same and approach a common value of $26\,J\,mol^{-1}\,K^{-1}$. This observation was described theoretically by F. Richarz in 1893. His argument was similar to the kinetic theory of gases, which states that the molar specific heat of a monoatomic gas equals $3R/2$ ($R = 8.31\,J\,mol^{-1}\,K^{-1}$ is the gas constant) and is the result of the kinetic energy of atoms. Richarz postulated that for solids not only kinetic but also potential energy associated with lattice binding needs to be considered. Therefore, for solids the molar specific heat is equal to $3R$ ($24.9\,J\,mol^{-1}\,K^{-1}$). According to the Dulong–Petit law, the specific heat of a solid at any temperature is

$$C_v = \frac{3R}{A} \tag{8.2}$$

where $A$ is the molecular weight ($g\,mol^{-1}$).

The Dulong–Petit law is quite accurate at room temperature with a few important exceptions, notably for diamond, germanium, and silicon, which have much smaller specific heats than predicted. Furthermore, specific heats of solids decrease sharply as the temperature is lowered and vanish at absolute zero ($0\,K$). This behavior can only be described by quantum theories.

*Einstein Theory*   A. Einstein in 1907[1] developed the first quantum theory of specific heat. In this theory each atom of a solid oscillates with a certain frequency

and the energy associated with this oscillation is responsible for the specific heat. The specific heat of a solid according to the Einstein model can be expressed as

$$C_v = 3R\left(\frac{\theta_E}{T}\right)^2 \frac{e^{\theta_E/T}}{(e^{\theta_E/T} - 1)^2}$$
(8.3)

where $T$ is the absolute temperature, $\theta_E$ is the Einstein temperature, and $R$ is the gas constant. The Einstein temperature is treated as an adjustable parameter that makes Equation (8.3) fit experimental values of specific heat.

*Debye Theory* P. Debye in 1912[2] developed another quantum theory for specific heats of solids. In his approach, as in the Einstein model, the energy associated with atomic oscillations is responsible for specific heat. However, in the Debye model the oscillations, known as phonons, have a continuous frequency spectrum instead of a single value and propagate throughout the continuous medium of a solid. The specific heat of a solid according to the Debye model can be expressed as

$$C_v = 9R\left(\frac{T}{\theta_D}\right)^3 \int_0^{\theta_D/T} \frac{(\theta_D/T)^4 e^{\theta_D/T}}{(e^{\theta_D/T} - 1)^2} d\left(\frac{\theta_D}{T}\right)$$
(8.4)

where $\theta_D$ is the Debye temperature, used as an adjustable parameter that makes Equation (8.4) fit experimental values.

Of the models described above, the Debye model is used most frequently and provides a more realistic physical description of specific heat. The Einstein model is too simple, although historically it was the first quantum mechanical description of specific heat at low temperatures. Figure 8.1 illustrates theoretical values of specific heat obtained from both models as well as experimental values for silver.[3] At high temperatures both models reasonably reproduce experimental data, assuming that proper values of $\theta_E$ and $\theta_D$ are used. However, at low temperatures only the Debye model is adequate.

### 8.2.1.2 Specific Heats of Polycrystalline Materials at Low Temperatures
Studying specific heats at very low absolute temperatures (typically 0 to 30 K) allows separation of the different physical mechanisms and application of a simpler theoretical description. It has been recognized that at these low temperatures two components are responsible for specific heats of solids. These are the lattice vibration contributions as described in the Debye model, and the electronic contribution associated with energy stored in electronic degrees of freedom. The electronic contributions was theoretically described by a Sommerfeld model that describes the properties of a free electron gas and assumes that energy stored by electrons is a
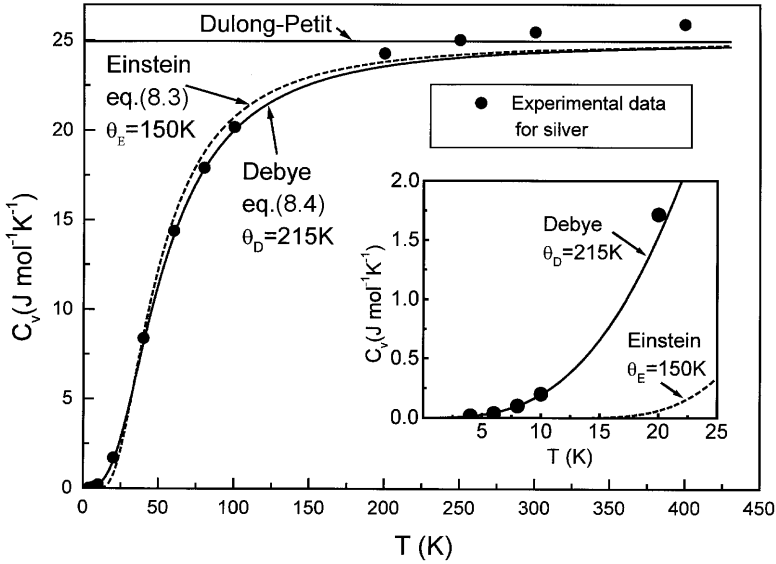
**FIGURE 8.1** Theoretical values of specific heat ($C_v$) obtained from the Einstein and Debye models and experimental values for silver. The inset shows the failure of the Einstein model at low temperatures. Experimental data from reference 3.

source of specific heat. The most important conclusion of this model is that the specific heat ($C_v$) is proportional to the first power of the absolute temperature:

$$C_v = \frac{\pi^2 k_B^2 T}{3\delta} \tag{8.5}$$

where $k_B$ is the Boltzmann constant ($k_B = 1.38 \times 10^{-23}\,\mathrm{J\,K^{-1}}$), $T$ is the absolute temperature, and $\delta$ is an average spacing between energy levels at the Fermi surface. Comparison between experimental measurements and predictions, based on the free electron gas expression (8.5), confirms a linear temperature dependence of the specific heat, but the absolute values for some metals are often under- or over-estimated by a factor of 30.[4] Due to this discrepancy, the Sommerfeld expression for electronic contribution to specific heat is often used as

$$C_v = \gamma T \tag{8.6}$$

where $\gamma$ (known as the Sommerfeld constant) is treated as an adjustable parameter to fit experimental data.

The second contribution to the specific heat at low temperatures is attributed to vibrations of atoms (ions) within a crystalline lattice, as in the Debye model. At very

low temperatures, the Debye form of specific heat (Equation 8.4) can be approximated by

$$C_v = \left(\frac{12\pi^4}{5}\right)nk_B\left(\frac{T}{\theta_D}\right)^3 \tag{8.7}$$

where $\theta_D$ is the Debye temperature. The specific heat at these low temperatures is proportional to the third power of the absolute temperature.

Since the specific heat at low temperatures contains both the electronic and lattice vibration contributions, frequently the specific heat of a solid is expressed as

$$C_v = \gamma T + BT^3 \tag{8.8}$$

where $B$ is a constant describing the relative strength of the lattice contribution. Expression (8.8) is referred to as the Debye–Sommerfeld model. The validity of this approach and the importance of both contributions to specific heat can be easily confirmed by plotting $C_p/T$ as a function of $T^2$. If the specific heat obeys expression (8.8), experimental points should form a straight line. The intercept on such a line gives the Sommerfeld constant $\gamma$, while the slope gives the relative strength of lattice contribution, $B$.

### 8.2.2  Specific Heats of Nanocrystalline Materials

Specific heats of nanocrystalline materials have been studied by many researchers. In most instances experimental measurements indicated that nanoparticles exhibit enhanced specific heat as compared to the bulk material. The sections below present some of these results at high and low temperature ranges.

*Intermediate and High Temperatures*  The work of J. Rupp and R. Birringer[5] is a good example of an experimental investigation into specific heat effects associated with nanometer-sized particles at high temperatures. The authors studied nanometer-sized crystalline copper and palladium with crystallite sizes (obtained by X-ray diffraction) of 8 nm and 6 nm, respectively. Both samples were pressed into pellets and the specific heat was determined using a differential scanning calorimeter. Specific heat was measured over a temperature range from 150 K to 300 K and the results are shown in Figure 8.2. For both metals, the specific heat of nanocrystalline particles is larger than for polycrystalline metals. In the case of palladium this enhancement varies between 29% and 53%, and for copper between 9% and 11%, depending on the temperature. This work shows a general enhancement of specific heat at intermediate and high temperatures for nanocrystalline materials. Table 8.1 compares experimental values of specific heat for several nanocrystalline and bulk materials at high temperatures. For some materials, the enhancement of specific heat is significant (palladium, copper, ruthenium, and diamond), for others ($Ni_{80}P_{20}$ and selenium) it is negligible.
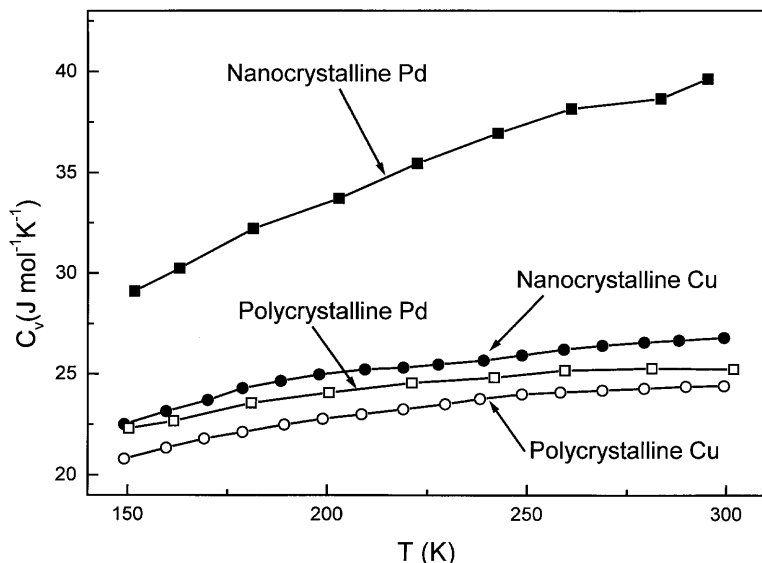
**FIGURE 8.2**   Specific heat ($C_v$) of polycrystalline and nanocrystalline palladium and copper at high temperatures. Solid lines are drawn to guide the eye. Figure based on reference 5. Used with permission from J. Rupp and R. Birringer, Enhanced specific-heat capacity ($C_p$) measurements, (150–300 K) of nanometer-sized crystalline material, *Physical Review B*, *36* (15), **1987**, 7888, The American Physical Society 1987.

*Low Temperatures.*   The results obtained by H. Y. Bai, J. L. Luo, D. Jin, and J. R. Sun[8] are typical for low-temperature studies of specific heats of nanoparticles. The authors measured specific heat of nanocrystalline iron particles at very low temperatures (below 25 K). The sample studied was prepared by a thermal evaporation method and the resulting particles were 40 nm in size as determined by transmission electron microscopy. The experimentally obtained specific heats of bulk (polycrystalline) iron and nanocrystalline iron are shown in Figure 8.3. The specific

**TABLE 8.1   Comparison of experimental specific heats for selected nanocrystalline and polycrystalline materials. Significant enhancement is evident for palladium, copper, ruthenium, and diamond; the effect is negligible for Ni$_{80}$P$_{20}$ and selenium**

| Material | $C_p$ (J mol$^{-1}$ K$^{-1}$) Polycrystalline | Nanocrystalline | Enhancement (%) | Nanocrystallite Size (nm) | Temperature (K) | Ref. |
|---|---|---|---|---|---|---|
| Pd | 25 | 37 | 48 | 6 | 250 | 5 |
| Cu | 24 | 26 | 8.3 | 8 | 250 | 5 |
| Ru | 23 | 28 | 22 | 15 | 250 | 6 |
| Ni$_{80}$P$_{20}$ | 23.2 | 23.4 | 0.9 | 6 | 250 | 6 |
| Se | 24.1 | 24.5 | 1.7 | 10 | 245 | 6 |
| Diamond | 7.1 | 8.2 | 15 | 20 | 323 | 7 |

heat for nanocrystalline iron is larger compared to bulk iron for temperatures above approximately 10 K. The specific heat for bulk iron was found to closely follow the Debye–Sommerfeld relation (Equation 8.8). The relative strengths of electronic and lattice vibration contributions were obtained by fitting to experimental data. The specific heat for nanocrystalline iron followed approximately the Debye–Sommerfeld model, although Figure 8.3 indicates a possibility of other contributions. The authors suggested that besides the usual $T$ and $T^3$ terms the specific heat of nanocrystalline iron contains a $T^2$ contribution and a component similar to that predicted by the Einstein model. For the purpose of this simplified description we do not discuss these effects and focus only on electronic and lattice vibration contributions. The electronic contribution to specific heat (as determined by the intercept on a $C_p/T$ versus $T^2$ plot) is reduced by 41% for nanocrystalline iron. The reduction of the electronic contribution to specific heat was first recognized by H. Fröhlich in 1937.[9] This observation was supplemented in 1962 by R. Kubo,[10] who published a theoretical study calculating the changes in electronic properties of small metal particles. This paper predicted changes in magnetic resonance, infrared and optical absorption, specific heat, electronic susceptibility, and Knight shift. The Kubo theory predicts that for nanoparticles at low temperatures (below a few kelvins), the electronic contribution to specific heat will be reduced to two-thirds of its bulk value. The reduction of the Sommerfeld constant by 41%, as observed for nanocrystalline iron, supports this prediction. A detailed description of Kubo theory is beyond the scope of this chapter. The lattice vibration contribution for nanocrystalline iron (as determined by the slope on a $C_p/T$ versus $T^2$ plot) is twice that of polycrystalline iron and this effect is responsible for the increase in the overall specific heat.
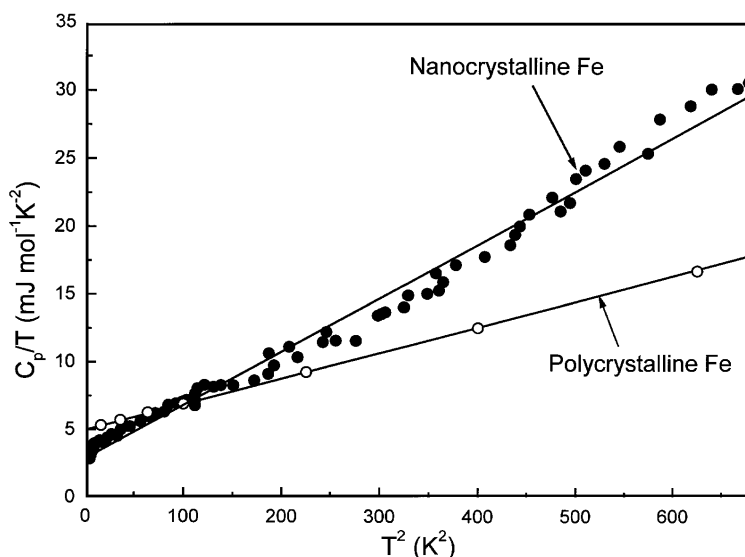


**FIGURE 8.3** Plot of $C_p/T$ versus $T^2$ for nanocrystalline and polycrystalline iron. Solid lines represent linear fits described in the text. Figure based on reference 8. Reprinted with permission from Bai et al, *Journal of Aplied Physics*, 79 (1), **1996**, American Institute of Physics.
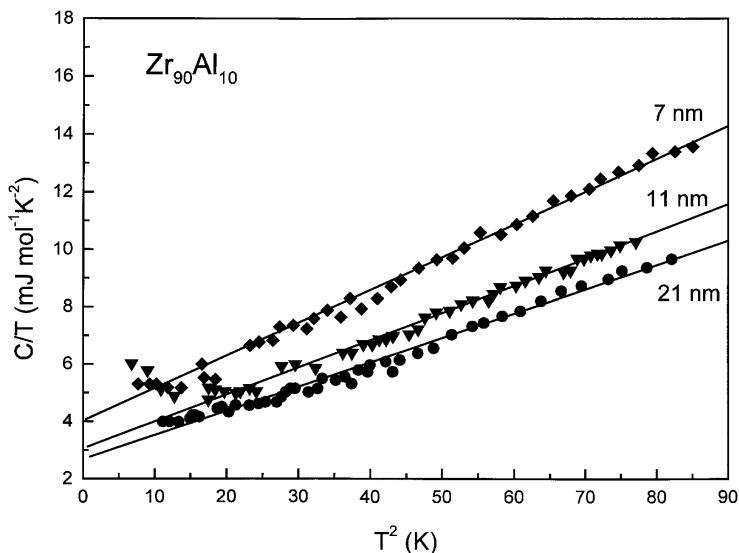
**FIGURE 8.4** Experimental values of specific heat for $Zr_{90}Al_{10}$ nanocrystallites in a $C/T$ versus $T^2$ plot. Figure based on reference 11. Reprinted with permission from U Herr et al, *Philosophical Magazine A*, **77**:3, (1998) p. 646.

Another example of low-temperature studies is the work of U. Herr, H. Geigl, and K. Samwer,[11] in which the specific heat of nanocrystalline $Zr_{1-x}Al_x$ alloy was measured. The results of this study are illustrated in Figure 8.4 for 7 nm, 11 nm, and 21 nm particles. Experimental data points roughly follow a linear relation between $C_p/T$ and $T^2$ indicating that the Debye–Sommerfeld model applies for this material. Since in this work nanoparticles of different sizes were investigated, correlation between the size and the specific heat can be made. Figure 8.4 indicates that the specific heat increases with decrease in the particle's size.

Results presented above for high- and low-temperature materials demonstrate enhancement in the specific heat except at the lowest temperatures, below a few kelvins. This general finding was reproduced throughout the literature for a number of nanocrystalline materials. However, it needs to be pointed out that there is no well-established intuitive explanation for this effect. Clearly, the answer must be connected with the small sizes of the particles, the large number of surface atoms, or effects associated with interparticle grain boundaries. Perhaps this issue will soon be clarified since the specific heats of nanocrystals are still being investigated by various research groups.

## 8.3 MELTING POINTS OF NANOPARTICLE MATERIALS

The melting point characteristic for a given material is the transition temperature between solid and liquid phase. It is also the temperature above which the crystalline structure of the solid disappears and is replaced by unordered atomic arrangement in

the liquid. It was first recognized by M. Takagi in 1954[12] that nanosized particles melt below their corresponding bulk melting temperatures. Since that time various experiments have demonstrated this effect for different nanocrystalline materials. The sections below present typical experimental results and two models used to describe this phenomenon.

### 8.3.1   Thermodynamic Predictions of the Melting Temperatures of Nanomaterials

The lowering of the melting point for nanocrystals can be explained using thermodynamic considerations. These arguments not only predict changes in the melting point for small particles but also help to understand the process of surface melting. The transition from solid to liquid as the temperature increases will start at the surface of the particle, with the internal core still preserved as a solid. This surface melting is due to the surface tension at the solid–liquid interface affecting the energy balance of the system. Suppose that a small solid spherical particle with radius $r$ is at equilibrium with surrounding liquid shell, as shown in Figure 8.5. The infinitesimally small outer layer of the solid particle melts such that a mass $dw$ of the material goes from solid to liquid phase. This change in the particle's mass and its size will result in an infinitesimally small reduction of the particle surface area, $dA$. For a spherical particle the relationship between $dw$ and $dA$ is

$$\frac{dA}{dw} = \frac{2}{\rho r} \tag{8.9}$$

where $\rho$ is the density of the material. The energy balance associated with this change can be expressed as follows:

$$\Delta U \, dw - \Delta S \, \theta_r \, dw - \sigma \, dA = 0 \tag{8.10}$$

where $\Delta U$ is the change of internal energy and $\Delta S$ is the change of entropy per unit mass of a metal during melting, $\sigma$ is the surface tension coefficient for a liquid–solid
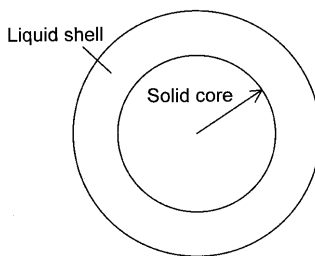


**FIGURE 8.5**   Illustration of the surface melting phenomena during melting of small particles. The solid core is in equilibrium with the surrounding liquid shell.

interface, and $\theta_r$ is the melting temperature of a small particle. A similar expression for a bulk material does not contain the surface tension term:

$$\Delta U \, dw - \Delta S \, T_0 \, dw = 0 \tag{8.11}$$

where $T_0$ is the melting temperature of the bulk material. From Equation (8.11) and the assumption that $\Delta U$ and $\Delta S$ are independent of temperature, the entropy change can be expressed as

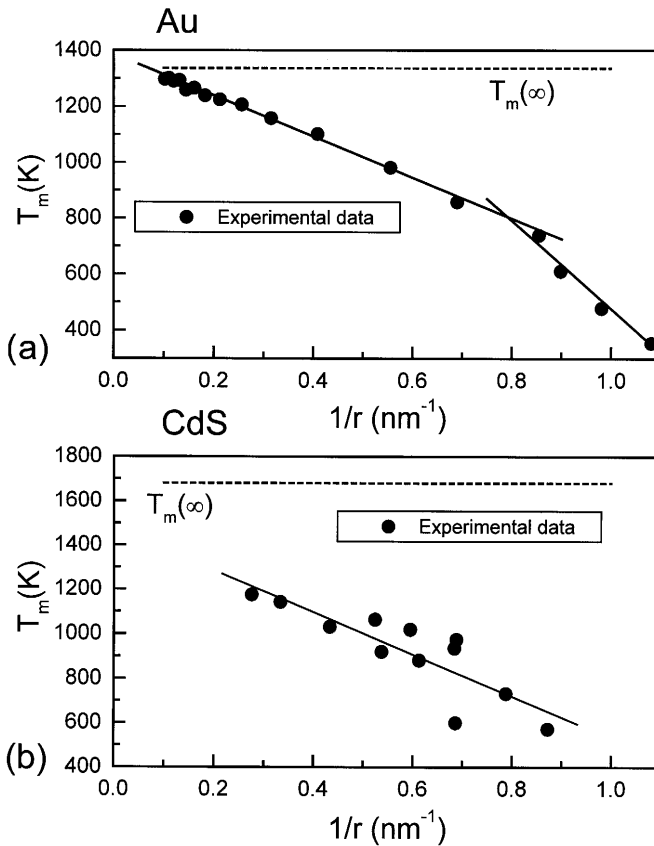$$\Delta S = \frac{\Delta U}{T_0} = \frac{L}{T_0} \tag{8.12}$$



**FIGURE 8.6** Dependence of the melting temperature $T_m$ on the size for (a) gold and (b) CdS nanocrystals: a test of the $1/r$ relation predicted by the thermodynamical relation (8.13). Figure based on reference 13 and references therein. Used with permission.

where $L$ is the latent heat of fusion. From Equations (8.9), (8.10), and (8.12), the following estimate for the lowering of the melting temperature can be derived:

$$\Delta\theta = T_0 - \theta_r = \frac{2T_0\sigma}{\rho L r} \qquad (8.13)$$

This relation predicts that the lowering of the melting point is inversely proportional to the first power of the particle size. The above equation can be used to determine the lowering in the melting temperature if all quantities appearing on the right-hand side are known. However, frequently the surface tension coefficient $\sigma$ is unknown, but it can be obtained from Equation (8.13) if the melting temperature of the nanocrystal is measured. By plotting the experimentally obtained melting temperatures of small particles as a function of their radius or diameter, the $1/r$ relationship can be tested. If the experimental points follow a straight line, Equation (8.13) holds. Generally, experiments of this type yield satisfactionary $1/r$ dependence if small ranges of particle sizes are considered. This is illustrated in Figure 8.6, which shows the lowering of the melting point for nanocrystalline gold and cadmium sulfide particles.[13] For cadmium sulfide nanoparticles, which have a limited size range and show significant scatter in measured melting temperatures, the experimental points approximately follow a straight line. Gold nanoparticles do not exhibit as large a scatter and have a bigger size range. The entire range of data points does not follow a straight line, but considering small and large particles separately the $1/r$ relation is valid. The more interesting feature of the data presented in Figure 8.6 is a very large lowering of melting temperature for small particles. For gold particles in the 1 nm range, the melting temperature can be as much as 900 K lower than the corresponding bulk value. For cadmium sulfide nanoparticles, the shift is also very significant, approaching 1000 K.

## 8.3.2   Melting Temperatures of Nanomaterials Described in Terms of Atomic Vibrations

The melting behavior of small particles can be understood in terms of the Lindemann criterion,[14] which states that a crystal will melt when the root-mean-square displacement of the atoms in the crystal, $\delta$, exceeds a certain fraction of the interatomic distance $a$:

$$\frac{\delta}{a} \geq \text{const.} \qquad (8.14)$$

As the temperature increases, the amplitude of oscillations increases, and at a certain temperature these oscillations are strong enough to break the crystal structure of a solid and cause melting. Surface atoms are not as strongly bound and can experience higher-amplitude vibrations at a given temperature than can atoms within

the volume of the particle. This effect can be described by the ratio of mean-square atom displacement on the surface, $\delta_s$, and inside of the particle, $\delta_v$:

$$\alpha = \frac{\delta_s}{\delta_v} \tag{8.15}$$

The value of parameter $\alpha$ is typically 2 to 4. Since nanoparticles have very large fractions of atoms on the surface (for 3 nm spherical particles about 50% of the atoms are on the surface), their oscillations will significantly affect the Lindemann criterion. This reasoning is consistent with the surface melting and can be used to quantitatively evaluate the lowering of the melting temperature without the thermodynamic arguments presented above. F. G. Shi[13] developed a theoretical model that describes the lowering of melting points of nanoparticles. In this model the mean-square atom displacement averaged over the entire volume of the particle,
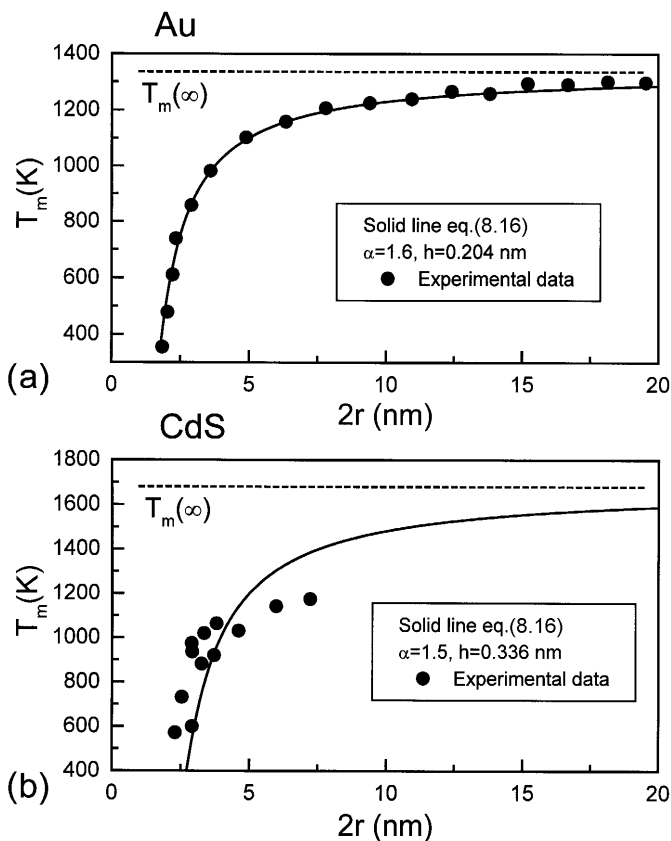


**FIGURE 8.7** Dependence of the melting temperature $T_m$ on the size for (a) gold and (b) CdS nanocrystals: a test of the model by Shi and Equation (8.16). Figure based on reference 13 and references therein. Used with permission.

including its surface, was evaluated. As the particle size decreases, the increased number of surface atoms enhances the average value of atomic displacement. According to the Lindemann criterion this causes a decrease in the melting temperature. On the basis of these arguments Shi derived the following relation for a melting temperature:

$$\frac{T_m(r)}{T_m(\infty)} = \exp\left[-(\alpha-1)\left(\frac{r}{3h}-1\right)^{-1}\right] \tag{8.16}$$

where $T_m(r)$ is the melting temperature of a nanocrystal, $T_m(\infty)$ is the melting temperature of the bulk material (both expressed in kelvins), and $h$ corresponds to the height of a monolayer of atoms in its crystal structure. This equation can be used to predict the lowering of the melting point for nanocrystals if the parameter $\alpha$ is known. In practice this is not the case and parameter $\alpha$ is adjusted to fit experimental data. Figure 8.7 shows melting temperatures for gold and CdS nanoparticles as a
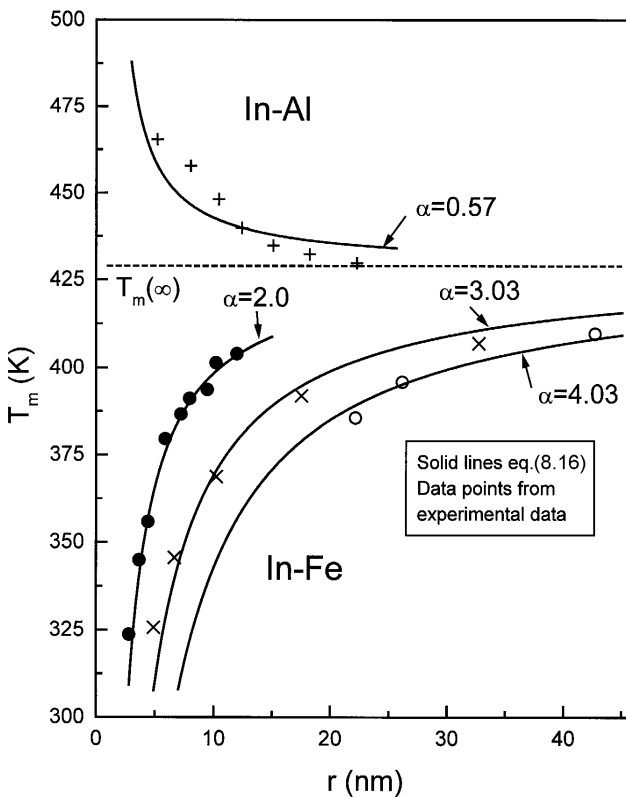


**FIGURE 8.8**  Dependence of the melting temperature $T_m$ on the size for indium nanocrystals in aluminum and iron matrices. Figure based on reference 13 and references therein. Used with permission.

function of the particle size. The solid lines represent predictions from Shi's model given by Equation (8.16). There is excellent agreement between the theory and experimental data for gold and fair agreement for CdS nanoparticles.

Some nanocrystalline materials consist of nanoparticles embedded in another solid material. As shown by experiments, in such a case the melting temperature can be lower or higher than the bulk value depending on the specific combination of nanoparticle and matrix material. For instance, indium nanocrystals will exhibit lower melting temperature when embedded in an iron matrix but an increase in the melting temperature in an aluminum matrix. Figure 8.8 presents these effects as a function of particle size. Interestingly, Equation (8.16) can still be applied to describe increased melting temperature, if the value of parameter $\alpha$ is less than 1. This occurs, according to Equation (8.15), for smaller amplitude of vibrations on the surface than in the bulk, a situation that is plausible if the surface atoms interact strongly with the matrix material. Figure 8.8 shows reasonable agreement for indium nanoparticles in various matrices.

## 8.4   SUMMARY

In summary, the melting points of nanoparticles can be substantially different from the corresponding values of the bulk materials. The difference can be as large as 1000 K in some instances. For free nanoparticles the melting temperature is always lower than the bulk value. In the case of nanoparticles embedded in a solid matrix, the melting point may be lower or higher, depending on the strength of interaction between the nanoparticles and the matrix. There are two explanations used in the literature for this phenomenon. The first is based on thermodynamic considerations and the importance of the surface tension at the solid–liquid interface during melting. The second approach considers amplitudes of atomic vibrations for bulk and surface atoms and uses the Lindemann criterion to evaluate changes in the melting point.

## REFERENCES

1. A. Einstein, *Ann. Phys.*, **1906**, *22*, 180–190.

2. P. Debye, *Ann. Phys.*, **1912**, *39*, 789–839.

3. R. H. Perry, D. W. Green, *Perry's Chemical Engineers' Handbook*, 7th edition, McGraw-Hill, New York, **1997**.

4. N. W. Ashcroft, N. D. Mermin, D. Mermin, *Solid State Physics*, Harcourt College Publishers, New York, **1976**.

5. J. Rupp, R. Birringer, *Phys. Rev. B*, **1987**, *36*(15), 7888–7890.

6. N. X. Sun, K. Lu, *Phys. Rev. B*, **1996**, *54*(9), 6058–6061.

7. C. Moelle, M. Werner, F. Szücs, D. Wittorf, M. Sellschopp, J. von Borany, H. J. Fecht, C. Johnston, *Diamond Relat. Mater.*, **1998**, *7*, 499–503.

 8. H. Y. Bai, J. L. Luo, D. Jin, J. R. Sun, *J. Appl. Phys.*, **1996**, *79*(1), 361–364.

 9. H. Fröhlich, *Physica*, **1937**, *4*, 406–412.

10. R. Kubo, *J. Phys. Soc. Japan*, **1962**, *17*, 976–986.

11. U. Herr, M. Geigl, K. Samwer, *Phil. Mag. A*, **1998**, *77*(3), 641–652.

12. M. Takagi, *J. Phys. Soc. Japan*, **1954**, *9*, 359–363.

13. F. G. Shi, *J. Mater. Res.*, **1994**, *9*(5), 1307–1313.

14. F. A. Lindemann, *Phys. Z.*, **1910**, *11*, 609–612.

# 9    Applications of Nanocrystals

JOHN PARKER

Cirqon Technologies Corp.
Gurnee, IL

## 9.1    INTRODUCTION

The driving force behind the fundamental research into nanocrystals is the perceived and demonstrated properties that can be exploited into applications. The application of these properties falls largely into two broad categories: improved properties and unique properties. The improved, or incremental, group covers those applications that have already been conceived but can benefit from the use of nanocrystals in terms of either particle size or surface area. Many of these types of applications have found nearly instant commercial success and have opened the door to larger use. The "unique" group of applications is a smaller set but holds the greatest potential. This group consists of properties that are exclusively attributed to nanostructuring and includes electronic and optical quantum confinement effects, superparamagnetism, and ceramic superplasticity, to name a few. To date, these have created niche commercial opportunities, but acceptance and interest are growing.

In this chapter we will present a variety of applications associated with nanocrystals and nanostructure engineering. The intent is to give the reader an overview of the current state of the art as well as a look into the future use of nanocrystals in commercial and industrial applications.

## 9.2    HISTORICAL

One might ask, whether nanocrystals are really new. The answer would have to be yes and no, with a qualification for each. For over a century the properties of small particles have been exploited in applications ranging from catalysis to the colors of stained glass. Some of the earliest recorded evidence came in 1856 when Michael

Faraday discovered that nanometer-sized particles create the color variations of metal-particle colloids through surface charge effects. He found that colloids of 6 nm gold particles are red and those of 12 nm particles are blue. There is even evidence that nature has made use of nanoparticles in areas of biomineralization that take place in bones and teeth. The reason we might say that nanostructuring is new is largely attributable to the developments of modern science as it has investigated the ever-shrinking world of matter. Advances in theoretical and experimental tools and techniques have increased our understanding of matter in both the micro and the nano regimes, largely motivated by the development of applications and technology. Consider the development of atomic force and scanning tunneling microscopy that has led to sophisticated machines that change the landscape of surfaces atom by atom. An obvious example of this revolution is in the world of semiconductor electronics, which is driven by the demand to reduce the size of circuits, pushing the envelope of both science and technology. This applies not only to materials, but to a host of areas including optics, manufacturing, chemicals, and electronic design.

## 9.3   STRUCTURAL AND MECHANICAL MATERIALS

The initial investigation of nanostructuring began with the property enhancements of bulk materials that were assembled entirely or partially from nanoparticles. The earliest work began with metals that demonstrated a transfer from normal, soft ductility to a hard, brittle nature when nanostructuring occurred. A similar property reversal effect was later discovered in brittle ceramic materials that could be made ductile at temperatures near one-half their melting point. Some of the earliest commercial development in nanostructuring was focused on these unique properties. For example, improved properties of cutting tool materials have been achieved through the nanostructuring of materials like tungsten carbide (WC), which benefits in hardness and toughness via nanoscale distribution of tungsten particles throughout the matrix. Increases in tool life and performance have been commercially established as a result of this technology.

In the case of a technical ceramic material, usually desired for their mechanical and chemical features, the fabrication of shapes or components is largely through traditional "whiteware" processing followed by extensive machining and finishing. In some cases, the machining and finishing operations are not only costly but can also introduce defects and flaws that lower the predictable strength of the component. Nanostructuring is changing the way in which ceramic components can be fabricated, by making use of the enhanced ductility property. This is due to the fact that plastic flow rate (strain rate) of ceramics is inversely proportional to the cube of the grain dimensions. Plastic shaping of metals is applied to several aluminum metal alloys used in aerospace applications. These metals are superplastically formed to net shape components, at strain rates of 5–6% per minute, in a closed die system, allowing full replication of the die geometry. To date, several ceramic compositions are achieving or approaching these strain rates, through the use of nanostructuring, making use of the inverse relation to particle size. Parts with high dimensional tolerances can be forged from nanostructured ceramic preforms in less than half an
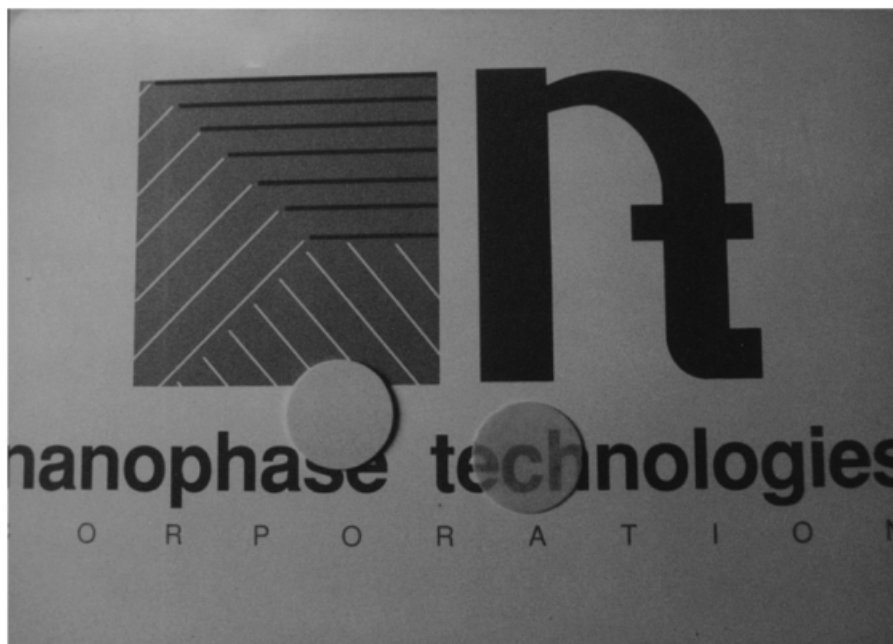
**FIGURE 9.1**   The ceramic disks show the behavior of physical vapor synthesized (PVS) nanocrystals that were formed with weak and strong agglomeration. The weak agglomerates break down easily to form the transparent disk on the right, while the strong agglomerates create a coarse pore structure, resulting in the opaque sample on the left. Used with permission from *Nanomaterials: Synthesis, Properties and Applications*, edited by A. S. Edelstein and R. C. Cammarata, **1996**, IOP Publishing.

hour. Figure 9.1 shows an engine valve seat that was superplastically stamped in a manner of minutes.

To achieve the benefits of ceramics (wear, hardness, corrosion resistance) while maintaining the ambient ductility of metals, several methods of coating metals with ceramics have been developed. In many of these methods, nanostructuring or nanocrystals have played a major role in improving the end-use properties. For example, oxide nanocrystals have been thermal-plasma sprayed onto metal surfaces, forming dense, hard coatings that are superior to coatings made with conventional micron size particulates. Nearly fourfold increases in wear resistance of nanocrystal plasma spray coatings have been observed. Other nanocrystal coatings have been formulated for a variety of uses including wear-resistant laminate floorings, where thin layers of aluminum oxide are bound to synthetic material surfaces in thin layers.

## 9.4   COLORANTS AND PIGMENTS

Significant research and development of ultraviolet (UV) light-attenuating pigments has taken place in the past decade, due to an increased awareness of the degradation effects of solar radiation. Protection of synthetic and natural substances has been the

**FIGURE 9.2**    A plastically forged ceramic component moldined from a nanostructure, dense preform. The forming operation was performed at 1400 C in less than 15 minutes. Used with permission from *Nanomaterials: Synthesis, Properties and Applications*, edited by A. S. Edelstein and R. C. Cammarata, **1996**, IOP Publishing.


focus of a host of industrial applications; ranging from colored fabrics to human skin. Inorganic particles have long served as optical opacifiers and "whiteners" in a wealth of commercial and industrial products, where particle sizes can be tailored to provide the highest degree of optical light scattering. For example, thousands of tons of titanium dioxide ($TiO_2$) are synthesized every year to provide whitening of a variety of products ranging from paint coatings to low-fat dairy substitutes. When the same material, and others like it, are reduced to the nanometer size regime it has been discovered that the scattering efficiency shifts to the higher-frequency UV light range, in particular to the UVA and UVB regions (200–400 nm), which produces the highest degradation of organic materials. In addition to a more efficient scattering in the UV range the nanosizing reduces optical scattering and allows for the passage of visible light. Therefore, coatings made from these nanometer pigments form optically transparent films that attenuate harmful UV radiation. This effect is most obvious from the photograph (Figure 9.2) that shows two powder consolidated disks. The transparent disk was formed by the ambient consolidation of nanocrystals that are 10 nm in dimension. Both pores and solid grains are well below the wavelength of visible light and thus allow light to pass through. The opaque disk was formed by the ambient consolidation of 100 nm particles that easily scatter visible light, thus forming an optically opaque system.

Inkjet printer inks generally make use of dyes or pigments to provide color. Dye-based inks provide a high chroma, while pigmented inks offer a high lightfastness but poor hue and saturation. This effect is generally attributed to the particle size distributions that overlap the dimensions of the optical wavelengths. New, nanometer-sized pigments are being developed to overcome the limitations of conventional pigment technology. Pigments with average particle sizes in the 10–20 nm range, creating the standard cyan, magenta, and yellow colors, display a greatly improved printed color that is superior to that of commercially available dye-based inks. In addition, the colorfastness can be dramatically improved due to the UV-attenuating effects discussed above.

## 9.5   BIOMEDICAL APPLICATIONS

A wealth of interest has developed for nanocrystals as applied to health and biological systems. In the area of medical diagnostics, colloidal or imbedded iron-based particles are being used to separate specific substances present in body fluid samples. Antibodies can be attached to magnetic colloidal particles, typically silica-coated iron oxides or polystyrene spheres with embedded iron oxides; when these are mixed with a blood sample the antibody reacts and binds with the target hormone. Because the nanoparticle size creates both high surface area for reaction and a tendency to move rapidly in solution due to thermal Brownian motion, reactions can be quite rapid. The magnetic functionality of the particle permits detection of the antibody/hormone complex by separating and concentrating the reacted material from the blood sample. Even DNA detection through colorimetric techniques has been developed through the use of oligonucleotide-functionalized gold nanocrystals that can be assembled into periodic network materials.

Similar particles are also being developed for drug delivery. In this application, biochemical drugs can be bound to the magnetic nanocrystals and with applied magnetic fields can be steered into regions of the body where they are required. For example, malignant tumors can be attached with targeted drug delivery and concentration through the use of magnetic fields. Rare, tumor-causing cells can also be targeted by nanocrystals with attached chemicals that bind to the cells and sweep them from the bloodstream before they have had a chance to degrade. Some previous examples showed that 100 tumor cells could be captured and removed from 50 million blood cells in less than one hour.

## 9.6   ELECTRONICS AND MAGNETICS

Many of the applications that have developed and will develop in this area can be attributed to the "unique" properties that create new physics for the industry. As discussed in previous chapters, the quantum confinement effects observed in important semiconductors like silicon will reshape the way in which electronic and optoelectronic devices are designed and made. Thirty years of development have gone into two-dimensional quantum electronics through thin-film processing. Less

than a third of that time has been spent in the three-dimensional nanoparticle world, and already a series of devices and fabrication methods have emerged. Proof-of-principle heterojunction devices based on three-dimensional quantum confinement have been fabricated, but materials and long-term performance may inhibit immediate application. Developments with silicon-based quantum confined devices are progressing, and when completed will offer better economics and performance. From this effort commercially robust digital switching devices can be fabricated and integrated into $10^{12}$ devices on a single chip.

Some semiconducting, metal-oxide nanocrystal thick films are being screen-printed into high-sensitivity, high-selectivity environmental sensor devices. Sensor materials are highly dependent on grain size, especially as dimensions approach the Debye length where space charge depth becomes a factor. Both n-type and p-type materials are designed to sense gaseous chemicals such as CO, NO, $NO_2$, and $O_3$ in high-pollution environments. Although commercial products based on nanocrystal thick-film sensors are still under development, field tests have shown that low-cost sensor arrays can be fabricated with accuracy approaching that of a high-cost gas analysis system. This type of breakthrough in sensor technology would allow routine monitoring of high-traffic environments in densely populated areas, where pollutants could be studied for traffic pattern adjustments.

Electroluminescent devices will also benefit from nanocrystal technology. Electroluminescence results from the optical recombination of electrons with holes that are injected into the active semiconductor. The color of the emission is completely dependent on the semiconductor bandgap. Bandgap tailoring can be achieved through the size effects of nanoparticles such as those of CdSe and other II–IV compounds. When these band-gap-engineered donor-type particles are contacted to a hole-carrying material like a polymer, an applied electric field can introduce carriers that recombine and emit light. Through the use of successive layers of tailored particles, a palette of colors can be generated. Materials such as these can be used in a variety of flat-panel display technologies, such as signs, computer monitors, and televisions, or in color-changing fabrics for decorative applications. Some groups are investigating the fabrication of such devices utilizing elastomeric pad-transfer printing or the inkjet printing methodologies discussed above, where color images can be easily patterned in computer-aided design fashion. These same nonlithographic techniques also create an opportunity to fabricate large-area, low-cost electronic devices that are currently being developed with organic materials. For this application, inorganic nanocrystals offer superior electrical properties compared to organic materials, especially when conductor mobility greater than 1 cm$^2$ V$^{-1}$ s$^{-1}$ can be achieved.

Through a set of chemical reactions using iron and platinum, newly discovered magnetic nanoparticles have been found to self-arrange automatically. Chemical reactions of this type could lead to the mass fabrication of precision materials with controlled particle size and spacing. The separation and size of these particles are expected to lead to magnetic storage devices that have 100 times the density of current, state-of-the-art magnetic disk technology, allowing terabyte storage capabilities.

## 9.7   CONCLUSIONS

Nanocrystals and nanotechnology are rapidly developing into a stand-alone industry that covers a host of applications and industries. As the science and technology grows, it will reach several stages of commercial success over the next five to ten years. Most of the current commercial activity has been centered on marginal to significant improvements of existing consumer and industrial products. However, nano-only type applications exist today in many academic, governmental, and industrial laboratories around the United States and the world, and many are beginning to emerge while many more are being conceived. In the decades to come, nanocrystals and nanotechnology will permeate many of the products and technologies we use in our daily lives, either directly or indirectly.